TU Dortmund University

Department of Chemistry and Chemical Biology

Charge-Neutral Zn(II) Helicates for Chiroptical Recognition and Guest Exchange

Dissertation submitted for the degree of

Doctor rerum naturalium (Dr. rer. nat.)

Malavika G. Kalarikkal

Dortmund, November 2025

technische universität dortmund

This work has been conducted from November 2021 to October 2025 at the Department of Chemistry and Chemical Biology, TU Dortmund University.

1st examiner:	Dr. David Van Craen Department of Chemistry and Chemical Biology TU Dortmund University
2nd examiner:	Prof. Dr. Guido H. Clever Department of Chemistry and Chemical Biology TU Dortmund University
Submission date:	13.11.2025

A course more promising
Than a wild dedication of yourselves
To unpathed waters, undreamed shores ...
— The Winter's Tale, William Shakespeare

Eidesstattliche Versicherung (Affidavit)

_____ _____

Name, Vorname
(Surname, first name)

Matrikel-Nr.
(Enrolment number)

Belehrung:

Wer vorsätzlich gegen eine die Täuschung über Prüfungsleistungen betreffende Regelung einer Hochschulprüfungsordnung verstößt, handelt ordnungswidrig. Die Ordnungswidrigkeit kann mit einer Geldbuße von bis zu 50.000,00 € geahndet werden. Zuständige Verwaltungsbehörde für die Verfolgung und Ahndung von Ordnungswidrigkeiten ist der Kanzler/die Kanzlerin der Technischen Universität Dortmund. Im Falle eines mehrfachen oder sonstigen schwerwiegenden Täuschungsversuches kann der Prüfling zudem exmatrikuliert werden, § 63 Abs. 5 Hochschulgesetz NRW.

Die Abgabe einer falschen Versicherung an Eides statt ist strafbar.

Wer vorsätzlich eine falsche Versicherung an Eides statt abgibt, kann mit einer Freiheitsstrafe bis zu drei Jahren oder mit Geldstrafe bestraft werden, § 156 StGB. Die fahrlässige Abgabe einer falschen Versicherung an Eides statt kann mit einer Freiheitsstrafe bis zu einem Jahr oder Geldstrafe bestraft werden, § 161 StGB.

Die oben stehende Belehrung habe ich zur Kenntnis genommen:

Official notification:

Any person who intentionally breaches any regulation of university examination regulations relating to deception in examination performance is acting improperly. This offence can be punished with a fine of up to EUR 50,000.00. The competent administrative authority for the pursuit and prosecution of offences of this type is the chancellor of the TU Dortmund University. In the case of multiple or other serious attempts at deception, the candidate can also be unenrolled, Section 63, paragraph 5 of the Universities Act of North Rhine-Westphalia.

The submission of a false affidavit is punishable.

Any person who intentionally submits a false affidavit can be punished with a prison sentence of up to three years or a fine, Section 156 of the Criminal Code. The negligent submission of a false affidavit can be punished with a prison sentence of up to one year or a fine, Section 161 of the Criminal Code.

I have taken note of the above official notification.

_____ _____

Ort, Datum
(Place, date)

Unterschrift
(Signature)

Titel der Dissertation:
(Title of the thesis):

_____

_____

_____

Ich versichere hiermit an Eides statt, dass ich die vorliegende Dissertation mit dem Titel selbstständig und ohne unzulässige fremde Hilfe angefertigt habe. Ich habe keine anderen als die angegebenen Quellen und Hilfsmittel benutzt sowie wörtliche und sinngemäße Zitate kenntlich gemacht.
Die Arbeit hat in gegenwärtiger oder in einer anderen Fassung weder der TU Dortmund noch einer anderen Hochschule im Zusammenhang mit einer staatlichen oder akademischen Prüfung vorgelegen.

I hereby swear that I have completed the present dissertation independently and without inadmissible external support. I have not used any sources or tools other than those indicated and have identified literal and analogous quotations.

The thesis in its current version or another version has not been presented to the TU Dortmund University or another university in connection with a state or academic examination.*

*Please be aware that solely the German version of the affidavit ("Eidesstattliche Versicherung") for the PhD thesis is the official and legally binding version.

_____ _____

Ort, Datum
(Place, date)

Unterschrift
(Signature)

Abstract

The discipline of anion recognition chemistry is integral to the domain of supramolecular chemistry, with the primary aim of formulating receptors that can selectively bind anions, particularly under competitive conditions. The field has witnessed substantial progress through the innovation of our charge-neutral double-stranded zinc(II) helicates. These helicates are designed to facilitate high-affinity binding of various aliphatic and aromatic dicarboxylates that are both environmentally and biologically significant. Notably, the hydroxyquinoline-based L_2Zn_2 helicates demonstrate remarkable binding constants that exceed $10^{8}\,M^{-1}$, enabling the size-selective binding of dicarboxylate anions at nanomolar concentrations. This helicate effectively bridges the gap between conventional organic and charged metal-assembled receptors, providing a stable, charge-neutral platform that is resistant to interference from counter anions.

Building on this high-affinity anion recognition, we explored the chiroptical properties of zinc(II) helicates that incorporate stereodynamic quinolinate zinc complex units to form either a *meso* structure or racemic mixtures of right- and left-handed helicates. Upon the specific recognition of chiral mono- or dicarboxylates, these helicates demonstrate distinct circular dichroism (CD) responses, facilitating precise chirality analysis and determination of enantiomeric excess. Notably, the binding of tartrate results in the enrichment of one of the helicate enantiomers within the racemic population, producing pronounced Cotton effects in the CD spectrum. This receptor-based methodology offers high-throughput screening capabilities with minimal solvent use and waste generation, presenting a practical alternative to chromatographic techniques that depend on chiral stationary phases.

The strong coordinative interaction with the guest is advantageous in most cases, as it provides high binding constants and enables highly sensitive recognition of carboxylates even at nanomolar levels. However, this interaction poses challenges in the release of the guest from the system. The helicate's notable size-selectivity for various guests, which could be a beneficial characteristic for sensing applications, is compromised by the inability to achieve controlled guest release within the coordination framework. In an approach to establish a controlled release mechanism for guests without necessitating alterations to the host framework, which could potentially modify its inherent properties, a stimuli-responsive guest was incorporated into the system. Azobenzene-4,4'-dicarboxylate, which can utilize its light- and temperature-responsive isomerization states, serves as a competing guest within the L_2Zn_2 receptor. The size difference between its bent *cis* isomer and its extended *trans* form permits the selective accommodation of the former within the zinc pocket, thereby facilitating photo- and thermally induced guest exchange cycles in the presence of

a secondary, non-photoactive guest. The azobenzene guest's transition between its different geometric states provides a mechanistic pathway for the second guest to bind and release in a controlled manner.

In order to further exploit the selective binding properties, we aimed to design a colorimetric sensor unit for the helicate in the context of guest binding. To achieve this, the host design was modified by integrating a triphenylamine (TPA) unit into the backbone, with the intention of enhancing the photophysical properties of the host. Although the assembly was successfully executed, it did not result in the anticipated improvements. Subsequent investigations involving environmentally relevant perfluorinated guests revealed low-affinity behavior. The incorporation of TPA as a donor moiety in this new receptor design may open up potential applications in donor-acceptor systems and related fields.

Zusammenfassung

Die Disziplin der Anionenerkennungschemie ist ein wesentlicher Bestandteil der supramolekularen Chemie, deren primäres Ziel die Entwicklung von Rezeptoren ist, die selektiv Anionen binden können, insbesondere unter kompetitiven Bedingungen. Durch die Innovation unserer ladungsneutralen doppelsträngigen Zink(II)-Helikate wurden in diesem Bereich erhebliche Fortschritte erzielt. Diese Helikate wurden entwickelt, um die hochaffine Bindung verschiedener aliphatischer und aromatischer Dicarboxylate zu erleichtern, die sowohl ökologisch als auch biologisch von Bedeutung sind. Insbesondere die auf Hydroxychinolin basierenden L_2Zn_2-Helikate weisen bemerkenswerte Bindungskonstanten von über $10^{8}\,M^{-1}$ auf, was die größenabhängige Bindung von Dicarboxylatanionen in nanomolaren Konzentrationen ermöglicht. Dieses Helikat schließt effektiv die Lücke zwischen herkömmlichen organischen und geladenen metallbasierten Rezeptoren und bietet eine stabile, ladungsneutrale Plattform, die gegen Störungen durch Gegenanionen resistent ist.

Aufbauend auf dieser hochaffinen Anionenerkennung untersuchten wir die chiroptischen Eigenschaften von Zink(II)-Helikaten, die stereodynamische Chinolinat-Zink-Komplexeinheiten enthalten und entweder eine *meso*-Struktur oder racemische Mischungen aus rechts- und linksdrehenden Helikaten bilden. Bei der spezifischen Erkennung von chiralen Mono- oder Dicarboxylaten zeigen diese Helikate deutliche zirkuläre Dichroismuseffekte (CD), was eine präzise Chiralitätsanalyse und die Bestimmung des Enantiomerenüberschusses erleichtert. Bemerkenswert ist, dass die Bindung von Tartrat zu einer Anreicherung eines der Helikat-Enantiomere innerhalb der racemischen Population führt, was zu ausgeprägten Cotton-Effekten im CD-Spektrum führt. Diese rezeptorbasierte Methodik bietet Hochdurchsatz-Screening-Möglichkeiten bei minimalem Lösungsmittelverbrauch und minimaler Abfallerzeugung und stellt eine praktische Alternative zu chromatographischen Techniken dar, die auf chiralen stationären Phasen beruhen.

Die starke koordinative Wechselwirkung mit dem Gastmolekül ist in den meisten Fällen vorteilhaft, da sie hohe Bindungskonstanten bietet und eine hochempfindliche Erkennung von Carboxylaten selbst im Nanomolarbereich ermöglicht. Diese Wechselwirkung stellt jedoch eine Herausforderung für die Freisetzung des Gastmoleküls aus dem System dar. Die bemerkenswerte Größenselektivität des Helikats für verschiedene Gastmoleküle, die für Sensoranwendungen von Vorteil sein könnte, wird durch die Unfähigkeit beeinträchtigt, eine kontrollierte Freisetzung des Gastmoleküls innerhalb des Koordinationsgerüsts zu erreichen. Um einen kontrollierten Freisetzungsmechanismus für Gäste zu etablieren, ohne

das Wirtsgerüst verändern zu müssen, was möglicherweise dessen inhärente Eigenschaften verändern könnte, wurde ein auf Reize reagierender Gast in das System integriert. Azobenzol-4,4'-dicarboxylat, mit licht- und temperatursensiblen Isomerisierungszuständen nutzen kann, dient als konkurrierender Gast innerhalb des L_2Zn_2-Rezeptors. Der Größenunterschied zwischen dem gebogenen *cis*-Isomer und der gestreckten *trans*-Form ermöglicht die selektive Aufnahme des ersteren in die Zink-Tasche, wodurch photo- und thermisch induzierte Gast-Austauschzyklen in Gegenwart eines sekundären, nicht-photoaktiven Gastes erleichtert werden. Der Übergang des Azobenzol-Gastes zwischen seinen verschiedenen geometrischen Zuständen bietet einen mechanistischen Weg für den zweiten Gast, sich auf kontrollierte Weise gebunden und freigesetzt zu werden.

Um die selektiven Bindungseigenschaften weiter zu nutzen, haben wir uns zum Ziel gesetzt, eine kolorimetrische Sensoreinheit für das Helikat im Zusammenhang mit der Gastbindung zu entwickeln. Um dies zu erreichen, wurde das Wirtsdesign durch die Integration einer Triphenylamin (TPA)-Einheit in das Grundgerüst modifiziert, mit der Absicht, die photophysikalischen Eigenschaften des Wirts zu verbessern. Obwohl die Synthese und Assemblierung erfolgreich durchgeführt wurde, führte er nicht zu den erwarteten Verbesserungen. Nachfolgende Untersuchungen mit umweltrelevanten perfluorierten Gästen ergaben ein Erkennungsverhalten mit geringer Affinität. Die Einbindung von TPA als Donor-Gruppe in dieses neue Rezeptor-Design könnte potenzielle Anwendungen in Donor-Akzeptor-Systemen und verwandten Bereichen eröffnen.

Awards

- Poster prize, ISMSC Conference, Reykjavík, Iceland, June 2023
- Poster prize (3rd), Girona seminar, Girona, Spain, May 2024

Conferences and Contributions

Oral presentations

June 2022	Tag der Chemie, TU Dortmund
Feb 2025	Tag der Chemie, TU Dortmund
Feb 2025	Koordinationschemietreffen, Münster, Germany
June 2025	PhD seminar, TU Dortmund

Poster presentation

July 2022	Suprachem Mainz, Germany
Sept 2022	International Symposium on Confinement-controlled Chemistry, Bochum
June 2023	ISMSC, Reykjavík, Iceland
Sept 2023	796^{th} Heraeus-Seminar, Bad Honnef, Germany
Feb 2023	Tag der Chemie, TU Dortmund
May 2024	Girona seminar, Spain
April 2025	Supramolecular chemistry and catalysis symposium, TU Dortmund

Publications

- D. Van Craen*, **M. G. Kalarikkal**, J. J. Holstein, *"A Charge-Neutral Self-Assembled L_2Zn_2 Helicate as Bench-Stable Receptor for Anion Recognition at Nanomolar Concentration,"* *J. Am. Chem. Soc.* **2022**, *144*, 39, 18135-18143.
- **M. G. Kalarikkal**, C. Drechsler, G. Tusha, L. V. Schäfer, D. Van Craen*, *"Chiroptical Recognition of Carboxylates with Charge-Neutral Double-Stranded Zinc(II) Helicates,"* *Chem. Eur. J.* **2023**, e202301613.
- **M. G. Kalarikkal**, B. Grabe, D. Van Craen*, *"Stimuli-Responsive Reversible Guest Exchange in a Charge-Neutral Helicate,"* in preparation

Contents

1 GENERAL INTRODUCTION

1.1 ANION RECOGNITION CHEMISTRY

> "**PFAS, the 'forever chemicals' contaminating all of humanity**: In April 2024, the U.S. EPA finalized national drinking-water standards for PFAS—4 ppt for PFOA and PFOS, 10 ppt for PFNA, PFHxS, and HFPO-DA (GenX)—reflecting health risks at trace concentrations."[1,2]
>
> "**Chloride breath is a biomedical emergency**: With every breath you take, epithelial cells in your lungs shuttle roughly 10^6 chloride ions across their membranes to maintain mucus hydration. Mutations in CFTR disrupt this process and cause cystic fibrosis."[3]
>
> "**Rocket fuel perchlorate infiltrated drinking water systems**: Perchlorate blocks iodide uptake by the thyroid; even trace levels could endanger fetuses and infants."[4]

Anions permeate a prevalent part of environmental, chemical, and biological processes.[5] From perchlorate used in rocket fuels affecting thyroid function to toxic PFAS, known as the "forever chemicals" in non-stick cookware coatings[6], fluoride in drinking water[7], and nitrate-rich fertilized fields[8], anions shape nearly every aspect of our lives. Although sulfates are key for stabilizing personal care products[9], and hexafluorophosphate and tetrafluoroborate keep lithium ion batteries stable[10], both are hazardous if exposed to moisture or high heat, as they can decompose to release corrosive gases (e.g., HF, POF_3, BF_3). The human body is no stranger to pivotal anions. Bicarbonates shuttling CO_2, phosphate powering ATP production[11], and chloride channeling neural signals[12] are just a few examples. Iodide deficiency induces thyroid dysfunction[13], oxalate overproduction damages the kidneys[14], and succinate accumulation contributes to fibrosis[15]. Everyday headlines such as the above alarm us and shed light on the urgency of understanding and taming anions and their behaviors. Anion recognition chemistry addresses this challenge by designing and synthesizing molecules that selectively bind or sense species that carry a negative charge and have become a key element of supramolecular host-guest chemistry scaffolds.

Researchers have faced many challenges while designing anion receptors along the way.[16] Anions are generally larger than their equivalent isoelectronic cations; their often more diffused electronic clouds only provide weak electrostatic interactions, leading to poor binding. Anions come in diverse geometries and charge distributions. Consequently,

designing a precise shape and size complementary receptor for a single target anion has been a significant hurdle. In real-world applications, the analyte might contain multiple anions and therefore, receptors must be not only strong but also highly selective. Furthermore, anions are highly solvated, struggling to overcome the solvation energy, especially in polar solvents like water, which raises a demand for water-soluble receptors.[17] Most synthetic receptors work well only in organic solvents. However, anion binding in polar solvents or hydroxylic protic solvents is often hindered by the competition provided by the solvent, which forms strong hydrogen bonds with the anions. Neutral receptors suffer more in this regard compared to their charged counterparts. Designing an effective anion receptor often leads to complex, large molecules with challenging synthesis and purification, and many also suffer from poor solubility[18] (Figure 1.1).

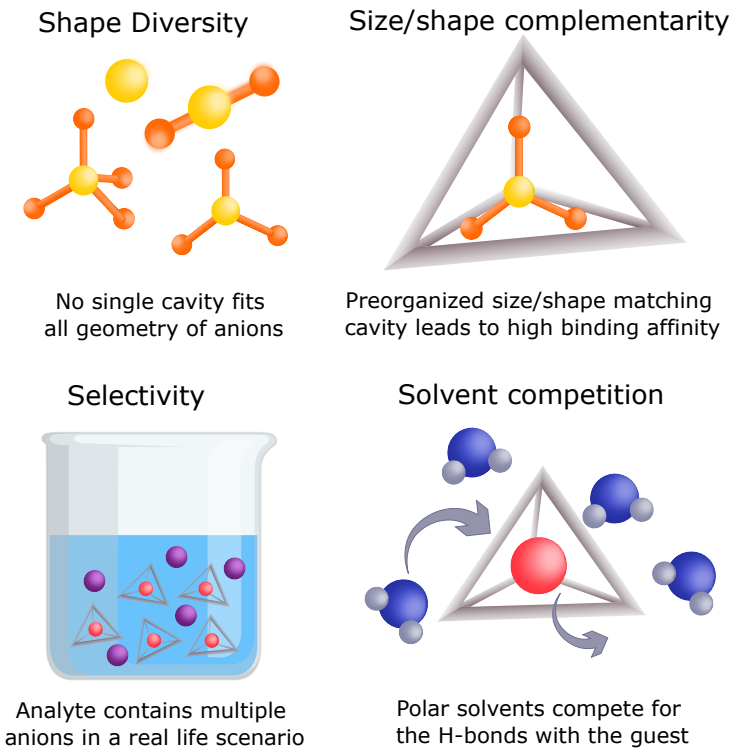

Figure 1.1 Key challenges to be addressed while designing an effective anion receptor.

1.1.1 Evolution of early anion receptors

The history of anion recognition chemistry dates back to the late 1960s, when Shriver and Biallas demonstrated a chelating bidentate boron-based Lewis acid moiety cooperatively binding an anion.[19] In the following years, Park and Simmons reported a halide binding cryptand-like receptor containing ammonium, which is one of the first true synthetic anion receptors. In this 'katapinand' receptor, two ammonium bridgeheads connected by alkyl linkers were shown to bind chloride via convergent $N-H\cdots Cl^-$ hydrogen bonds, albeit very weakly .[20] This pioneering 'host-guest' complex unveiled that an artificial

molecule could capture anions, commencing the origin of the supramolecular chemistry of anions. Later in the 1970s, Jean-Marie Lehn and co-workers extended their cryptand chemistry to anions by developing preorganized polyammonium cryptands and macrocyclic guanidinium receptors for anionic guests with high selectivity simply by matching the cavity size and geometry to the guest.[21,22] In a subsequent phase, Schmidtchen introduced cationic quaternary ammonium 'cages' that encapsulate halides.[23,24] This represented a new strategy that relied on preorganized positive charge to attract negatively charged guests (Figure 1.2). Although these seminal studies established the concept of anion recognition, more advances in sophisticated anion binding units were necessary to achieve strong encapsulation.[25]

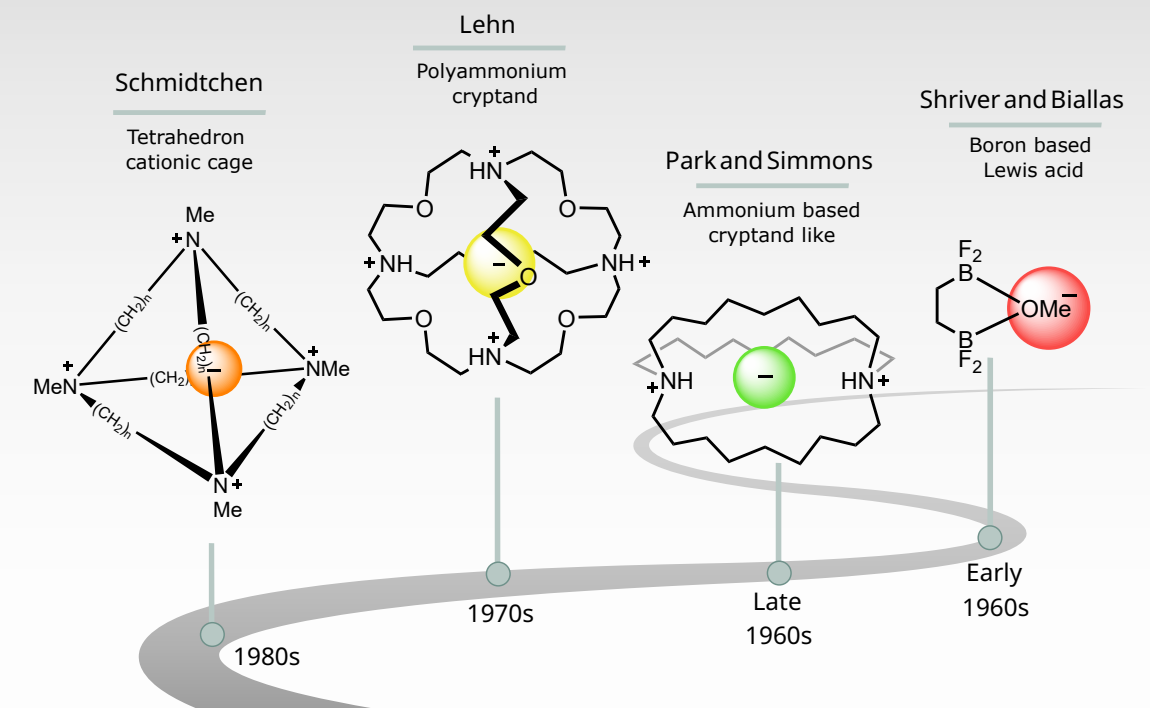

Figure 1.2 Evolutionary cationic anion receptors that paved the way to contemporary receptors.

1.1.2 Neutral organic receptors

In the ensuing decades, research focused on purely organic neutral anion receptors. Several design principles were established that significantly improved anion binding affinities and functions. They evolved through several distinct structural classes, from flexible acyclic hosts to conformationally constrained macrocycles and preorganized three-dimensional cages.[26] Most of the neutral receptor designs leveraged hydrogen bonding moieties, incorporating N–H donors such as ureas, thioureas, amides, sulfonamides, and pyrroles, as well as unconventional C–H donors like triazoles.[27] Acyclic hosts typically feature two or more binding groups incorporated into an aromatic or aliphatic framework to form a convergent binding pocket. Early examples, such as simple bis-ureas or bis-amides, were

quite flexible, and thereby an energy penalty had to be paid upon binding by folding around the anion.[28,29] The binding affinity was highly solvent-dependent due to the lack of a locked framework, requiring receptors to overcome significant competition from the solvent.[30] However, over the years, rigid acyclic hosts have been developed to achieve high binding constants, even with nontraditional C−H hydrogen bond donors. For example, Flood and colleagues engineered a preorganized aryl-triazole receptor exhibiting high affinities for chloride.[31] Whereas Gale and coworkers reported a steroidal squaramide receptor with a strong binding constant of 10^{14} M^{-1} for sulfate, which is the highest ever for a neutral receptor[32] (Figure 1.3).

Macrocyclic hosts, on the other hand, are one step ahead of preorganization and minimize the entropic cost of binding. Acyclic binding clefts are covalently joined to form a cyclic host, creating a defined preformed cavity with enhanced size and shape complementarity. The "macrocyclic effect" is a classic concept in supramolecular chemistry, which is also held responsible for better anion binding. A foundational example is the calix[4]pyrrole reported by Sessler *et al.* in 1996 to bind halides in the cradle created by four pyrrole N−H donors.[33] This enforced cavity size and complementary size enable strong and selective binding, evidenced by a perfect fit for fluoride compared to larger halides. Subsequently, other receptors with enhanced functional abilities emerged, such as Schalley's hexakis-urea double helix, which accommodates two chloride ions[34], Kubic's cyclopeptide receptors, which bind sulfate or dihydrogen phosphate in water via hydrophobic shielding[35], and Flood's cyanostar, achieving picomolar affinity and exceptional size selectivity for hexafluorophosphate through C−H donors enhanced by electron-withdrawing cyano groups[36,37]. Despite the fact that typical neutral macrocycles perform exceptionally well for anion recognition, the synthetic efforts, time, and resources demanded by these systems pose a significant disadvantage.

Three-dimensional organic cages offer the highest degree of preorganization of all. They offer high binding strength by confining the guest within the cavity, thereby providing maximum enthalpic stabilization and shielding it from solvent molecules.[38] Furthermore, these designs offer high selectivity due to their shape and size complementary cavity, which was demonstrated by Bowman-James's tris-amide cryptands in distinguishing between linear azide and spherical chlorides, preferring the former.[39] A record-breaking binding constant of 10^{17} M^{-1} was reported for chloride binding with C−H donors by Flood in a cryptand cage. This high selectivity for Cl^- was possible due to the extreme rigidity and size-selective cage design.[40] However, creating cages is a challenging multistep process, often resulting in low yields and necessitating substantial optimization and purification. Furthermore, complex cage formation is mostly template-based, and these constructs are also less tunable compared to simpler acyclic hosts.

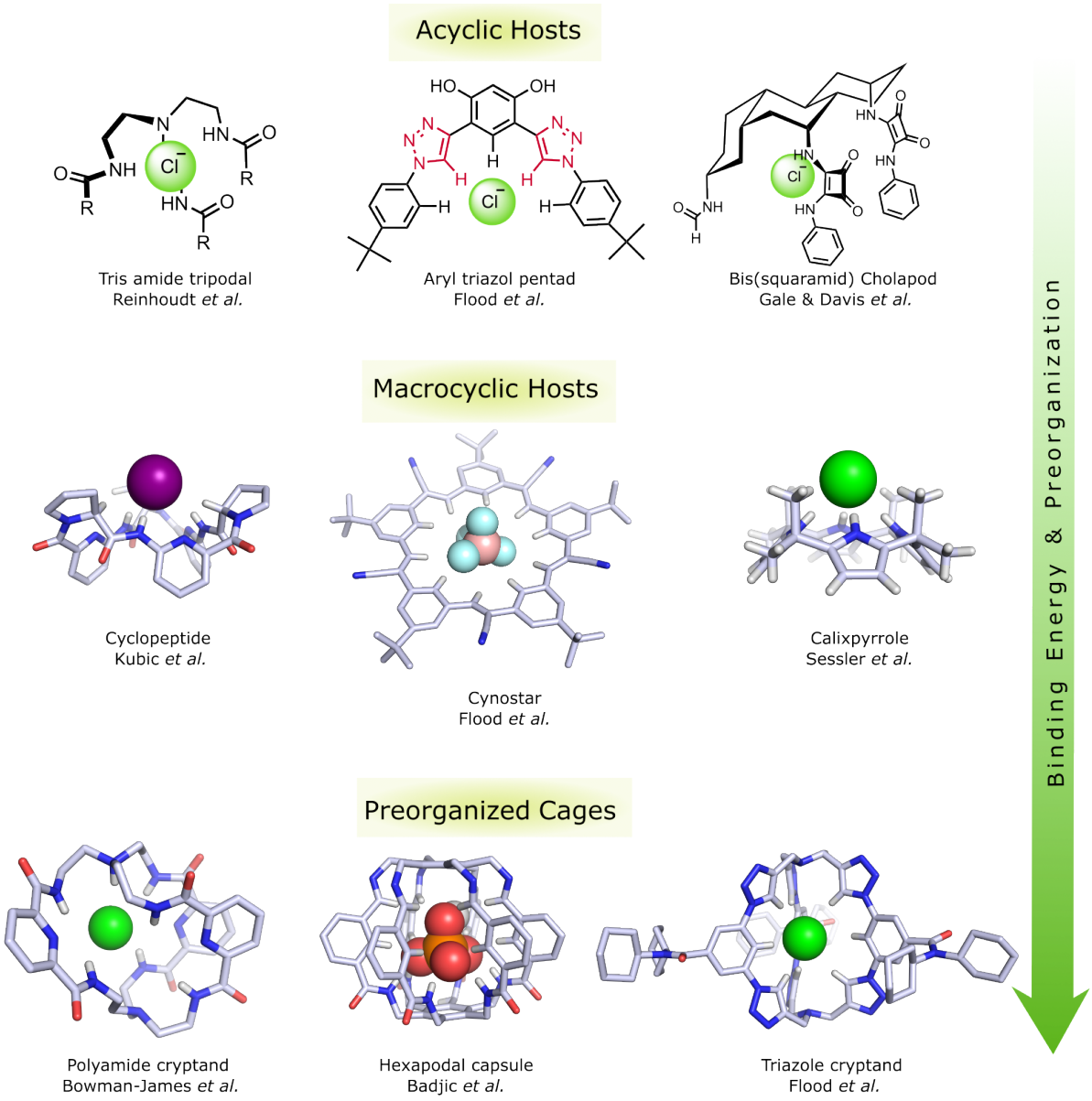

Figure 1.3 Representative examples of neutral organic receptors, ranging from simple acyclic hosts to macrocycles and highly preorganized organic cages. Binding affinities generally increase along this series, reflecting the enhanced preorganization and enthalpic advantages provided by the more rigid architectures.

In short, as we move from early acyclic clefts to today's sophisticated encapsulating neutral organic cages, the degree of preorganization increases, and hence the binding affinity and selectivity are also enhanced; unfortunately, so does the synthetic burden. While neutral covalent hosts avoid complications from counter-ions, the multi-step, often template-guided syntheses required for advanced macrocycles and cages often hold back further exploration.

1.1.3 Self-assembled metal-based hosts

Inspired by nature's metal-mediated self-assembled structures, including metalloproteins and enzyme active sites, supramolecular chemists have developed artificial coordination assemblies. These are formed by combining metal precursors with bridging organic ligands to create well-preorganized architectures such as metallacycles,[41,42] cages[43,44], or helicates.[45,46] These metal-organic hosts offer extensive control over cavity size and geometry, enabling enhanced selective encapsulation. Additionally, their tunable modular design is a significant benefit, often achievable through simpler one-pot complexation by mixing metal ions with the ligands. Their cationic nature inherently boosts electrostatic interactions with anions, also expanding their scope in various solvents.[47–51]

Numerous coordination-driven, self-assembled metal-based anion receptors have been reported over the years by leading groups, including those of Lehn,[52] Fujita,[53] Stang,[54] Raymond,[55] Nitschke,[56] Clever,[57] and Shionoya.[58] An early instance of anion encapsulation in such a construct is the $[Pd_2L_4]^{4+}$ quadruple-stranded helicate reported by McMorran and Steel. The helical framework twists around a PF_6^- anion that also bridges the two Pd centers by weak F$\cdots$ Pd coordination bonds[59] (Figure 1.4a). Nitschke and coworkers developed their $[Fe_4L_6]^{8+}$ tetrahedron utilizing a subcomponent self-assembly approach, where dynamic covalent C=N bonds and coordination bonds form simultaneously. This cage demonstrated various anion recognition properties.[60]

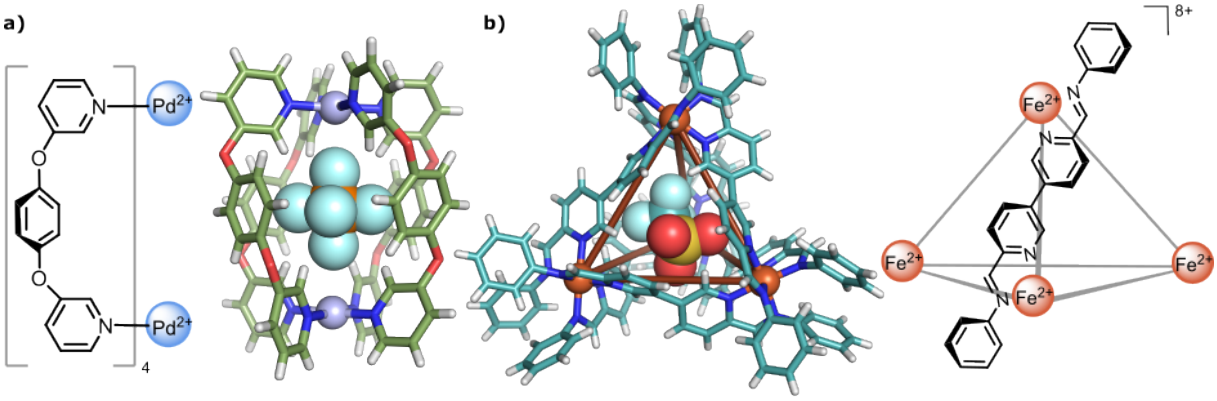

Figure 1.4 (a) The quadruple-stranded helicate by McMorran and Steel formed with four bidentate ligands wrap helically around the bound PF_6^- guest. (b) A Tetrahedral cage from Nitschke obtained by subcomponent self-assembly, shown with an encapsulated $CF_3SO_3^-$ anion.

This system, initially templated with sulfate, could exchange sulfate with PF_6^- by varying the imine subcomponents with different electron densities during self-assembly (Figure 1.4b).

Coordination cages can often undergo complex, anion-induced dynamics. Clever and co-workers' work on interpenetrated double cages presents an example of how the bound anion allosterically alters the cage conformation. The standard $[Pd_2L_4]^{4+}$ cage formed from dibenzosuberone-derived ligands threads into an interpenetrated $[Pd_4L_8]^{8+}$ dimer, templated by one BF_4^- anion in its central cavity, while two additional BF_4^- anions initially occupy the outer pockets and cooperatively exchange for halides[61,62] (Scheme 1.1a). The steric modification of the ligand inverted the selectivity, allowing for the targeted binding of larger anions[63] (Scheme 1.1b).

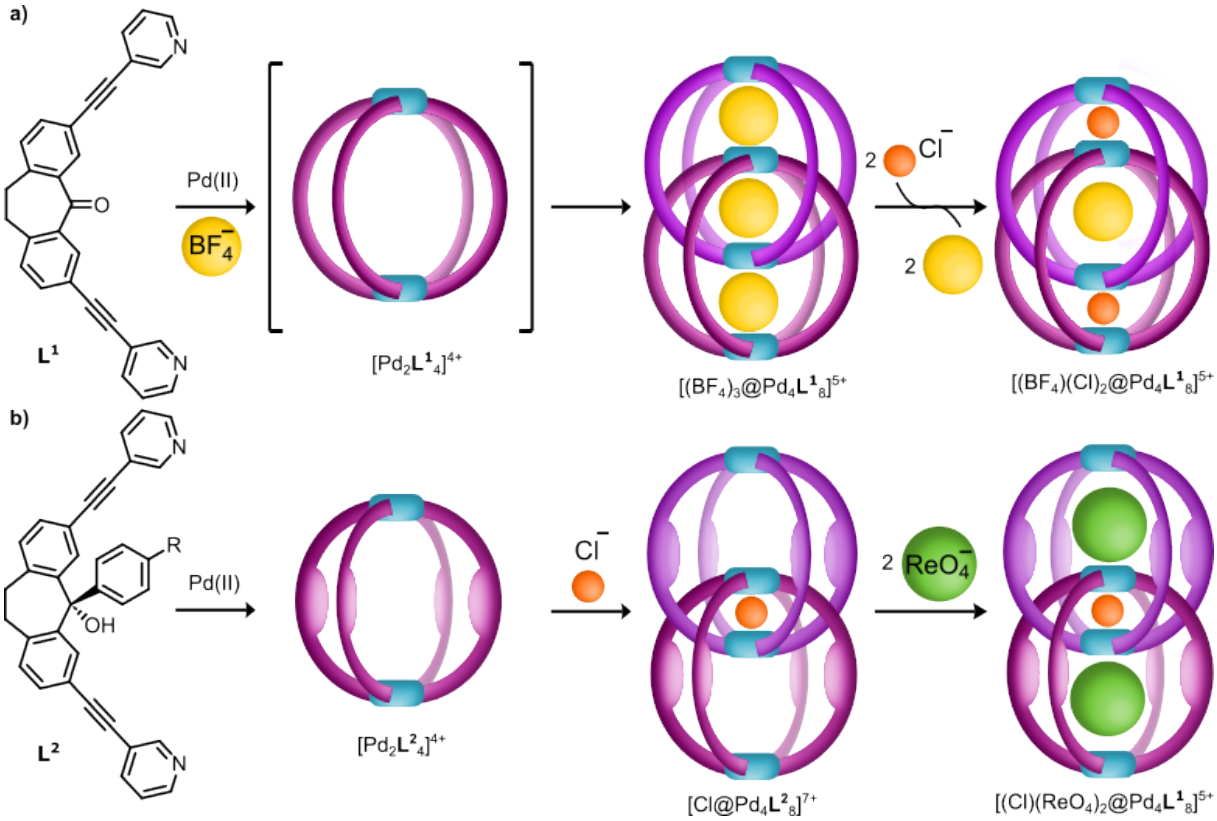

Scheme 1.1 Guest-templated formation and anion exchange in interpenetrated double cages. (a) Anion templated dimerization of a $[Pd_2\mathbf{L^1}_4]^{4+}$ cage into $[Pd_4\mathbf{L^1}_8]^{8+}$ with BF_4^- anion occupied all the cavities, followed by allosteric exchange of two loosely bound outer BF_4^- anions by two Cl^- anions. (b) Self-assembly of $[Pd_2\mathbf{L^2}_4]^{4+}$ with bulky ligand which does not lead to double cage directly with BF_4^- directly. Addition of Cl^- induces catenated dimerization into $[Pd_4\mathbf{L^2}_8]^{8+}$. The larger outer cavities occupies larger anions like ReO_4^-.

Notwithstanding the many significant advantages associated with cationic metal self-assembled hosts, the role played by the counter-anion accompanying the assembly is frequently unaccounted for. Lusby's group, in their recent study, investigated the influence of the counter-anion associated with the $[Pd_2L_4]^{4+}$ capsule on the binding strength of a neutral

naphthoquinone guest.[64] The cage was previously shown to encapsulate coordinating counter-anions like OTf^- within the cavity and thus hinder the target analyte. However, after varying the anion to weakly coordinating bulky anions such as $BArF^-$, the cavity was liberated, leading to a high binding strength. The use of highly lipophilic $BArF^-$ also made the cage soluble in apolar solvents, contributing to even higher association constants (Figure 1.5). Apart from crowding the target binding site and imparting a competitive environment, it has been established that counter-anions occupy the cavity surfaces and block access to the target analyte,[65] or heavily influence which anion is encapsulated in the cage.[66] In some cases, as we observed before in the interpenetrated double cage, host-associated anions induce allosteric cage transformations.[62] Designing an anion receptor by choosing a middle ground between purely organic neutral hosts and highly charged metal cages would result in a charge-neutral, metal-based, self-assembled host that can retain structural preorganization and modularity while also eliminating competing background counter-anions.

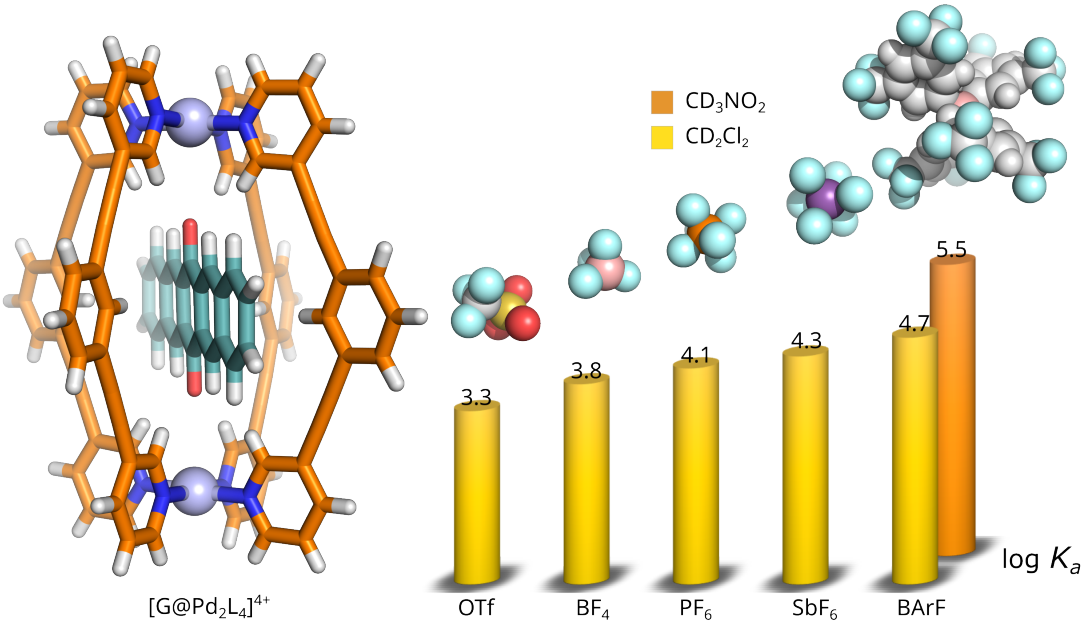

Figure 1.5 Counter-anion interference on host-guest interactions. (left) Lusby's $[Pd_2\mathbf{L}_4]^{4+}$ cage with a centrally bound neutral pentacenedione guest. (right) Trend on the association constants, log K_a, for naphthoquinone guest, with various capsule ion-pairs in CD_3NO_2 and CD_2Cl_2. Highly competing smaller anions lead to lower K_a, while less interfering bulky anions result in higher K_a values.

1.2 CHARGE-NEUTRAL METAL-BASED SELF-ASSEMBLED HELICATE

To combine the strengths of both neutral organic macrocycles and highly preorganized metal-coordinated hosts, our group developed what we believe is the first fully charge-

neutral, self-assembled double-stranded helicate-based anion receptor, which also demands less synthetic effort and is free of competing counter-anions (Figure 1.6).[67] The structural design incorporates a modular 'click' ligand composed of two 8-hydroxyquinoline units and an aryl spacer. Zn^{2+} was the metal ion of choice to achieve neutrality. Upon chelation with two monoanionic quinolinate complexing units, this results in an overall zero charge. When $Zn(OAc)_2$ was used, the acetate anions acted as Brønsted bases, deprotonating the hydroxyquinolines. The acetic acid residues were removed by lyophilization. This deprotonation-driven self-assembly generates the neutral host without any extrinsic anions.

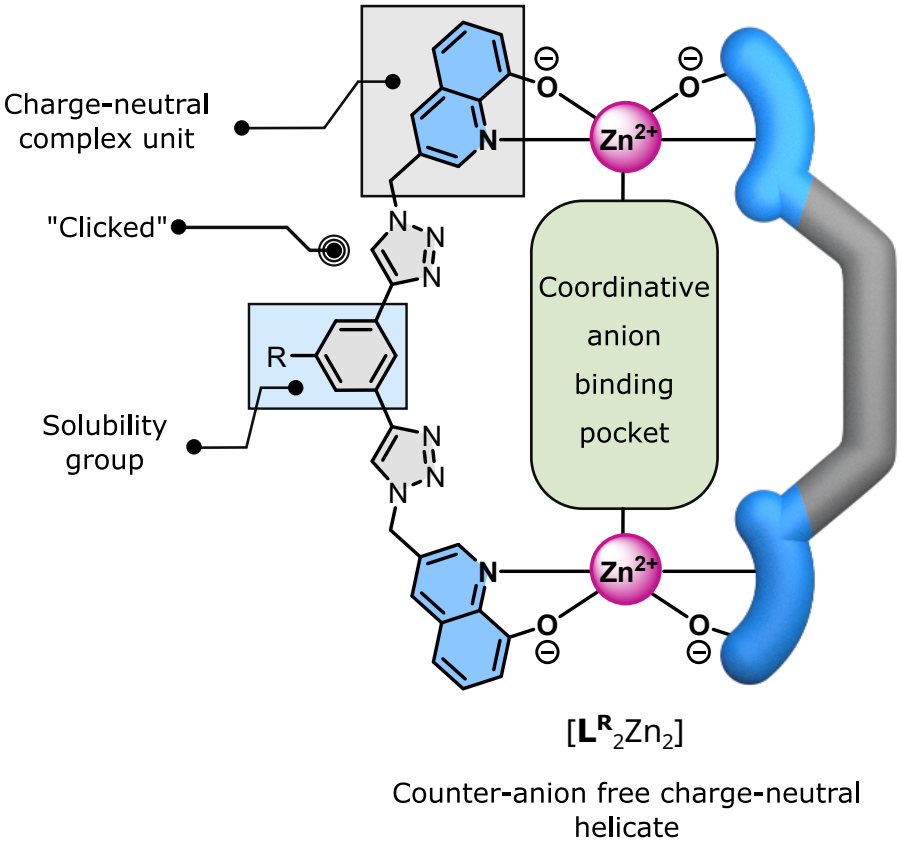

Figure 1.6 Metal-based helical anion receptor design for charge-neutrality and counter-anion free environment with a coordinative binding pocket targeting carboxylate anions.

1.2.1 Size-selective dicarboxylate recognition

Dicarboxylic acids and dicarboxylates are of paramount importance in industry and biological realms. In living systems, amino acids such as aspartic acid and glutamic acid serve as crucial metabolic intermediates and signaling molecules, while succinic acid is involved in the citric acid cycle.[68] Industrially, the formulation of drugs and food products involves tartaric acid and maleic acid; additionally, and in plastics production, phthalates are a notable example.[69] Their diverse roles, coupled with their impact on health (e.g., oxalic acid toxicity[70]) and the environment, highlight the significant interest in their detection and monitoring. However, they pose a challenge for receptor systems due to

their distinct shapes, sizes, pKa profiles, and hydrophobic properties.

Undeniably, hydrogen bonds constitute a successful receptor for oxyanionic guests. One key example demonstrating this is the charge-neutral organic receptor reported by Sessler and co-workers, based on a vibration-induced emission (VIE) phenazine core (DPAC) flanked by two calix[4]pyrrole moieties, which enables quantitative detection of dicarboxylate ions. Moreover, they could distinguish between various linear saturated dicarboxylates and the three phthalate isomers on the basis of their distinct chromaticity readouts. This 'molecular cursor caliper' system senses the dianions by the formation of pseudomacrocyclic host-guest complexes with a unique chromaticity readout[71] (Figure 1.7).

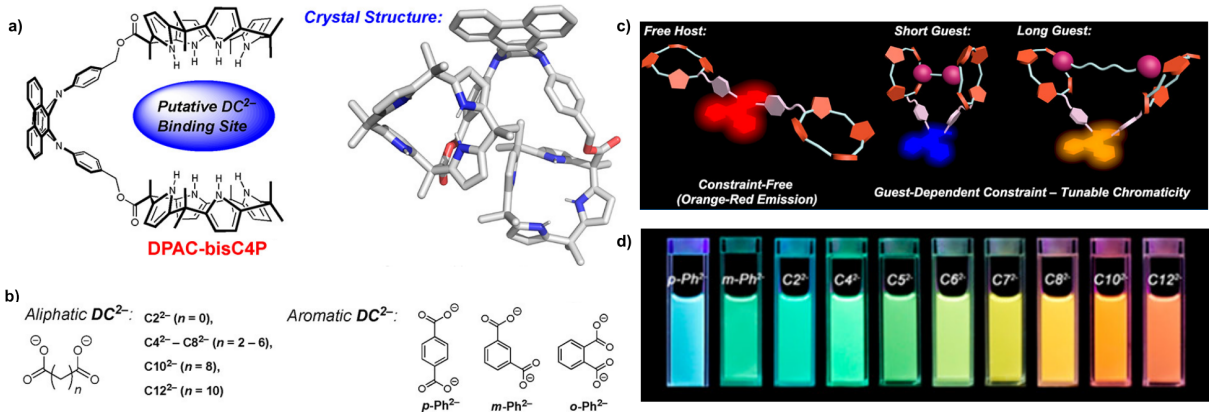

Figure 1.7 Molecular cursor caliper sensor for dicarboxylate dianions. (a) Structural design of DPAC-bisC4P receptor motif for DC^{2-} and the crystal structure of the host. (b) Chemical structures of various dicarboxylate guests used in the study. (c) Mechanism of fluorescence tuning and dicarboxylate anion sensing. The free host emits at longer wavelengths (orange–red). Short, rigid dicarboxylates induce hypsochromic shift, yielding blue-shifted emission. Longer, more flexible guests give intermediate (yellow) colors. (d) Photographs of DC^{2-}@DPAC-bisC4P in acetonitrile obtained under 365 nm UV light illumination. Reproduced from ref. [71] with permission from the American Chemical Society, Copyright 2019.

In most cases, carboxylate guests are equipped to chelate metal ions that are not saturated by the ligands, resulting in a strong coordinative interaction. Stang *et al.* leveraged this property and synthesized a series of platinum(II) metallacycles with dicarboxylates as building blocks. The emission properties of the metallacycles varied as the bite angle between the carboxylate groups decreased and showed a blue shift[72] (Figure 1.8). Zonta's group developed positively charged imine-based tris(2-pyridylmethyl)amine (TPMA) zinc complexes and studied their recognition properties with various dicarboxylates, ranging from succinic acid (C4) to tetradecanedioic acid (C14). They found that longer dicarboxylate guests can accelerate cage disassembly through a strain-release mechanism. This study highlights how the structural features of the guest modulate the dynamic behavior of the cage.[73]

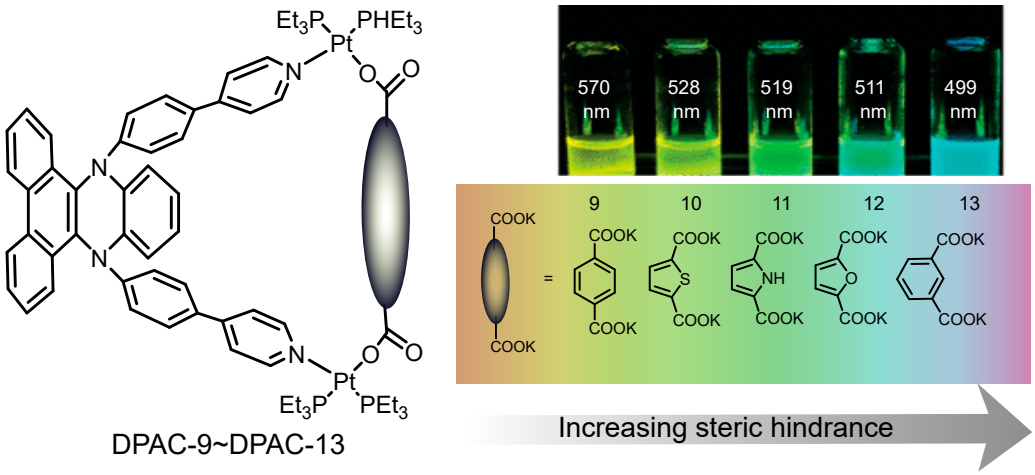

Figure 1.8 Steric-controlled fluorescence of phenazine-cored Pt(II) metallacycles. (left) Chemical structure of DPAC-9 DPAC-13. (right) Various dicarboxylates used in the study and the photograph showing corresponding metallacycle formed in solution, obtained under 365 nm UV light illumination. The added steric bulk restricts intramolecular motion and causes a blue-shifted emission. The photograph is reproduced from ref. [72] with permission from the American Chemical Society, Copyright 2019.

The charge-neutral $[L_2Zn_2]$ helicate of the Van Craen group is also configured with a binding motif for dianions, particularly dicarboxylates, which coordinate with it between its two zinc centers[67] (Figure 1.9a). This is another example of a caliper-like system, which effectively clamps dianions, chelating them between the metal centers. The binding pocket effectively traps monocarboxylate and other monoanionic guests in 1:2 and dicarboxylate guests in 1:1 fashion.

Despite the fact that all binding studies were carried out in DMSO, a highly adverse environment considering the competition for anions, the neutral host exhibited remarkably high binding constants for various aliphatic and aromatic dicarboxylates, partly owing to the competing counter-anion-free conditions. For aliphatic guests, association constants increased from shorter glutarate (C_5) to longer pimelate (C_7), indicating an optimal fit with the host. Affinity then decreases for longer chains, likely due to an energy penalty incurred as they must fit within the binding pocket. The same trend held true for aromatic guests as well; the perfectly fitting guest naphthalene-2,6-dicarboxylate (ND) showed a binding constant of 145 x 10^6 M^{-1} (Figure 1.9b). The box-like shape observed in the crystal structure confirms that an 8 Å long guest fits perfectly, providing maximal rigidity to the receptor. Beyond being highly size-selective, the helicate can also utilize its emissive properties to sense anions down to nanomolar concentrations (Figure 1.9c,d). Since the same scaffold is used throughout most of this thesis, it provides an ideal benchmark for more exciting studies to follow.

Consequently, in a later study, the Van Craen group used a similar topological host and successfully tamed highly competitive oxalate (C_2), without losing structural integrity. This was achieved by shortening the helical backbone and adding more flexible components

to the ligand design.[74]

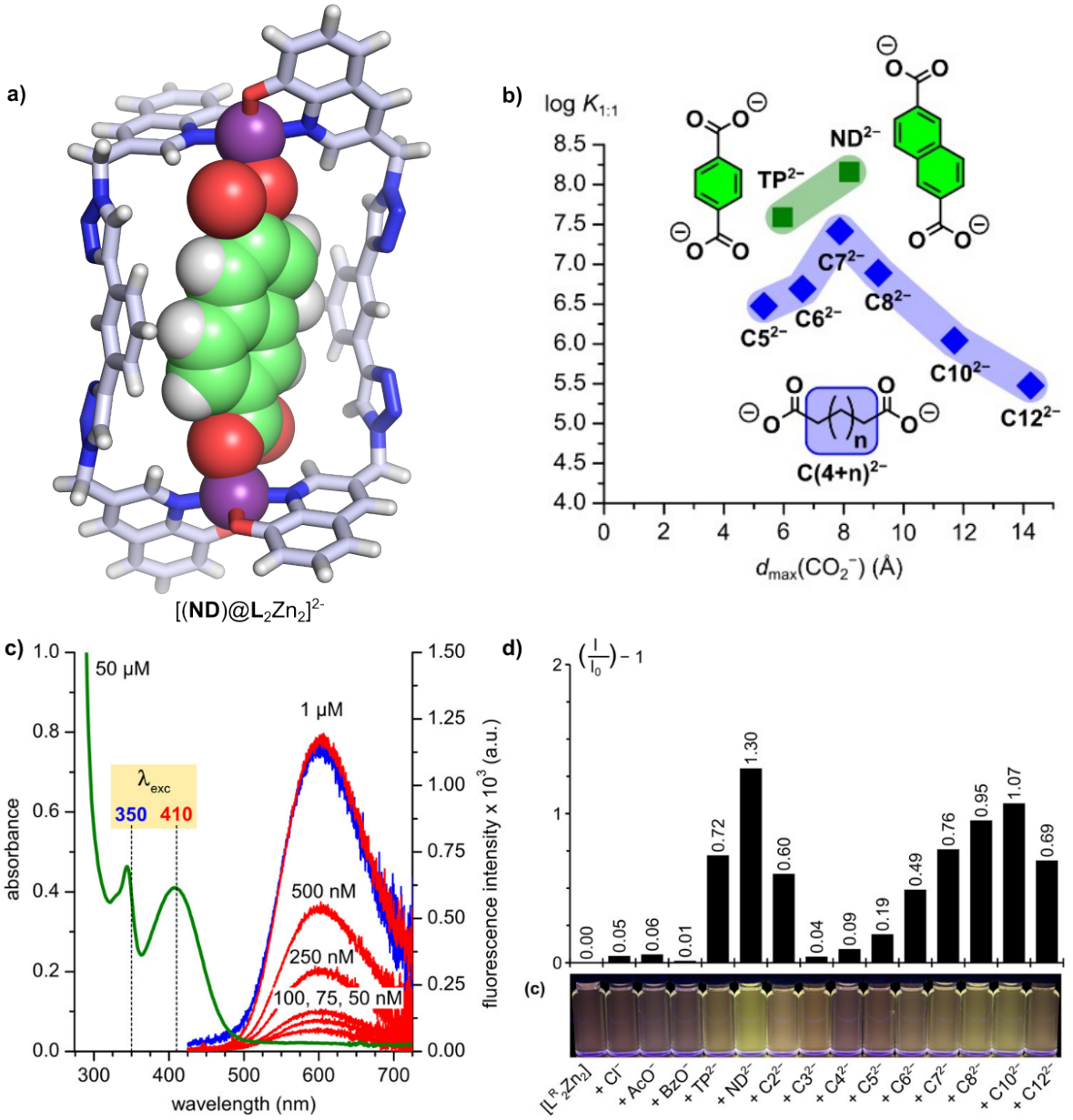

Figure 1.9 Charge-neutral helicate for size-selective recognition at nanomolar concentrations for dicarboxylates. a) Crystal structure of $[(\mathbf{ND})@\mathbf{L}_2Zn_2]^{2-}$ b) Correlation between binding affinity (log $K_{1:1}$) and the C-C distance, d_{max} for investigated aliphatic and aromatic dicarboxylate anions shows size selective rise and fall in affinity. c) Absorption spectrum (green) at 50 μM and emission spectra of the receptor at various concentrations. d) Normalized fluorescence intensity change with addition of various guests into the host solution at 500 nM. Photographs underneath show the naked-eye response at 50 μM under 365 nm light. Reproduced from ref. [67] with permission from the American Chemical Society, Copyright 2022.

1.3 CHIROPTICAL RECOGNITION

Chirality is an intrinsic property of numerous natural products and essential compounds, contributing to their efficacy as biomolecules, drugs, pharmaceuticals, and agrochemicals.[75,76] Chiral dicarboxylic acids are particularly relevant, as they are used as building blocks or precursors in many essential compounds, such as amino acids, and a number of synthetic drugs bear carboxylic acid residues.[77–79] Both enantiomers of these chiral compounds present distinct chemical environments and binding affinities, facilitating chiroptical recognition, as well as the qualitative and quantitative analysis of isolated or mixed enantiomers. Many synthetic receptors have proven their compatibility with this goal over the years, and this area still holds the limelight as a growing research domain.[80]

1.3.1 Chiroptical recognition and chirality analysis

As previously elucidated, chiral molecules are fundamental components of biological processes and are extensively employed across various other domains. Owing to the distinct chemical environments, often only one of the enantiomers demonstrates the desired efficacy and necessity for the intended application.[81] Chiroptical sensing and chirality analysis, aimed at determining the absolute configuration and quantifying different enantiomers, have thus proven to be of utmost importance in evaluating the success of asymmetric reactions and controlling the quality of chiral products. A multitude of analytical methods has been employed throughout several years of investigation to distinguish and measure enantiomers.

One well-established spectroscopic method for assessing enantiomeric excess (*ee*) involves utilizing Mosher's acid (α-methoxy-α-trifluoromethylphenylacetic acid) or the corresponding acid chloride, which are chiral derivatizing agents that readily react with chiral analytes, such as secondary alcohols or amines. The generated diastereomeric derivatives can subsequently be quantified by tracking changes and integrating the distinct NMR signals, facilitating the determination of the enantiomeric ratio or excess of the modified sample.[82–84] Later on, chiral chromatographic methods, such as High Performance Liquid Chromatography (HPLC), Gas Chromatography (GC), and Supercritical Fluid Chromatography (SFC), are frequently employed in the analysis of enantiomeric mixtures and are considered the 'gold standard' due to their precision.[81,85] These techniques have remained mainstream since the introduction of the first commercially available chiral stationary phases (CSPs) by Pirkle and coworkers in the early 1980s.[86] A wide variety of CSPs, including polysaccharide derivatives, protein-based, and cyclodextrin-based molecules, have been developed and display robust enantioseparations to this day.[87,88] However, in practice, these relatively expensive methods have failed to meet the ever-increasing demand for chirality analysis of the numerous chiral samples being produced

in high-throughput experiments, an issue attributed to the high cost of chiral columns, solvents, and instruments.

However, in later years, the straightforward, cost-effective, and sensitive nature of fast spectroscopic techniques was recognized and applied for high-throughput chirality analysis.[89,90] Optical chirality sensing techniques, including UV-Vis and fluorescence when coupled with a chiral receptor, as well as circular dichroism (CD) spectroscopy, enable real-time monitoring of enantiomeric excess (*ee*) in stereoselective reactions and have the advantage of not requiring prior purification. Since most chiral analytes lack strong chromophores to yield distinct CD signals, their chirality analysis is often challenging. This can be remedied by binding these chiral molecules in an optically active, racemic, stereodynamic host. Helicates are particularly good candidates for this approach, given that chirality is an inherent property of their structure. Guests bias the receptor's handedness and produce a diagnostic Cotton effect, allowing the determination of the analyte's absolute configuration and enantiomeric excess.[91–103]

1.3.2 Supramolecular helicates

The previous section established various classes of supramolecular metallo-architectures. Helicates, in particular, are among the most extensively studied constructs, especially as potential anion receptors. The term 'helicate' was coined by Lehn *et al.* in 1987 to describe structures characterized by ligands winding around metal ions in a helical fashion.[104] Their initial work demonstrated a double-stranded helicate similar to DNA formed from poly(2,2'-bipyridine) ligands with copper(I) ions. Since then, numerous structures have been published, categorized as double-stranded,[46] triple-stranded,[105,106] or even up to six-stranded and circular helicates.[107–111] These helical structures often form a cylindrical or capsule-like central cavity that can accommodate guest molecules. The size and shape of the anions that can be encapsulated within this cavity are determined by the number of strands in the helix, as well as by the length and shape of the connecting spacers between their coordinating units.[107,112,113] For instance, a dinuclear triple helicate $[Co_2L_3]^{2+}$ reported by Rice and coworkers generates a binding pocket that peripherally encapsulates guests such as perchlorate anions.[114] Additionally, Nitschke and coworkers showed a series of hollow six-stranded helicates that demonstrate that the bound anions also template the integral helicate structure.[108]

In most cases, helicates are inherently chiral, although there are multiple means to induce chirality in a metal-organic helicate.[115] The foremost and commonly implemented strategy is to self-assemble enantiomerically pure ligands with either point or axial chirality, together with metal ions, to result in a helicate with predetermined chirality. This process involves diastereoselective control of one of the helical twists, either P or M.[116–118] Alternatively, an

optically active chiral auxiliary unit can be attached to the ligand or metal center to bias the configuration of the stereogenic centers.[119,120] Instead of these 'hard' approaches, chirality may originate from the secondary structure, particularly from the spatial arrangement of ligands around the metal center, providing different diastereomeric helical configurations right-handed $\Delta\Delta$, left-handed $\Lambda\Lambda$, and frequently *meso* $\Delta\Lambda$.[121,122] Alternatively, the inherent chirality of a helicate arises from the twisting of the ligands in the P/M helical path.[46,123]

1.3.3 Guest-induced chirality

If the external stimuli for inducing 'hard' chirality are lacking, self-assembly with achiral components may lead to a racemic mixture of left- and right-handed helicates or an achiral structure with opposite handedness at the metal center, coined as *meso*-helicate.[124,125] The conversion from mesocate to helicate can be achieved by external stimuli, including solvent, counter-ion effects, temperature, and light;[126–128] however, the most mechanistically insightful aspect is guest-induced chirality.[102] Helical assemblies with open cavities for chiral molecules are biased towards one of the P/M or Δ/Λ enantiomers through selective guest binding. Resulting diastereomeric host-guest complexes differ significantly in free energy and undergo guest-templated hierarchical chirality transfer.[129–131] This chiral induction often produces strong CD signals corresponding to the enantiomeric enrichment of one handedness in chiral guest-bound helicates, with opposite Cotton effects. Quantifying the induced CD signal can be used for chirality analysis by determining the enantiomeric excess (*ee*) of the guest.[80,132,133]

The enantiomeric quadruple-stranded $[Eu_2L_4]^{2-}$ helicate from Rancan and coworkers perfectly illustrates hierarchical guest-to-host chirality transfer using circular dichroism (CD) and circularly polarized luminescence (CPL).[134] The helicates exhibit chirality at the secondary level and initially exist as a racemic mixture of helicate and *meso*-helicate forms. Subsequently, they adopt distinct chiral handedness in response to the encapsulation of enantiomers of chiral α-methylcholine guests within the confined helical cavity, followed by the ensuing conformational transformations (Scheme 1.2). The helicity inversion mechanism occurred through a Bailar twist by rearranging ligands around the metal atom without breaking any bonds. This system benefits from its adaptive CPL emission, chirality sensing, and enantiomeric excess determination capabilities.

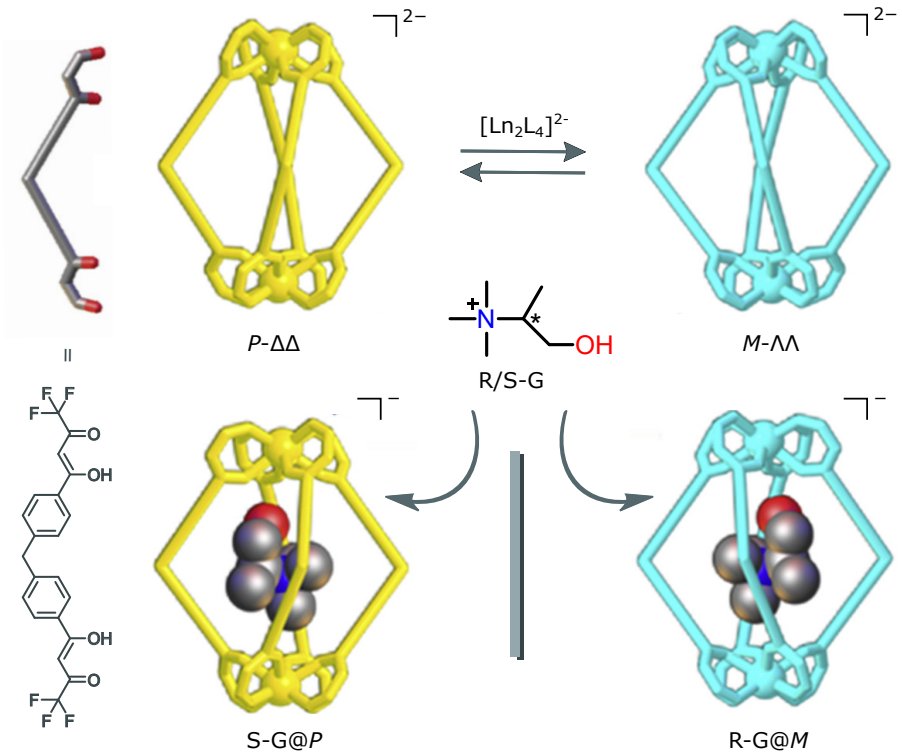

Scheme 1.2 Guest dictated chirality. Self-assembly of a racemic mixture of quadruple-stranded helicate-cages and hierarchical chirality transfer from chiral guest to the host. Adapted from [134] with permission from Elsevier, Copyright 2022 (open access).

Similarly, Mukherjee and co-workers reported a guest-directed enantioselective self-assembly of an octahedral Pd_6L_4 nanocapsule.[135] In the absence of a chiral guest as a template, self-assembly results in a complex mixture of interconverting diastereomers. A reverse chiral recognition is observed by encapsulating the enantiomers of BINOL through H-bonds, enabling effective diastereoselective interaction and selectively shifting the equilibrium toward a single homochiral cage, dictating the helicity (Scheme 1.3). Aside from inducing one enantiomeric state, certain guests may also trigger helicity inversion by actively flipping a helicate from one handedness to another. Akine and co-workers illustrated chirality inversion in a nickel(II) cryptand under the influence of a bound alkali metal ion.[136]

As elucidated previously, the zinc-based charge-neutral helicate synthesized by our group exhibits a high affinity for chiral dianionic guests. We performed chiroptical binding studies for chiral dianionic guests in this helicate and established the receptor as a potential probe for the chirality analysis of chiral dicarboxylates, with the results already published[137] and to be presented in detail in Chapter 3.

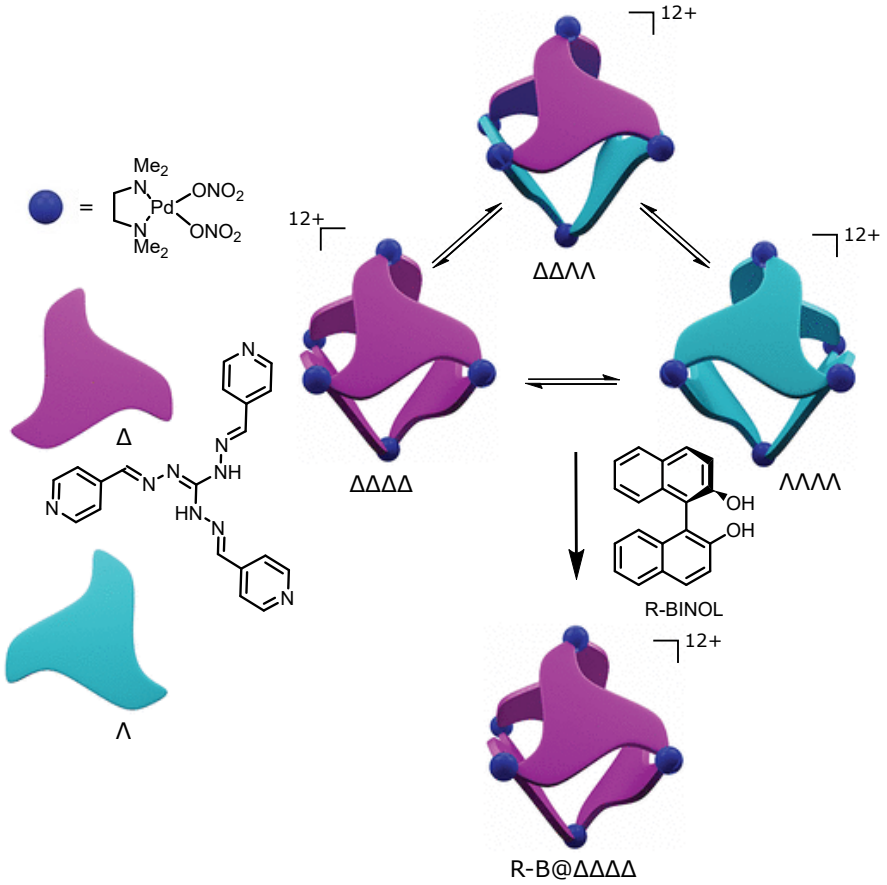

Scheme 1.3 Tris-pyridyl donor ligand self-assembles with Pd into a mixture of diastereomers of octahedral nanocapsules. A single enantiopure homochiral cage (ΔΔΔΔ) is obtained upon addition of R-BINOL as a chiral guest. Adapted from [135] with permission from the American Chemical Society, Copyright 2020.

1.4 REVERSIBLE GUEST EXCHANGE

Controlled guest release and regeneration of the free host have always been a bottleneck in host-guest chemistry. This recyclability is crucial for applications such as drug delivery, molecular devices, catalysis, and sensing. In catalytic systems, especially, the efficiency of the receptor is determined by the rate of guest exchange between substrates and products, specifically by the prevention of product inhibition. Furthermore, reversible host-guest interactions enable dynamic control over the reactivity and functionality of the system, allowing it to adapt to complex processes. Therefore, enabling hosts for tunable guest release and high recyclability is the key to unlocking their full functional potential.

1.4.1 Stimuli-responsive guest release and uptake mechanisms

Stimuli-responsive systems are indispensable for the design of inherently dynamic ensembles whose properties can be switched on demand. Within host-guest chemistry, this behavior enables controlled guest binding, sequential separations, and molecular-level

logic-gate functions.[138,139] Switchable materials exhibit two or more interconvertible stable states displaying distinctive geometric, optical, or chemical properties in response to external stimuli such as light,[140–144] pH,[145] solvent,[146,147] temperature,[148] concentration, stoichiometry,[149] chemicals,[150] and redox processes[151]. Stimuli-responsive architectures are widely employed for controlled guest exchange, as they undergo structural reconfiguration, allow for on-demand variation in conformations, cavity size, or shape, and thereby facilitate control over reversible guest uptake and release.

Guest capture and release in metallosupramolecular hosts can be regulated by implementing three different pathways (Scheme 1.4). One approach involves the partial disassembly or complete rupture of the host cage through the controlled and reversible removal of its ligands or metal ions. This method ensures that guests remain unaffected while producing inert by-products. Another approach involves altering the host to modify the environment of its internal cavity. Methods such as photoisomerization of the ligand or redox switching can achieve this, thereby weakening host-guest contacts while keeping the framework intact. And finally, a guest modification approach can be utilized. This strategy involves the chemical modification of the guest molecule within the host, converting it into a non-binding species that can be released.[152] While the subsequent subsections address guest release mechanisms under the influence of various stimuli, light as a stimulus for photo-responsive systems is deliberately excluded and will be discussed thereafter.

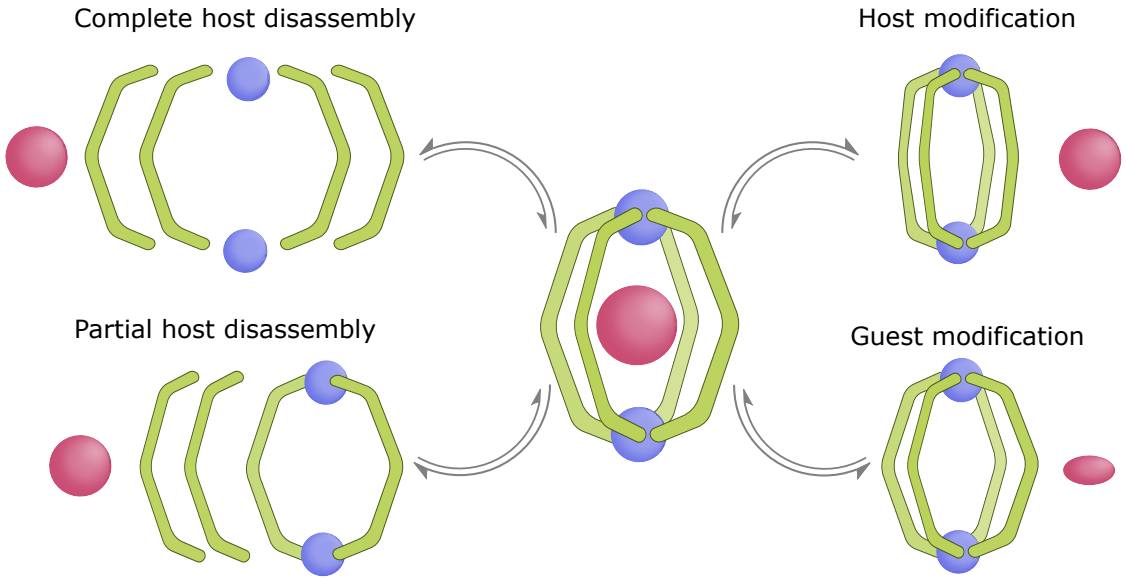

Scheme 1.4 Various stimuli facilitate the release of guests through different mechanisms.

1.4.1.1 Cage disassembly/reassembly

Metallo-organic cages can be deliberately and reversibly disassembled and reassembled under external stimuli by embedding redox switches, photochromic units, and pH-sensitive sites into the ligand backbone or by introducing a competing ligand.[153–157] Metal-driven self-assemblies benefit from their labile metal-ligand coordination bonds, which allow partial or complete disassembly under appropriate stimuli. Among them, pH-triggered assembly and guest release are widely implemented across a range of research domains. A classical example is the water-soluble $[Fe_2L_4]^{4-}$ tetrahedron from Nitschke's group, formed by the subcomponent assembly approach, by reacting 4,4'-diaminobiphenyl-2,2'-disulfonic acid and 2-formylpyridine with $FeSO_4$ in an alkaline aqueous solution[158] (Scheme 1.5).

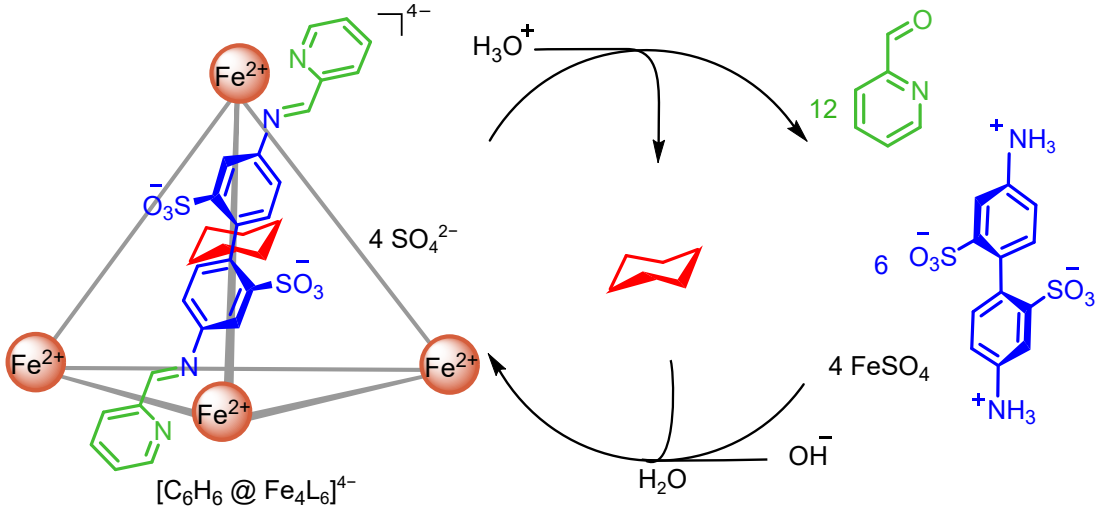

Scheme 1.5 pH-driven reversible cage disassembly/resassembly accompanied by guest release and uptake demonstrated by a tetrahedral Fe_4L_6 capable of binding cyclohexane guests.

This cage selectively traps many hydrophobic guests, namely cyclohexane, within its rigid cavity, effectively isolating them from the surrounding aqueous environment. Reversible guest binding and release were carried out in a pH-dependent manner. Adding ten equivalents of p-toluenesulfonic acid to the host-guest complex completely disassembles the cage into its constituent subcomponents, releasing the bound guest. This was made reversible by adding 15 equivalents of sodium bicarbonate, which regenerates the tetrahedron with cyclohexane trapped inside.

Alternatively, redox processes offer a powerful means of cage disassembly. Sallé and co-workers have reported a series of cages characterized by their redox active components[159]. The tetrathiafulvalene(TTF)-based $[Pd_4L_2]^{8+}$ cage adopts a bent butterfly conformation, enabling cage assembly and allowing it to encapsulate two $B_{12}F_{12}{}^{2-}$ anions. TTF, being a redox-active compound, can switch between neutral and dicationic charge states. Consequently, the oxidation forces the TTF panels to flatten, causing the cage to disassemble and release the guest (Scheme 1.6). Remarkably, this process is fully reversible,

as the reduction rebuilds the cage and allows the guest to bind again.[160] Correspondingly, cages incorporating ferrocene units also exhibit redox-switchable properties. A water soluble ferrocene-based metallacapsule was shown to disassemble upon oxidation of ferrocene to ferrocenium, releasing bound aromatic guests and reversing this process upon reduction.[161]

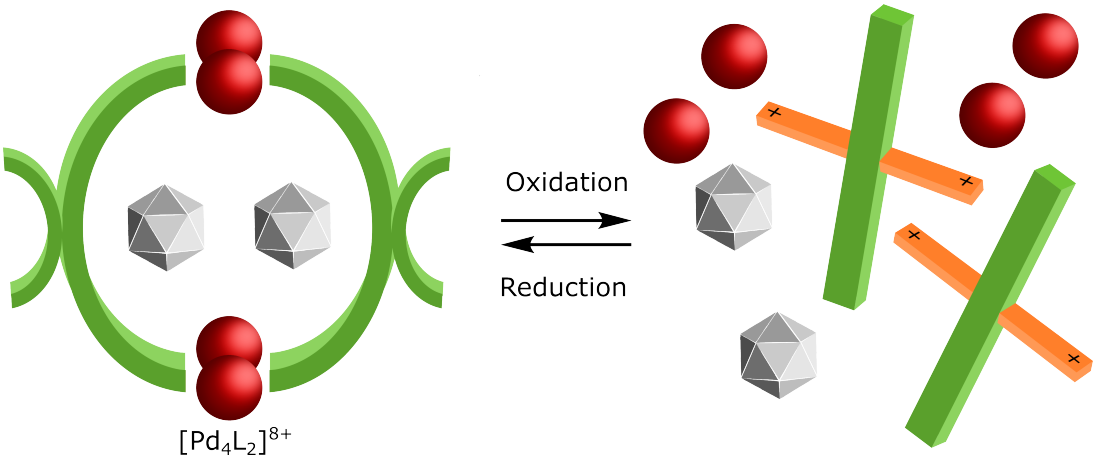

Scheme 1.6 Schematic representation of the reversible uptake/release of $B_{12}F_{12}{}^{2-}$ guest by redox stimuli triggered disassembly/reassembly of the TTF-based cage

Instead of employing a complete breaking of the cage, controllable guest uptake and release can be achieved by partial disassembly. This involves removing just enough of the non-covalent interactions to alter the cavity's properties, making it inhospitable for the guest. Such a system was demonstrated by Yoshizawa and colleagues. A quadruply stranded $[Hg_2L_4]^{4+}$ coordination capsule and a $[Hg_2L_2]^{4+}$ coordination tube that reversibly interconvert based on metal-to-ligand stoichiometry. The $[Hg_2L_4]^{4+}$ cage, formed at a 1:2 ratio, binds C_{60} guests; altering the ratio to 1:1 converts it to a $[Hg_2L_2]^{4+}$ macrocycle, thereby releasing the guest.[162]

1.4.1.2 Host modification

In contrast to previous approaches, a system can also be designed to locally alter the hospitable cavity's properties by inducing conformational changes, modifying the aperture opening, or shifting its polarity.[163–165] The $[Cd_4L_2]^{8+}$ cage developed by Nitschke and colleagues,[166] selectively and cooperatively binds oxocarbon anions. The flexible coordination spheres of the Cd(II) centers allow the receptor to dynamically adjust its structure, enabling strong cooperative binding. Substituting Cd(II) with Cu(I), facilitated by a solvent switch from acetonitrile, prompts a structural reorganization of the host. With transmetalation, Cu(I) ions form a saturated tetrahedral geometry, and the encapsulated oxocarbon anions are released. With a second transmetallation step, the original Cd(II) cages can be regenerated.

Yet another stimuli-responsive cage from Nitschke and co-workers demonstrates reversible guest exchange, but this time it is controlled by thermal stimuli. This thermoswitchable $[Zn_4L_4]^{8+}$ cage interconverts between two diastereomeric isomers: T1 at lower temperatures and T2 at higher temperatures (Scheme 1.7). The compact T1 isomer selectively binds small aliphatic guests (G1), while the larger, less enclosed T2 isomer forms upon heating, favoring bulkier aromatic guests (G2). Cooling reverses this process, restoring the original binding profile.[167]

Another variant of Sallé and coworkers' redox-responsive hosts is a neutral Pt-based metallacage featuring two extended tetrathiafulvalene (exTTF).[168] In its neutral state, this cage selectively binds planar polyaromatic guests like coronene. However, upon chemical or electrochemical oxidation, the host undergoes structural reconfiguration and expels the guest as the BF_4^- anions are introduced to the system, and this counter-anion outcompetes the guest. The neutral cage is recovered by adding a reducing agent, which allows the coronene to bind again.

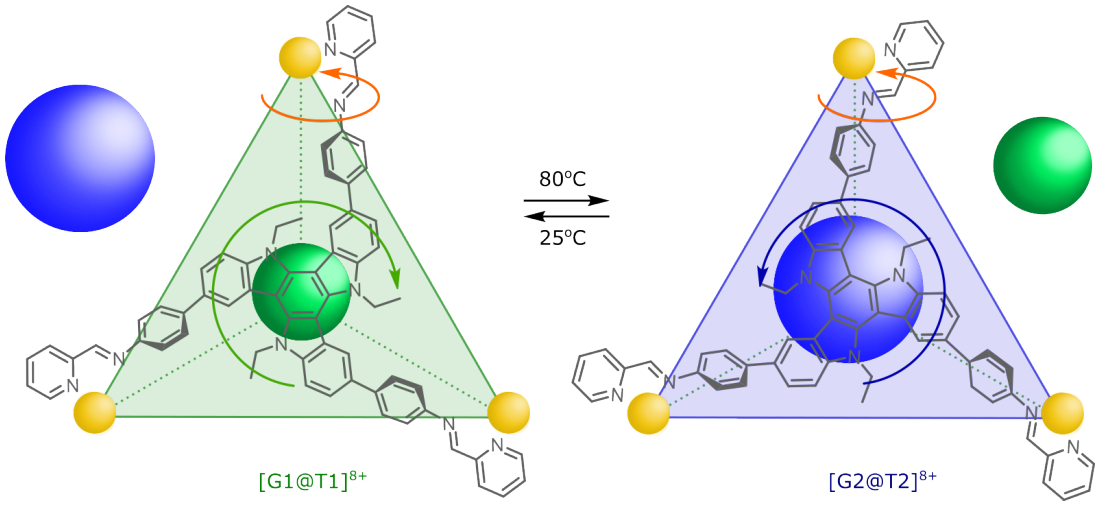

Scheme 1.7 Reversible guest exchange between dibromoadamantane (G1, green) and calix[4]arene (G2, blue) by the two diastereomeric states T1 and T2 of the $[Zn_4L_4]^{8+}$ tetrahedron under the influence of temperature.

1.4.1.3 Guest modification

As opposed to altering the host architecture or its cavity, modifying the guest, whereby the new guest variant has reduced affinity and thus facilitates expulsion from the cavity, has proven to be an effective method for this bidirectional encapsulation. This is often achieved by exposing the guest to chemical transformations, likely by switching between protonated or deprotonated states,[169,170] altering redox states, or inducing different photoactive conformational states. An early instance of a pH gated guest release was reported by Fujita *et al.* with their Pt(II) octahedral based nanocage. This thermally switchable cage constructively traps bulky aromatic guests at elevated temperatures. However, the cage

was also shown to accommodate pH sensitive dimethylaniline, which, in its protonated state, is expelled from the cage as it becomes more hydrophilic and is repelled by the cationic cage.[171] The water soluble $[Co_8L_{12}]^{12+}$ cubic cage from Ward *et al.* selectively binds various neutral organic guests. By changing the pH and thereby altering the guest's protonation state, it flips their affinity and releases them into the water. With this strategy, they managed the exchange of three distinct guest classes: acidic, neutral, and basic.[65,172] Similarly, a pH responsive pseudorotaxane was developed by Clever, Shionoya, and coworkers by threading a $[Pd_2L_4]^{4+}$ cage with a bis-sulfonate guest as an axle, powered by hydrogen bonding in the deprotonated state. An acid promotes dethreading or release of the neutral axle by weakening host-guest interactions, whereas a base restores the initial state (Scheme 1.8).[173]

Redox-responsive guests such as ferrocene and quinones have been extensively investigated for their ability to release cargo in a controlled manner. Fujita's polycationic nanocage $[Pd_6L_4]^{12+}$ is capable of encapsulating neutral guests, particularly ferrocene, within its cavity. Following electrochemical oxidation, the encapsulated ferrocene is converted to cationic ferrocenium, resulting in declathration as a consequence of Coulombic repulsion. This redox-active system is capable of undergoing multiple reversible cycles of clathration and declathration.[174] Sallé, Ribas, and coworkers demonstrated reversible guest exchange within a tetragonal Zn-porphyrin-based prismatic nanocage between C_{60} and a competing exTTF guest. In its reduced state, exTTF displays weak interactions, leading to its ejection and the re-uptake of C_{60}. Subsequent oxidation restores exTTF to its bound state.[175]

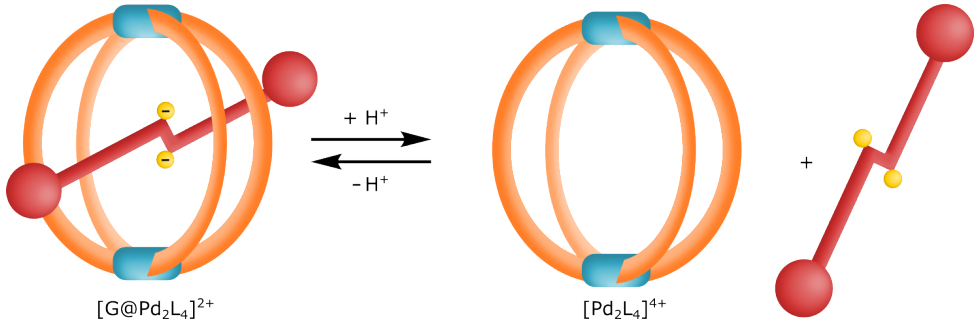

Scheme 1.8 Schematic representation of a pseudorotaxane with bisanionic axle, threading and dethreading promoted by pH changes.

1.4.2 Photo-induced guest release

Light is the most favored among external stimuli, owing to the fact that it is rapid, clean, remotely applied, and demonstrates high spatiotemporal precision without the production of waste. Consequently, one may frequently encounter comprehensive research on light-responsive metal-organic cages and their applications.[138,144] Incorporating photoswitchable components such as dithienylethene, diazocine,[176] spiropyran,[177,178] or

azobenzene[154,179–183] into the ligand design represents an effective approach to achieving guest release from the host cavity.

An initial instance of light-induced host structural modification was envisioned by Shinkai and coworkers with their azobenzene-linked bis(crown ether). In its original *trans* state, the two crown ether sites independently engage with smaller Na^+ cations. Under UV irradiation and thermal back reaction, the system undergoes conformational changes akin to the opening and closing of butterfly wings, respectively. In its closed conformation, the crown ether sites are able to bind larger alkali cations, such as Cs^+, through the establishment of a sandwich-like cooperative binding arrangement (Scheme 1.9).[184]

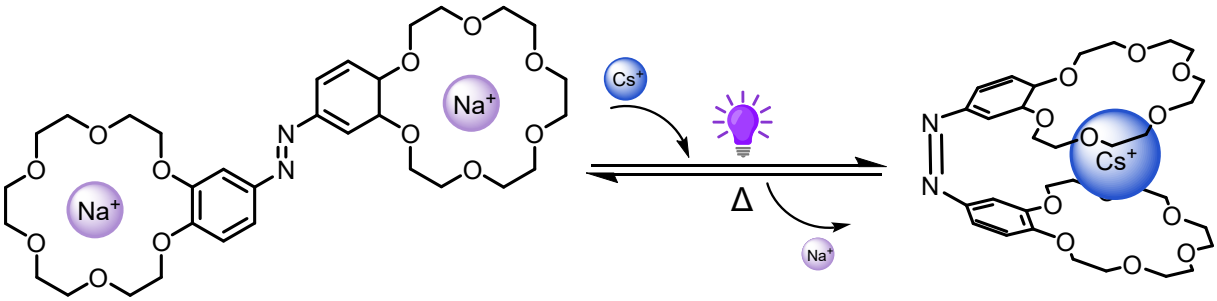

Scheme 1.9 Shinkai's photoresponsive azobenzene-linked bis(crown ether). Isomerization of azobenzene renders an open bis-monotopic *trans* form for Na^+ to a closed ditopic sandwich-like *cis* form for Cs^+

Another fundamental instance of light-driven structural transformation in the host is the photochromic coordination cage developed by Clever and colleagues. The lantern-shaped $[Pd_2L_4]^{4+}$ cage was made to integrate dithienylethene (DTE) photoswitches within its pyridine-based bis-monodentate ligands (Scheme 1.10).[185] Upon irradiation, the cage is capable of existing in two interconvertible states: a conformationally flexible open ring form (o-C) and a rigid closed ring form (c-C), achieved using 365 nm UV light and 617 nm light, respectively. The cages demonstrate affinities towards spherical guests such as $B_{12}F_{12}{}^{2-}$. Notably, the open ring cage exhibits a higher association constant with $B_{12}F_{12}{}^{2-}$ compared to the closed form; consequently, the closed cage releases the guest, enabling reversible uptake-release cycles mediated by light signals. Subsequently, the same group disclosed a series of cages utilizing diarylethene photoswitches that could be toggled, showing fascinating and diverse properties such as reversible transformations in topology, selective guest encapsulation/release, and retention or release of chiral information.[186–188]

Delving further into the realm of photoswitches, Clever and colleagues were the first to introduce diazocine units into metallacages. Diazocine resembles a bridged azobenzene but is characterized by greater rigidity and reduced conformational freedom, thus enabling a more regulated photochemical movement. But in contrast to the latter, the *cis* isomeric form of diazocines is the thermodynamically stable state and can be converted to the metastable *trans* state under irradiation with 385 nm. Reverting to the *cis* state is possible

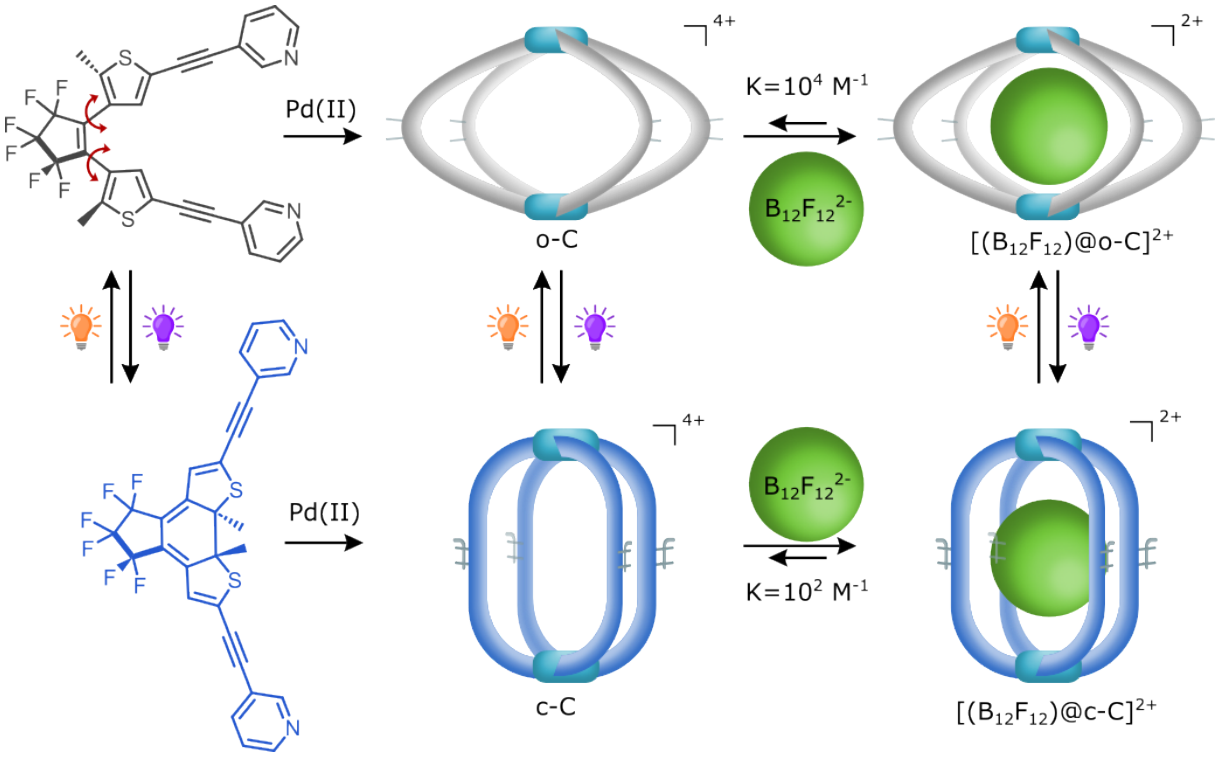

Scheme 1.10 Photoisomerisation of DTE-based metallacage demonstrating light-driven guest uptake and release.Cages switch from their open form (o-C) to closed form (c-C) with 365 nm light while 617 nm light switches it back to the open form. The o-C cage binds $B_{12}F_{12}^{2-}$ guest with higher affinity compared to c-C enabling controlled sequestration and release of the guest.

by irradiation with 530 nm UV light or through thermal relaxation. Interestingly enough, the *trans* form of the cage is capable of encapsulating a bisulfonate guest, while the *cis* form is not. Hence, a dissipative host-guest self-assembly system was established as long as it is exposed to continuous irradiation with 385 nm light.[189]

Furthermore, Fujita *et al.* incorporated azobenzene units endohedrally into a $[Pd_{12}L_{24}]^{24+}$ spherical complex. *Cis-trans* photoisomerization of these moieties altered the hydrophobicity of the cavity, which led to uptake/release processes for guests such as 1-pyrenecarboxaldehyde.[190] Building upon this, Nitschke *et al.* designed a $[Zn_4L_4]^{8+}$ tetrahedron with 12 azobenzene groups attached to the vertices. Isomerization from the *trans* to the *cis* form creates a steric clash, triggering cage disassembly, whereby it releases the formerly bound guest, particularly the bistriflimide (NTf_2^-) counter-anion. Visible light or heat reassembles the cage, and guest uptake is restored.[191]

Drawing inspiration from these light-responsive host-guest dynamics, our objective was to implement a photoswitchable moiety as a competing guest to induce reversible guest exchange within the host. This topic will be elaborated upon in Chapter 4.

1.5 References

[1] U.S. Environmental Protection Agency, Drinking Water Utilities and Professionals: Technical Overview of PFAS NPDWR, Accessed: 2025-09-17, **2024**, https://www.epa.gov/system/files/documents/2024-04/drinking-water-utilities-and-professionals-technical-overview-of-pfas-npdwr.pdf.

[2] H. Brunn, G. Arnold, W. Körner, G. Rippen, K. G. Steinhäuser, I. Valentin, *Environmental Sciences Europe* **2023**, *35*.

[3] M. A. Mall, P.-R. Burgel, C. Castellani, J. C. Davies, M. Salathe, J. L. Taylor-Cousar, *Nature Reviews Disease Primers* **2024**, *10*, 53.

[4] E. Stokstad, *Science* **2005**, *307*, 507–507.

[5] J. L. Sessler, P. A. Gale, W.-S. Cho, *Anion receptor chemistry*, *Vol. 8*, Royal Society of Chemistry, **2006**.

[6] P. Thomas, *Surface Coatings International* **1998**, *81*, 604–609.

[7] J. Podgorski, M. Berg, *Nature Communications* **2022**, *13*, 4232.

[8] M. J. Luna Juncal, P. Masino, E. Bertone, R. A. Stewart, *Science of The Total Environment* **2023**, *874*, 162408.

[9] J. R. G. Asio, J. S. Garcia, C. Antonatos, J. B. Sevilla-Nastor, L. C. Trinidad, *Emerging Contaminants* **2023**, *9*, 100205.

[10] B. Salomez, S. Grugeon, P. Tran-Van, S. Laruelle, *Journal of Power Sources* **2024**, *613*, 234901.

[11] M. Greiser, M. Karbowski, A. D. Kaplan, A. K. Coleman, N. Verhoeven, C. A. Mannella, W. J. Lederer, L. Boyman, *eLife* **2023**, *12*, (Eds.: D. J. Paterson, B. Kornmann, P. Swietach), e84204.

[12] I. Medina, P. Friedel, C. Rivera, K. T. Kahle, N. Kourdougli, P. Uvarov, C. Pellegrino, *Frontiers in Cellular Neuroscience* **2014**, *Volume 8 - 2014*.

[13] M. B. Zimmermann, K. Boelaert, *The Lancet Diabetes & Endocrinology* **2015**, *3*, 286–295.

[14] Baggio Bruno, Gambaro Giovanni, Marchini Francesco, Cicerello Elisa, Tenconi Romano, Clementi Maurizio, Borsatti Arturo, *New England Journal of Medicine* **1986**, *314*, 599–604.

[15] R. Rajesh, A. A. Mooslechner, H. Schweighofer, S. Pahernik, I. Lanz, R. Atallah, W. Platzer, C. Aigner, A. Benazzo, S. Angiari, L. Marsh, G. Kwapiszewska, A. Heinemann, T. Bärnthaler, *American Journal of Physiology-Lung Cellular and Molecular Physiology* **2025**, *328*, L671–L684.

[16] P. D. Beer, P. A. Gale, *Angewandte Chemie International Edition* **2001**, *40*, 486–516.

[17] M. J. Langton, C. J. Serpell, P. D. Beer, *Angewandte Chemie International Edition* **2016**, *55*, 1974–1987.

[18] X. Wu, A. M. Gilchrist, P. A. Gale, *Chem* **2020**, *6*, 1296–1309.

[19] D. F. Shriver, M. J. Biallas, *Journal of the American Chemical Society* **1967**, *89*, 1078–1081.

[20] C. H. Park, H. E. Simmons, *Journal of the American Chemical Society* **1968**, *90*, 2431–2432.

[21] E. Graf, J. M. Lehn, *Journal of the American Chemical Society* **1975**, *97*, 5022–5024.

[22] E. Graf, J. M. Lehn, *Journal of the American Chemical Society* **1976**, *98*, 6403–6405.

[23] F. P. Schmidtchen, *Angewandte Chemie International Edition in English* **1977**, *16*, 720–721.

[24] F. P. Schmidtchen, *Chemische Berichte* **1980**, *113*, 864–874.

[25] P. A. Gale, *Chemical Communications* **2011**, *47*, 82–86.

[26] G. W. Bates, P. A. Gale in *Recognition of Anions*, (Ed.: R. Vilar), Springer Berlin Heidelberg, Berlin, Heidelberg, **2008**, pp. 1–44.

[27] V. Amendola, M. Bonizzoni, D. Esteban-Gómez, L. Fabbrizzi, M. Licchelli, F. Sancenón, A. Taglietti, *Inorganic Chemistry in Italy* **2006**, *250*, 1451–1470.

[28] S. Valiyaveettil, J. F. Engbersen, W. Verboom, D. N. Reinhoudt, *Angewandte Chemie International Edition in English* **1993**, *32*, 900–901.

[29] K. Kavallieratos, S. R. de Gala, D. J. Austin, R. H. Crabtree, *Journal of the American Chemical Society* **1997**, *119*, 2325–2326.

[30] L. M. Eytel, A. C. Brueckner, J. A. Lohrman, M. M. Haley, P. H.-Y. Cheong, D. W. Johnson, *Chemical Communications* **2018**, *54*, 13208–13211.

[31] S. Lee, Y. Hua, H. Park, A. H. Flood, *Organic Letters* **2010**, *12*, 2100–2102.

[32] S. J. Edwards, H. Valkenier, N. Busschaert, P. A. Gale, A. P. Davis, *Angewandte Chemie International Edition* **2015**, *54*, 4592–4596.

[33] P. A. Gale, J. L. Sessler, *Coordination Chemistry Reviews* **1996**, *148*, 1–28.

[34] T. Becherer, D. Meshcheryakov, A. Springer, V. Böhmer, C. A. Schalley, *Journal of Mass Spectrometry* **2009**, *44*, 1338–1347.

[35] S. Kubik, *Accounts of Chemical Research* **2017**, *50*, 2870–2878.

[36] S. Lee, C.-H. Chen, A. H. Flood, *Nature Chemistry* **2013**, *5*, 704–710.

[37] Y. Li, A. H. Flood, *Angewandte Chemie International Edition* **2008**, *47*, 2649–2652.

[38] P. Ballester, *Chemical Society Reviews* **2010**, *39*, 3810–3830.

[39] S. O. Kang, J. M. Llinares, D. Powell, D. VanderVelde, K. Bowman-James, *Journal of the American Chemical Society* **2003**, *125*, 10152–10153.

[40] Y. Liu, W. Zhao, C.-H. Chen, A. H. Flood, *Science* **2019**, *365*, 159–161.

[41] T. R. Cook, P. J. Stang, *Chemical Reviews* **2015**, *115*, 7001–7045.

[42] G.-Y. Wu, W.-T. Dou, F. Zheng, H.-B. Yang, *Coordination Chemistry Reviews* **2024**, *519*, 216107.

[43] S. Saha, I. Regeni, G. H. Clever, *Coordination Chemistry Reviews* **2018**, *374*, 1–14.

[44] S. Pullen, J. Tessarolo, G. H. Clever, *Chemical Science* **2021**, *12*, 7269–7293.

[45] C. Piguet, G. Bernardinelli, G. Hopfgartner, *Chemical Reviews* **1997**, *97*, 2005–2062.

[46] M. Albrecht, *Chemical Reviews* **2001**, *101*, 3457–3498.

[47] R. Custelcean, *Chemical Society Reviews* **2014**, *43*, 1813–1824.

[48] D. J. Mercer, S. J. Loeb, *Chemical Society Reviews* **2010**, *39*, 3612–3620.

[49] H. Amouri, C. Desmarets, J. Moussa, *Chemical Reviews* **2012**, *112*, 2015–2041.

[50] C. R. Rice, *Anion Coordination Chemistry II* **2006**, *250*, 3190–3199.

[51] C. J. T. Cox, J. Hale, P. Molinska, J. E. M. Lewis, *Chemical Society Reviews* **2024**, *53*, 10380–10408.

[52] B. Hasenknopf, J.-M. Lehn, N. Boumediene, E. Leize, A. Van Dorsselaer, *Angewandte Chemie International Edition* **1998**, *37*, 3265–3268.

[53] M. Yoshizawa, J. K. Klosterman, M. Fujita, *Angewandte Chemie International Edition* **2009**, *48*, 3418–3438.

[54] R. Chakrabarty, P. S. Mukherjee, P. J. Stang, *Chemical Reviews* **2011**, *111*, 6810–6918.

[55] D. L. Caulder, R. E. Powers, T. N. Parac, K. N. Raymond, *Angewandte Chemie International Edition* **1998**, *37*, 1840–1843.

[56] E. G. Percástegui, T. K. Ronson, J. R. Nitschke, *Chemical Reviews* **2020**, *120*, 13480–13544.

[57] G. H. Clever, P. Punt, *Accounts of Chemical Research* **2017**, *50*, 2233–2243.

[58] S. Tashiro, Y. Yamada, L. A. Kringe, Y. Okajima, M. Shionoya, *Journal of the American Chemical Society* **2024**, *146*, 34501–34509.

[59] D. A. McMorran, P. J. Steel, *Angewandte Chemie International Edition* **1998**, *37*, 3295–3297.

[60] Y. R. Hristova, M. M. J. Smulders, J. K. Clegg, B. Breiner, J. R. Nitschke, *Chemical Science* **2011**, *2*, 638–641.

[61] S. Freye, J. Hey, A. Torras-Galán, D. Stalke, R. Herbst-Irmer, M. John, G. H. Clever, *Angewandte Chemie International Edition* **2012**, *51*, 2191–2194.

[62] S. Freye, D. M. Engelhard, M. John, G. H. Clever, *Chemistry – A European Journal* **2013**, *19*, 2114–2121.

[63] S. Freye, R. Michel, D. Stalke, M. Pawliczek, H. Frauendorf, G. H. Clever, *Journal of the American Chemical Society* **2013**, *135*, 8476–8479.

[64] D. P. August, G. S. Nichol, P. J. Lusby, *Angewandte Chemie International Edition* **2016**, *55*, 15022–15026.

[65] W. Cullen, A. J. Metherell, A. B. Wragg, C. G. P. Taylor, N. H. Williams, M. D. Ward, *Journal of the American Chemical Society* **2018**, *140*, 2821–2828.

[66] J. Yang, X.-Y. Chang, K.-C. Sham, S.-M. Yiu, H.-L. Kwong, C.-M. Che, *Chemical Communications* **2016**, *52*, 5981–5984.

[67] D. Van Craen, M. G. Kalarikkal, J. J. Holstein, *Journal of the American Chemical Society* **2022**, *144*, 18135–18143.

[68] D. A. Bender, *Amino Acid Metabolism*, John Wiley & Sons, **2012**.

[69] M.-L. Hou, C.-M. Lu, C.-H. Lin, L.-C. Lin, T.-H. Tsai, *Molecules* **2016**, *21*.

[70] B. Hoppe, *Nature Reviews Nephrology* **2012**, *8*, 467–475.

[71] W. Chen, C. Guo, Q. He, X. Chi, V. M. Lynch, Z. Zhang, J. Su, H. Tian, J. L. Sessler, *Journal of the American Chemical Society* **2019**, *141*, 14798–14806.

[72] Z. Zhou, D.-G. Chen, M. L. Saha, H. Wang, X. Li, P.-T. Chou, P. J. Stang, *Journal of the American Chemical Society* **2019**, *141*, 5535–5543.

[73] C. Bravin, E. Badetti, F. A. Scaramuzzo, G. Licini, C. Zonta, *Journal of the American Chemical Society* **2017**, *139*, 6456–6460.

[74] D. Ocklenburg, D. Van Craen, *Beilstein Journal of Organic Chemistry* **2024**, *20*, 3007–3015.

[75] H. Buschmann, M. Hauptmann, D. Niessing, C. W. Lloyd, A. R. Schäffner, *The Plant Cell* **2009**, *21*, 2090–2106.

[76] G. Song, J. Ren, *Chemical Communications* **2010**, *46*, 7283–7294.

[77] R. Barret, *Medicinal Chemistry: Fundamentals*, Elsevier, **2018**.

[78] R. B. Silverman, M. W. Holladay, *The Organic Chemistry of Drug Design and Drug Action*, Academic press, **2014**.

[79] C. Ballatore, D. M. Huryn, A. B. Smith III, *ChemMedChem* **2013**, *8*, 385–395.

[80] F. Begato, G. Licini, C. Zonta, *Angewandte Chemie International Edition* **2023**, *62*, e202311153.

[81] H. Yamamoto, E. M. Carreira, *Comprehensive Chirality*, *Vol. 1*, Newnes, **2012**.

[82] J. A. Dale, D. L. Dull, H. S. Mosher, *The Journal of organic chemistry* **1969**, *34*, 2543–2549.

[83] D. A. Allen, A. E. Tomaso Jr, O. P. Priest, D. F. Hindson, J. L. Hurlburt, *Journal of chemical education* **2008**, *85*, 698.

[84] T. R. Hoye, C. S. Jeffrey, F. Shao, *Nature protocols* **2007**, *2*, 2451–2458.

[85] H. Y. Aboul-Enein, I. Ali, *Chiral Separations by Liquid Chromatography and Related Technologies*, *Vol. 90*, CRC Press, **2003**.

[86] W. H. Pirkle, J. M. Finn, J. L. Schreiner, B. C. Hamper, *Journal of the American Chemical Society* **1981**, *103*, 3964–3966.

[87] Y. Okamoto, E. Yashima, *Angewandte Chemie International Edition* **1998**, *37*, 1020–1043.

[88] G. K. Scriba, *Enantioseparations* **2016**, *1467*, 56–78.

[89] D. Leung, S. O. Kang, E. V. Anslyn, *Chemical Society Reviews* **2012**, *41*, 448–479.

[90] B. T. Herrera, S. L. Pilicer, E. V. Anslyn, L. A. Joyce, C. Wolf, *Journal of the American Chemical Society* **2018**, *140*, 10385–10401.

[91] Z. Chen, Q. Wang, X. Wu, Z. Li, Y.-B. Jiang, *Chemical Society Reviews* **2015**, *44*, 4249–4263.

[92] Y. Mizuno, T. Aida, K. Yamaguchi, *Journal of the American Chemical Society* **2000**, *122*, 5278–5285.

[93] R. B. Prince, S. A. Barnes, J. S. Moore, *Journal of the American Chemical Society* **2000**, *122*, 2758–2762.

[94] J.-L. Hou, X.-B. Shao, G.-J. Chen, Y.-X. Zhou, X.-K. Jiang, Z.-T. Li, *Journal of the American Chemical Society* **2004**, *126*, 12386–12394.

[95] D.-W. Zhang, X. Zhao, Z.-T. Li, *Accounts of Chemical Research* **2014**, *47*, 1961–1970.

[96] N. Chandramouli, Y. Ferrand, G. Lautrette, B. Kauffmann, C. D. Mackereth, M. Laguerre, D. Dubreuil, I. Huc, *Nature Chemistry* **2015**, *7*, 334–341.

[97] Y. Ferrand, A. M. Kendhale, B. Kauffmann, A. Grélard, C. Marie, V. Blot, M. Pipelier, D. Dubreuil, I. Huc, *Journal of the American Chemical Society* **2010**, *132*, 7858–7859.

[98] S. Saha, B. Kauffmann, Y. Ferrand, I. Huc, *Angewandte Chemie International Edition* **2018**, *57*, 13542–13546.

[99] F. Riobé, A. P. Schenning, D. B. Amabilino, *Organic & Biomolecular Chemistry* **2012**, *10*, 9152–9157.

[100] J.-m. Suk, D. A. Kim, K.-S. Jeong, *Organic Letters* **2012**, *14*, 5018–5021.

[101] L. Vial, M. Dumartin, M. Donnier-Maréchal, F. Perret, J.-P. Francoia, J. Leclaire, *Chemical communications* **2016**, *52*, 14219–14221.

[102] W. Zuo, Z. Huang, Y. Zhao, W. Xu, Z. Liu, X.-J. Yang, C. Jia, B. Wu, *Chemical Communications* **2018**, *54*, 7378–7381.

[103] J. Ji, Y. Li, C. Xiao, G. Cheng, K. Luo, Q. Gong, D. Zhou, J. J. Chruma, W. Wu, C. Yang, *Chemical Communications* **2020**, *56*, 161–164.

[104] J. M. Lehn, A. Rigault, J. Siegel, J. Harrowfield, B. Chevrier, D. Moras, *Proceedings of the National Academy of Sciences* **1987**, *84*, 2565–2569.

[105] X.-S. Du, Y. Han, C.-F. Chen, *Chemical Communications* **2022**, *58*, 1326–1329.

[106] M. Imperato, A. Nicolini, J. Ribas-Ariño, M. Antkowiak, O. Roubeau, A. Cornia, V. Novikov, L. A. Barrios, G. Aromí, *Dalton Transactions* **2024**, *53*, 12301–12306.

[107] Q. Lin, L. Gao, B. Kauffmann, J. Zhang, C. Ma, D. Luo, Q. Gan, *Chemical Communications* **2018**, *54*, 13447–13450.

[108] C. T. McTernan, T. K. Ronson, J. R. Nitschke, *Journal of the American Chemical Society* **2021**, *143*, 664–670.

[109] M. Albrecht, *European Journal of Inorganic Chemistry* **2020**, *2020*, 2227–2237.

[110] D. A. McNaughton, W. G. Ryder, A. M. Gilchrist, P. Wang, M. Fares, X. Wu, P. A. Gale, *Chem* **2023**, *9*, 3045–3112.

[111] S. Fernández-Fariña, U. Barreiro-Sisto, M. Martínez-Calvo, R. Pedrido, A. M. González-Noya, *Dalton Transactions* **2024**, *53*, 18451–18457.

[112] S. Goetz, P. E. Kruger, *Dalton Transactions* **2006**, 1277–1284.

[113] P. J. Steel, D. A. McMorran, *Chemistry – An Asian Journal* **2019**, *14*, 1098–1101.

[114] L. P. Harding, J. C. Jeffery, T. Riis-Johannessen, C. R. Rice, Z. Zeng, *Chemical Communications* **2004**, 654–655.

[115] L.-J. Chen, H.-B. Yang, M. Shionoya, *Chemical Society Reviews* **2017**, *46*, 2555–2576.

[116] N. Struch, C. Frömbgen, G. Schnakenburg, A. Lützen, *European Journal of Organic Chemistry* **2017**, *2017*, 4984–4989.

[117] Y.-Q. Zou, D. Zhang, T. K. Ronson, A. Tarzia, Z. Lu, K. E. Jelfs, J. R. Nitschke, *Journal of the American Chemical Society* **2021**, *143*, 9009–9015.

[118] B. Quinodoz, G. Labat, H. Stoeckli-Evans, A. von Zelewsky, *Inorganic Chemistry* **2004**, *43*, 7994–8004.

[119] O. Chepelin, J. Ujma, X. Wu, A. M. Z. Slawin, M. B. Pitak, S. J. Coles, J. Michel, A. C. Jones, P. E. Barran, P. J. Lusby, *Journal of the American Chemical Society* **2012**, *134*, 19334–19337.

[120] S. Akine, H. Miyake, *Coordination Chemistry Reviews* **2022**, *468*, 214582.

[121] Z.-H. Yan, D. Li, X.-B. Yin, *Science Bulletin* **2017**, *62*, 1344–1354.

[122] L. Zhang, E. Meggers, *Accounts of Chemical Research* **2017**, *50*, 320–330.

[123] M. Albrecht, *Templates in Chemistry I: -/-* **2005**, 105–139.

[124] M. Albrecht, S. Kotila, *Angewandte Chemie International Edition in English* **1995**, *34*, 2134–2137.

[125] M. Albrecht, *Chemistry – A European Journal* **2000**, *6*, 3485–3489.

[126] E. Benchimol, K. E. Ebbert, A. Walther, J. J. Holstein, G. H. Clever, *Chemistry – A European Journal* **2024**, *30*, e202401850.

[127] M. Rancan, L. Armelao, *Chemical Communications* **2015**, *51*, 12947–12949.

[128] G. A. Hembury, V. V. Borovkov, Y. Inoue, *Chemical reviews* **2008**, *108*, 1–73.

[129] G. Wu, Y. Chen, S. Fang, L. Tong, L. Shen, C. Ge, Y. Pan, X. Shi, H. Li, *Angewandte Chemie International Edition* **2021**, *60*, 16594–16599.

[130] A. Ikeda, H. Udzu, Z. Zhong, S. Shinkai, S. Sakamoto, K. Yamaguchi, *Journal of the American Chemical Society* **2001**, *123*, 3872–3877.

[131] J. M. Rivera, T. Martín, J. Rebek Jr, *Science* **1998**, *279*, 1021–1023.

[132] M. Quan, X.-Y. Pang, W. Jiang, *Angewandte Chemie* **2022**, *134*, e202201258.

[133] C. Wolf, K. W. Bentley, *Chemical Society Reviews* **2013**, *42*, 5408–5424.

[134] M. Rancan, J. Tessarolo, A. Carlotto, S. Carlotto, M. Rando, L. Barchi, E. Bolognesi, R. Seraglia, G. Bottaro, M. Casarin, G. H. Clever, L. Armelao, *Cell Reports Physical Science* **2022**, *3*, 100692.

[135] P. Howlader, S. Mondal, S. Ahmed, P. S. Mukherjee, *Journal of the American Chemical Society* **2020**, *142*, 20968–20972.

[136] S. A. Ikbal, P. Zhao, M. Ehara, S. Akine, *Science Advances*, *9*, eadj5536.

[137] M. G. Kalarikkal, C. Drechsler, G. Tusha, L. V. Schäfer, D. Van Craen, *Chemistry – A European Journal* **2023**, *29*, e202301613.

[138] A. J. McConnell, C. S. Wood, P. P. Neelakandan, J. R. Nitschke, *Chemical Reviews* **2015**, *115*, 7729–7793.

[139] Y. Takashima, A. Harada, *Journal of Inclusion Phenomena and Macrocyclic Chemistry* **2017**, *88*, 85–104.

[140] F. Xu, B. L. Feringa, *Advanced Materials* **2023**, *35*, 2204413.

[141] E. Benchimol, J. Tessarolo, G. H. Clever, *Nature Chemistry* **2024**, *16*, 13–21.

[142] D.-H. Qu, Q.-C. Wang, Q.-W. Zhang, X. Ma, H. Tian, *Chemical Reviews* **2015**, *115*, 7543–7588.

[143] A. Díaz-Moscoso, P. Ballester, *Chemical Communications* **2017**, *53*, 4635–4652.

[144] S. J. Wezenberg, *Chemistry Letters* **2020**, *49*, 609–615.

[145] V. Sivalingam, M. Parbin, S. Krishnaswamy, D. K. Chand, *Angewandte Chemie International Edition* **2024**, *63*, e202403711.

[146] B. Kilbas, S. Mirtschin, R. Scopelliti, K. Severin, *Chemical Science* **2012**, *3*, 701–704.

[147] A. Walther, G. Tusha, B. Schmidt, J. J. Holstein, L. V. Schäfer, G. H. Clever, *Journal of the American Chemical Society* **2024**, *146*, 32748–32756.

[148] S.-G. Chen, Z.-X. Zhao, X.-N. Jiang, L. Wang, T.-Y. Zhou, C.-L. Lu, X. Zhao, X.-K. Jiang, Y. Ma, R.-X. Wang, Z.-T. Li, *Chemistry – An Asian Journal* **2016**, *11*, 465–469.

[149] F. Wang, C.-L. Feng, *Chemistry – A European Journal* **2018**, *24*, 1509–1513.

[150] E. Benchimol, B.-N. T. Nguyen, T. K. Ronson, J. R. Nitschke, *Chemical Society Reviews* **2022**, *51*, 5101–5135.

[151] R. A. S. Vasdev, J. A. Findlay, A. L. Garden, J. D. Crowley, *Chemical Communications* **2019**, *55*, 7506–7509.

[152] T. Y. Kim, R. A. S. Vasdev, D. Preston, J. D. Crowley, *Chemistry – A European Journal* **2018**, *24*, 14878–14890.

[153] J. E. M. Lewis, E. L. Gavey, S. A. Cameron, J. D. Crowley, *Chemical Science* **2012**, *3*, 778–784.

[154] S. Fu, Q. Luo, M. Zang, J. Tian, Z. Zhang, M. Zeng, Y. Ji, J. Xu, J. Liu, *Materials Chemistry Frontiers* **2019**, *3*, 1238–1243.

[155] Y. Yang, T. K. Ronson, P. C. Teeuwen, Y. Du, J. Zheng, D. J. Wales, J. R. Nitschke, *Chem* **2025**, *11*, 102288.

[156] M. R. Black, S. Bhattacharyya, S. P. Argent, B. S. Pilgrim, *Journal of the American Chemical Society* **2024**, *146*, 28233–28241.

[157] R.-J. Li, J. Tessarolo, H. Lee, G. H. Clever, *Journal of the American Chemical Society* **2021**, *143*, 3865–3873.

[158] P. Mal, D. Schultz, K. Beyeh, K. Rissanen, J. R. Nitschke, *Angewandte Chemie International Edition* **2008**, *47*, 8297–8301.

[159] S. Bivaud, J.-Y. Balandier, M. Chas, M. Allain, S. Goeb, M. Sallé, *Journal of the American Chemical Society* **2012**, *134*, 11968–11970.

[160] V. Croué, S. Goeb, G. Szalóki, M. Allain, M. Sallé, *Angewandte Chemie International Edition* **2016**, *55*, 1746–1750.

[161] K. Toyama, Y. Tanaka, M. Yoshizawa, *Angewandte Chemie International Edition* **2023**, *62*, e202308331.

[162] N. Kishi, M. Akita, M. Yoshizawa, *Angewandte Chemie International Edition* **2014**, *53*, 3604–3607.

[163] K. Mahata, P. D. Frischmann, F. Würthner, *Journal of the American Chemical Society* **2013**, *135*, 15656–15661.

[164] W. Wang, Y.-X. Wang, H.-B. Yang, *Chemical Society Reviews* **2016**, *45*, 2656–2693.

[165] A. Sørensen, A. M. Castilla, T. K. Ronson, M. Pittelkow, J. R. Nitschke, *Angewandte Chemie International Edition* **2013**, *52*, 11273–11277.

[166] Q. Gan, T. K. Ronson, D. A. Vosburg, J. D. Thoburn, J. R. Nitschke, *Journal of the American Chemical Society* **2015**, *137*, 1770–1773.

[167] D. Zhang, T. K. Ronson, S. Güryel, J. D. Thoburn, D. J. Wales, J. R. Nitschke, *Journal of the American Chemical Society* **2019**, *141*, 14534–14538.

[168] G. Szalóki, V. Croue, V. Carré, F. Aubriet, O. Alévêque, E. Levillain, M. Allain, J. Aragó, E. Ortí, S. Goeb, *Angewandte Chemie* **2017**, *129*, 16490–16494.

[169] M. M. J. Smulders, S. Zarra, J. R. Nitschke, *Journal of the American Chemical Society* **2013**, *135*, 7039–7046.

[170] M. Dekhtiarenko, S. Pascal, M. Elhabiri, V. Mazan, D. Canevet, M. Allain, V. Carré, F. Aubriet, Z. Voitenko, M. Sallé, O. Siri, S. Goeb, *Chemistry – A European Journal* **2021**, *27*, 15922–15927.

[171] F. Ibukuro, T. Kusukawa, M. Fujita, *Journal of the American Chemical Society* **1998**, *120*, 8561–8562.

[172] W. Cullen, S. Turega, C. A. Hunter, M. D. Ward, *Chemical Science* **2015**, *6*, 625–631.

[173] G. H. Clever, M. Shionoya, *Chemistry – A European Journal* **2010**, *16*, 11792–11796.

[174] W.-Y. Sun, T. Kusukawa, M. Fujita, *Journal of the American Chemical Society* **2002**, *124*, 11570–11571.

[175] C. Colomban, G. Szalóki, M. Allain, L. Gómez, S. Goeb, M. Sallé, M. Costas, X. Ribas, *Chemistry – A European Journal* **2017**, *23*, 3016–3022.

[176] D. Hugenbusch, M. Lehr, J.-S. von Glasenapp, A. J. McConnell, R. Herges, *Angewandte Chemie International Edition* **2023**, *62*, e202212571.

[177] D. Samanta, D. Galaktionova, J. Gemen, L. J. W. Shimon, Y. Diskin-Posner, L. Avram, P. Král, R. Klajn, *Nature Communications* **2018**, *9*, 641.

[178] S. Bhattacharyya, M. Maity, A. Chowdhury, M. L. Saha, S. K. Panja, P. J. Stang, P. S. Mukherjee, *Inorganic Chemistry* **2020**, *59*, 2083–2091.

[179] J. Gemen, M. J. Białek, M. Kazes, L. J. Shimon, M. Feller, S. N. Semenov, Y. Diskin-Posner, D. Oron, R. Klajn, *Chem* **2022**, *8*, 2362–2379.

[180] P. Cecot, A. Walczak, G. Markiewicz, A. R. Stefankiewicz, *Inorganic Chemistry Frontiers* **2021**, *8*, 5195–5200.

[181] M. B. Tipping, L. Pruñonosa Lara, A. B. Solea, L. K. S. von Krbek, M. D. Ward, *Chemical Science* **2024**, *15*, 8488–8499.

[182] R. G. DiNardi, S. Rasheed, S. S. Capomolla, M. H. Chak, I. A. Middleton, L. K. Macreadie, J. P. Violi, W. A. Donald, P. J. Lusby, J. E. Beves, *Journal of the American Chemical Society* **2024**, *146*, 21196–21202.

[183] A. D. W. Kennedy, R. G. DiNardi, L. L. Fillbrook, W. A. Donald, J. E. Beves, *Chemistry – A European Journal* **2022**, *28*, e202104461.

[184] S. Shinkai, T. Nakaji, T. Ogawa, K. Shigematsu, O. Manabe, *Journal of the American Chemical Society* **1981**, *103*, 111–115.

[185] M. Han, R. Michel, B. He, Y.-S. Chen, D. Stalke, M. John, G. H. Clever, *Angewandte Chemie International Edition* **2013**, *52*, 1319–1323.

[186] R.-J. Li, Julian. J. Holstein, W. G. Hiller, J. Andréasson, G. H. Clever, *Journal of the American Chemical Society* **2019**, *141*, 2097–2103.

[187] M. Han, Y. Luo, B. Damaschke, L. Gómez, X. Ribas, A. Jose, P. Peretzki, M. Seibt, G. H. Clever, *Angewandte Chemie International Edition* **2016**, *55*, 445–449.

[188] R.-J. Li, M. Han, J. Tessarolo, J. J. Holstein, J. Lübben, B. Dittrich, C. Volkmann, M. Finze, C. Jenne, G. H. Clever, *ChemPhotoChem* **2019**, *3*, 378–383.

[189] H. Lee, J. Tessarolo, D. Langbehn, A. Baksi, R. Herges, G. H. Clever, *Journal of the American Chemical Society* **2022**, *144*, 3099–3105.

[190] T. Murase, S. Sato, M. Fujita, *Angewandte Chemie* **2007**, *119*, 5225–5228.

[191] A. Ghosh, L. Slappendel, B.-N. T. Nguyen, L. K. S. von Krbek, T. K. Ronson, A. M. Castilla, J. R. Nitschke, *Journal of the American Chemical Society* **2023**, *145*, 3828–3832.

2 SCOPE OF THE THESIS

This thesis primarily explores the charge-neutral Zn(II) helicate synthesized within our research group and its application in anion recognition, particularly of carboxylates. Considering the biological and environmental significance of carboxylates, it is imperative to develop a receptor that demonstrates both high affinity and selectivity for these entities. Building on the established framework showing size-selective dicarboxylate binding, this study extends the application domain to chiroptical analysis, stimuli-responsive guest exchange, and colorimetric sensing methodologies.

The primary aims and objectives addressed in this dissertation can be outlined as follows:

- Quantify the binding of chiral dicarboxylates to the $[L_2Zn_2]$ helicate and control *meso* and racemic helicate populations via stereodynamic triazole linkers.
- Utilize the chiroptical readout in circular dichroism spectroscopy (CD) due to induced chirality to determine the enantiomeric excess (*ee*) of bound guests.
- Implement a geometry switchable, stimuli-responsive guest to modulate the binding and release of a secondary guest, aiming to achieve controlled guest exchange.
- Determine the influence of size-selectivity, analyze exchange kinetics, and broaden the guest scope to include more analytes.
- Incorporate a triphenylamine (TPA) unit into the ligand backbone and evaluate the impact on photophysics and colorimetric sensing upon guest binding.
- Investigate the binding interactions of hazardous perfluorinated compounds with the modified receptor.

3 CHARGE-NEUTRAL Zn(II) HELICATE FOR CHIROPTICAL RECOGNITION OF CARBOXYLATES

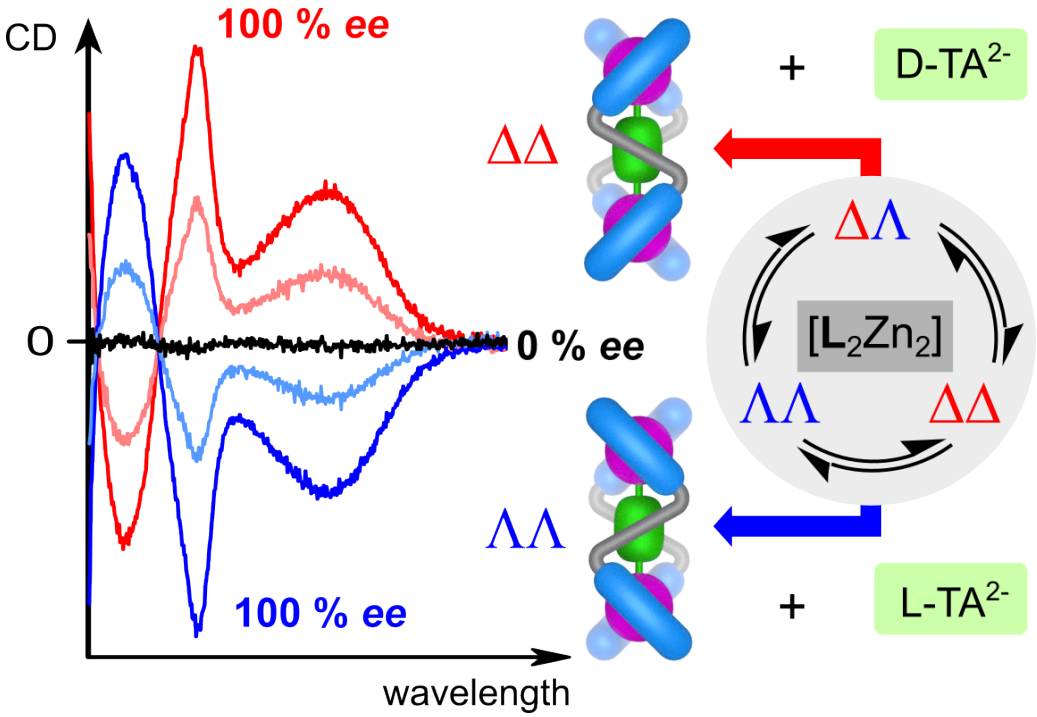

*Parts of this chapter were previously published in the peer-reviewed journal article "Chiroptical Recognition of Carboxylates with Charge-Neutral Double-Stranded Zinc(II) Helicates"[1] and are redrawn or adapted here for completeness. Unless otherwise stated, the procedures and data are consistent with the original work. All additions and modifications introduced in this thesis are indicated within the text.

3.1 Introduction

Chirality is a concept, fundamental across chemistry and the life sciences, and chiral molecules are pervasive in natural and synthetic systems. Chiral dicarboxylates, in particular tartrate, malate, and aspartate, play vital roles in metabolism, drug development, and food science, making their recognition and analysis significant. A multitude of metal-based supramolecular hosts are widely established as a probe for chiroptical recognition and chirality analysis.[2–23] Although metal-organic hosts extend distinct advantages through their preorganized, modular structures, stereodynamic metal-organic receptors for this purpose are profoundly underrepresented.[24]

The charge-neutral, metal-directed [L_2Zn_2] helicate, one of the first anion receptors synthesized by our group, was recognized as highly selective toward dicarboxylates, with association constants ranging up to 10^8 M^{-1}.[25] Hypothetically, given its established characteristic binding properties, this receptor holds the potential to be an effective chiroptical probe for both mono- and dicarboxylate analytes. This is based on two key points. Firstly, the receptor's strong anion recognition and binding affinities facilitate nearly quantitative host-guest complex formation with an optimal amount of the guest added. This is expected to enhance sensitivity by maximizing the enrichment of a single enantiomer. Secondly, the metal centers provide a direct coordinative interaction with the guest, which should enable an efficient transfer of chiral information from the guest to the optically-active complex units.

Another crucial requirement for the hypothesis to hold is for the helicate to exist in its chiral enantiomeric forms. If not, a racemic mixture capable of enhancing one of the enantiomers upon carboxylate binding is eminently desired. With the evidence on hand, the crystal structure from previous findings shows that the host exists in its *meso*-form (as a *meso*-helicate) with opposite configurations at the metal center and an inversion center when bound to a naphthalene-2,6-dicarboxylate guest (Figure 4.2). However, the effect of the host on the helicate's handedness upon the introduction of a chiral guest is unknown. As a substantial amount of studies report guest-induced transformation of non-chiral, racemic mixtures to the exclusive enhancement of one of the helicate enantiomers, studying this for our receptor is of great interest.[26] Evidently, from the aforementioned crystal structure, the ligand backbone operates in its *anti-anti* conformation, forming the *meso*-helicate.[25] As the ligand incorporates a triazole unit with rotational freedom, it is quite likely that the ligands can also exist in a *syn-syn* conformation, providing a less linear backbone that could result in racemic forms. It is highly probable that smaller guests favor the *syn-syn* conformation by shortening the zinc-zinc distance with twisted ligand strands. With distinct chiral forms with respect to each guest enantiomer, the receptor is anticipated to provide opposite mirror image CD signals and serve as a chirality analysis probe. This

capability will be further explored in the current chapter.

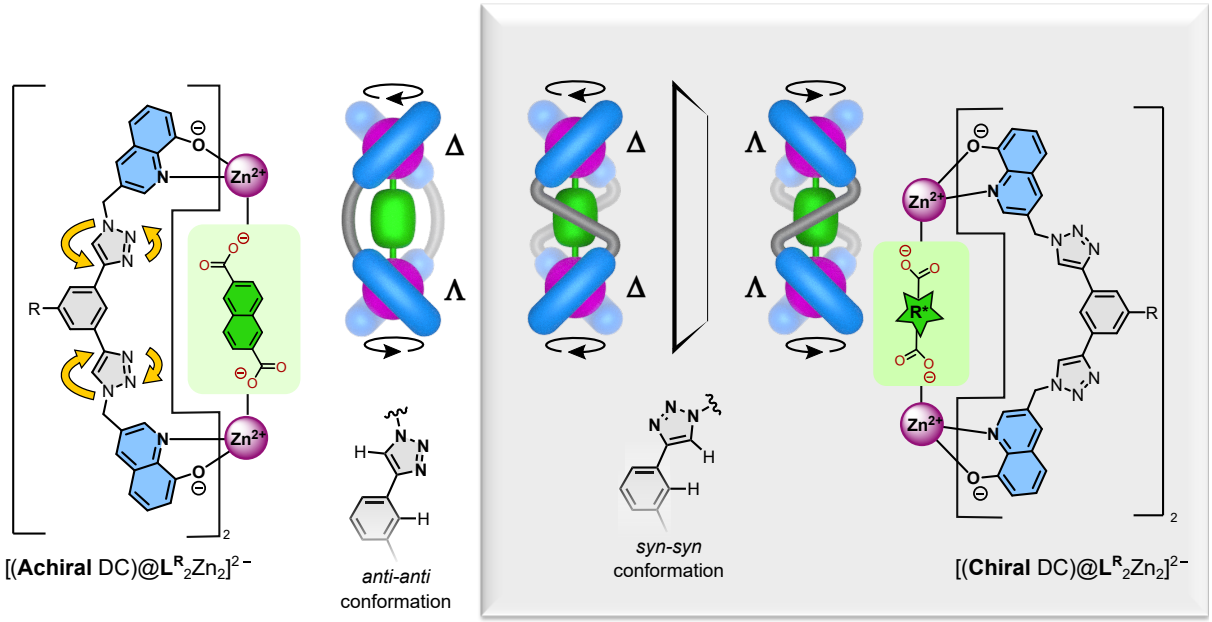

Figure 3.1 (Left) Previous findings: Charge-neutral [$\mathbf{L}^{\mathbf{R}}{}_2Zn_2$] receptor can adopt two conformations owing to the rotational freedom of triazole units when bound to mono- and dicarboxylate guests. With naphthalene-2,6-dicarboxylate, the crystal structure shows the *anti–anti* (*meso*) conformation.[25] (Right) Working hypothesis for this project: When smaller chiral dicarboxylates are introduced it is expected to induce a bias toward the twisted *syn-syn* conformation, enabling chiroptical recognition.

3.2 Results and discussion

3.2.1 Synthesis of the charge-neutral receptor

The ligand $\mathbf{L^R}$-H_2 was synthesized using the procedure adapted from our group's previously reported procedure[25] (Scheme 3.1). The synthesis involved two main parts. A five-step synthetic route is used to produce the hydroxyquinolinate complexation unit and a separate route to create the dialkyne backbone bearing a solubilizing group. These two synthons were "clicked" together via CuAAC to afford the triazole-based ligand. The subsequent complexation of the ligand with zinc acetate was carried out in DMSO. After lyophilization to remove the byproducts, it yielded the charge-neutral complex $[\mathbf{L^R}_2Zn_2]$. Detailed procedures are described in the experimental section, with all the conditions following the literature[25] unless otherwise stated.

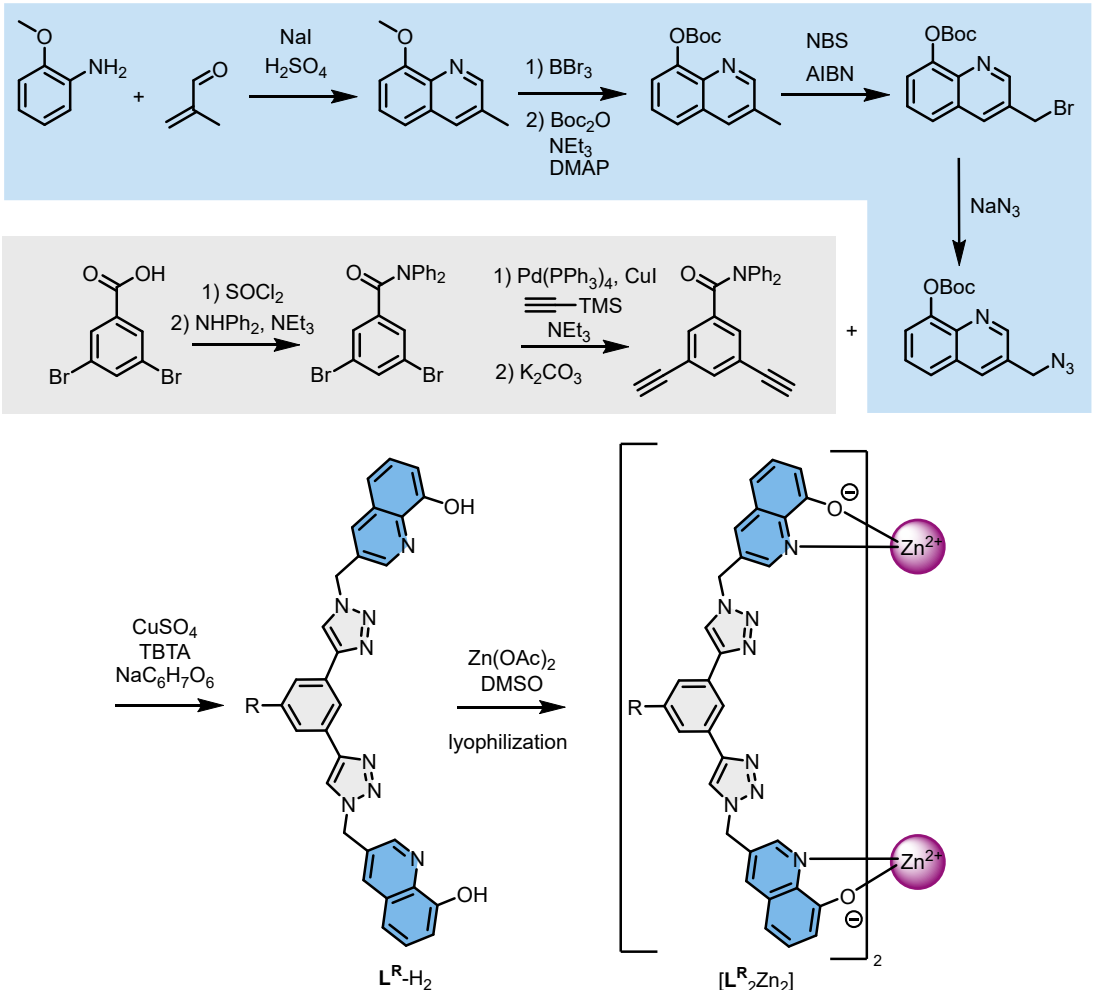

Scheme 3.1 Overall synthesis of ligand $\mathbf{L^R}$-H_2 and complexation of $[\mathbf{L^R}_2Zn_2]$. Synthetic procedure adapted from [25]

3.2.2 Investigation of the chiroptical recognition properties

Accounting for the receptor's size-selective coordinative guest recognition, tartrate ($\mathbf{TA^{2-}}$) was chosen as a model guest to test the working hypothesis. Its bidentate binding motif and two stereogenic centers are anticipated to result in a high binding affinity and significant enantiomeric enrichment of a single diastereomeric form.

^{1}H NMR titrations of D-(−)-tartrate ($\mathbf{D\text{-}TA^{2-}}$) and L-(+)-tartrate ($\mathbf{L\text{-}TA^{2-}}$) as their TBA salts with [$\mathbf{L^R}_2Zn_2$] depict an intermediate binding regime. In the titration with $\mathbf{D\text{-}TA^{2-}}$ (Scheme 3.2), the signals (gray) corresponding to the mixture of free host and host-guest species shift and broaden with each aliquot of the guest. The signals saturate at approximately 1.2 to 1.5 equiv. of guest, confirming a quantitative 1:1 [($\mathbf{D\text{-}TA}$)@$\mathbf{L^R}_2Zn_2$]$^{2-}$ host-guest complex formation, observed as clean, sharp signals (red). As intermediate

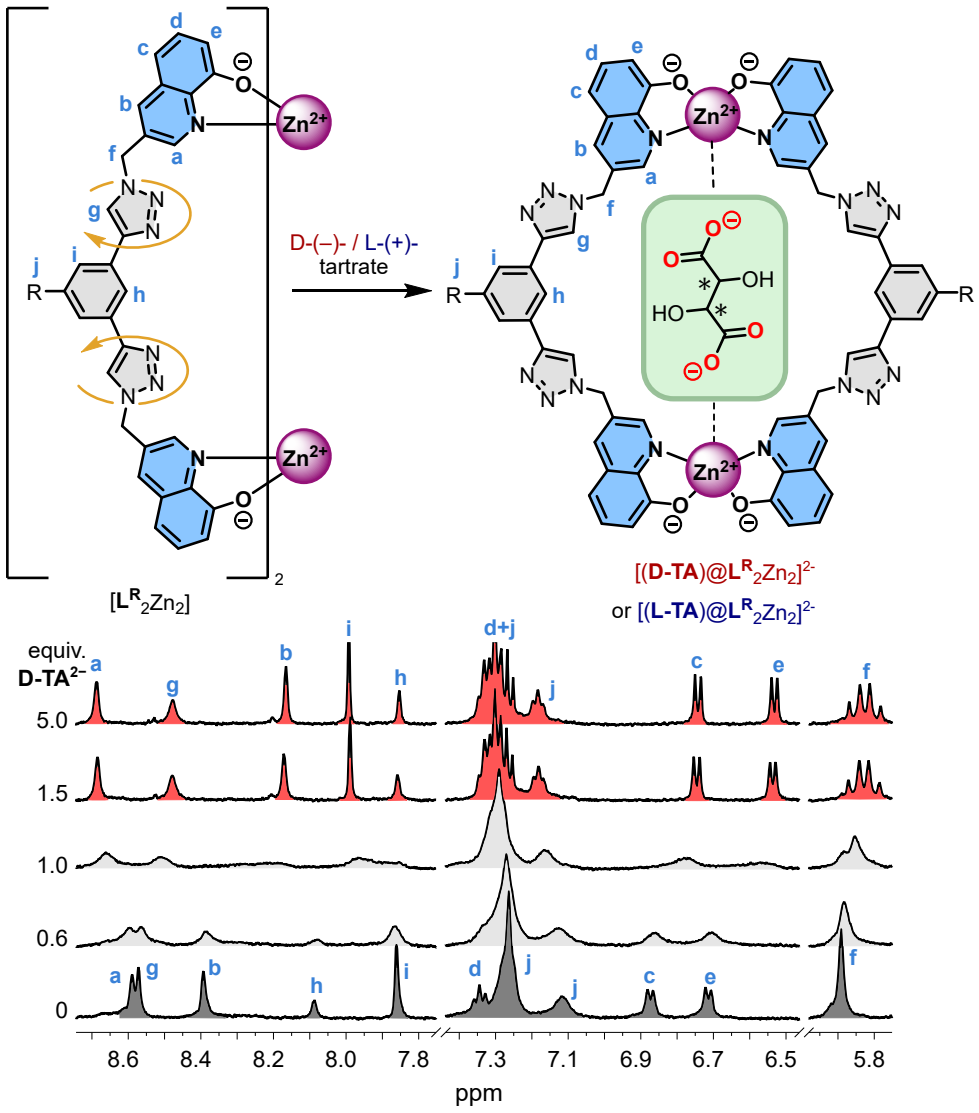

Scheme 3.2 (Top) Representation of recognition of D/L tartrate enantiomers by charge-neutral [$\mathbf{L^R}_2Zn_2$] by twisting the ligand arms. (bottom) ^{1}H NMR titration (500 MHz, 500 µM, DMSO-d_6, 298 K) of [$\mathbf{L^R}_2Zn_2$] with D-(−)-tartrate as its TBA salt. The titration data indicates an intermediate exchange binding process, leading to the formation of a 1:1 host-guest complex.

exchange titrations are not useful for binding constant calculations, we performed ITC measurements, and a binding constant of $(1.74 \pm 0.32) \times 10^5\,\mathrm{M}^{-1}$ was determined. This value is consistent with our expectations based on the guest's size and the previously established trend for aliphatic dicarboxylates.

To test the hypothesis, we recorded a NOESY spectrum of $[(\mathbf{D\text{-}TA})@\mathbf{L^R}_2Zn_2]^{2-}$ with five equivalents of the D-(−)-tartrate guest (Figure 3.2). A single through-space coupling cross-peak between the triazole proton H_g and the "inner" phenyl proton H_h was observed. This observation is diagnostic of the *syn-syn* arrangement, where these two protons are held in close proximity. In contrast to the free $[\mathbf{L^R}_2Zn_2]$ host, which shows cross peaks for both *syn-syn* and *anti-anti* conformations, indicating a more flexible ligand environment, the absence of the *anti-anti* cross peak in the bound complex is significant. This proves that all of the *meso*-helicates are converted into a single chiral helicate upon tartrate binding. Tartrate locks the triazole unit and eliminates the rotational freedom to access the *anti-anti* conformation.

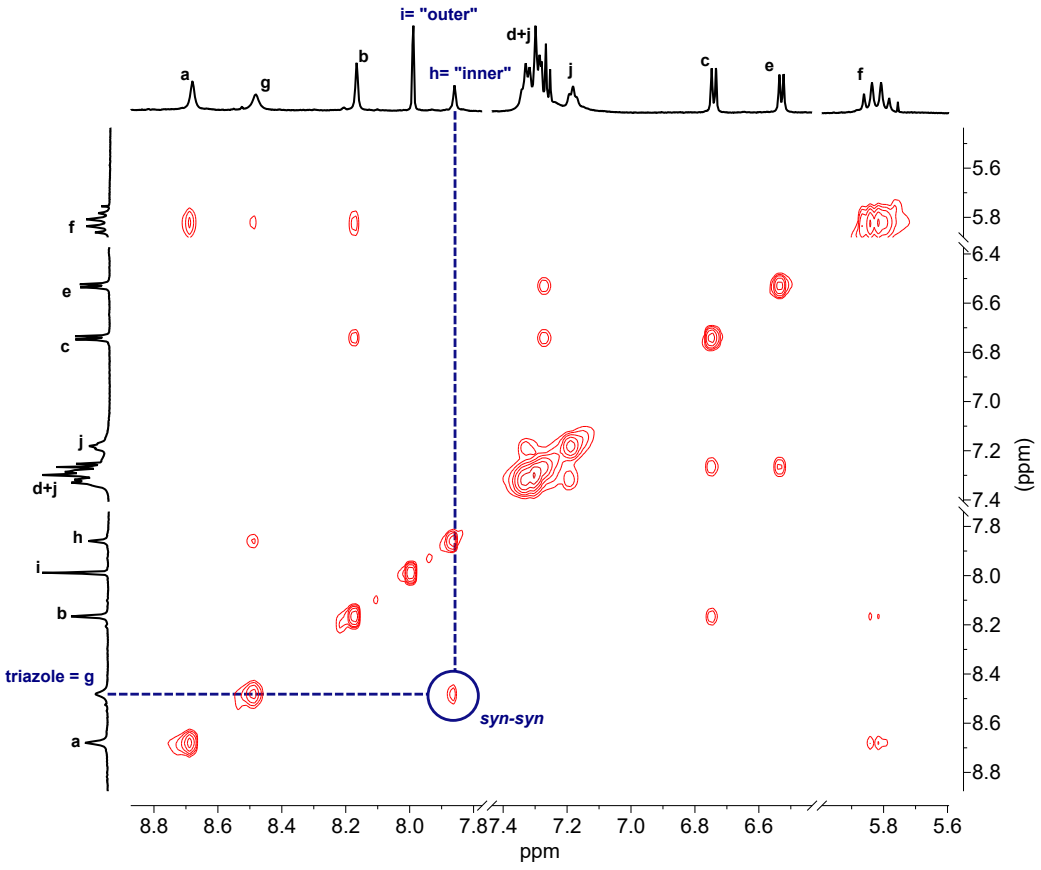

Figure 3.2 NOESY spectrum of the $[(\mathbf{D\text{-}TA})@\mathbf{L^R}_2Zn_2]^{2-}$ with five equiv. of $\mathbf{D\text{-}TA^{2-}}$ depicting exclusive *syn-syn* triazole conformation.

The hypothesis was further supported by the chiroptical responses observed from circular dichroism (CD) spectroscopy experiments. The host, which is otherwise CD silent, when combined with D-(−)-tartrate, shows a characteristic negative Cotton effect at 308 nm

and two positive bands at 350 nm and 420 nm. Notably, the tartrate guest does not absorb in this region, but the observed signals match the UV-Vis absorption maxima of the [(**D-TA**)@$\mathbf{L^R}_2Zn_2]^{2-}$ host-guest complex arising from the quinolinate-zinc complex unit chromophores. L-(+)-tartrate produces the exact mirror-image Cotton effect signals (Figure 3.3). A CD titration confirmed that the response does not change beyond one equiv. of the guest, forming a saturated 1:1 host-guest complex, consistent with NMR and ITC results, underlining the high affinity and sensitivity of the receptor. The mirror-image appearance of the CD signals, depending on D- and L-tartrate, provides evidence for the guest-induced enrichment of the right-handed ($\Delta\Delta$) and left-handed ($\Lambda\Lambda$) helicates, respectively.

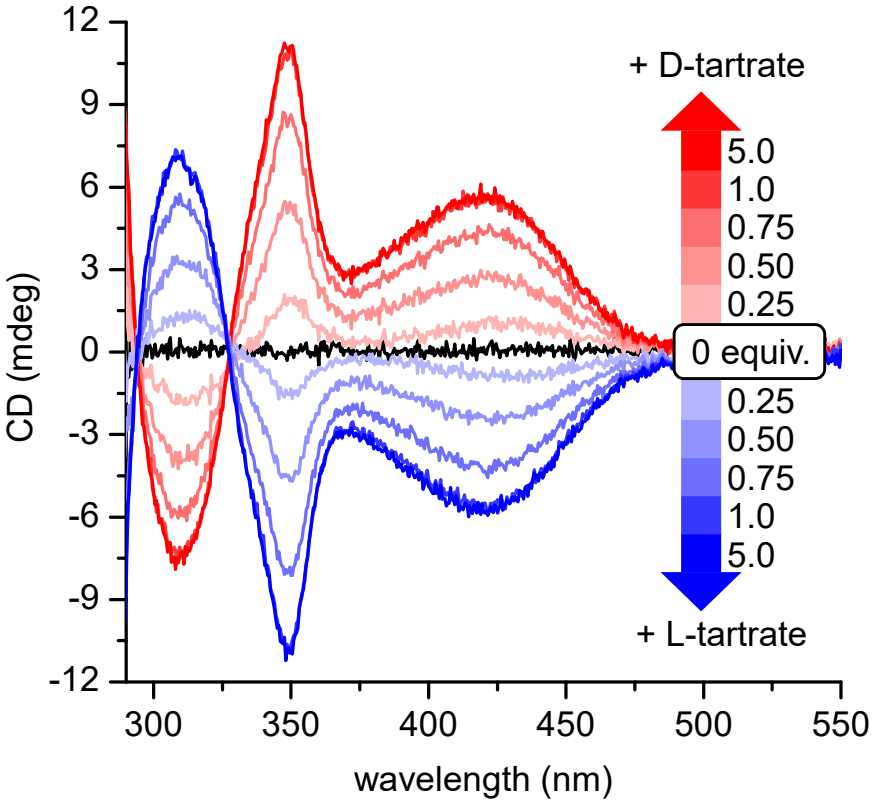

Figure 3.3 CD titration of [$\mathbf{L^R}_2Zn_2$] with D-(−)- and L-(+)-tartrate (500 µM, l = 2 mm, DMSO-d_6, 298 K) showing perfectly mirroring Cotton effects with 1:1 host-guest complex formation. The observed chiroptical response proves the guest-induced helicate enantiomeric enrichment.

After many unsuccessful attempts to grow single crystals from host-guest complexes with any of the guests investigated in this study, we turned to computational modeling. NOESY experiments explicitly identify helicates with triazole linkers in *syn-syn* conformation as the only species in solution. Also, prior knowledge from the solid-state evidence for naphthalene-2,6-dicarboxylate shows the guest bridging between two zinc(II) centers in the receptor.[25] Considering the coordinative dicarboxylate nature of tartrate and other guests involved in this study, we modeled host-guest structures in which $\mathbf{TA}^{2-}$ coordinates

between the metals.

For the ease of calculation, the preferred choice would be to use the simple [$\mathbf{L^H}_2Zn_2$] reported previously[25], lacking the bulky diphenylamide solubilizing groups as the host to reduce the atom count. NMR experiments show the same binding mode for both [$\mathbf{L^H}_2Zn_2$] and [$\mathbf{L^R}_2Zn_2$] with D-(−)-tartrate under the same conditions (Figure 3.4 and Figure 3.5). A 1:1 host-guest complex is observed in both cases while matching the observed chemical shifts and diastereotopic signal splitting of proton H_f. Since [$\mathbf{L^H}_2Zn_2$] also retains an identical, slightly more prominent CD response with five equivalents of D-(−)-tartrate (Figure 3.6), we proceeded with the simpler host for calculations.

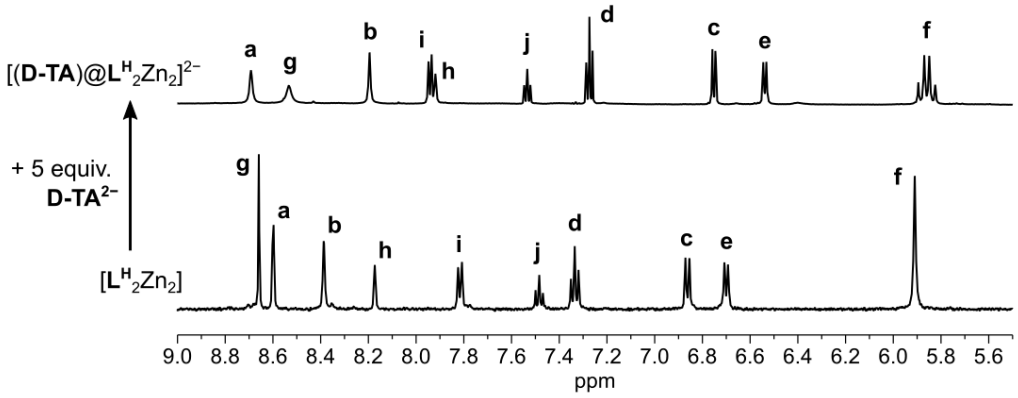

Figure 3.4 [$\mathbf{L^H}_2Zn_2$] with five equivalents of D-(−)-tartrate forms [(**D-TA**)@$\mathbf{L^H}_2Zn_2$]$^{2-}$.

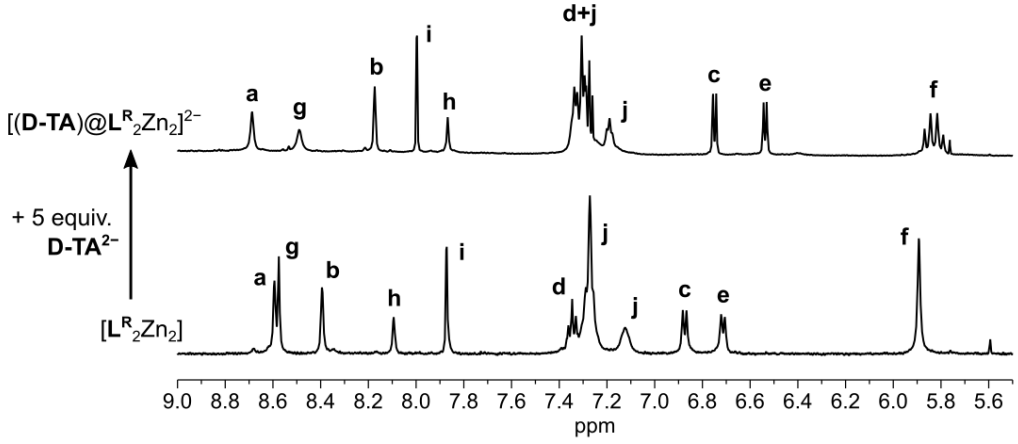

Figure 3.5 [$\mathbf{L^R}_2Zn_2$] with five equivalents of D-(−)-tartrate forms [(**D-TA**)@$\mathbf{L^R}_2Zn_2$]$^{2-}$.

Right- and left-handed enantiomers of the complex, ΔΔ- and ΛΛ-[(**D-TA**)@$\mathbf{L^H}_2Zn_2$]$^{2-}$, were calculated and geometry-optimized with r^{2}SCAN-3c[27] (ORCA 5.0.2)[28,29]. To determine the preferred helicity induced by **(D-TA^{2-})**, we computed electronic circular dichroism (ECD) spectra by TD-DFT (Gaussian16 Rev. B.01)[30] at the BHandHLYP[31]/def2-SVP[32,33] level with implicit DMSO solvation and compared the respective calculated CD spectrum with the measured ones (Figure 3.6).

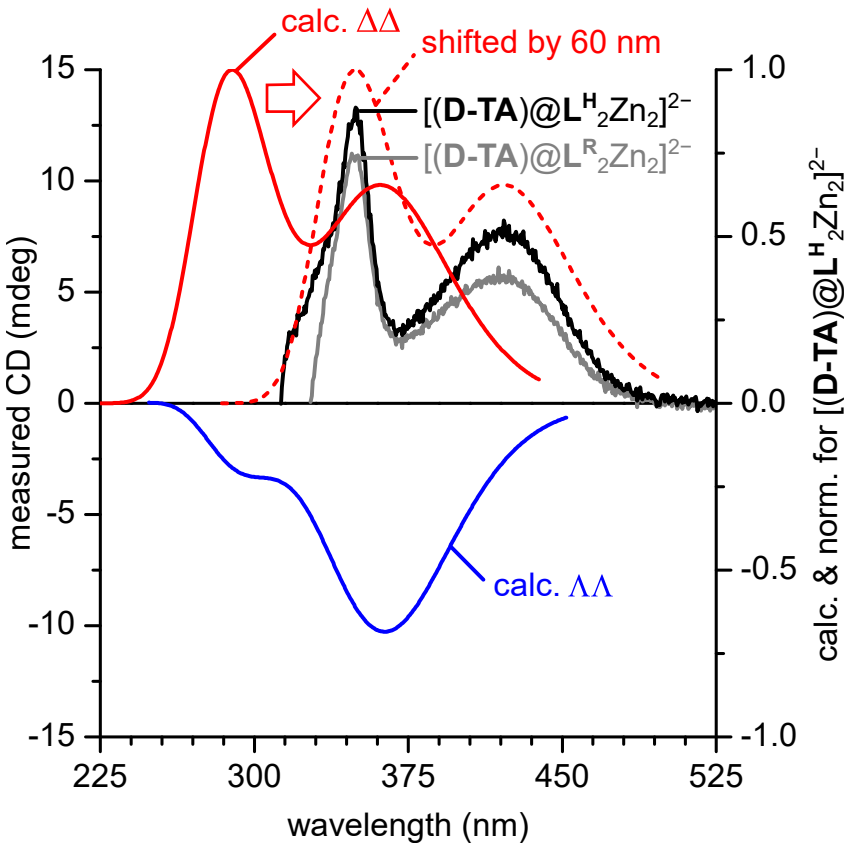

Figure 3.6 Comparison of experimental and computed CD spectra. Experimental traces measured for $[(\mathbf{D\text{-}TA})@\mathbf{L^R}_2Zn_2]^{2-}$ (gray) and $[(\mathbf{D\text{-}TA})@\mathbf{L^H}_2Zn_2]^{2-}$ (black) after addition of 5 equiv. of D-(−)-tartrate (500 µM, l = 2 mm, DMSO-d_6, 298 K) are overlaid with the TD-DFT calculated CD spectra for ΔΔ-$[(\mathbf{D\text{-}TA})@\mathbf{L^H}_2Zn_2]^{2-}$ (red) and ΛΛ-$[(\mathbf{D\text{-}TA})@\mathbf{L^H}_2Zn_2]^{2-}$ (blue). Geometry optimizations were done by using r^{2}SCAN-3c (ORCA 5.0.2) and CD spectra were computed with BHandHLYP/def2-SVP and implicit solvation.

The ΛΛ model does not reproduce the experimental spectrum (Figure 3.6, blue) and was therefore dismissed. In contrast, the ΔΔ model (Figure 3.6, red) aligns closely with the measured spectra of $[(\mathbf{D\text{-}TA})@\mathbf{L^H}_2Zn_2]^{2-}$ (Figure 3.6, black) and $[(\mathbf{D\text{-}TA})@\mathbf{L^R}_2Zn_2]^{2-}$ (Figure 3.6, gray) if an x-axis shift of 60 nm is applied (Figure 3.6, red-dashed). With this adjustment, the two dominant positive Cotton effects at 350 nm and 420 nm coincide, and even their relative intensities are matched well, supporting the formation and enrichment of the right-handed ΔΔ helicate upon the addition of D-(−)-tartrate.

The optimized ΔΔ-right-handed structure shows both upper and lower zinc centers with the same handedness, bridged by $(\mathbf{D\text{-}TA^{2-}})$ and a zig-zag orientation of the ligand strands. The triazole linkers retain some rotational freedom, in agreement with the unusually broad triazole signal (H_g) observed in the NMR (Figure 3.7 a,b).

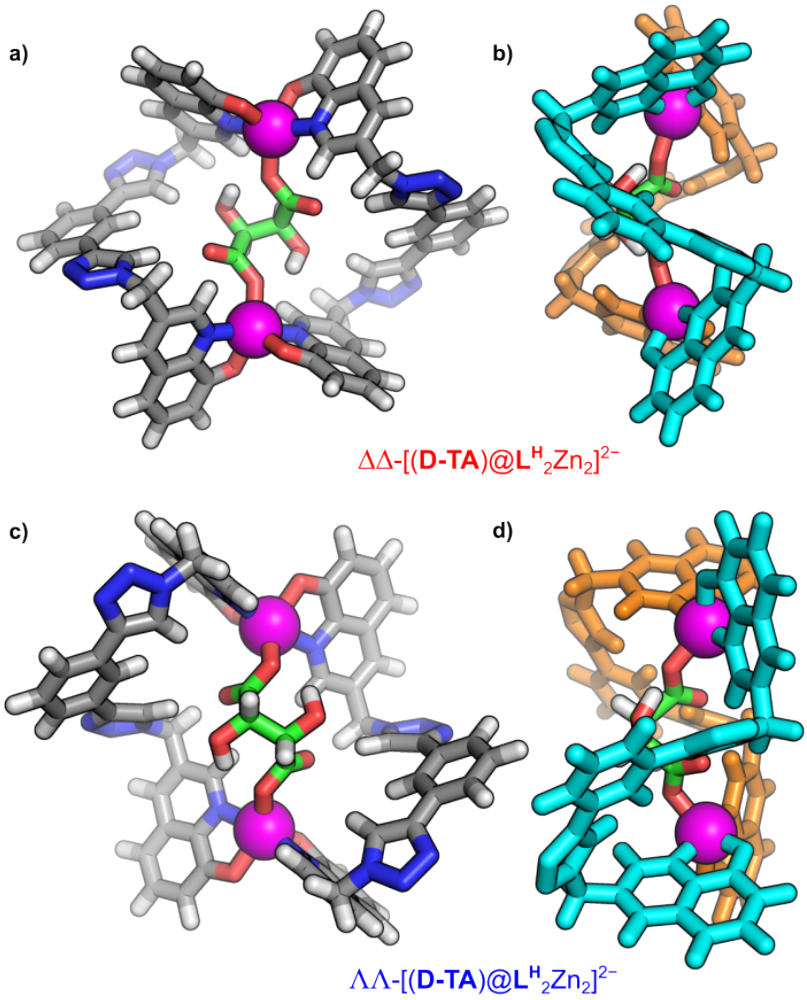

Figure 3.7 (a) Calculated model for ΔΔ-[(**D-TA**)@$\mathbf{L^{H}}_2Zn_2]^{2-}$ (b) Side view of the calculated model for ΔΔ-[(**D-TA**)@$\mathbf{L^{H}}_2Zn_2]^{2-}$ (c) Calculated model for ΛΛ-[(**D-TA**)@$\mathbf{L^{H}}_2Zn_2]^{2-}$ (d) Side view of the calculated model for ΛΛ-[(**D-TA**)@$\mathbf{L^{H}}_2Zn_2]^{2-}$. Geometry optimizations done by using r^{2}SCAN-3c (ORCA 5.0.2)

The optimized ΛΛ-left-handed structure appears to contain more strain than its ΔΔ-right-handed counterpart (Figure 3.7,c,d). It was also ruled out solely based on the differing computed CD spectrum compared to the experimental one.

To probe this dynamic effect, we carried out relaxed potential-energy surface scans for the rotation of each triazole ring in implicit solvent (DMSO)[34] at the ωB97X-D3[35]/def2-SVP[32,33] level using ORCA 5.0.2 software, with the optimized ΔΔ-[(**D-TA**)@$\mathbf{L^{H}}_2Zn_2]^{2-}$as the starting point (Figure 3.8). Harmonic frequencies were computed to verify that the stationary points are minima. The C_2 axis of symmetry of the complex gives two pairs of symmetry-equivalent ring moieties as triazoles 1 & 3 and triazoles 2 & 4, with each of the triazole moieties individually rotated around the phenyl-triazole dihedral angle with a 10 °step size. The red shading around each minimum marks the range of dihedral-angle

excursions that are thermally accessible at 300 K within roughly one RT of energy. The two lowest-energy *anti–syn* conformers (-131 °and -164 °) were generated by rotating, in turn, each of the two symmetry-inequivalent triazole units into the *anti–syn* arrangement and then optimizing the structures without any constraints. The potential energy surface exhibits a shallow minimum near the *syn-syn* conformation geometry (dihedral angle $\approx \pm$ 25°), whereas the *anti-syn* conformation is disfavored by at least 2.5 kcal $\cdot$ mol^{-1}. Around the *syn-syn* minimum, thermal fluctuations at 300 K permit triazole rotations over a broad range of 45°, accounting for the observed broadening of the triazole signal.

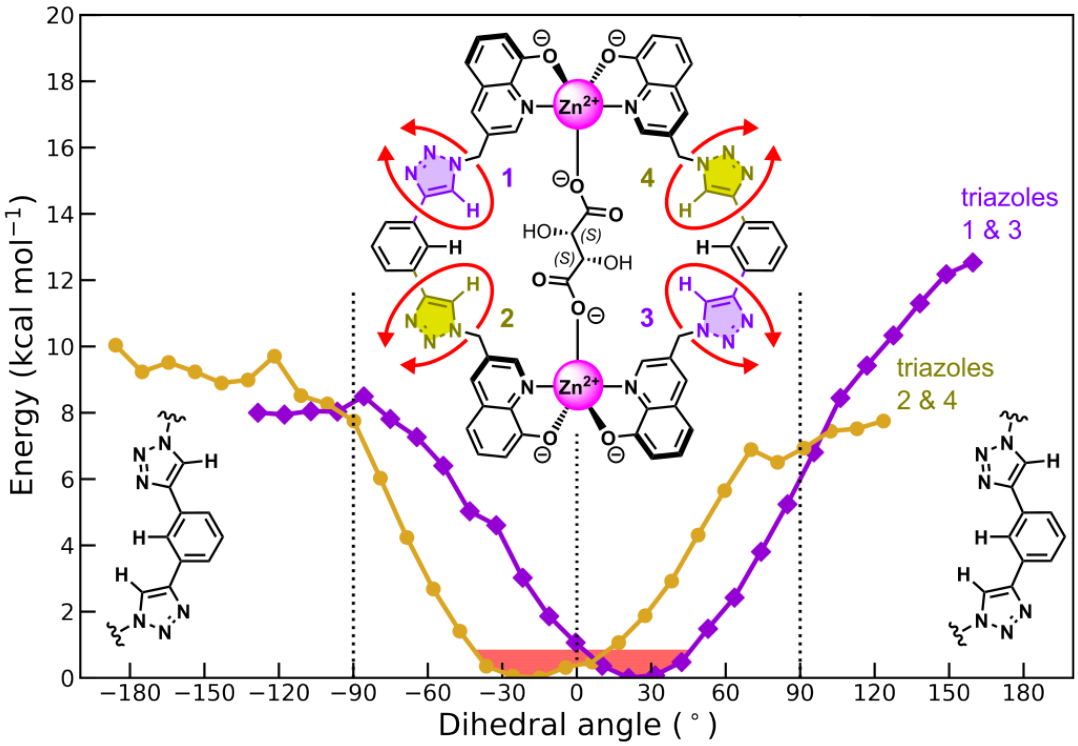

Figure 3.8 Potential energy surface scans (PES) for the rotation of symmetry-independent triazole moieties in ΔΔ-[(**D-TA**)@**L**$^{\mathbf{H}}{}_2$Zn$_2$]$^{2-}$.

3.2.3 Binding studies for other chiral carboxylates

D-(−)- and L-(+)-Tartrate serve as excellent model guests, providing promising results that highlight the potential of our [**L**$^{\mathbf{R}}{}_2$Zn$_2$] host as a chiral probe. To further expand its scope, we examined various other carboxylate guests bearing chiral units (Figure 3.9). Their binding behaviors were analyzed by ^{1}H NMR titrations, and the association constants were calculated either by ^{1}H NMR in the applicable cases or by ITC titrations (Table 4.1). Hypothetically, monocarboxylates (**C**$^-$) are expected to bind in a 1:2 fashion to result in a [**C**$_\mathbf{2}$@**L**$^{\mathbf{R}}{}_2$Zn$_2$]$^{2-}$ host-guest complex, whereas dicarboxylates (**DC**$^{\mathbf{2-}}$) should bind in a 1:1 fashion and generate a [(**DC**)@**L**$^{\mathbf{R}}{}_2$Zn$_2$]$^{2-}$ host-guest complex.

Indeed, monocarboxylates such as (*S*)-(+)-hydratropate (***S*-HT**$^-$), (*S*)-(+)-2-(6-methoxy-

2-naphthyl)propionate (deprotonated naproxen, ***S*-NP**$^-$), *N*-Boc-L-prolinate (**L-BPro**$^-$), and *N*-Boc-L-pipecolinate (**L-BPip**$^-$) display inflection points characteristic of 1:2 binding for at least one proton of the phenyl unit from the ligand backbone. The 1:1 binding constants are notably high for ***S*-HT**$^-$ and ***S*-NP**$^-$ with $\log K_{1:1} = 4.45$ and 4.51, respectively. Corresponding 1:2 constants are over an order of magnitude smaller, attributing to the inability of the cavity to resolve the steric crowding when two bulky guests occupy the cavity simultaneously. **L-BPro**$^-$ and **L-BPip**$^-$ follow the same trend, although with overall lower values. In contrast, (*S*)-(+)-mandelate (***S*-MD**$^-$) shows no 1:2 inflection point and binds much more weakly ($\log K_{1:1} = 2.38$) than its methyl analog ***S*-HT**$^-$ ($\log K_{1:1} = 4.45$), which is consistent with the electron-withdrawing hydroxyl group in (*S*)-(+)-mandelate compared to the electron-donating methyl group in (*S*)-(+)-hydratropate. The same observation was true for (*R*)-3,3,3-trifluoro-2-methoxy-2-phenylpropanoate (***R*-PProp**$^-$), likely due to the CF_3 electron withdrawing group. (*S*)-2-(4-isobutylphenyl)propanoate (deprotonated ibuprofen, ***S*-Ibu**$^-$) showed a fast exchange regime and a $\log K_{1:1} = 4.18$. Other monocarboxylates investigated are (1*R*,4a*R*,4b*R*,10a*R*)-7-isopropyl-1,4a-dimethyl-1,2,3,4,4a,4b,5,6,10,10a-decahydrophenanthrene-1-carboxylate (deprotonated abietic acid, ***R*-Abe**$^-$) and (*S*)-indoline-2-carboxylate (***S*-Ind**$^-$). Both guests initially exhibited a fast exchange. However, at elevated concentrations, the NMR spectra became complex and increasingly challenging to interpret; hence, the binding constant was not determined.

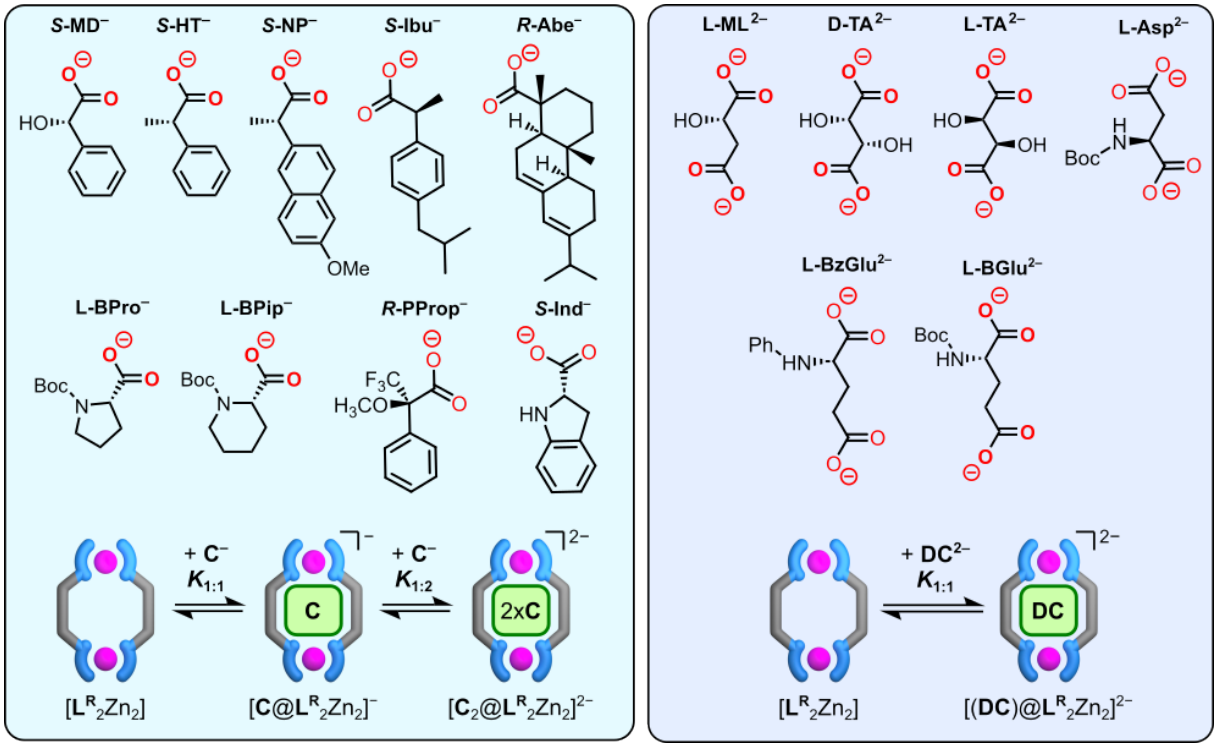

Figure 3.9 Monocarboxylates and dicarboxylates investigated in this study. Monocarboxylates bind in a 1:2 fashion while dicarboxylates bind in a 1:1 fashion.

Table 3.1 Association constants calculated for the examined carboxylate guests as TBA salts in DMSO-d_6

Monocarboxylate (**C⁻**)	$K_{1:1}$ (M^{-1})[a]	$K_{1:2}$ (M^{-1})[a]
(S)-(+)-mandelate (**S-MD⁻**)	240 ± 20	-
(S)-(+)-hydratropate (**S-HT⁻**)	28 000 ± 2 000	1 700 ± 100
Deprotonated naproxen (**S-NP⁻**)	32 000 ± 6 000	1 800 ± 100
Deprotonated ibuprofen (**S-Ibu⁻**)	15 000 ± 6 000	1430 ± 100
Deprotonated abietic acid (**Abe⁻**)	n.d	-
N-Boc-L-prolinate (**L-BPro⁻**)	4 700 ± 800	680 ± 40
N-Boc-L-pipecolinate (**L-BPip⁻**)	1 900 ± 400	700 ± 120
(R)-3,3,3-trifluoro-2-methoxy-2-phenylpropanoate (**R-PProp⁻**)	100 ± 5	-
(S)-indoline-2-carboxylate (**S-Ind⁻**)	n.d	-

Dicarboxylate (**DC²⁻**)	$K_{1:1}$ (M^{-1})
L-(−)-malate (**L-ML²⁻**)	n.d.
D-(−)-tartrate (**D-TA²⁻**)	174 000[b] ± 32 000
L-(+)-tartrate (**L-TA²⁻**)	202 000[c] ± 18 000
N-Boc-L-aspartate (**L-Asp²⁻**)	12 000[a] ± 100
N-Benzyl-L-glutamate (**L-BzGlu²⁻**)	5 600 [d] ± 1 900
N-Boc-L-glutamate (**L-BGlu²⁻**)	193 000[d] ± 101 000

*[a] Binding constant was determined by fitting ^{1}H NMR shifts with BindFit. [b] Average value determined by three ITC titrations. [c] The binding constant obtained from a single ITC titration, with the reported error representing the goodness of the fit. [d] The average value was determined by integration of slow exchange ^{1}H NMR signals.

Dicarboxylates ($\mathbf{DC^{2-}}$) mostly exhibit intermediate to slow exchange on the NMR timescale within the [$\mathbf{L^R}_2Zn_2$] host. No quantitative analysis was done for L-(−)-malate ($\mathbf{L\text{-}ML^{2-}}$), as multiple undefined minor species appear at sub-stoichiometric ratios, and the equilibria could not be defined. Although [($\mathbf{L\text{-}ML}$)@$\mathbf{L^R}_2Zn_2$]$^{2-}$ is the major species between 1.5 and 2.0 equivalents of guest, it becomes unstable at higher amounts. As tartrate enantiomers bind in intermediate exchange, straightforward NMR integration or bindFit calculation is not possible. Thus, an average association constant for D-(−)-tartrate ($\mathbf{D\text{-}TA^{2-}}$) was determined by Isothermal Titration Calorimetry (ITC) as $\log K_{1:1} = 5.24$ from three measurements. This value is in accordance with expectations, considering the short length of the dicarboxylate. L-(+)-tartrate ($\mathbf{L\text{-}TA^{2-}}$) affords a similar value of $\log K_{1:1} = 5.31$ from a single ITC experiment. The similarity in the association constants represents the identical affinities of these enantiomeric guests toward the host. The slow exchange conditions exhibited by *N*-Boc-L-glutamate ($\mathbf{L\text{-}BGlu^{2-}}$) and *N*-Benzyl-glutamate ($\mathbf{L\text{-}BzGlu^{2-}}$) allowed NMR integration to yield binding constants $\log K_{1:1} = 5.29$ and 3.75, respectively. Smaller *N*-Boc-L-aspartate, however, exhibits a fast exchange and an association constant calculated from NMR as $\log K_{1:1} = 4.08$.

3.2.4 Chiroptical recognition

Building on the enantiomeric enrichment of the helicate by tartrate, we evaluated additional chiral guests to probe whether they also demonstrated a similar effect (Figure 3.10). *N*-Boc-L-prolinate (**L-BPro**$^-$), *N*-Boc-L-pipecolinate (**L-BPip**$^-$), L-(−)-malate (**L-ML**$^-$), and *N*-Boc-L-glutamate (**L-BGlu**$^{2-}$) in fact enrich one of the two helicate enantiomers, albeit with substantially weaker CD responses than D-(−)-tartrate or L-(+)-tartrate. L-(−)-malate produces the same pattern of Cotton effects as D-(−)-tartrate, which includes two positive bands at 350 nm and 420 nm, and one negative band at 308 nm. Considering the similar structure to D-(−)-tartrate, L-(−)-malate was expected to promote the same preferential formation of the ΔΔ-right-handed helicate, as indicated by the CD Cotton effects and in line with the TD-DFT results for the former. Conversely, L-(+)-tartrate and the amino-acid-derived guests **L-BGlu**$^{2-}$, **L-BPro**$^-$, and **L-BPip**$^-$ display an inverted pattern with two negative and one positive Cotton effect, consistent with the enrichment of the ΛΛ-left-handed helicate enantiomer.

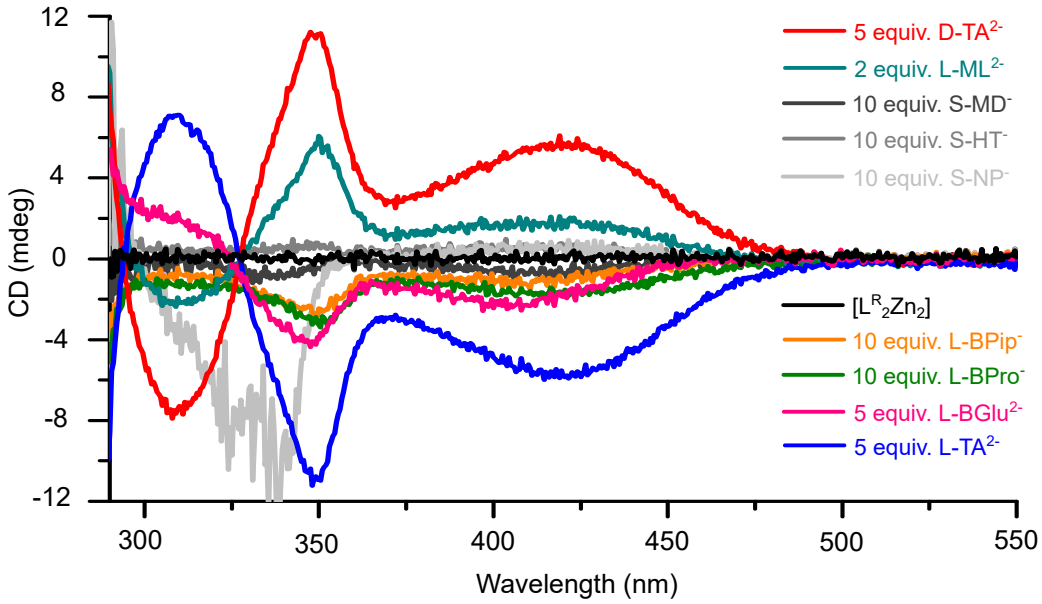

Figure 3.10 CD responses of the host upon the addition of different chiral carboxylate guests (500 µM, l = 2 mm, DMSO-d_6, 298 K).

Guests bearing aromatic residues such as (*S*)-(+)-mandelate (***S*-MD**$^-$), (*S*)-(+)-hydratropate (***S*-HT**$^-$), and (*S*)-(+)-2-(6-methoxy-2-naphthyl)propionate (***S*-NP**$^-$) do not generate appreciable induced CD signals attributable to the host-guest complexes. For ***S*-NP**$^-$, the guest's intrinsic CD band is observed because its absorption lies within the measurement window. Notably, the presence or absence of an induced CD signal does not relate to the binding affinity, as ***S*-HT**$^-$ and ***S*-NP**$^-$ bind more strongly than **L-BPro**$^-$, while **L-BPro**$^-$ and **L-BPip**$^-$ yield a comparitively lower intensity chiroptical response than anticipated which can be attributed to their increased steric demand as saturated

cyclic compounds possessing Boc-protected groups, which can enhance asymmetry transfer to the receptor.The stronger CD effects observed for dicarboxylates are plausibly linked to their bridging topology, which reduces the conformational degree of freedom across the host-guest assembly and amplifies chiral bias. To validate the lack of correlation between binding affinity and CD intensity, competition CD experiments were conducted by adding a 1:5 ratio of **D-TA**$^{2-}$ and monocarboxylates, respectively (Figure 3.11). ***S*-HT**$^{-}$ actively competes with **D-TA**$^{2-}$ and reduces the amount of CD active $[(\mathbf{D\text{-}TA})@\mathbf{L^R}_2Zn_2]^{2-}$, which, in turn, decreases the intensity of the resulting CD signal. Although **L-BPro**$^{-}$ is expected to compete less compared to **S-HT**$^{-}$, the CD signal of the solution containing both **D-TA**$^{2-}$ and excess **L-BPro**$^{-}$ shows lower intensity. This is due to a lower amount of $[(\mathbf{D\text{-}TA})@\mathbf{L^R}_2Zn_2]^{2-}$ resulting from competition and the compensation of the inverse CD signal of $[(\mathbf{L\text{-}BPro})@\mathbf{L^R}_2Zn_2]^{2-}$.

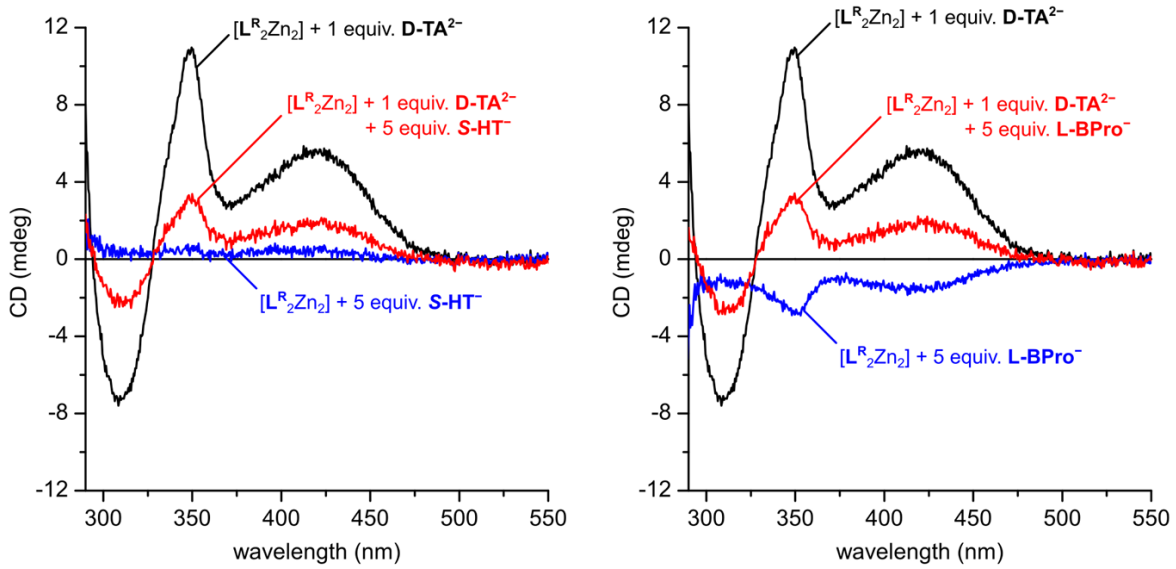

Figure 3.11 Competition CD experiments (500 µM, $l = 2$ mm, DMSO-d_6, 298 K) with **D-TA**$^{2-}$ and monocarboxylates. 1:5 ratio of **D-TA**$^{2-}$/ ***S*-HT**$^{-}$ (left) and **L-BPro**$^{-}$ (right) is added to observe a decrease in CD signal intensity in both cases.

3.2.5 Chirality analysis

As a final step, we tried to implement the bias toward helicate enantiomers by chiral guests and the induced circular dichroism (CD) produced by the host-guest complex into the analytical determination of the enantiomeric composition of those chiral guests (Figure 3.12). Solutions were prepared by mixing enantiopure D-(−) and L-(+)-tartrate to generate five reference points at ±100 % ee, ±50 % ee, and 0 % *ee*, with a total of five equivalents of guest. Linear regression of the CD band intensity at the selected Cotton effect versus *ee* afforded excellent linearity with $R^2 \approx 0.99$.

Measurements for samples at low *ee* as 25 % *ee* were carried out under varied conditions,

such as concentrations and cuvette path length, with a single case for 10 % *ee* to verify the accuracy of the receptor at lower values. Only the Cotton effects at 350 and 420 nm were considered for fitting since significant deviations were observed for the Cotton effect at 308 nm (Figure 3.13). This is assumed to be a result of the increasing solvent (DMSO-d_6) absorption in the area. That way, we could demonstrate that the host can also detect and quantify low *ee* values. Nevertheless, when using a cuvette with a 1 cm path length, the host concentration should not be lower than 50 μM. With an analyte concentration of 250 μM containing five equivalents of the guest, it can be considered the practical limit of quantification (LOQ) for samples with 25 % *ee* (Table 3.2). Samples with lower *ee* should be measured at proportionally higher concentrations to maintain an adequate signal-to-noise ratio. Collectively, these results establish that the receptor enables CD-based chirality analysis of chiral carboxylates.

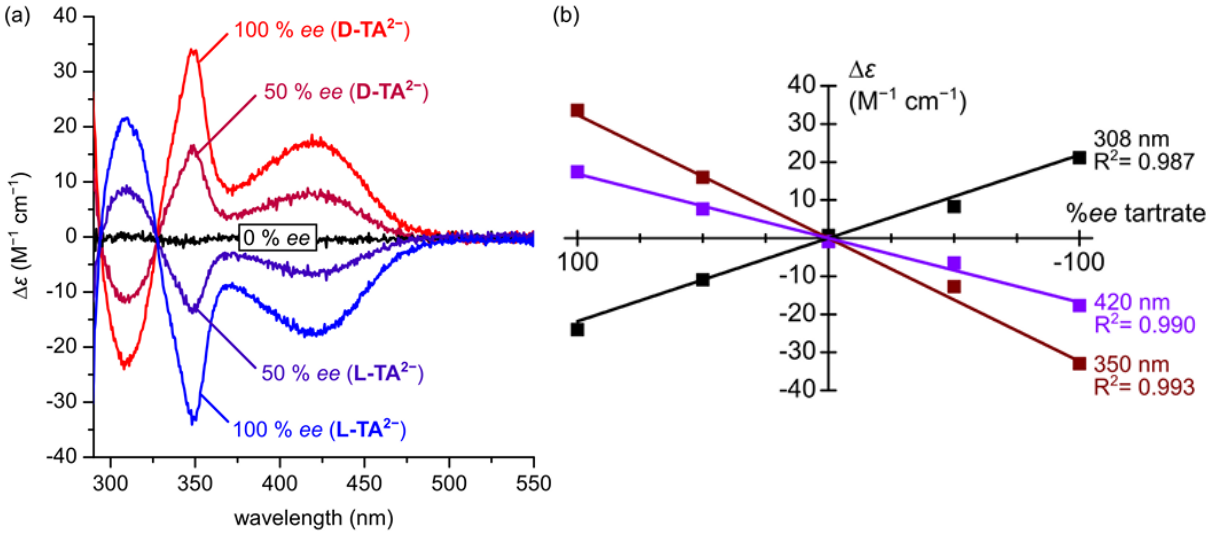

Figure 3.12 Chirality analysis of tartrate with CD spectroscopy (500 µM, l = 2 mm, DMSO-d_6, 298 K). (a) CD spectra correspond to solutions with different ratio of **D-** and **L-TA**$^{2-}$ (5 equiv). (b) In the linear regression of the three main Cotton effects, a positive enantiomeric excess (*ee*) value indicates an excess of D-(−)-tartrate, while a negative value signifies an excess of L-(+)-tartrate.

Table 3.2 Chirality determination of tartrate samples with low *ee* (DMSO-d_6). Limit of quantification (LOQ) for ≥25% *ee* is ∼250 μM guest at 50 μM host in a 1 cm cell.

Prepared *ee* (%)	25	25	25	25	25	10
c_{host} (μM)	500	500	440	100	50	440
c_{guest} (μM)	2500	2500	2500	500	250	2500
Pathlength (cm)	0.2	0.2	0.2	1.0	1.0	0.2
Measured *ee* at 350 nm (%)	19.0	24.9	22.4	21.3	27.5	8.1
Measured *ee* at 420 nm (%)	24.1	27.1	19.7	18.5	36.6	13.6
Average ± standard dev. : 350 nm = 23.0 ± 3.3, 420 nm = 25.2 ± 7.2						

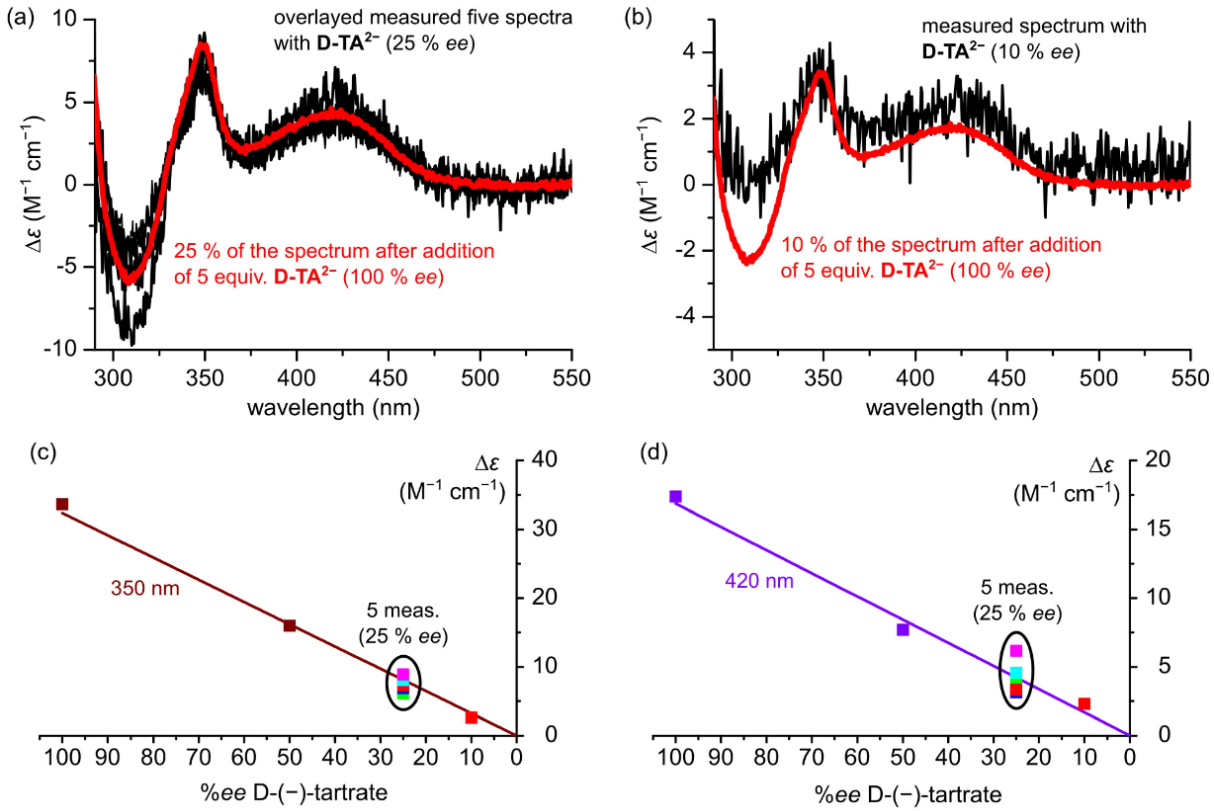

Figure 3.13 (a,b) CD spectra of tartrate samples with 25 % *ee* and 10 % *ee* respectively. The expected spectrum (red) deviates significantly from the observed Cotton effect at 308 nm (c,d). Scattering of the data points in respect to the obtained linear regressions (Figure 3.12) for 350 nm and 420 nm.

3.2.6 Limitations

Carboxylates, particularly in biological systems, exist as sodium salts rather than TBA salts. We wanted to test the feasibility of our system as a chiral probe when it comes to real-life analytes. However, the sodium salts tend to be poorly soluble in DMSO. As a solution, the sodium salts of the guests were dissolved in water and added as aliquots to the receptor solution in DMSO-d_6. Consequently, comparable CD Cotton effects were observed, though with lower intensities compared to those of TBA salts. Water, being highly competitive with the guest, can be the culprit behind the diminishing of the CD signal. To test this hypothesis, pure water was added sequentially to the analyte solution, and the CD signals were observed to disappear with each aliquot of water added, up to 15 % with respect to DMSO-d_6 (Figure 3.14). Notably, NMR spectra of the host-guest solution containing five equivalents of sodium salts of tartrate indicate complete host-guest complex formation (Figure 3.16). This observation suggests that competitive solvation by water might weaken the host-guest interactions, likely through the disruption of intermolecular hydrogen bonds within the tartrate. Therefore, sodium salts were dissolved in a 50:50 DMSO-d_6 / D_2O to create highly concentrated guest solutions to limit the net amount of water introduced with each addition (Figure 3.15). The results, however,

positively indicate that even within the competitive solvent environment, [$\mathbf{L^R}_2Zn_2$] can be used to quantitatively probe the chirality of biological samples, such as sodium salt analytes.

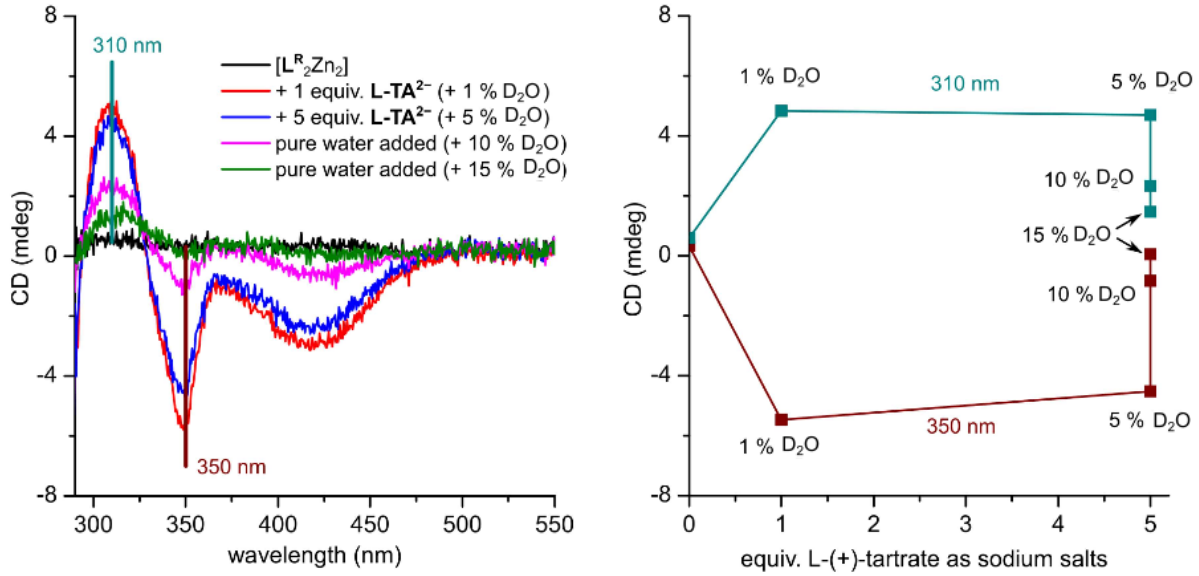

Figure 3.14 CD experiment to quantify the influence of water (500 µM, l = 2 mm, DMSO-d_6, 298 K). Aliquots of water were added to the analyte mixture containing [$\mathbf{L^R}_2Zn_2$] with L-(+)-tartrate as sodium salt. Guest added as D_2O solution. Percentage of D_2O is shown with respect to the DMSO-d_6 in the cuvette.

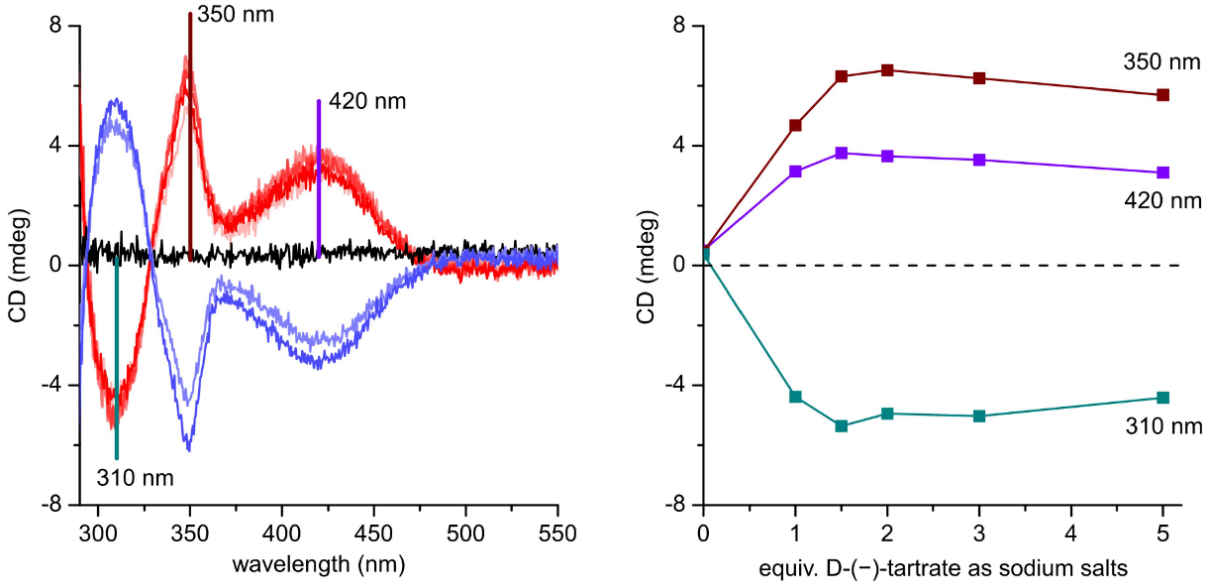

Figure 3.15 CD titration of [$\mathbf{L^R}_2Zn_2$] with D-(−)- and L-(+)-tartrate as sodium salts, added as a 50:50 DMSO-d_6/D_2O mixture (500 µM, l = 2 mm, DMSO-d_6, 298 K). **D-TA**$^{2-}$ added in 1, 1.5, 2, 3, and 5 equivalent steps while **L-TA**$^{2-}$ is added as 1 and 2 equivalent steps.

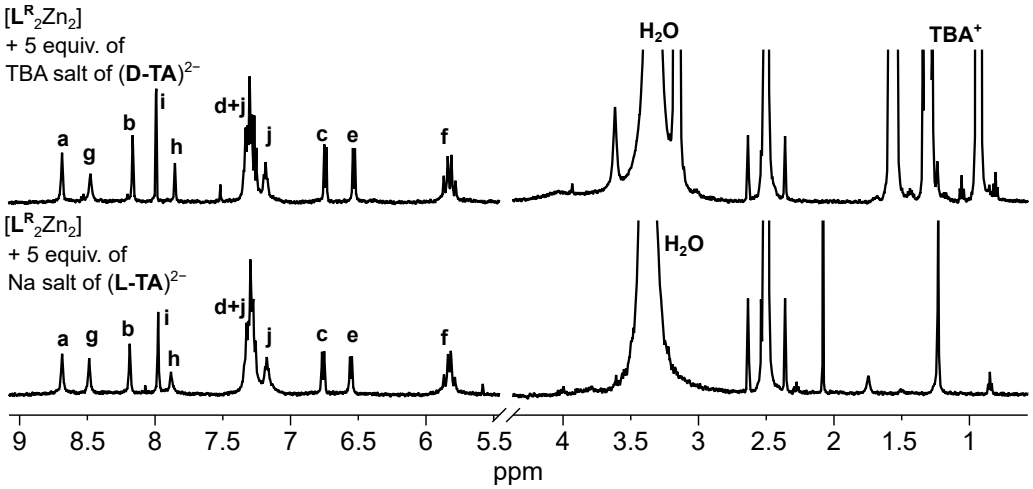

Figure 3.16 (top) ^{1}H NMR of $[\mathbf{L^R}_2Zn_2]$ with five equivalents of TBA salts of D-(−)-tartrate forming $[(\mathbf{D\text{-}TA})@\mathbf{L^R}_2Zn_2]^{2-}$ to compare with (bottom) $[\mathbf{L^R}_2Zn_2]$ with five equivalents of sodium salts of L-(+)-tartrate forming $[(\mathbf{L\text{-}TA})@\mathbf{L^R}_2Zn_2]^{2-}$.

3.3 Conclusion

This chapter establishes a charge-neutral, double-stranded Zn(II) helicate $[\mathbf{L^R}_2Zn_2]$ as a practical tool for the chiroptical recognition of carboxylates. Dicarboxylates bind in a 1:1 stoichiometry with association constants ranging up to $10^{\,5}\,M^{-1}$ in DMSO, while monocarboxylate guests bind in a 1:2 fashion. The binding event of chiral guests enriches one of the enantiomers of the receptor, as analyzed by tracking their Cotton effects using CD spectroscopy. NOESY experiments, TD-DFT computations, and relaxed potential energy surface scans provide a deeper understanding of the underlying processes. In this context, we demonstrated that the *syn-syn* arrangement of the triazole units plays a critical role in forming a helicate-type host-guest complex, which is vital for chiroptical recognition.

The receptor's high affinity guarantees an almost complete uptake of the guest species, making the system suitable for probing chirality analysis for *ee* determinations at concentrations as low as 250 µM for compounds with enantioselectivity greater than 25% *ee*. This was demonstrated with tartrate, where the intensity of the Cotton effect showed a linear correlation with changes in enantiomeric excess.

3.4 Experimental section

3.4.1 General methods

3.4.1.1 Materials

Unless otherwise stated, reagents were purchased from Sigma-Aldrich, chemPUR, TCI, BLDpharm, Alfa Aesar, and VWR and were used as received. Tetrabutylammonium hydroxide (1.0 M in MeOH) was procured from Sigma-Aldrich. DMSO-d_6 (99.8% D) for binding and spectroscopic studies was sourced from Deutero and Eurisotop. Experiments were performed under an inert argon atmosphere using standard Schlenk techniques where required. Reactions were monitored using thin-layer chromatography (TLC) with pre-coated silica plates (Merck, silica 60, F254). For column chromatography, silica (Merck, silica 60, 0.02–0.063 mesh) was used as the stationary phase. Lyophilization was performed on a CHRIST Alpha 2-4 LSC basic freeze dryer (coil -80 °C, $\sim 1 \times 10^{-3}$ mbar). NMR spectra were recorded on Bruker AVANCE III NEO 500 and 600 instruments. Chemical shifts are reported in δ (ppm) and multiplicities as s (singlet), d (doublet), t (triplet), and m (multiplet). Isothermal titration calorimetry (ITC) was carried out on a Malvern Microcal PEAQ-ITC (Hastelloy cell) device. UV-Vis spectra were recorded on an Agilent DAD HP-8453 UV-Vis spectrometer, and circular dichroism (CD) measurements were performed at a Photophysics Chirascan qCD Spectrometer using Hellma QS cuvettes (l = 2 mm) at room temperature. The CD spectra were accumulated twice, with a step size of 0.5 nm and a bandwidth of 1 nm, and then averaged to reduce the amount of noise, so that smoothing of the data was not necessary. ESI-MS spectra were measured using a Bruker timsTOF spectrometer.

3.4.1.2 Procedures for binding studies

Preparation of TBA salts of the guests

Purchased chiral carboxylic acids were converted to their respective tetrabutylammonium (TBA) salts by deprotonation prior to use. Carboxylic acids were dissolved in 5 mL of MeOH, and one and two equivalents of tetrabutylammonium hydroxide (1 M solution in MeOH) were added for mono- and dicarboxylic acids, respectively. The mixture was vortexed for 30 min, and the solvents were removed under reduced pressure. A small amount of water was added to aid subsequent freeze-drying, as pure MeOH freezes poorly, and it was lyophilized for up to three days. The resulting TBA carboxylates were used without further purification.

Analysis of titration data

Binding constants corresponding to fast exchange processes were obtained by fitting with BindFit.[36–38] The titrations were performed at the most sensitive concentration regime ($10 \geq c(host)_0/K_d \geq 0.1$) to ensure accurate and reliable values.[39,40] **D-TA^{2-}** and **L-TA^{2-}** were bound in intermediate exchange with respect to the NMR time scale; thus, determining the binding constants from NMR was not possible and were therefore calculated from ITC measurements.

Isothermal Titration Calorimetry (ITC)

ITC measurements were performed on a Malvern MicroCal PEAQ-ITC (Hastelloy cell) and analyzed using the MicroCal PEAQ-ITC Analysis Software. A typical run used a total of 25 injections (1 × 0.4 µL followed by 24 × 1.5 µL) at 25.0 °C, with a reference power of 10.0 µcal/s, high feedback, and a stir rate of 750 rpm. The initial delay was 60 s; subsequent injections were spaced by 180 s, with an injection duration of 3.0 s.

3.4.2 Synthesis of ligands

3.4.2.1 Synthesis of 8-methoxy-3-methylquinoline (3)

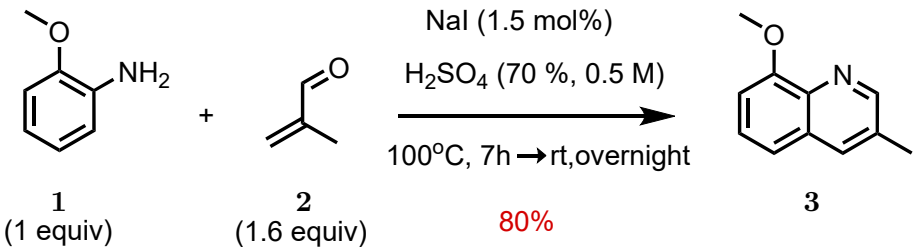

Ortho-anisidine **(1)**, (3.95 mL, 35.0 mmol, 1.0 equiv.) and sodium iodide (78.7 mg, 525 µmol, 15 mol%) were added to a 50 mL round-bottom flask equipped with a magnetic stir bar. The solids were dissolved in sulfuric acid (70% wt, 17.5 mL, 0.5 M), and the resulting mixture was heated to 100 °C. Methacrolein **(2)** (4.73 mL, 56.0 mmol, 1.6 equiv.) was added dropwise over 4 h using a syringe pump while stirring at 100 °C. After the complete addition, the reaction mixture was stirred at 100 °C for an additional 3 h, then allowed to cool to room temperature and stirred overnight. The mixture was carefully neutralized with saturated solution of sodium bicarbonate, and the resulting mixture was extracted with dichloromethane (2 × 100 mL). The combined organic layers were dried over anhydrous magnesium sulfate, filtered, and concentrated under reduced pressure. The crude product was purified by column chromatography (silica, pentane/ethyl acetate 1:2) to obtain 8-methoxy-3-methylquinoline **(3)** as a brown solid (4.8 g, 27.7 mmol, 79%).

*8-Methoxy-3-methylquinoline **(3)** was synthesized as described in the literature.[41,42]

^{1}H NMR (500 MHz, $CDCl_3$, 298 K): δ = 8.79 (d, J = 2.3 Hz, 1H), 7.93–7.89 (m, 1H), 7.44 (t, J = 8.0 Hz, 1H), 7.32 (dd, J = 8.2, 1.1 Hz, 1H), 7.00 (dd, J = 7.7, 1.2 Hz, 1H), 4.09 (s, 3H), 2.52 (s, 3H) ppm.

3.4.2.2 Synthesis of 3-methylquinolin-8-ol (4)

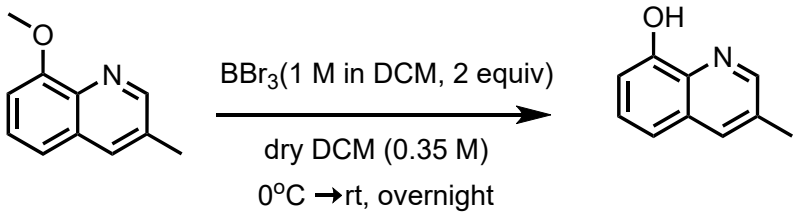

3 90% **4**

A solution of 8-Methoxy-3-methylquinoline **(3)**, (2.17 g, 12.50 mmol, 1.0 equiv.) in dry dichloromethane (35.7 mL, 0.35 M) was made in a two-necked round bottom flask under argon atmosphere and it was cooled to 0 °C in an ice bath. Boron tribromide (1 M in dichloromethane, 25 mL, 25.0 mmol, 2.0 equiv) was added dropwise over 30 minutes to the cooled solution using the syringe pump. The reaction was allowed to warm to room temperature and stirred overnight. The reaction was quenched with water and carefully neutralized with saturated aqueous sodium bicarbonate. The mixture was then extracted three times with ethyl acetate, and the combined organic layers were dried over anhydrous magnesium sulfate, filtered, and concentrated under reduced pressure to afford 3-methylquinolin-8-ol **(4)** (1.81 g, 11.37 mmol, 91%) as a red solid. The crude product was used in the next step without any further purification.

^{1}H NMR (600 MHz, $CDCl_3$, 298 K): δ = 8.63 (s, 1H), 7.95 – 7.89 (m, 1H), 7.42 (t, 1H), 7.26 (dd, J= 8.2, 1.2 Hz, 1H), 7.11 (dd, J= 7.6, 1.2 Hz, 1H), 2.53 (s, 3H)

3.4.2.3 Synthesis of *tert*-butyl (3-methylquinolin-8-yl) carbonate (5)

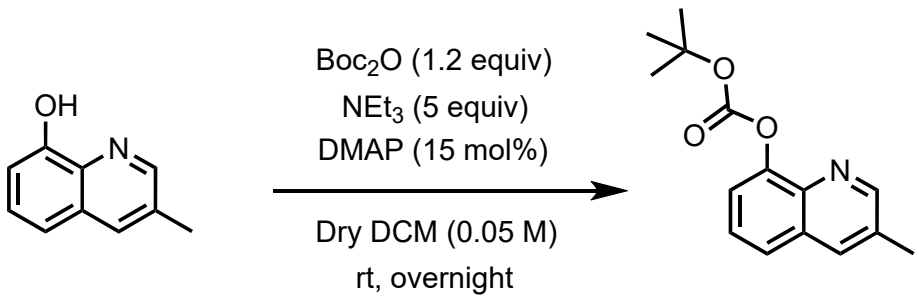

4 71% **5**

*3-methylquinolin-8-ol **(4)** was synthesized as described in the literature[42]
*(3-methylquinolin-8-yl) carbonate **(5)** was synthesized as described in the literature[42]

The crude 3-methylquinolin-8-ol **(4)** was dissolved in dry dichloromethane (150 mL) in a Schlenk tube under an argon atmosphere. *N*,*N*-Dimethyl-4-aminopyridine (DMAP, 198 mg, 1.62 mmol, 14 mol%) was added, followed by a solution of Boc-anhydride (Boc_2O, 2.83 g, 12.97 mmol, 1.14 equiv) in dry dichloromethane (50 mL), and triethylamine (7.53 mL, 54.02 mmol, 4.8 equiv.). The reaction mixture was stirred at room temperature overnight. After completion, the mixture was washed with brine, and the organic layer was dried over anhydrous magnesium sulfate, filtered, and concentrated under reduced pressure. The crude product was purified by column chromatography (silica gel, pentane/ethyl acetate 6:1) to afford *tert*-butyl (3-methylquinolin-8-yl) carbonate **(5)** as a yellowish oil, which crystallized upon storage in a refrigerator as a colorless solid (2.1 g, 8.10 mmol, 71%).

^{1}H NMR (500 MHz, $CDCl_3$, 298 K): δ =8.78 (d, J= 2.1 Hz, 1H), 7.93 – 7.90 (m, 1H), 7.62 (dd, J= 7.9, 1.7 Hz, 1H), 7.48 (t, J= 7.7 Hz, 1H), 7.44 (dd, J= 7.5, 1.6 Hz, 1H), 2.51 (s, 3H), 1.60 (s, 9H) ppm.

3.4.2.4 Synthesis of 3-(bromomethyl)quinolin-8-yl *tert*-butyl carbonate (6)

Literature conditions:

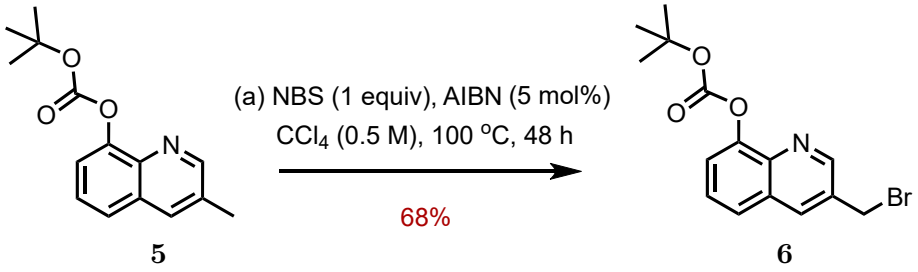

5 **6**

Modified conditions (this work):

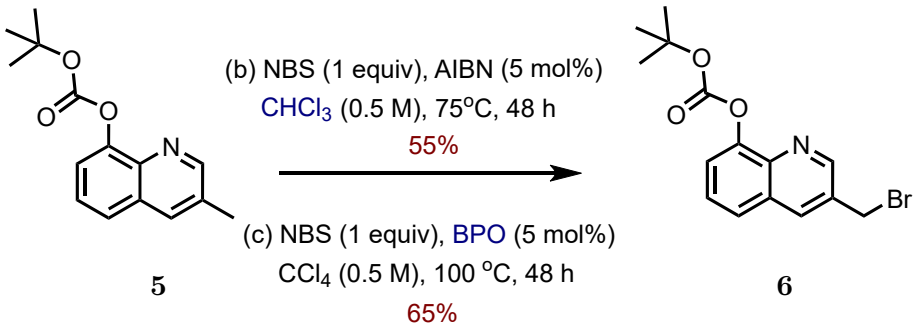

5 **6**

Entry (a) (literature conditions) : *Tert*-butyl (3-methylquinolin-8-yl) carbonate **(5)**, (500 mg, 1.93 mmol, 1 equiv.), *N*-bromosuccinimide (343.2 mg, 1.93 mmol, 1 equiv.), and AIBN (15.83 mg, 0.096 mmol, 0.05 equiv.) were added to a Schlenk tube under an argon atmosphere and dissolved in carbon tetrachloride (40 mL, 0.05 M). The reaction mixture was refluxed for two days. The suspension was filtered while still being hot, and the filtrate was concentrated under reduced pressure. The residue was purified by column

chromatography (silica, pentane/ethyl acetate 6:1) to obtain 3-(bromomethyl)quinolin-8-yl *tert*-butyl carbonate **(6)** (445.0 mg, 1.32 mmol, 68%)

modified conditions:

Entry (b) : The reaction was performed as in general procedure (a) except that chloroform was used in place of carbon tetrachloride (0.5 M), and refluxed at 75 °C for 48 h. Work-up and purification were identical, giving **(6)** in 55 % yield.

Entry (c) : The reaction was performed as in general procedure (a) except that benzoyl peroxide (5 mol %) was used as the radical initiator instead of AIBN. CCl_4 was used as solvent and the mixture was refluxed at 100 °C for 48 h. Work-up and purification were identical, giving **(6)** in 65 % yield.

^{1}H NMR (500 MHz, $CDCl_3$, 298 K): δ = 8.95 (d, J = 2.2 Hz, 1H), 8.16 (d, J = 2.2 Hz, 1H), 7.70 (dd, J = 7.2, 2.3 Hz, 1H), 7.56 – 7.53 (m, 2H), 4.65 (s, 2H), 1.61 (s, 9H) ppm.

3.4.2.5 Synthesis of 3-(azidomethyl)quinolin-8-yl *tert*-butyl carbonate (7)

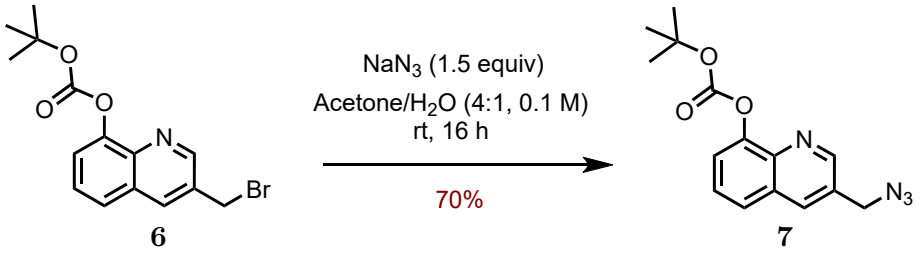

A round-bottom flask was equipped with 3-(bromomethyl)quinolin-8-yl *tert*-butyl carbonate **(6)** (500 mg, 1.48 mmol, 1.0 equiv.) and a 4 : 1 mixture of acetone / water (15 mL, 0.10 M). Sodium azide (144 mg, 2.22 mmol, 1.5 equiv.) was added and the resulting solution was stirred at room temperature overnight. The reaction mixture was diluted with dichloromethane and washed with brine, dried over anhydrous magnesium sulfate, filtered, and concentrated. Purification by flash chromatography on silica gel (pentane / ethyl acetate 3 : 1) afforded 3-(azidomethyl)quinolin-8-yl *tert*-butyl carbonate **(7)** as a colourless oil, which crystallized to a colorless solid upon refrigeration (312 mg, 1.04 mmol, 70%).

^{1}H NMR (500 MHz, $CDCl_3$, 298 K): δ = 8.87 (d, J = 2.2 Hz, 1H), 8.11 (d, J = 2.2 Hz, 1H), 7.72 (dd, J = 7.2, 2.3 Hz, 1H), 7.58 – 7.51 (m, 2H), 4.57 (s, 2H), 1.60 (s, 9H) ppm.

3.4.2.6 Synthesis of 3,5-dibromo-*N*,*N*-diphenylbenzamide (9)

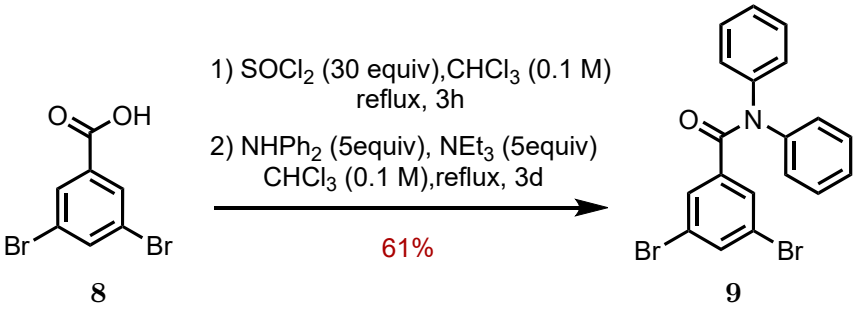

8 **9**

A round-bottom flask was equipped with 3,5-dibromobenzoic acid **(8)** (2 g, 7.15 mmol, 1.0 equiv.) and chloroform (70 mL, 0.10 M), after which thionyl chloride (15.6 mL, 214.35 mmol, 30 equiv.) was added. The suspension was refluxed for 3 hours. Solvents were then removed under reduced pressure to afford the crude acid chloride as a pale-brown residue, which was directly used for the follow-up reaction by dissolving in 25 mL chloroform.

A solution of diphenylamine (6.04 g, 35.70 mmol, 5.0 equiv.) and triethylamine (5.0 mL, 35.7 mmol, 5.0 equiv.) in chloroform (15 mL) was added to the reaction mixture, which was heated to refluxed for 3 days. The mixture was then washed with saturated aqueous $NaHCO_3$, and the organic phase was dried over anhydrous magnesium sulfate, filtered, and concentrated under reduced pressure. Column chromatography on silica gel (pentane/diethyl ether 12 : 1) yielded 3,5-dibromo-*N*,*N*-diphenylbenzamide **(9)** as a colorless solid (1.87 g, 4.34 mmol, 61%).

^{1}H NMR (500 MHz, $CDCl_3$, 298 K): δ = 7.50 (t, J = 1.8 Hz, 1H), 7.42 (d, J = 1.7 Hz, 2H), 7.26 (t, J = 7.6 Hz, 4H), 7.20 – 7.15 (m, 2H), 7.08 (d, J = 7.8 Hz, 4H) ppm.

3.4.2.7 Synthesis of 3,5-diethynyl-*N*,*N*-diphenylbenzamide (10)

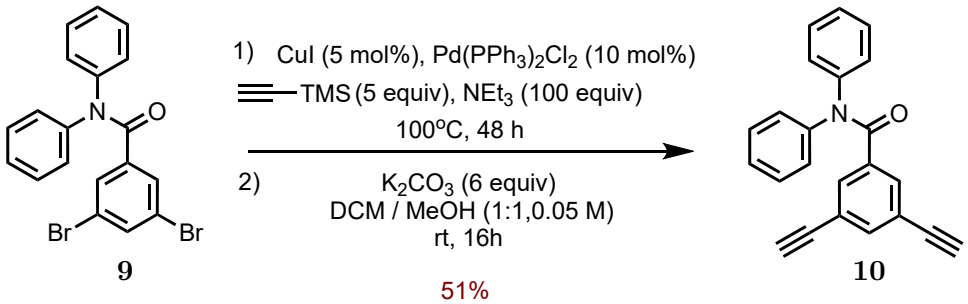

9 **10**

A Schlenk tube was charged with 3,5-dibromo-*N*,*N*-diphenylbenzamide **(9)** (1 g, 2.32 mmol, 1.0 equiv.), $Pd(PPh_3)_2Cl_2$ (162.81 mg, 0.232 mmol, 10 mol%), and triethylamine (32.33 mL, 232 mmol, 100 equiv.), which was then degassed by three freeze–pump–thaw cycles, after which CuI (44.18 mg, 0.232 mmol, 10 mol%) and trimethylsilylacetylene (1.14 mL,

11.6 mmol, 5 equiv.) were added under argon. The sealed tube was heated at 100 °C for 24 h. After cooling to room temperature, the reaction mixture was diluted with dichloromethane and washed with saturated aqueous NH_4Cl. The aqueous layer was extracted with dichloromethane, and the combined organic phases were dried over anhydrous magnesium sulfate, filtered, and concentrated under reduced pressure. Purification by column chromatography on silica gel (pentane/diethyl ether 25 : 1) afforded the TMS-protected diyne (605 mg, 1.30 mmol, 56 %).

The TMS-protected product was then deprotected in a 1 : 1 mixture of dichloromethane and methanol (25 mL, 0.05 M) with K_2CO_3 (1.08 g, 7.79 mmol, 6.0 equiv.) and stirred at room temperature overnight. The mixture was diluted with dichloromethane and washed with water. The combined organic layers were dried over anhydrous magnesium sulfate, filtered, and concentrated under reduced pressure. Filtration through a silica plug (pentane/diethyl ether 5:1) yielded 3,5-diethynyl-*N*,*N*-diphenylbenzamide **(10)** (376 mg, 1.17 mmol, 90 %).

^{1}H NMR (500 MHz, $CDCl_3$, 298 K): δ = 7.51 (d, J = 1.5 Hz, 2H), 7.49 (t, J = 1.5 Hz, 1H), 7.31 (t, J = 7.7 Hz, 4H), 7.24 – 7.19 (m, 2H), 7.15 (d, J = 7.8 Hz, 4H), 3.04 (s, 2H) ppm.

3.4.2.8 Synthesis of 3,3'-((1,3-phenylenebis(1*H*-1,2,3-triazole-4,1-diyl))bis(methylene))bis(quinolin-8-ol) (L^H-H_2)

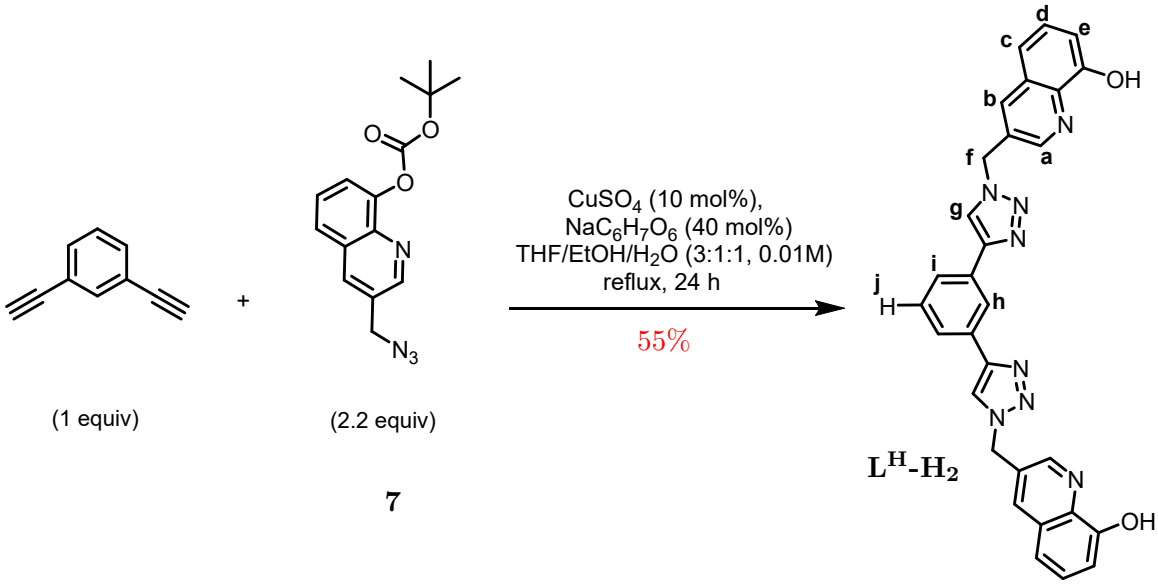

A Schlenk tube was equipped with azide **(7)** (100 mg, 0.333 mmol, 2.2 equiv.) and a 3 : 1 : 1 mixture of THF/EtOH/H_2O (10 mL, 0.015 M). The solution was degassed for 30 min by vigorous argon bubbling. Under argon, $CuSO_4$ (2.42 mg, 0.015 mmol, 10 mol %) and sodium

ascorbate (11.99 mg, 0.060 mmol, 40 mol %), were added successively. TBTA was omitted in contrast to the literature procedure for the ease of purification and was observed not to affect the yield significantly. Commercially available 1,3-diethynylbenzene (0.020 mL, 0.151 mmol, 1.0 equiv.) was then introduced, the tube was sealed, and the mixture was heated at 100 °C for 24 h. After cooling to room temperature, the reaction mixture was diluted with dichloromethane and washed with 0.025 M basic aqueous EDTA. The aqueous layer was extracted with dichloromethane, the combined organic phases were dried over anhydrous magnesium sulfate, filtered, and concentrated under reduced pressure. A separate treatment for Boc-deprotection was not required, as it was already cleaved during the workup. Purification by repeated dispersion and washing of the residue with methanol afforded (L^H-H_2) as a white solid (44 mg, 0.0836 mmol, 55 %).

^{1}H NMR (500 MHz, DMSO-d_6, 298 K): δ = 9.92 (s, 2H, OH), 8.91 (d, J = 2.2 Hz, 2H, H_a), 8.76 (s, 2H, H_g), 8.35 (s, 1H, H_h), 8.29 (s, 2H, H_b), 7.81 (d, J = 7.8 Hz, 2H, H_i), 7.50 (t, J = 7.8 Hz, 1H, H_J), 7.46 (t, J = 7.9 Hz, 2H, H_d), 7.40 (d, J = 8.2 Hz, 2H, H_c), 7.10 (d, J = 7.5 Hz, 2H, H_e), 5.92 (s, 4H, H_f) ppm.

^{13}C NMR (151 MHz, DMSO-d_6, 298 K): δ = 153.43, 148.21, 146.52, 138.04, 135.37, 131.21, 129.55, 129.27, 128.28, 128.19, 124.74, 121.96, 121.90, 117.82, 111.95, 50.80 ppm.

HRMS (positive ESI-MS, MeCN, acidified): m/z = 527.1960 (M + H^+, $C_{30}H_{23}N_8O_2^+$, calcd. 527.1938), 549.1780 (M + Na^+, $C_{30}H_{22}N_8O_2Na^+$, calcd. 549.1758).

(^{13}C NMR and HRMS data reproduced from previous literature[25].)

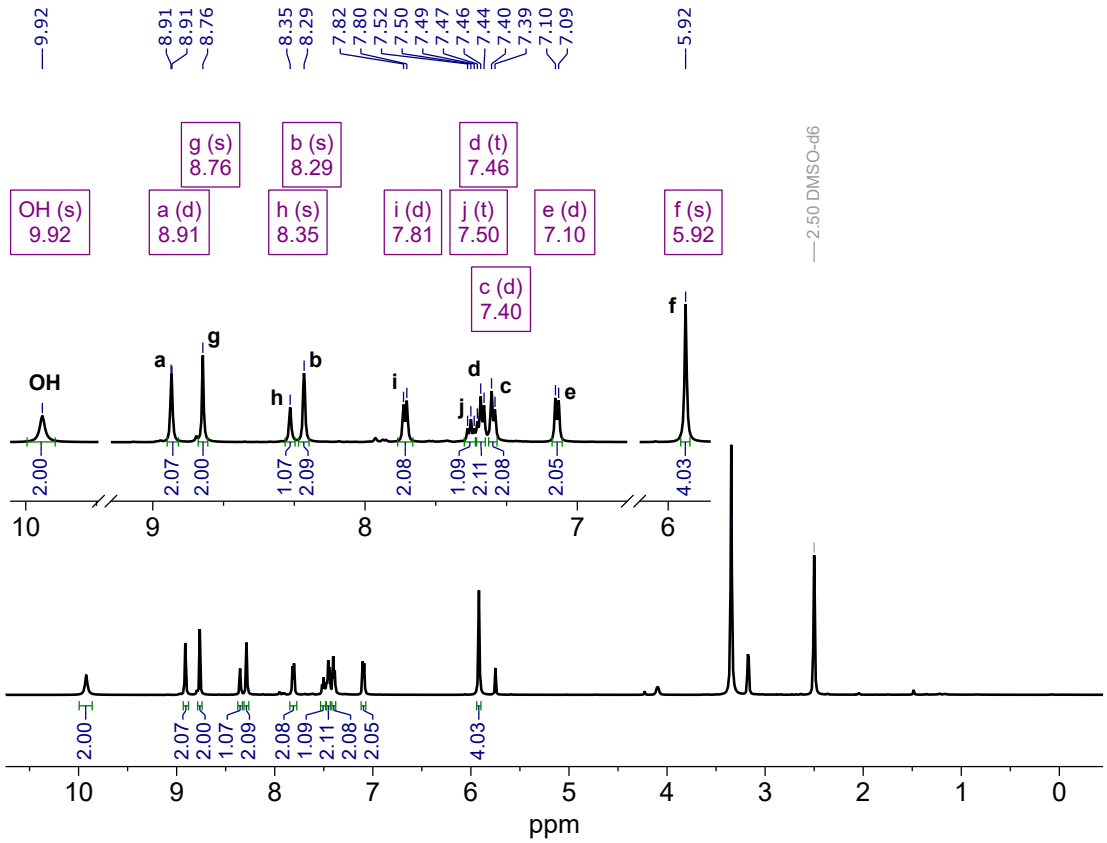

Figure 3.17 ^{1}H NMR spectrum of ligand $\mathbf{L^H}$-H_2.

3.4.2.9 Synthesis of 3,5-bis(1-((8-hydroxyquinolin-3-yl)methyl)-1*H*-1,2,3-triazol-4-yl)-*N*,*N*-diphenylbenzamide ($\mathbf{L^R}$-H_2)

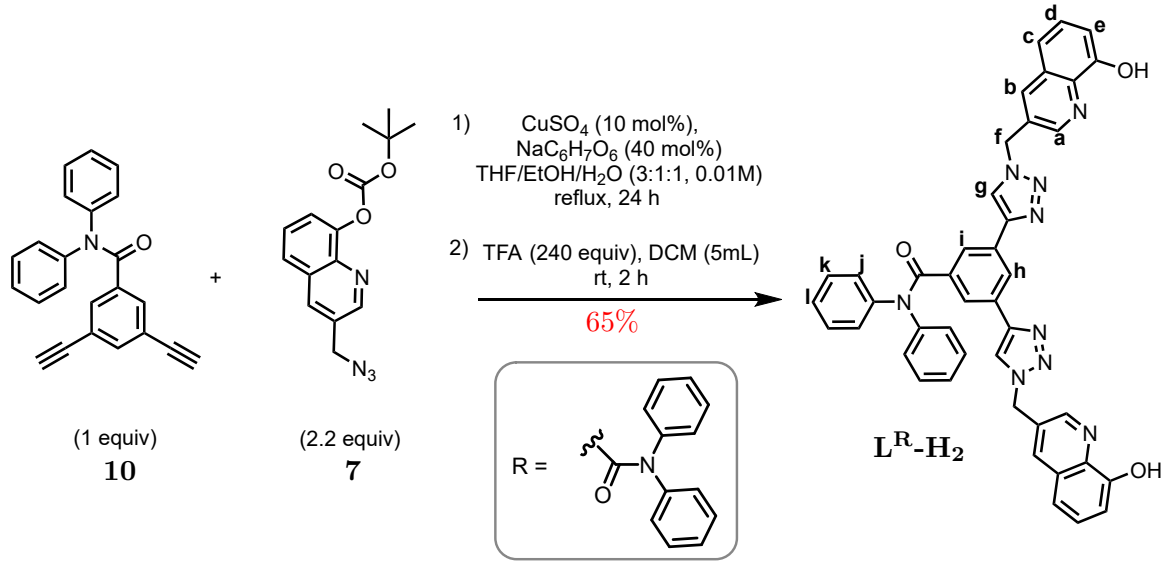

A Schlenk tube was equipped with azide **(7)** (71.95 mg, 0.240 mmol, 2.2 equiv.) and a 3 : 1 : 1 mixture of THF/EtOH/H_2O (10 mL, 0.01 M). The solution was degassed for 30 min by vigorous argon bubbling. Under argon, $CuSO_4$ (1.74 mg, 0.011 mmol, 10 mol %) and sodium

ascorbate (10.8 mg, 0.055 mmol, 50 mol %), were added successively. TBTA was omitted in contrast to the literature procedure for the ease of purification and was observed not to affect the yield significantly. Dialkyne **(10)** (35.0 mg, 0.109 mmol, 1.0 equiv.) was then introduced, the tube was sealed, and the mixture was heated at 100 °C for 24 h. After cooling to room temperature, the reaction mixture was diluted with dichloromethane and washed with 0.025 M basic aqueous EDTA. The aqueous layer was extracted with dichloromethane, the combined organic phases were dried over anhydrous magnesium sulfate, filtered, and concentrated under reduced pressure. Purification by column chromatography on silica gel (dichloromethane/methanol 1% → 10%) obtained final ligand. In most cases, the ligand was already deprotected of the Boc groups after the reaction; otherwise, the residue after column chromatography was dissolved in dichloromethane and treated with trifluoroacetic acid (240 equiv.) and stirred at rt for 16 hours. The mixture was neutralized with saturated $NaHCO_3$ solution and extracted with dichloromethane. The combined organic phases were dried over anhydrous magnesium sulfate, filtered, and concentrated under reduced pressure. This yielded the ligand $\mathbf{L^R\text{-}H_2}$ as a colorless solid (51 mg, 0.071 mmol, 65%).

^{1}H NMR (500 MHz, DMSO-d_6, 298 K): δ = 9.93 (s, 2H, OH), 8.90 (d, J = 2.1 Hz, 2H, H_a), 8.67 (s, 2H, H_g), 8.29 (d, J = 2.2 Hz, 2H, H_b), 8.25 (t, J = 1.6 Hz, 1H, H_h), 7.86 (d, J = 1.6 Hz, 2H, H_i), 7.46 (t, J = 7.9 Hz, 2H, H_d), 7.41 (dd, J = 8.3, 1.4 Hz, 2H, H_c), 7.33-7.25 (m, 8H, H_j and H_k), 7.19-7.13 (m, 2H, H_l), 7.11 (dd, J = 7.5, 1.4 Hz, 2H, H_e), 5.90 (s, 4H, H_f) ppm

^{13}C NMR (151 MHz, DMSO-d_6, 298 K): δ = 169.14, 153.43, 148.24, 145.75, 143.38, 138.06, 137.80, 135.47, 130.84, 129.15, 129.13, 128.27, 128.21, 127.71, 126.63, 124.61, 122.83, 122.14, 117.81, 111.98, 50.83 ppm.

HRMS (positive ESI-MS, MeCN, acidified): m/z = 722.2650 (M + H^+, $C_{43}H_{32}N_9O_3{}^+$, calcd. 722.2623).

(^{13}C NMR and HRMS data reproduced from previous literature[25].)

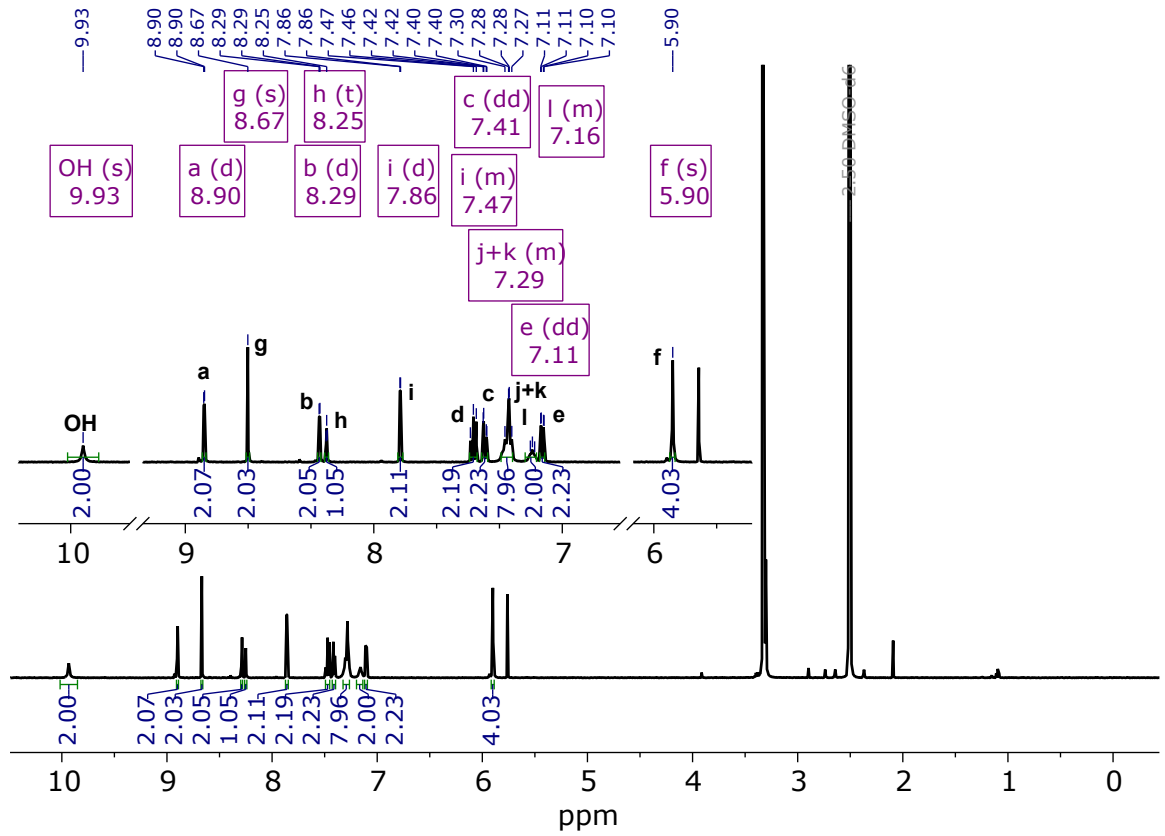

Figure 3.18 ^{1}H NMR spectrum of ligand $\mathbf{L^{R}}$-H_2.

3.4.3 Complexation of charge-neutral $[\mathbf{L^{R}}_2\mathbf{Zn_2}]$ helicate

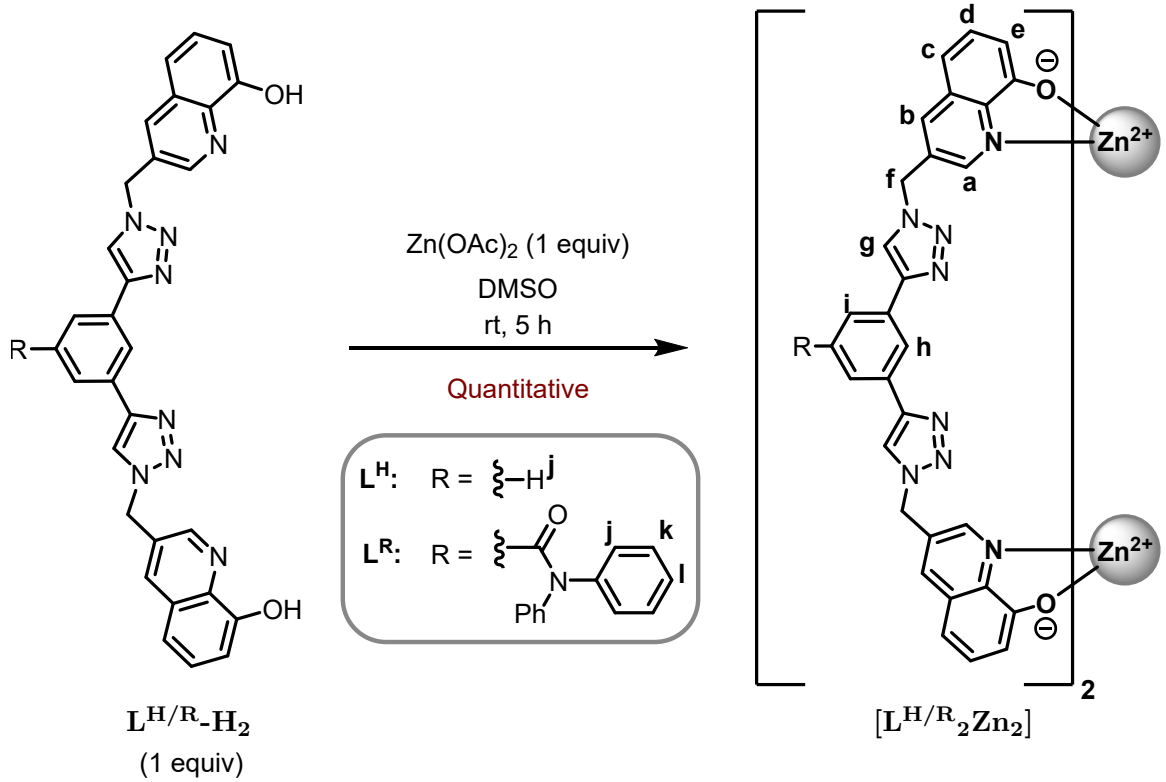

The corresponding ligand (1.0 equiv.) was dissolved in DMSO (0.005 M), and solid zinc acetate (1.0 equiv.) was added to the stirred solution. An immediate color change to yellow was observed. The reaction mixture was stirred at room temperature for 24 h. In certain instances, in contrast to the reported procedure, the reaction was carried out at 50 °C to ensure complete dissolution and conversion. The solution was subsequently lyophilized to afford the charge-neutral complexes [$\mathbf{L^H}_2Zn_2$] and [$\mathbf{L^R}_2Zn_2$] as yellow solids in quantitative yield.

[$\mathbf{L^H}_2Zn_2$]: **^{1}H NMR** (500 MHz, DMSO-d_6, 298 K): δ = 8.65 (s, 2H, H_g), 8.59 (d, J = 1.6Hz, 2H, H_a), 8.38 (s, 2H, H_b), 8.16 (s, 1H, H_h), 7.81 (d, J = 7.8Hz, 2H, H_i), 7.48 (t, J = 7.8Hz, 1H, H_j), 7.33 (t, J = 7.9Hz, 2H, H_d), 6.85 (d, J = 8.2Hz, 2H, H_c), 6.69 (d, J = 7.8Hz, 2H, H_e), 5.90 (s, 4H, H_f) ppm.

[$\mathbf{L^R}_2Zn_2$]: **^{1}H NMR** (500 MHz, DMSO-d_6, 298 K): δ = 8.58 (s, 2H, H_a), 8.57 (s, 2H, H_g), 8.38 (s, 2H, H_b), 8.09 (s, 1H, H_h), 7.86 (s, 2H, H_i), 7.34 (t, J = 8.0 Hz, 2H, H_d), 7.31 – 7.23 (m, 8H, H_j and H_k), 7.16 – 7.08 (m, 2H, H_l), 6.87 (d, J = 8.1 Hz, 2H, H_c), 6.71 (d, J = 6.0 Hz, 2H, H_e), 5.88 (s, 4H, H_f) ppm.

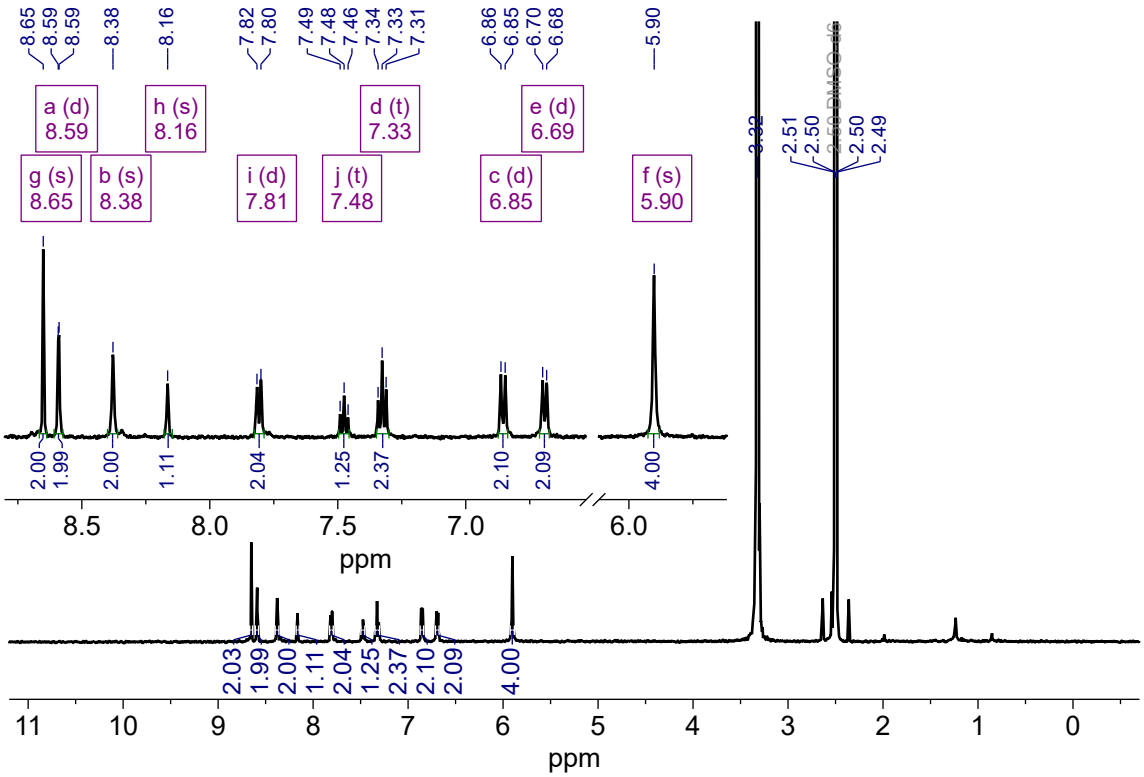

Figure 3.19 ^{1}H NMR spectrum of complex [$\mathbf{L^H}_2Zn_2$].

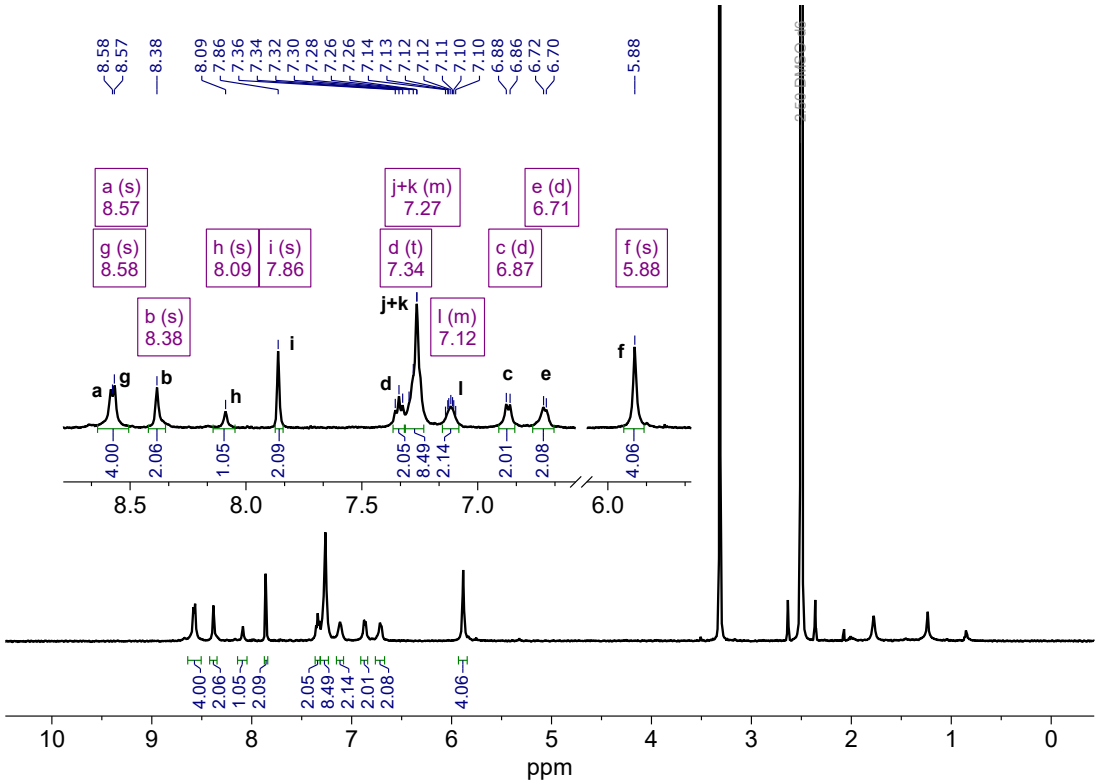

Figure 3.20 ^{1}H NMR spectrum of complex [$\mathbf{L}^{\mathbf{R}}{}_2Zn_2$].

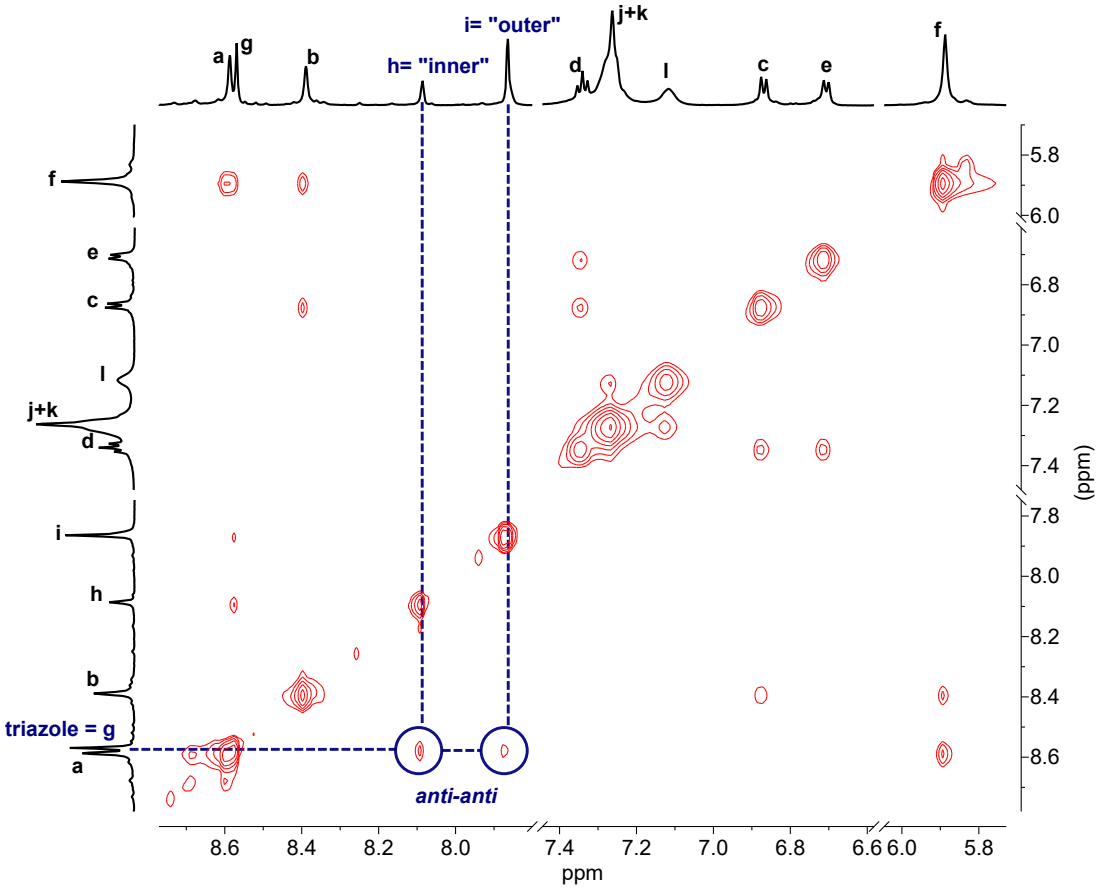

Figure 3.21 NOESY NMR spectrum of complex [$\mathbf{L}^{\mathbf{R}}{}_2Zn_2$].

3.4.4 Binding studies of carboxylate guests

3.4.4.1 (*S*)-(+)-Mandalate

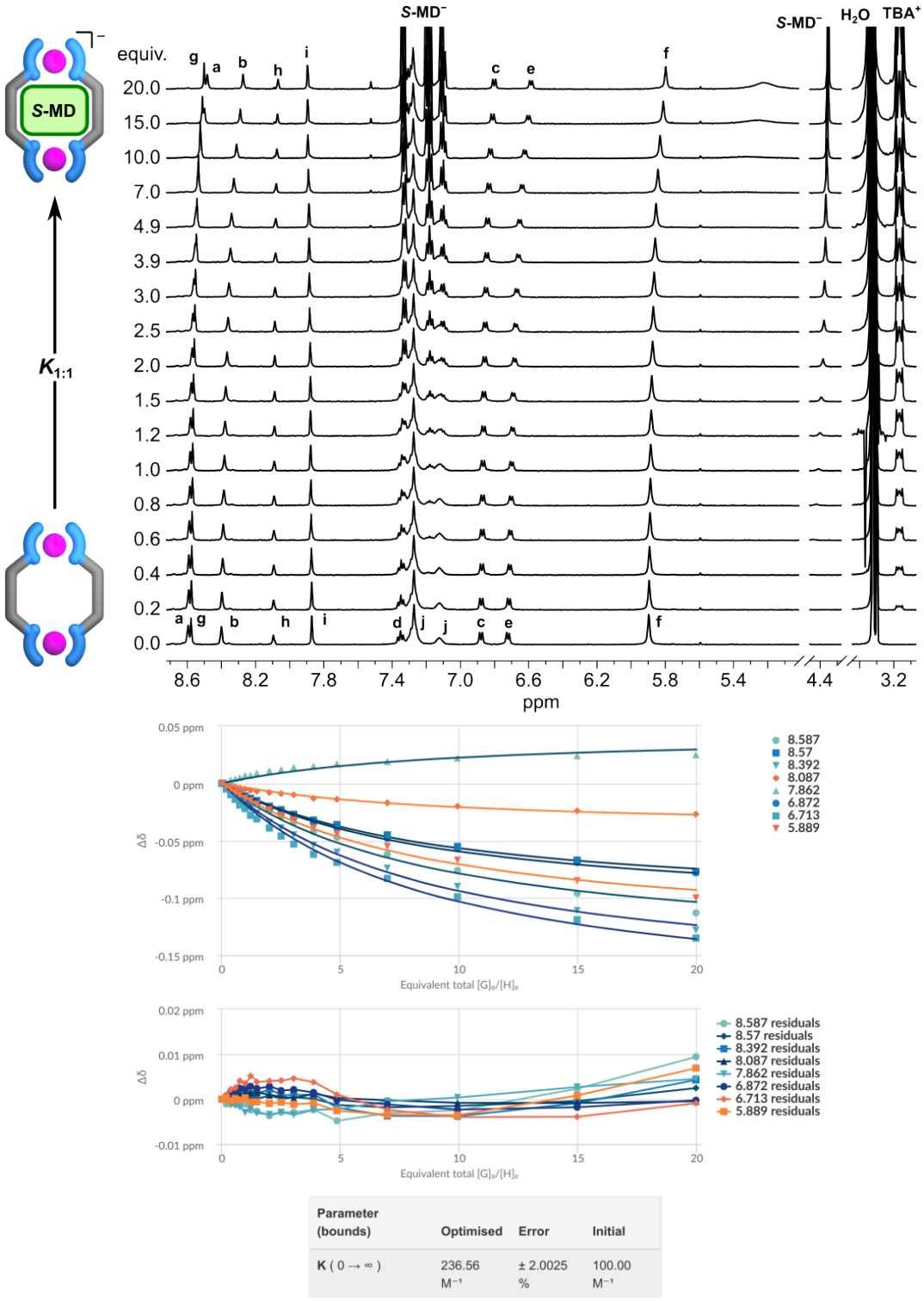

Parameter (bounds)	Optimised	Error	Initial
K (0 → ∞)	236.56 M^{-1}	± 2.0025 %	100.00 M^{-1}

Figure 3.22 Top: ^{1}H NMR titration of [$\mathbf{L^R}_2Zn_2$] with (*S*)-(+)-Mandalate (***S*-MD$^-$**) as TBA salts (500 MHz, 500 µM, DMSO-d_6, 298 K). Bottom: Binding isotherm obtained by fitting the chemical shift changes with BindFit using a 1:1 model. A 1:2 model was not implemented as no inflection point characteristic for monocarboxylate binding was observed. This absence can be attributed to the weak binding of ***S*-MD$^-$** due to the electron withdrawing hydroxy group.

3.4.4.2 (*S*)-(+)-Hydratropate

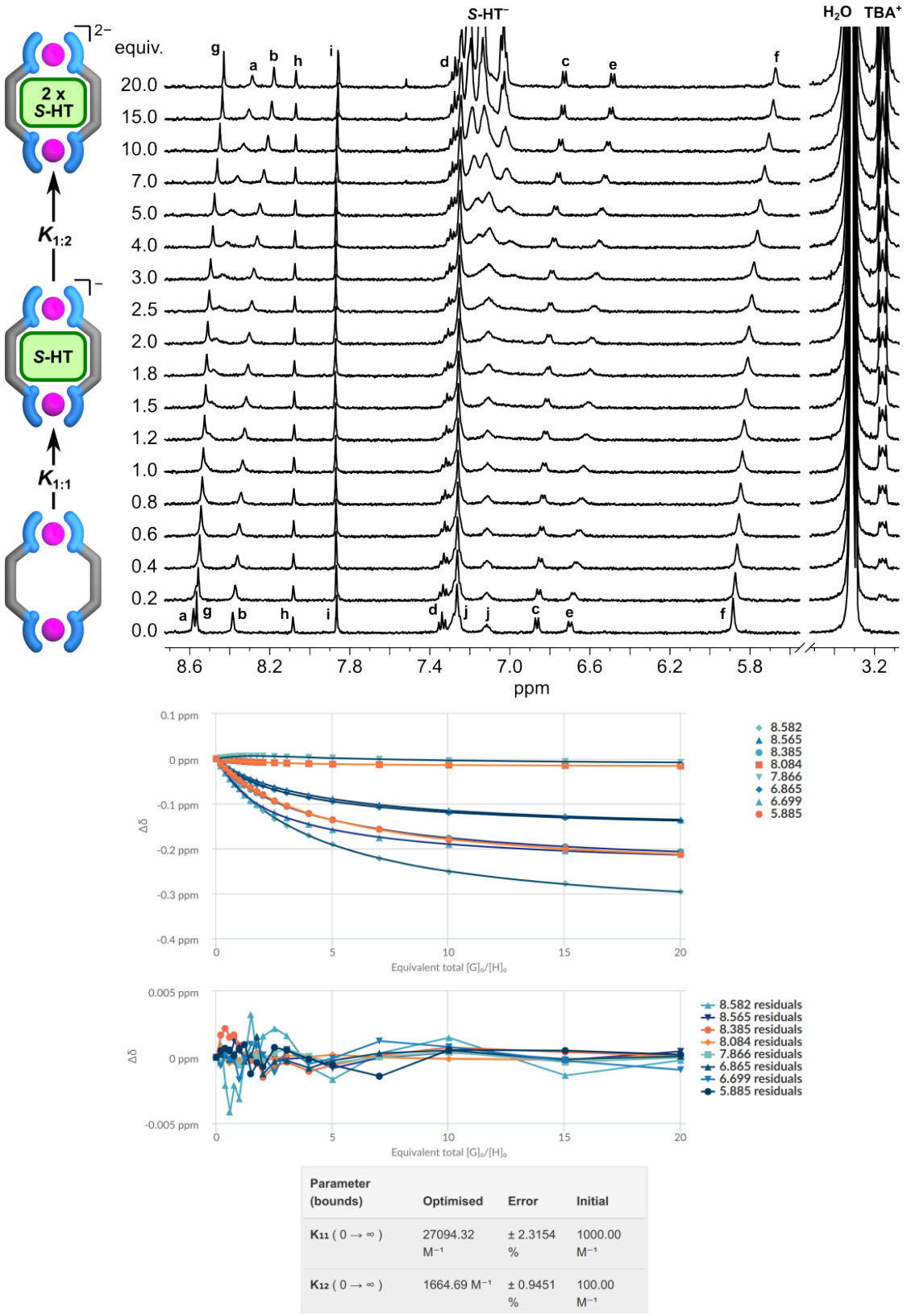

Parameter (bounds)	Optimised	Error	Initial
K11 (0 → ∞)	27094.32 M⁻¹	± 2.3154 %	1000.00 M⁻¹
K12 (0 → ∞)	1664.69 M⁻¹	± 0.9451 %	100.00 M⁻¹

Figure 3.23 Top: ^{1}H NMR titration of [$\mathbf{L^R}_2$Zn$_2$] with (*S*)-(+)-Hydratropate (***S*-HT$^-$**) as TBA salts (500 MHz, 100 µM, DMSO-d_6, 298 K). Bottom: Binding isotherm obtained by fitting the chemical shift changes with BindFit using a 1:2 model. Chemical shift changes of proton H$_i$ (δ = 7.86 ppm) showed the expected inflection point for a 1:2 binding event.

3.4.4.3 (*S*)-(+)-2-(6-Methoxy-2-naphthyl)propionate

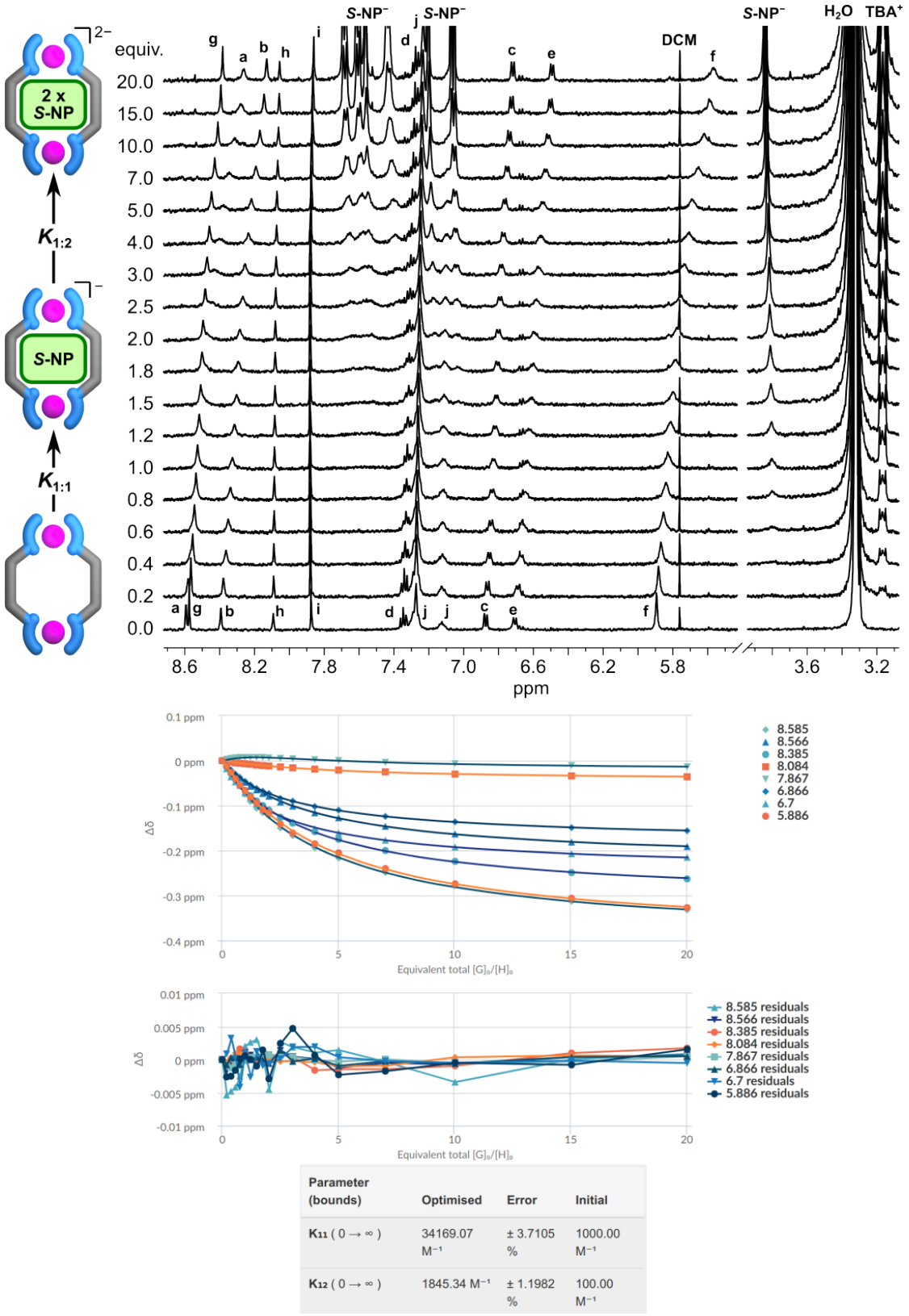

Parameter (bounds)	Optimised	Error	Initial
K_{11} (0 → ∞)	34169.07 M^{-1}	± 3.7105 %	1000.00 M^{-1}
K_{12} (0 → ∞)	1845.34 M^{-1}	± 1.1982 %	100.00 M^{-1}

Figure 3.24 Top: ^{1}H NMR titration of [$\mathbf{L^R}_2Zn_2$] with (*S*)-(+)-2-(6-Methoxy-2-naphthyl)propionate as TBA salts (***S*-NP$^-$**) (500 MHz, 100 µM, DMSO-d_6, 298 K). Bottom: Binding isotherm obtained by fitting the chemical shift changes with BindFit using a 1:2 model. Chemical shift changes of proton H_i (δ = 7.86 ppm) showed the expected inflection point for a 1:2 binding event.

3.4.4.4 (*S*)-2-(4-isobutylphenyl)propanoate

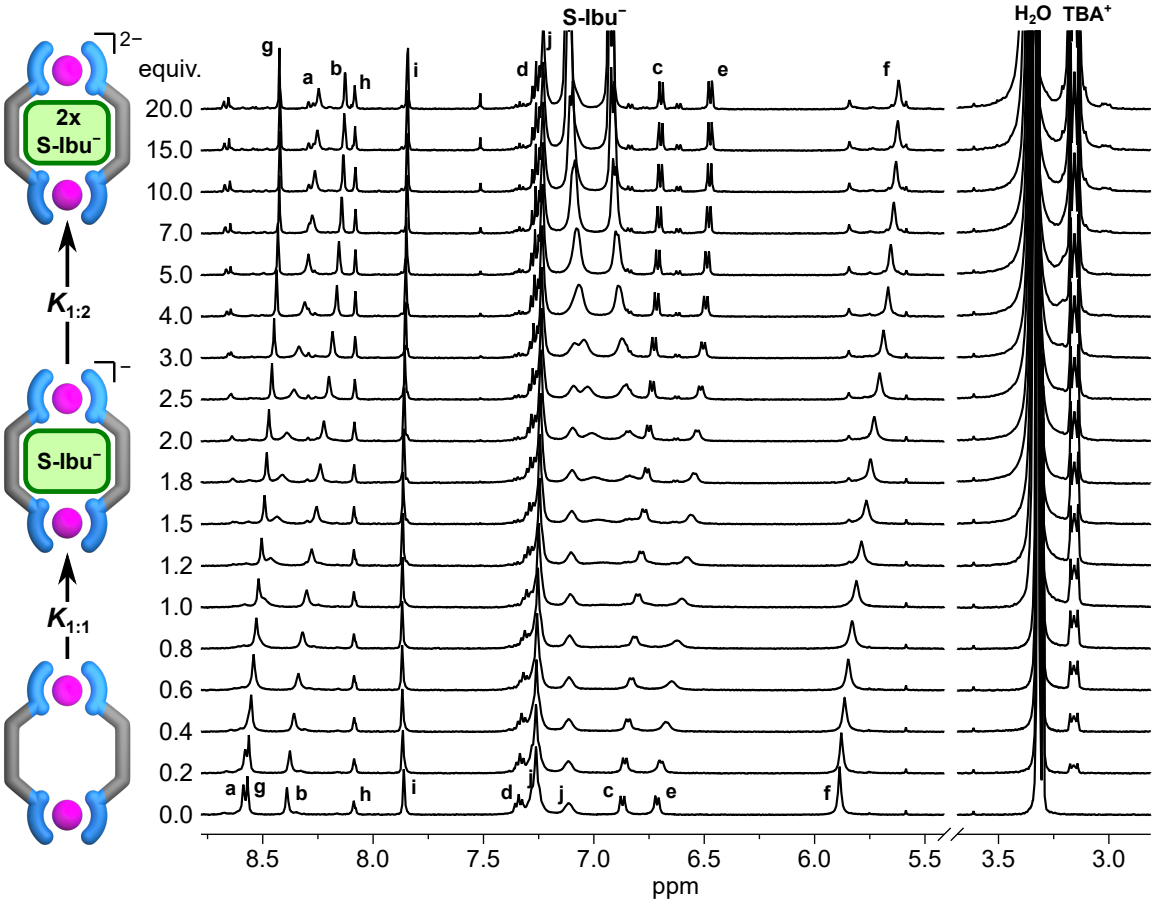

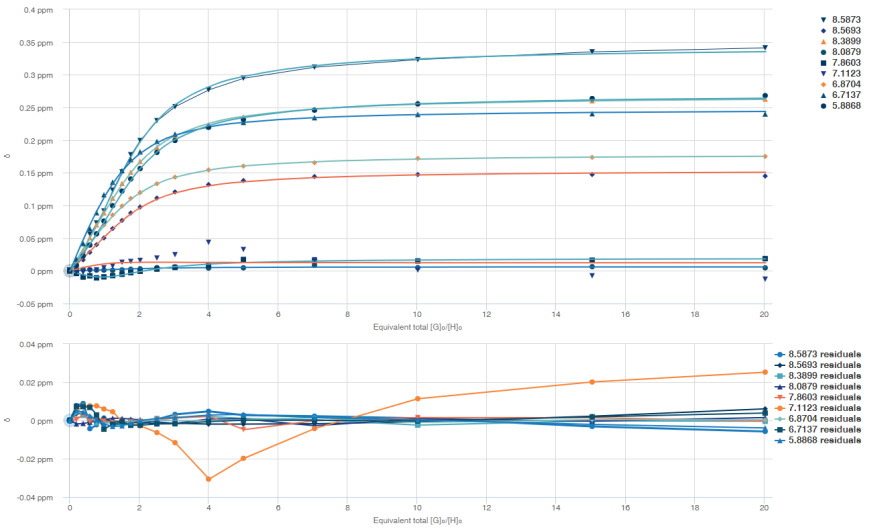

Parameter (bounds)	Optimised	Error	Initial
K_{11} (0 → ∞)	14810.85 M^{-1}	± 38.6356 %	1000.00 M^{-1}
K_{12} (0 → ∞)	1431.77 M^{-1}	± 6.4279 %	100.00 M^{-1}

Figure 3.25 Top: ^{1}H NMR titration of [$\mathbf{L^R}_2Zn_2$] with (*S*)-2-(4-isobutylphenyl)propanoate (deprotonated ibuprofen, ***S*-Ibu**$^-$) as TBA salts (500 MHz, 500 µM, DMSO-d_6, 298 K). Bottom: Binding isotherm obtained by fitting the chemical shift changes with BindFit using a 1:2 model.

3.4.4.5 (1R,4aR,4bR,10aR)-7-isopropyl-1,4a-dimethyl-1,2,3,4,4a,4b,5,6,10,10a-decahydrophenanthrene-1-carboxylate

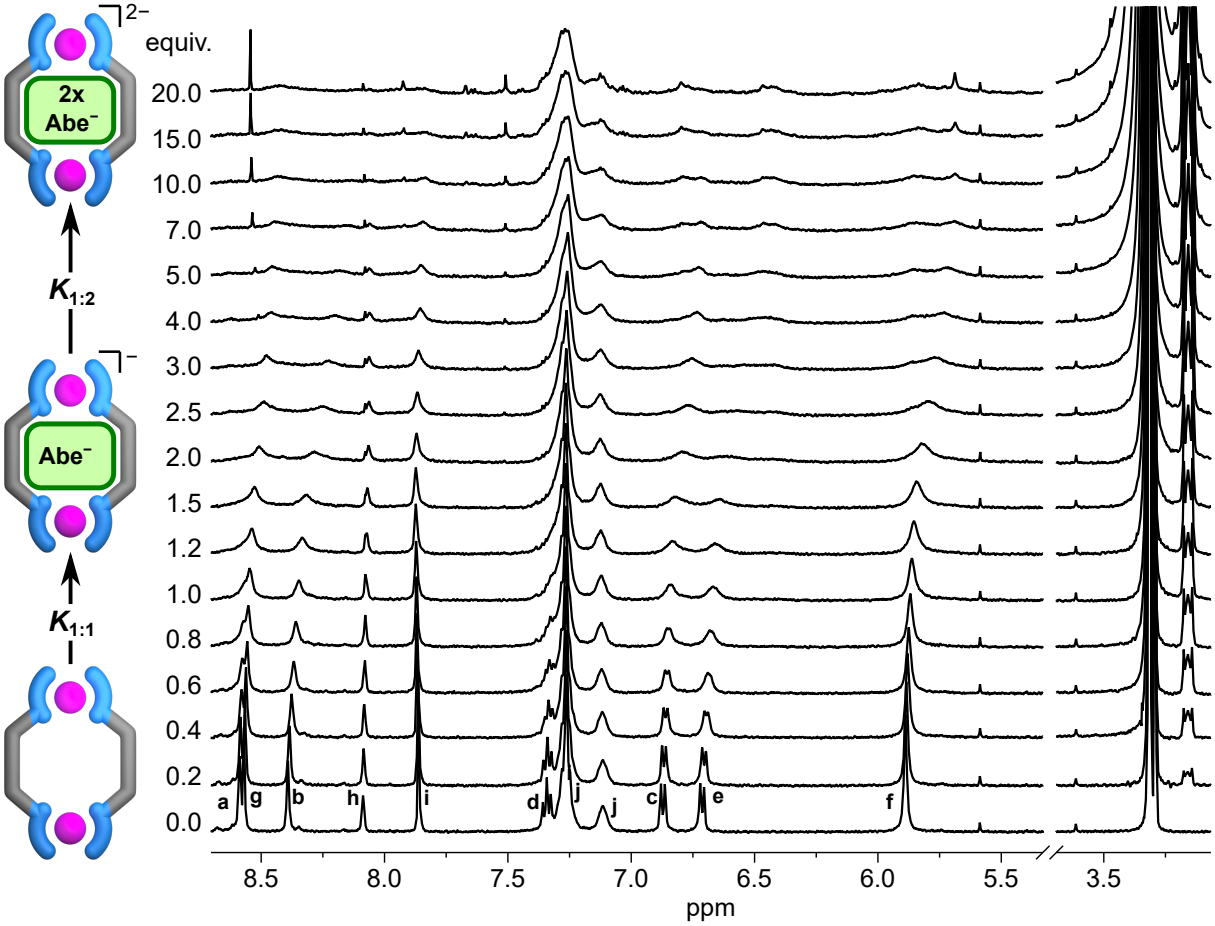

Figure 3.26 Top: ^{1}H NMR titration of [$\mathbf{L}^{\mathbf{R}}{}_2Zn_2$] with deprotonated abietic acid (***R*-Abe**$^-$) as TBA salts (500 MHz, 500 µM, DMSO-d_6, 298 K). With increasing amount of guest NMR spectra gets complicated which is either a result of the formation of unknown species or are related to the lower symmetry of the guest.

3.4.4.6 *N*-Boc-L-prolinate

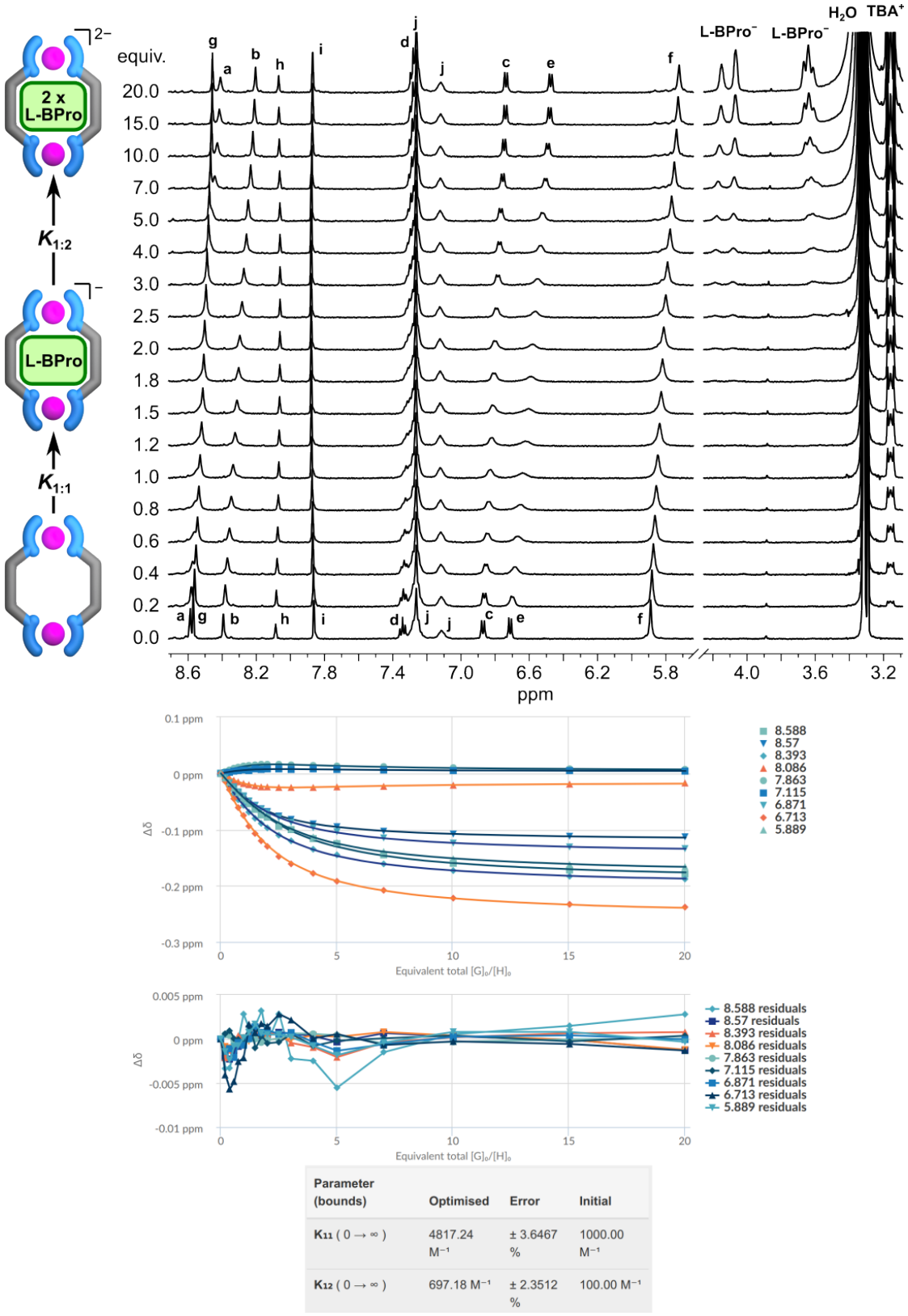

Parameter (bounds)	Optimised	Error	Initial
K11 (0 → ∞)	4817.24 M⁻¹	± 3.6467 %	1000.00 M⁻¹
K12 (0 → ∞)	697.18 M⁻¹	± 2.3512 %	100.00 M⁻¹

Figure 3.27 Top: ^{1}H NMR titration of [$\mathbf{L^R}_2Zn_2$] with *N*-Boc-L prolinate (**L-BPro**$^-$) as TBA salts (500 MHz, 500 µM, DMSO-d_6, 298 K). Bottom: Binding isotherm obtained by fitting the chemical shift changes with BindFit using a 1:2 model. Chemical shift changes of proton H_i (δ = 7.86 ppm) and H_j (δ = 7.11 ppm) showed the expected inflection point for a 1:2 binding event.

3.4.4.7 *N*-Boc-L-pipecolinate

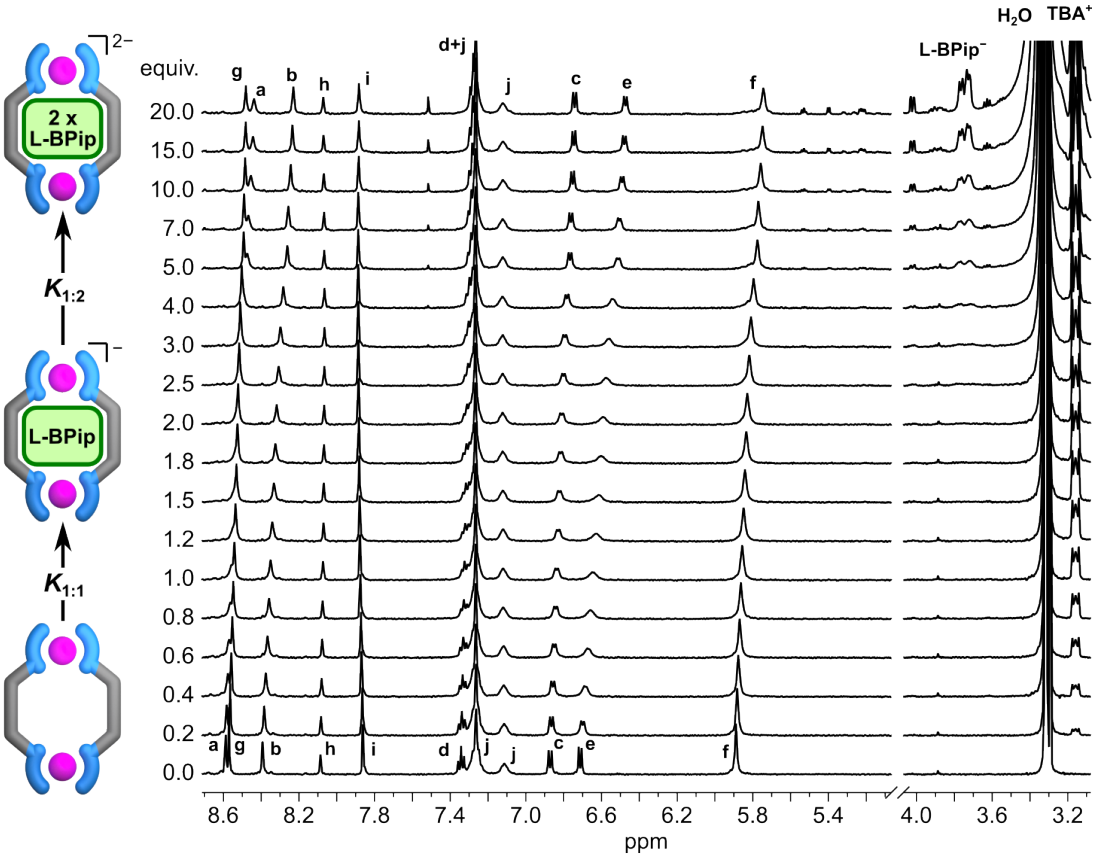

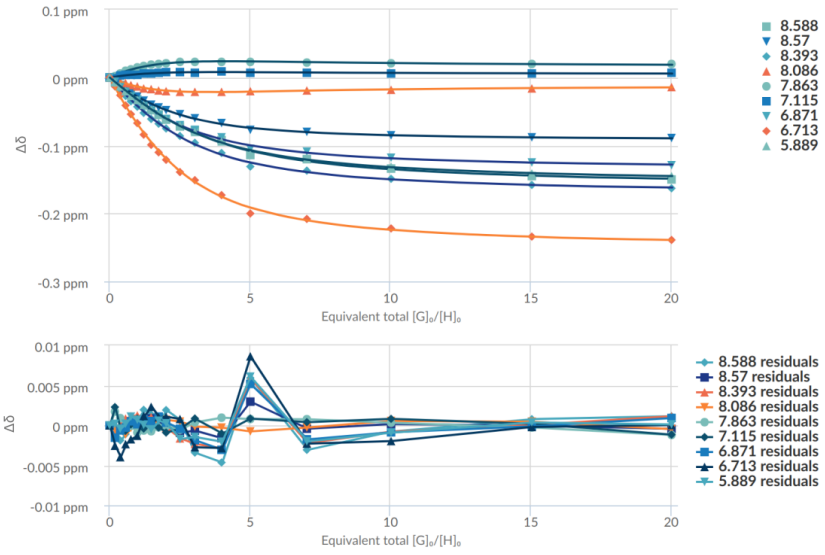

Parameter (bounds)	Optimised	Error	Initial
K11 (0 → ∞)	1850.97 M⁻¹	± 3.5212 %	1000.00 M⁻¹
K12 (0 → ∞)	738.99 M⁻¹	± 4.0219 %	100.00 M⁻¹

Figure 3.28 Top: ^{1}H NMR titration of [$\mathbf{L^R}_2Zn_2$] with *N*-Boc-L-pipecolinate (**L-BPip**$^-$) as TBA salts (500 MHz, 500 µM, DMSO-d_6, 298 K). Bottom: Binding isotherm obtained by fitting the chemical shift changes with BindFit using a 1:2 model. Chemical shift changes of proton H_i (δ = 7.86 ppm), H_j (δ = 7.11 ppm), and H_h (δ = 8.08 ppm) showed the expected inflection point for a 1:2 binding event.

3.4.4.8 (R)-3,3,3-trifluoro-2-methoxy-2-phenylpropanoate

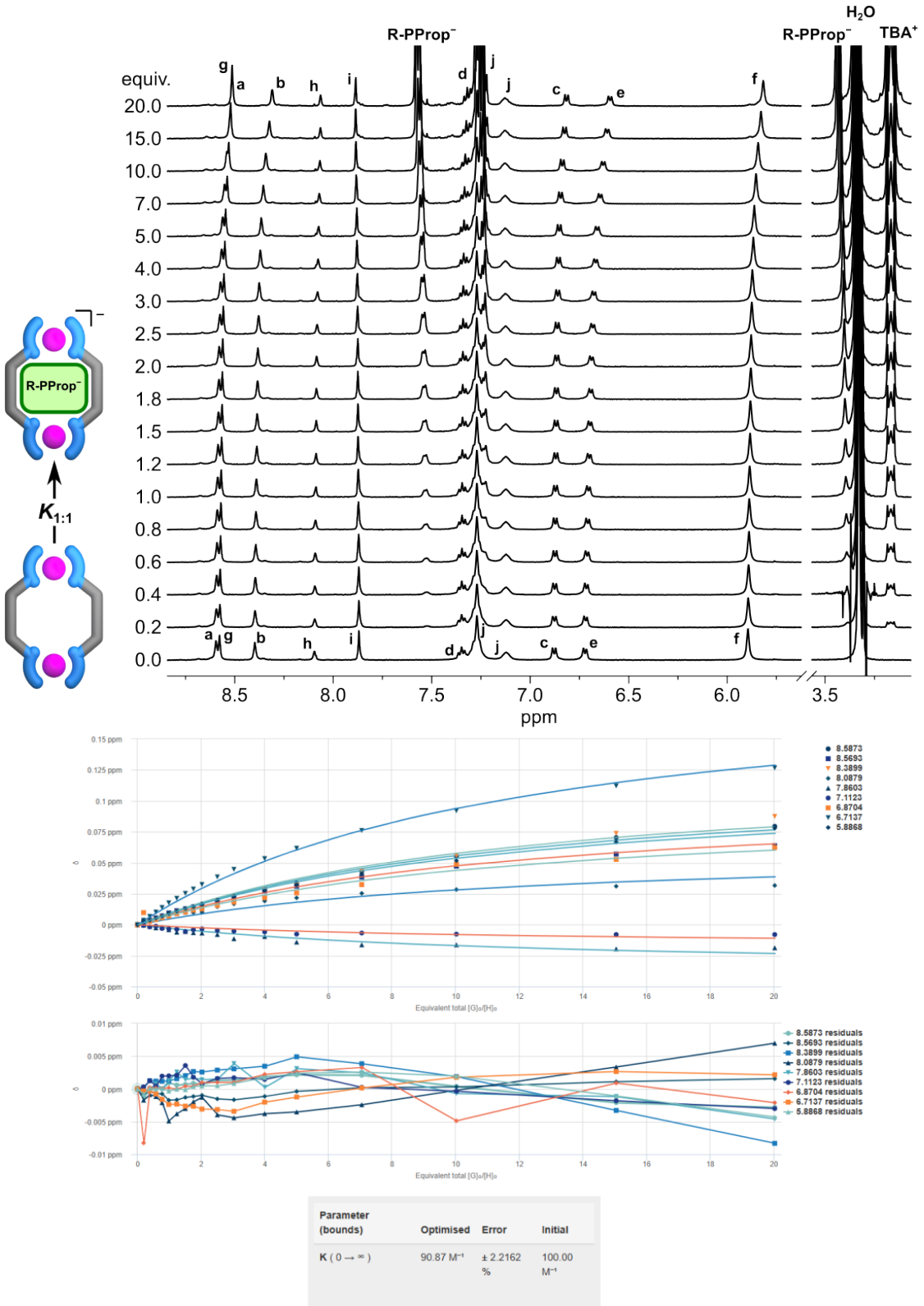

Figure 3.29 Top: ^{1}H NMR titration of [$\mathbf{L^R}_2Zn_2$] with (*R*)-3,3,3-trifluoro-2-methoxy-2-phenylpropanoate (***R*-PProp**$^-$) as TBA salts (500 MHz, 500 µM, DMSO-d_6, 298 K). Bottom: Binding isotherm obtained by fitting the chemical shift changes with BindFit using a 1:1 model. A 1:2 model was not implemented as no inflection point characteristic for binding two monocarboxylates was observed. This absence can be attributed to the weak binding of the guest due to the electron withdrawing CF_3 group.

3.4.4.9 (S)-indoline-2-carboxylate

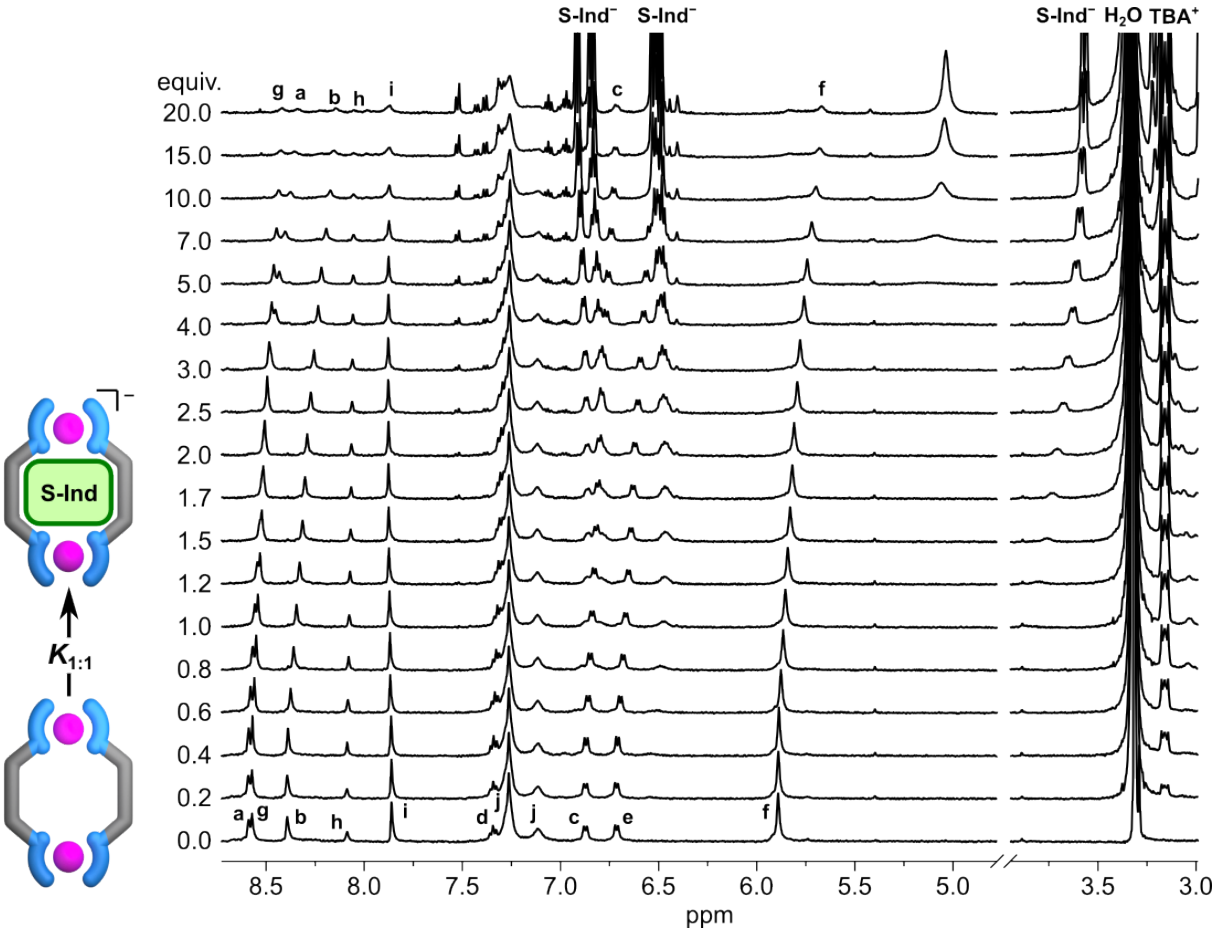

Figure 3.30 Top: ^{1}H NMR titration of [$\mathbf{L^R}_2Zn_2$] with (*S*)-indoline-2-carboxylate (***S*-Ind**$^-$) as TBA salts (500 MHz, 500 µM, DMSO-d_6, 298 K). At higher equivalents of guest NMR spectra gets complicated which are either a result of the formation of unknown species or are related to the lower symmetry of the guest.

3.4.4.10 L-(−)-malate

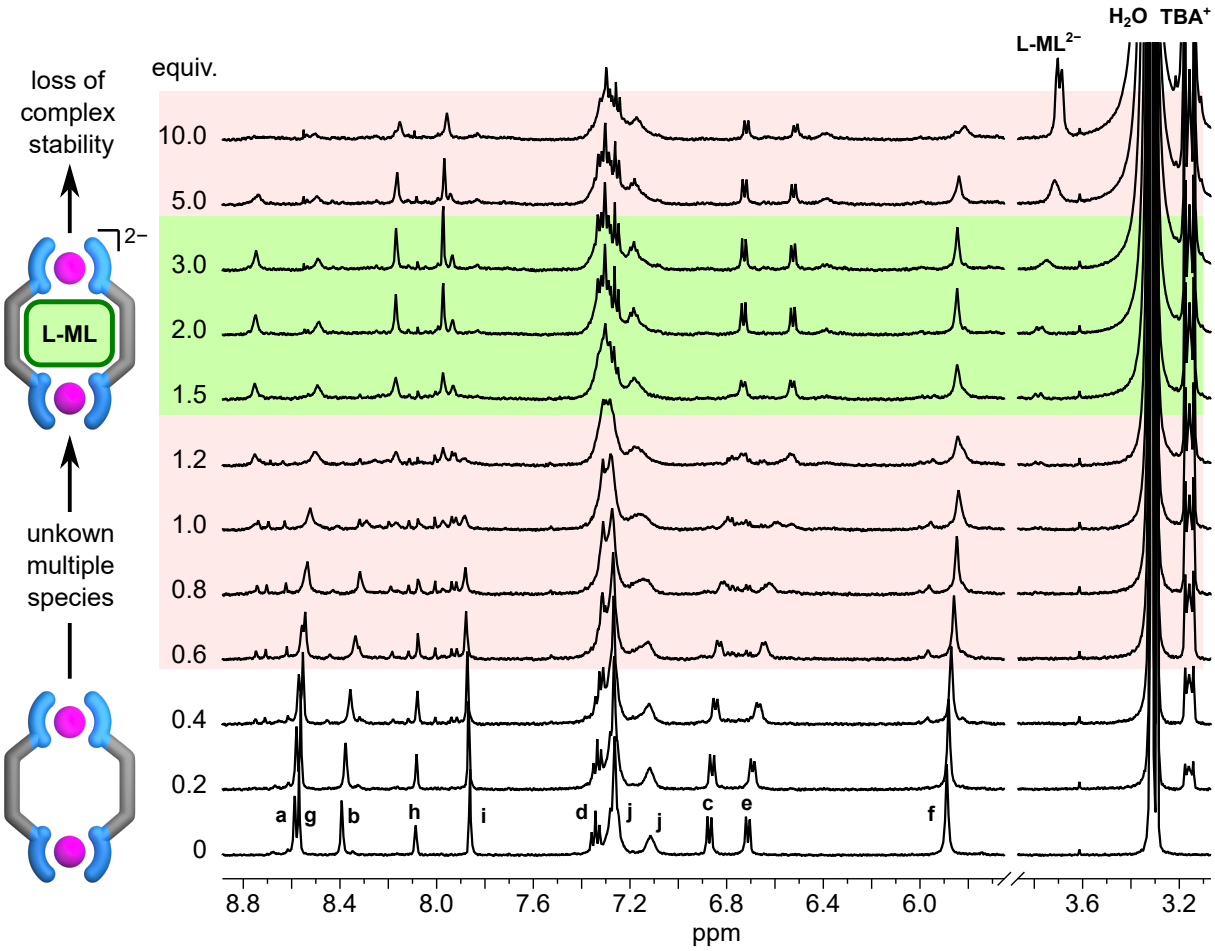

Figure 3.31 Top: ^{1}H NMR titration of [$\mathbf{L^R}_2Zn_2$] with L-(−)-malate (**L-ML^{2-}**) as TBA salts (500 MHz, 500 µM, DMSO-d_6, 298 K). At higher equivalents of guest NMR spectra gets complicated which are either a result of the formation of unknown species or are related to the lower symmetry of the guest.

3.4.4.11 D-(−)- and L-(+)-Tartrate

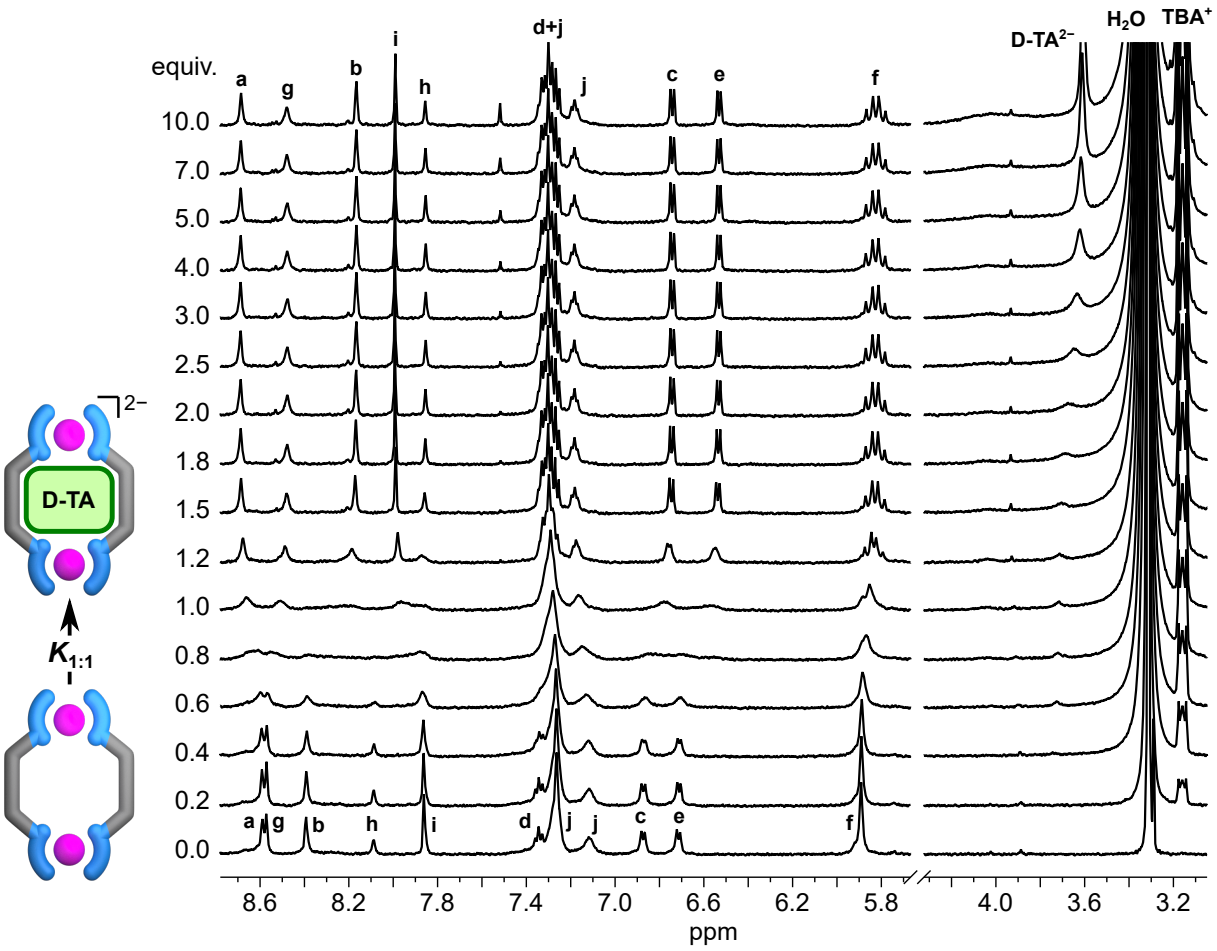

Figure 3.32 Top: ^{1}H NMR titration of [$\mathbf{L^R}_2Zn_2$] with D-(−)-tartrate (**D-TA^{2-}**) as TBA salts (500 MHz, 500 µM, DMSO-d_6, 298 K). Titration shows an intermediate exchange binding event.

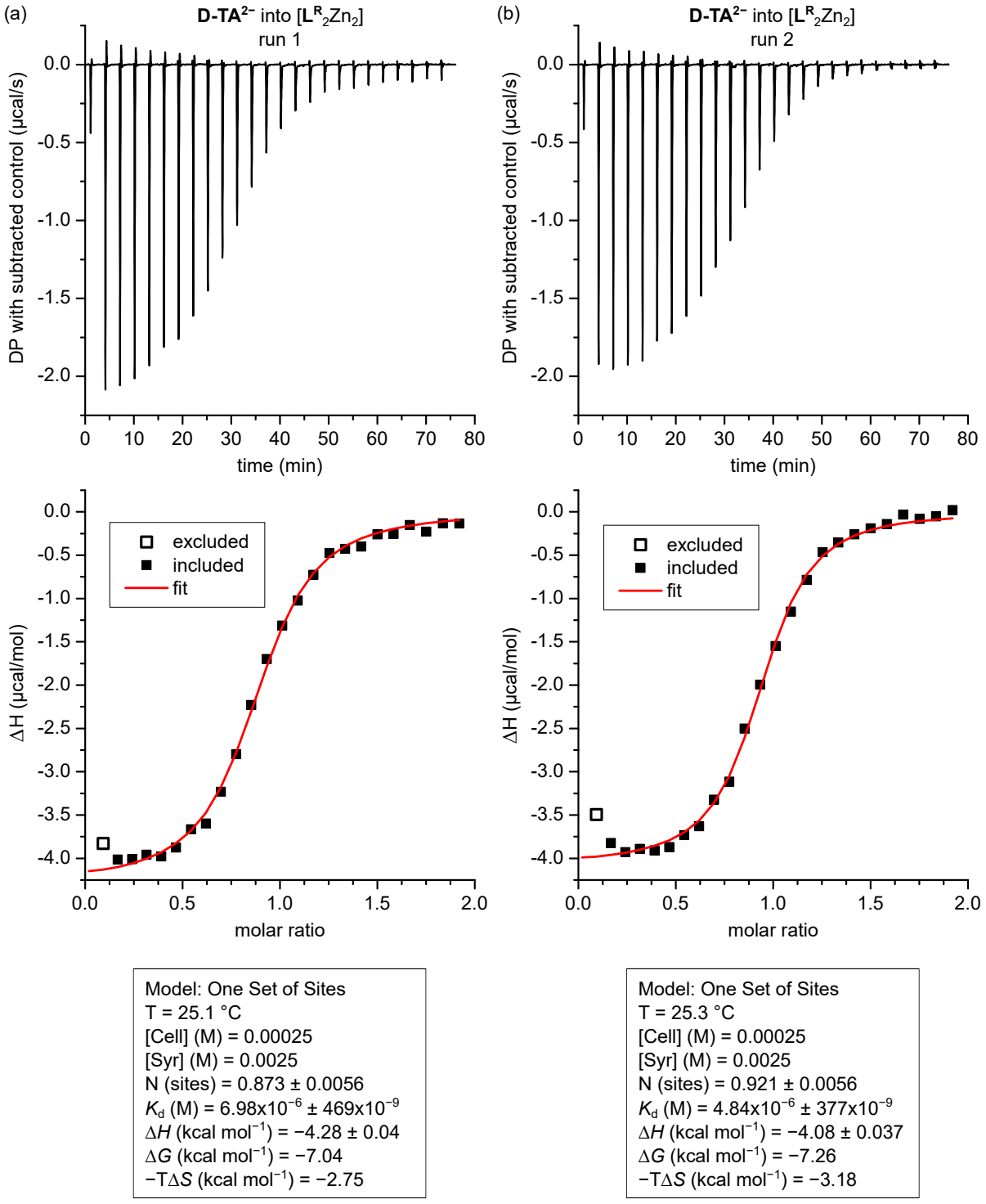

Figure 3.33 Binding constant determined from the ITC titration of [$\mathbf{L^R}_2Zn_2$] with D-(−)-tartrate ($\mathbf{D\text{-}TA^{2-}}$).

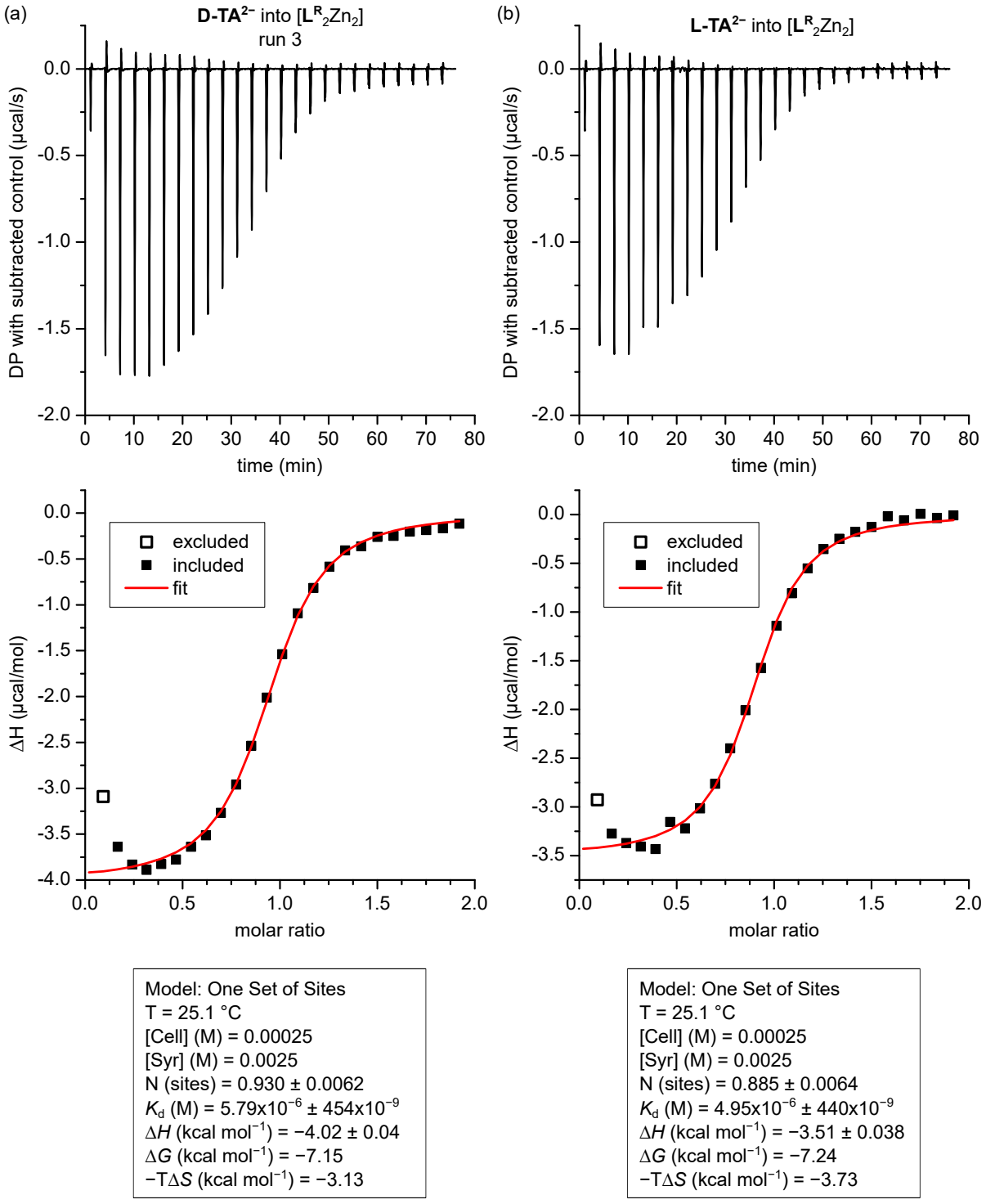

Figure 3.34 Binding constants determined from the ITC titrations of [$\mathbf{L^R}_2Zn_2$] with (a) D-(−)-tartrate ($\mathbf{D\text{-}TA^{2-}}$) and (b) L-(+)-tartrate ($\mathbf{L\text{-}TA^{2-}}$).

3.4.4.12 *N*-Boc-L-aspartate

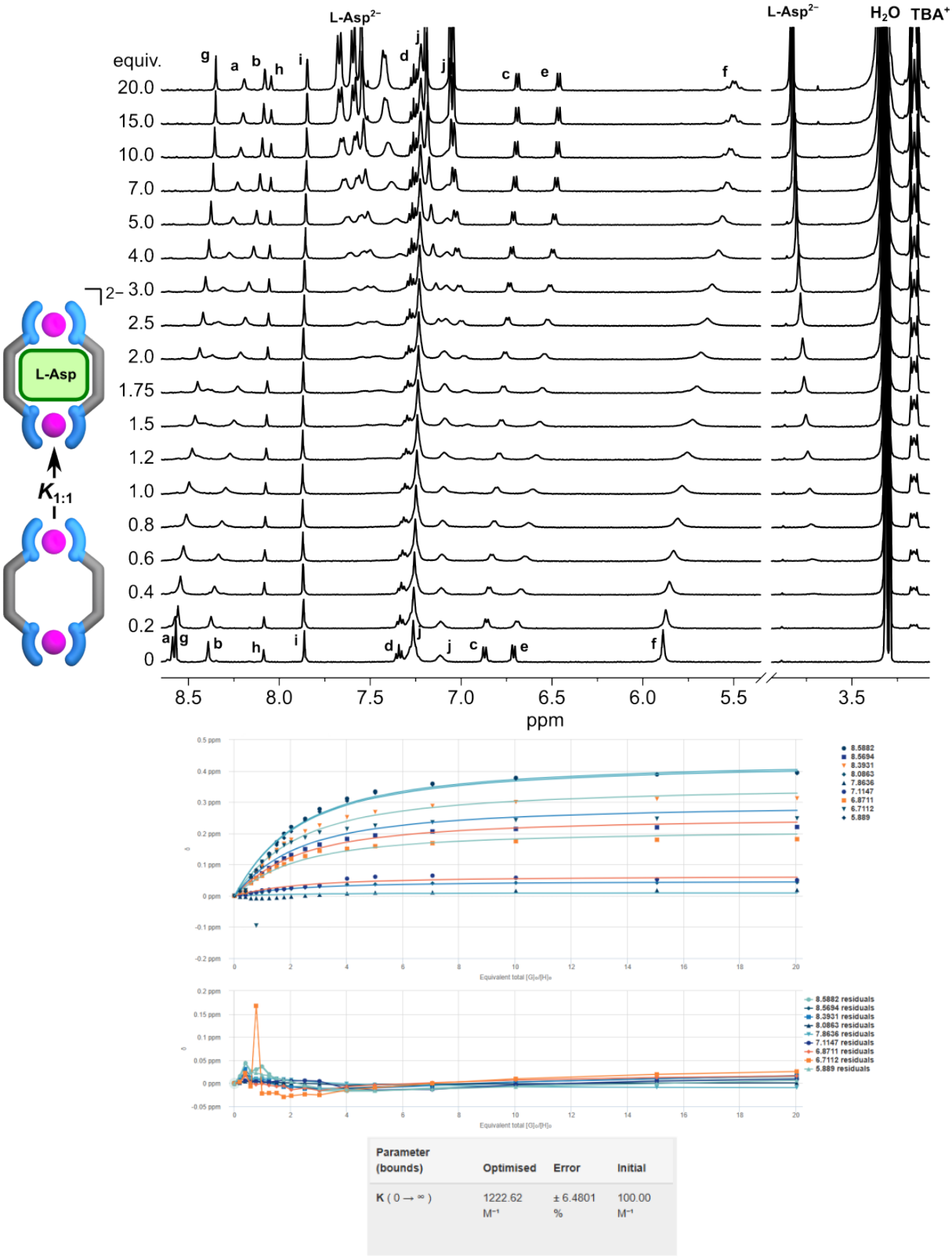

Figure 3.35 Top: ^{1}H NMR titration of [$\mathbf{L^R}_2Zn_2$] with *N*-Boc-L-aspartate (**L-Asp^{2-}**) as TBA salts (500 MHz, 500 µM, DMSO-d_6, 298 K). Bottom: Binding constant determined by integrating NMR signals.

3.4.4.13 *N*-Boc-L-glutamate

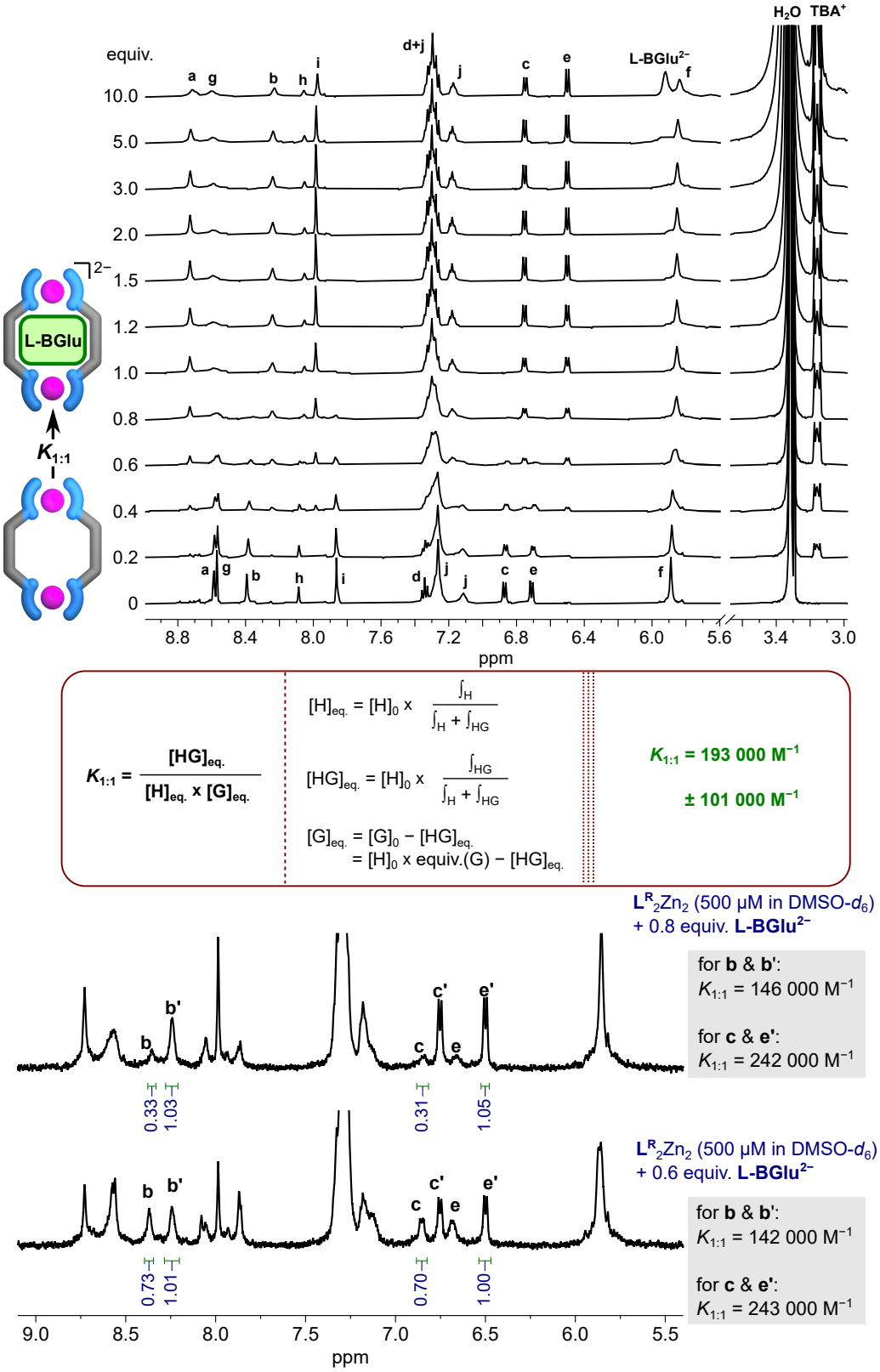

Figure 3.36 Top: ^{1}H NMR titration of [$\mathbf{L^R}_2Zn_2$] with *N*-Boc-L-glutamate (**L-BGlu^{2-}**) as TBA salts (500 MHz, 500 µM, DMSO-d_6, 298 K). Bottom: Binding constant determined by integrating NMR signals. Error estimated by taking the largest difference between the individual values in order to reflect the amount of uncertainty expected for this method.

3.4.4.14 *N*-Benzyl-L-glutamate

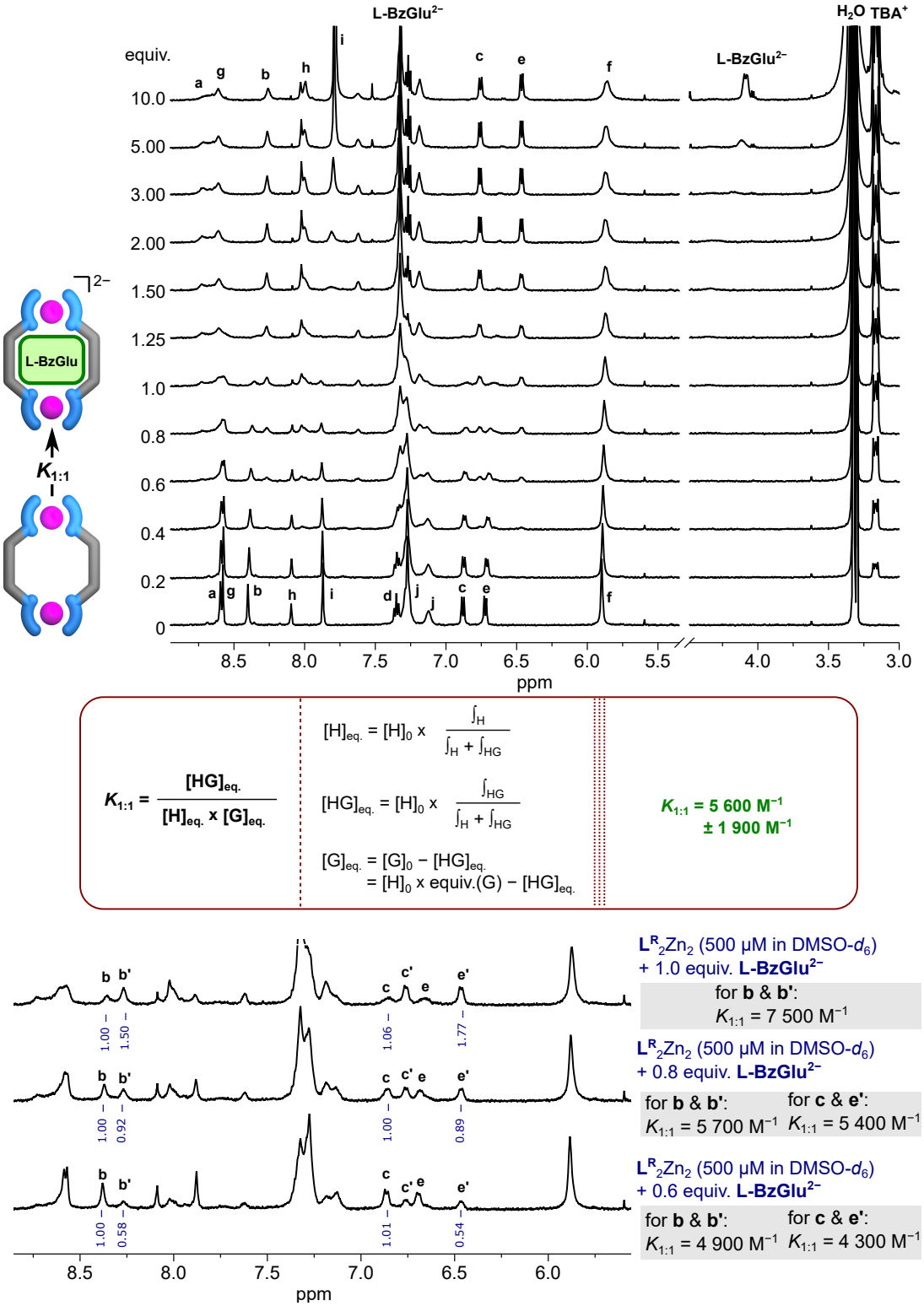

Figure 3.37 Top: ^{1}H NMR titration of [$\mathbf{L^R}_2Zn_2$] with *N*-Benzyl-L-glutamate (**L-BzGlu^{2-}**) as TBA salts (500 MHz, 500 µM, DMSO-d_6, 298 K). Bottom: Binding constant determined by integrating NMR signals. Error estimated by taking the largest difference between the individual values in order to reflect the amount of uncertainty expected for this method.

3.4.5 CD responses of carboxylate guests

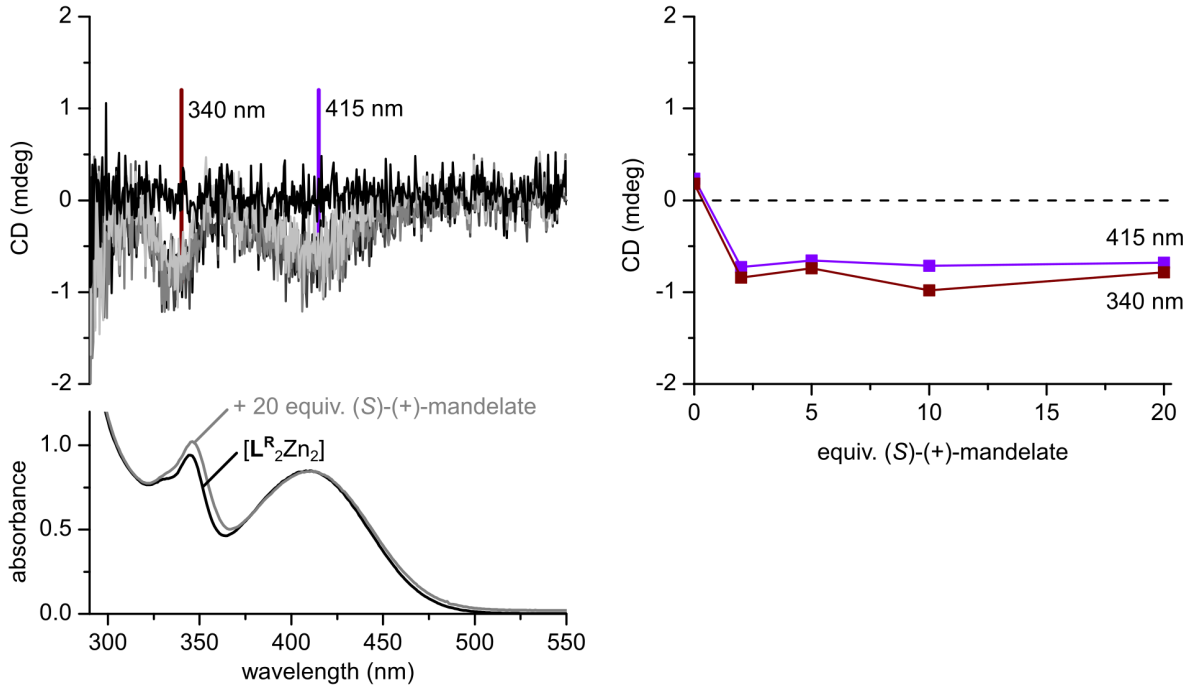

Figure 3.38 CD and UV-Vis spectra of titration of $[\mathbf{L^R}_2Zn_2]$ (500 µM, DMSO-d_6, l = 2 mm) with (*S*)-(+)-mandelate as TBA salts. CD spectra recorded after addition of 0, 2, 5, 10, and 20 equivalents of **S-MD**$^-$.

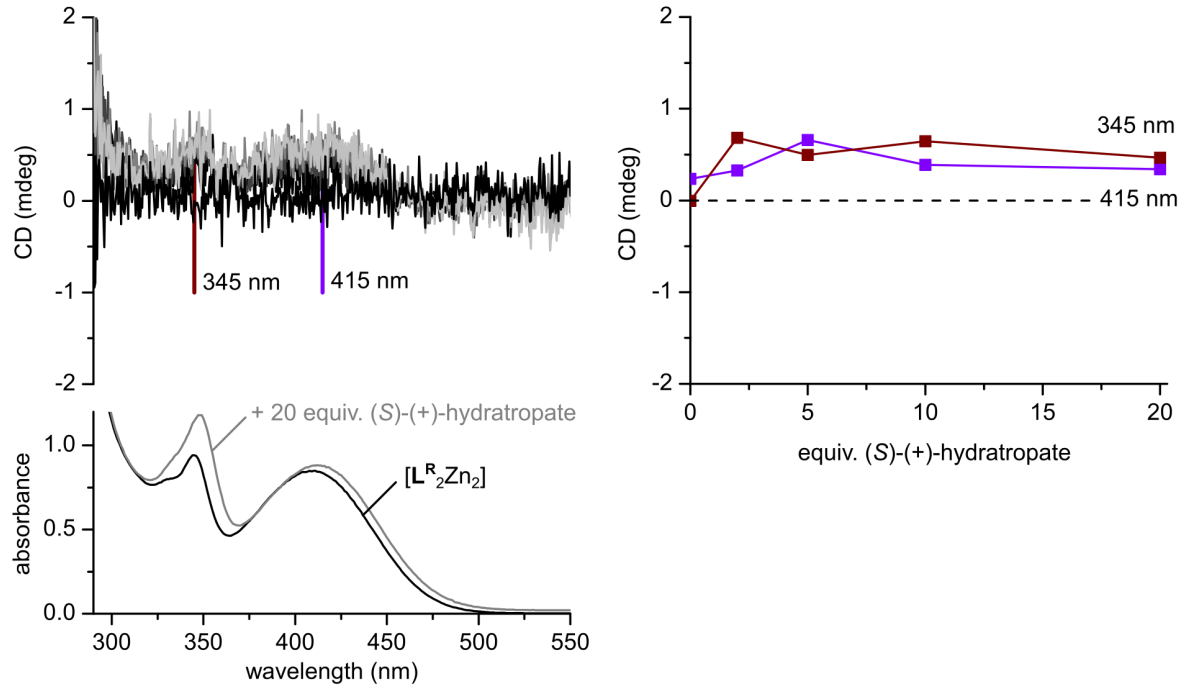

Figure 3.39 CD and UV-Vis spectra of titration of $[\mathbf{L^R}_2Zn_2]$ (500 µM, DMSO-d_6, l = 2 mm) with (*S*)-(+)-hydratropate as TBA salts. CD spectra recorded after addition of 0, 2, 5, 10, and 20 equivalents of **S-HT**$^-$.

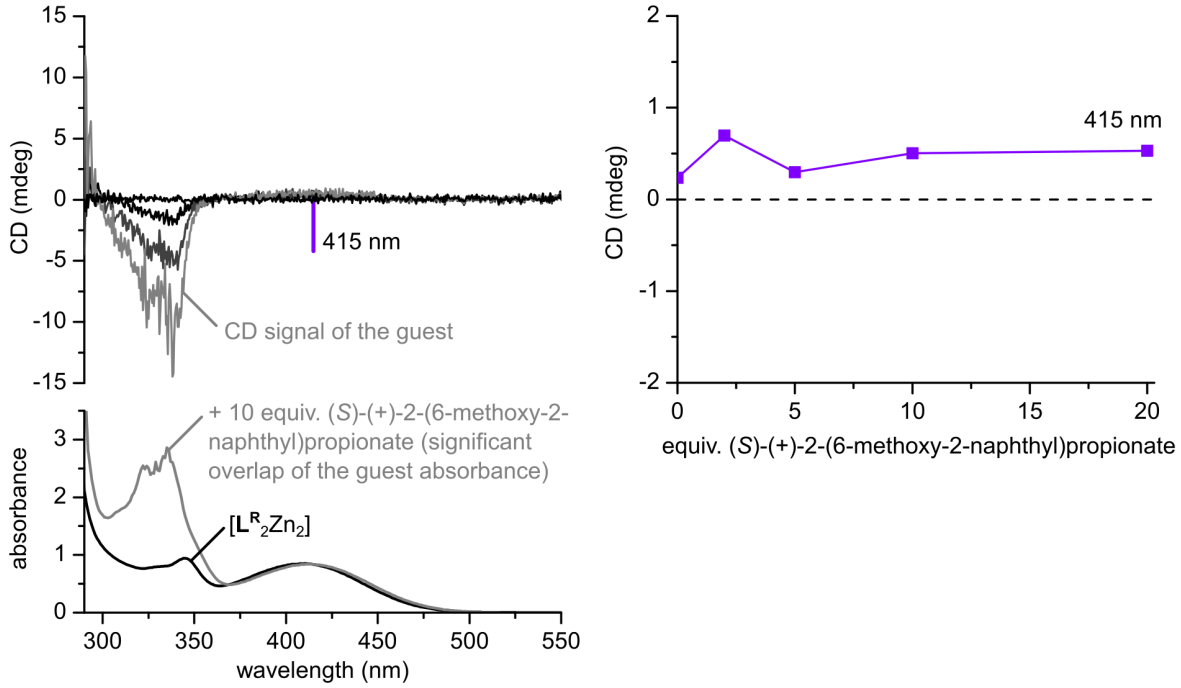

Figure 3.40 CD and UV-Vis spectra of titration of $[\mathbf{L^R}_2Zn_2]$ (500 µM, DMSO-d_6, l = 2 mm) with (*S*)-(+)-2-(6-methoxy-2-naphthyl)propionate as TBA salts. CD spectra recorded after addition of 0, 2, 5, 10, and 20 equivalents of ***S*-NP$^-$**. The CD and UV-Vis spectra with 20 equiv. ***S*-NP$^-$** are omitted (left) for clarity, as the high absorbance at this concentration resulted in excessive noise.

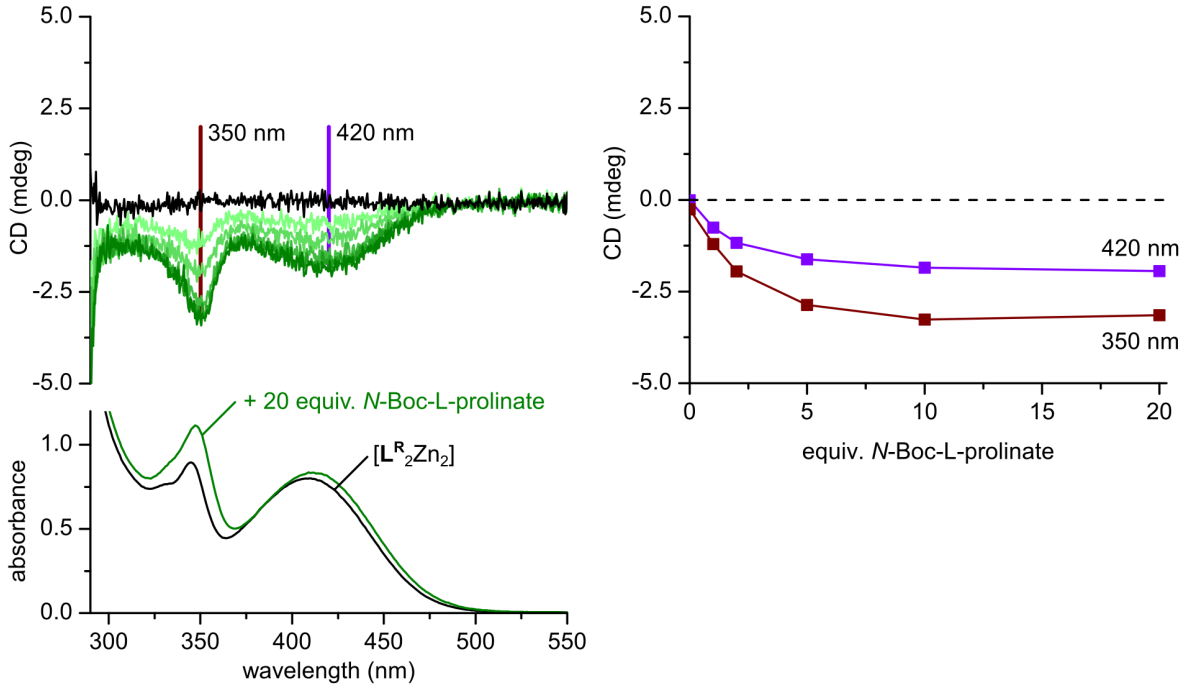

Figure 3.41 CD and UV-Vis spectra of titration of $[\mathbf{L^R}_2Zn_2]$ (500 µM, DMSO-d_6, l = 2 mm) with *N*-Boc-L-prolinate as TBA salts. CD spectra recorded after addition of 0, 1, 2, 5, 10, and 20 equivalents of **L-BPro$^-$**.

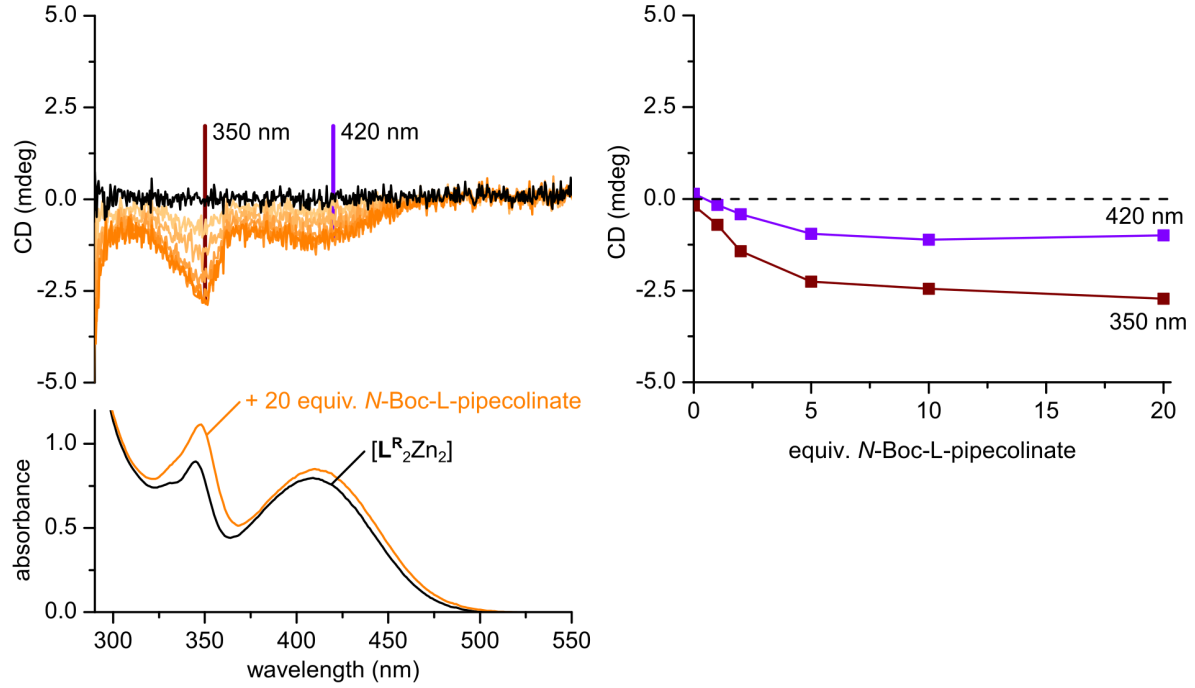

Figure 3.42 CD and UV-Vis spectra of titration of $[\mathbf{L^R}_2Zn_2]$ (500 µM, DMSO-d_6, l = 2 mm) with *N*-Boc-L-pipecolinate as TBA salts. CD spectra recorded after addition of 0, 1, 2, 5, 10, and 20 equivalents of **L-BPip**$^-$.

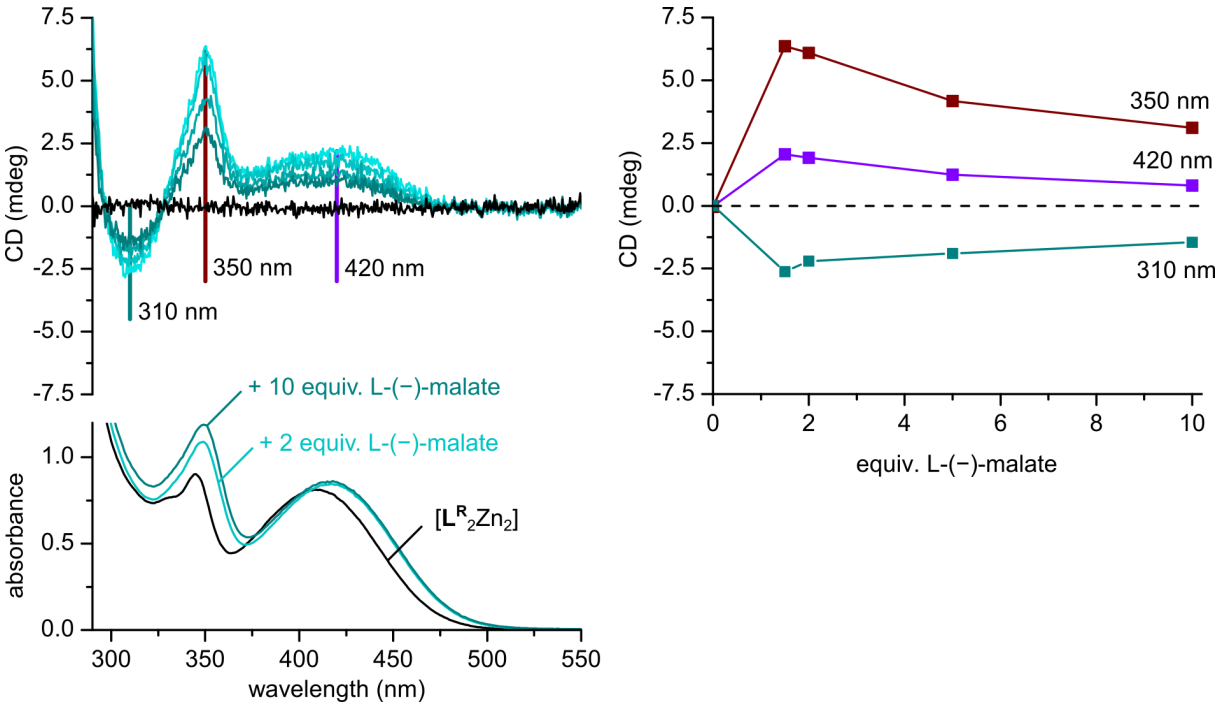

Figure 3.43 CD and UV-Vis spectra of titration of $[\mathbf{L^R}_2Zn_2]$ (500 µM, DMSO-d_6, l = 2 mm) with L-(−)-malate as TBA salts. CD spectra recorded after addition of 0, 1.5, 2, 5, and 10 equivalents of **L-ML**$^{2-}$.

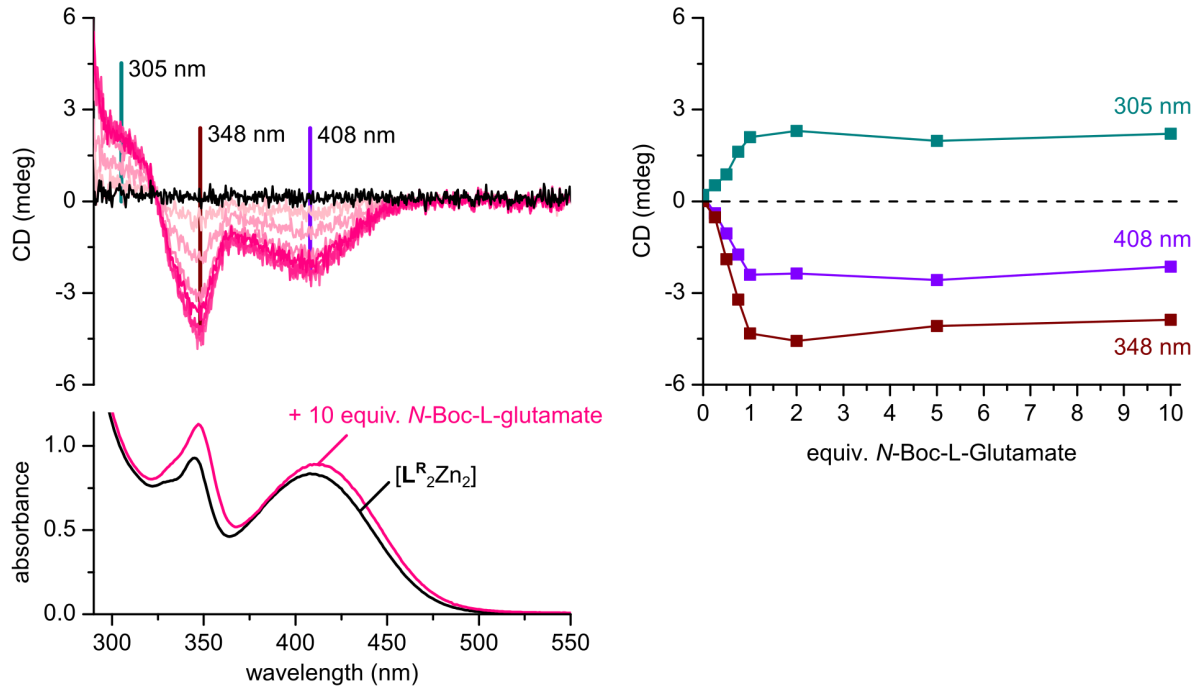

Figure 3.44 CD and UV-Vis spectra of titration of $[\mathbf{L^R}_2Zn_2]$ (500 µM, DMSO-d_6, l = 2 mm) with *N*-Boc-L-glutamate as TBA salts. CD spectra recorded after addition of 0, 0.25, 0.5, 0.75, 1, 2, 5, and 10 equivalents of $\mathbf{L\text{-}BGlu^{2-}}$.

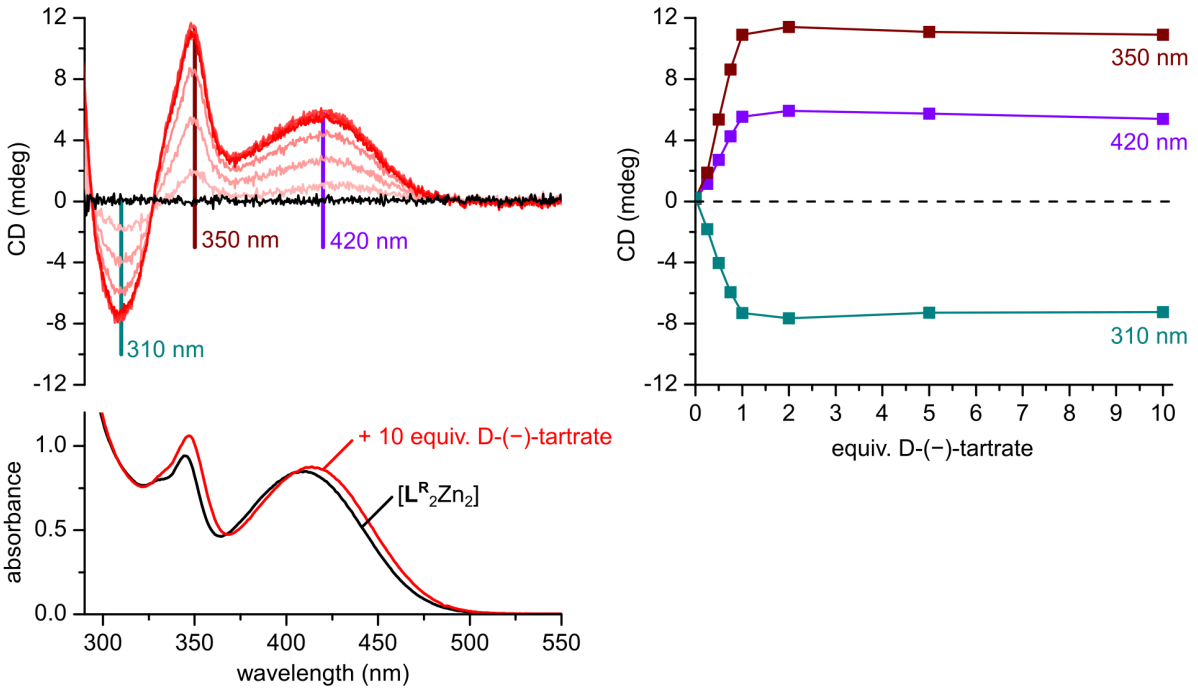

Figure 3.45 CD and UV-Vis spectra of titration of $[\mathbf{L^R}_2Zn_2]$ (500 µM, DMSO-d_6, l = 2 mm) with D-(−)-tartrate as TBA salts. CD spectra recorded after addition of 0, 0.25, 0.5, 0.75, 1, 2, 5, and 10 equivalents of $\mathbf{D\text{-}TA^{2-}}$.

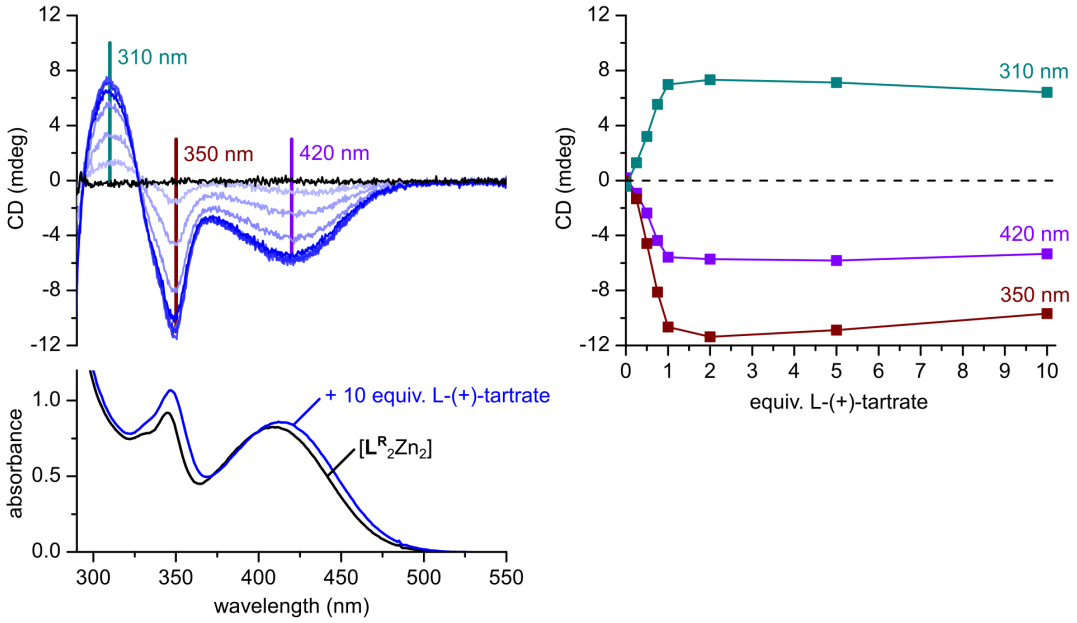

Figure 3.46 CD and UV-Vis spectra of titration of $[\mathbf{L^R}_2Zn_2]$ (500 µM, DMSO-d_6, l = 2 mm) with L-(+)-tartrate as TBA salts. CD spectra recorded after addition of 0, 0.25, 0.5, 0.75, 1, 2, 5, and 10 equivalents of $\mathbf{L\text{-}TA^{2-}}$.

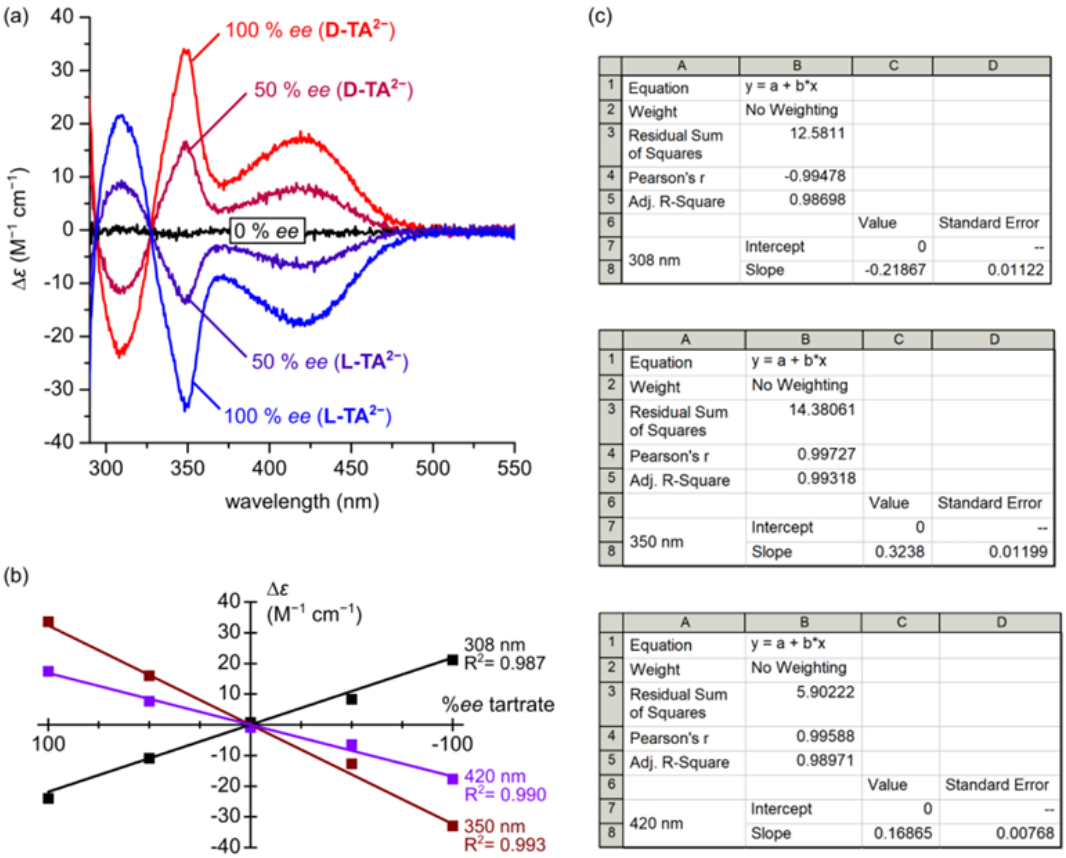

(c)

	A	B	C	D
1	Equation	y = a + b*x		
2	Weight	No Weighting		
3	Residual Sum of Squares	12.5811		
4	Pearson's r	-0.99478		
5	Adj. R-Square	0.98698		
6			Value	Standard Error
7	308 nm	Intercept	0	--
8		Slope	-0.21867	0.01122

	A	B	C	D
1	Equation	y = a + b*x		
2	Weight	No Weighting		
3	Residual Sum of Squares	14.38061		
4	Pearson's r	0.99727		
5	Adj. R-Square	0.99318		
6			Value	Standard Error
7	350 nm	Intercept	0	--
8		Slope	0.3238	0.01199

	A	B	C	D
1	Equation	y = a + b*x		
2	Weight	No Weighting		
3	Residual Sum of Squares	5.90222		
4	Pearson's r	0.99588		
5	Adj. R-Square	0.98971		
6			Value	Standard Error
7	420 nm	Intercept	0	--
8		Slope	0.16865	0.00768

Figure 3.47 Chirality analysis for D-(−)- and L-(+)-tartrate with CD spectroscopy. (a) CD spectra measured for five different enantiomeric excess (*ee*) values. b) Linear dependence of the CD effect on *ee*. c) Linear equations determined for the corresponding data sets.

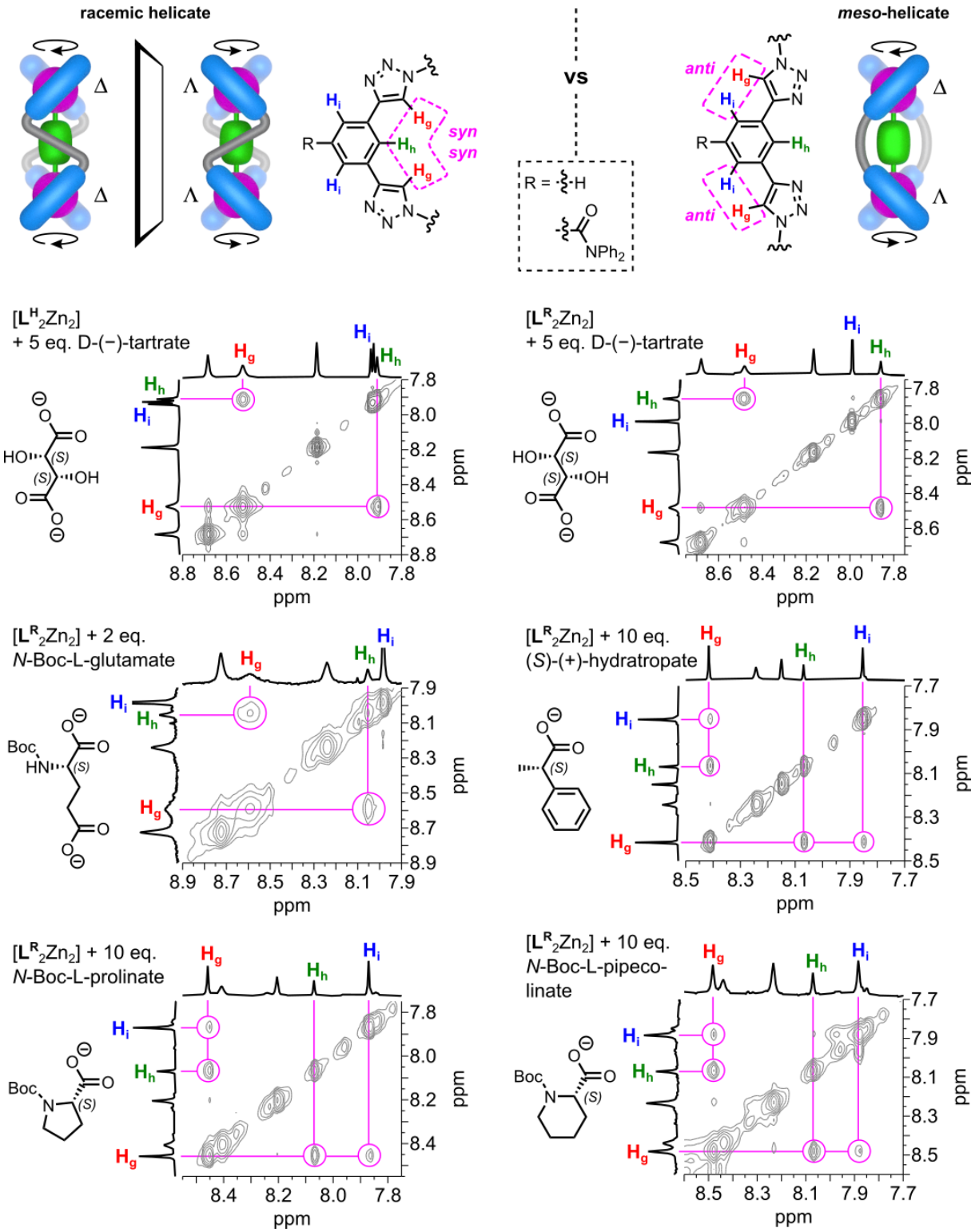

Figure 3.48 NOESY spectra (500 µM, DMSO-d_6, 298 K) of the complexes [(**D-TA**)@$\mathbf{L^R}_2Zn_2]^{2-}$, [(**D-TA**)@$\mathbf{L^H}_2Zn_2]^{2-}$, and [(**L-BGlu**)@$\mathbf{L^R}_2Zn_2]^{2-}$, together with examples exhibiting fast-exchange 1:2 binding behavior ([$\mathbf{L^R}_2Zn_2$] with ***S*-HT**$^-$, **L-BPro**$^-$, and **L-BPip**$^-$).

3.4.6 ESI-MS Spectra

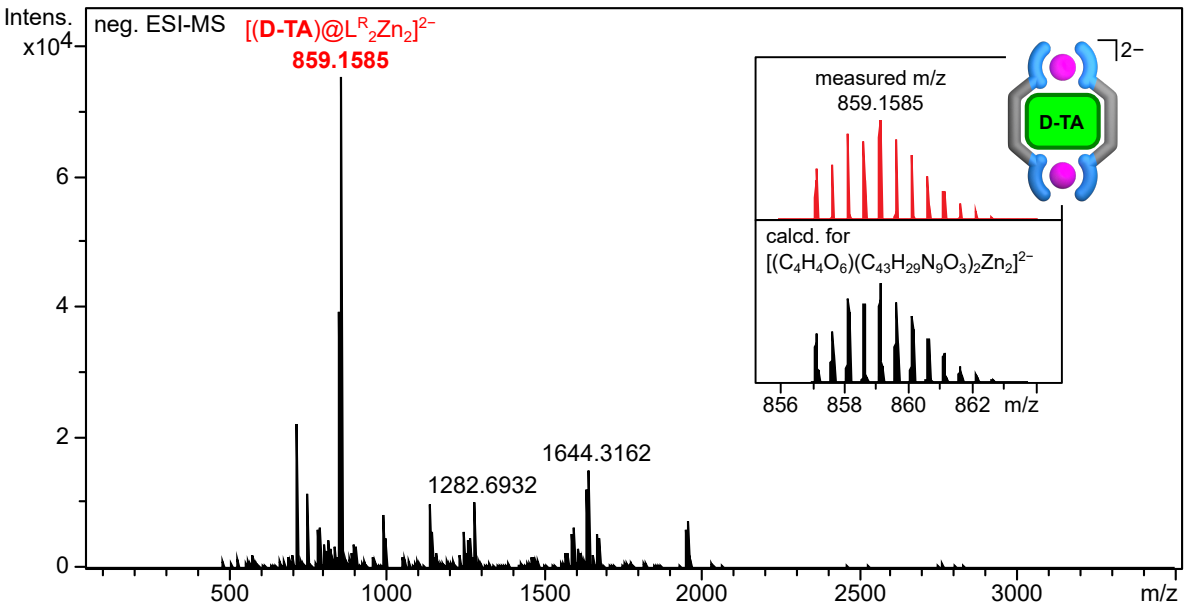

Figure 3.49 Negative ESI-MS spectrum (DMSO/MeCN 1:9) of $[\mathbf{L^R}_2Zn_2]$ with D-(−)-tartrate. The spectrum reveals the 1:1 complex $[(\mathbf{D\text{-}TA})@\mathbf{L^R}_2Zn_2]^{2-}$, consistent with the results from NMR, CD, and ITC studies.

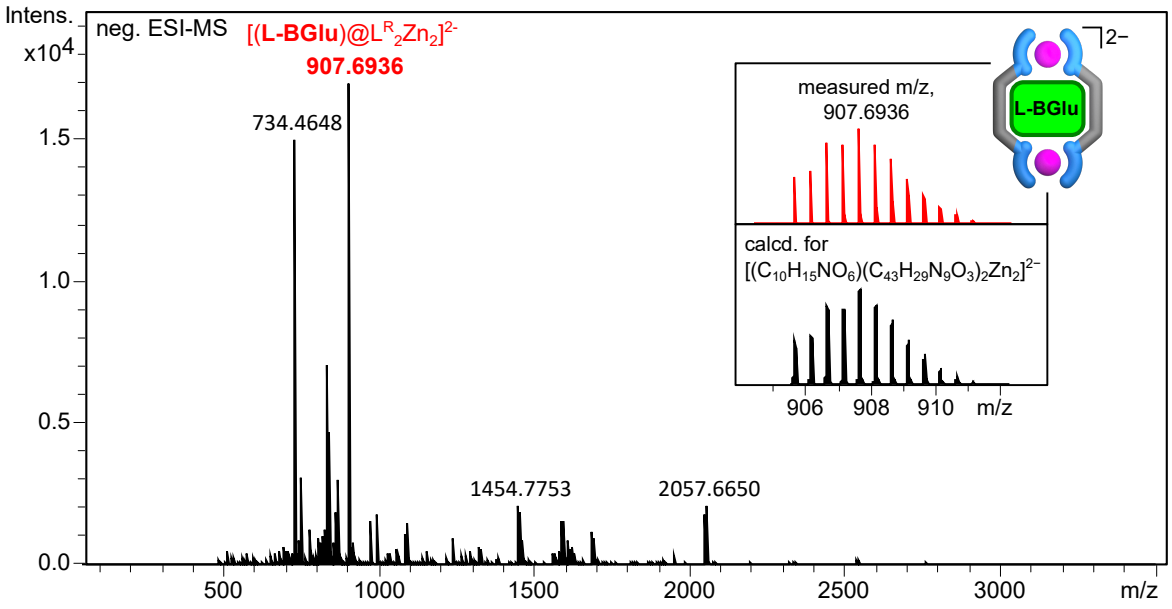

Figure 3.50 Negative ESI-MS spectrum (DMSO/MeCN 1:9) of $[\mathbf{L^R}_2Zn_2]$ with *N*-Boc-L-glutamate. The spectrum reveals the 1:1 complex $[(\mathbf{L\text{-}BGlu})@\mathbf{L^R}_2Zn_2]^{2-}$, consistent with the results from NMR and CD studies.

3.5 References

[1] M. G. Kalarikkal, C. Drechsler, G. Tusha, L. V. Schäfer, D. Van Craen, *Chemistry – A European Journal* **2023**, *29*, e202301613.

[2] P. Niedbała, K. Dąbrowa, S. Wasiłek, J. Jurczak, *Molecules* **2021**, *26*.

[3] L. A. Joyce, M. S. Maynor, J. M. Dragna, G. M. da Cruz, V. M. Lynch, J. W. Canary, E. V. Anslyn, *Journal of the American Chemical Society* **2011**, *133*, 13746–13752.

[4] L. A. Joyce, J. W. Canary, E. V. Anslyn, *Chemistry–A European Journal* **2012**, *18*, 8064–8069.

[5] Y. Tsunoda, K. Fukuta, T. Imamura, R. Sekiya, T. Furuyama, N. Kobayashi, T. Haino, *Angewandte Chemie* **2014**, *126*, 7371–7375.

[6] P. Howlader, S. Mondal, S. Ahmed, P. S. Mukherjee, *Journal of the American Chemical Society* **2020**, *142*, 20968–20972.

[7] G. Wu, Y. Chen, S. Fang, L. Tong, L. Shen, C. Ge, Y. Pan, X. Shi, H. Li, *Angewandte Chemie International Edition* **2021**, *60*, 16594–16599.

[8] I. Regeni, B. Chen, M. Frank, A. Baksi, J. J. Holstein, G. H. Clever, *Angewandte Chemie International Edition* **2021**, *60*, 5673–5678.

[9] M. M. Wootten, B. A. Le Bailly, S. Tshepelevitsh, I. Leito, J. Clayden, *Chemical Science* **2022**, *13*, 2258–2269.

[10] J. W. Canary, S. Mortezaei, J. Liang, *Coordination Chemistry Reviews* **2010**, *254*, 2249–2266.

[11] K. W. Bentley, Y. G. Nam, J. M. Murphy, C. Wolf, *Journal of the American Chemical Society* **2013**, *135*, 18052–18055.

[12] E. Badetti, K. Wurst, G. Licini, C. Zonta, *Chemistry–A European Journal* **2016**, *22*, 6515–6518.

[13] P. Zardi, K. Wurst, G. Licini, C. Zonta, *Journal of the American Chemical Society* **2017**, *139*, 15616–15619.

[14] R. Penasa, F. Begato, G. Licini, K. Wurst, S. Abbate, G. Longhi, C. Zonta, *Chemical Communications* **2023**, *59*, 6714–6717.

[15] S. R. Moor, J. R. Howard, B. T. Herrera, M. S. McVeigh, F. Marini, A. T. Keatinge-Clay, E. V. Anslyn, *Organic Chemistry Frontiers* **2023**, *10*, 1386–1392.

[16] Z.-M. Shi, S.-G. Chen, X. Zhao, X.-K. Jiang, Z.-T. Li, *Organic & Biomolecular Chemistry* **2011**, *9*, 8122–8129.

[17] A. Zeus, G. Yusin, C. Wolf, *Tetrahedron* **2019**, *75*, 1504–1509.

[18] M. J. Kim, Y. R. Choi, H.-G. Jeon, P. Kang, M.-G. Choi, K.-S. Jeong, *Chemical Communications* **2013**, *49*, 11412–11414.

[19] Y. Chen, L. Fu, B. Sun, C. Qian, R. Wang, J. Jiang, C. Lin, J. Ma, L. Wang, *Organic Letters* **2020**, *22*, 2266–2270.

[20] J. Ji, Y. Li, C. Xiao, G. Cheng, K. Luo, Q. Gong, D. Zhou, J. J. Chruma, W. Wu, C. Yang, *Chemical Communications* **2020**, *56*, 161–164.

[21] Y. Chen, B. Sun, H. Feng, R. Wang, M. Cheng, P. Wang, Z. Zhou, J. Jiang, L. Wang, *Chemistry–A European Journal* **2021**, *27*, 12305–12309.

[22] Y. Chen, B. Sun, R. Wang, C. Shi, M. Cheng, J. Jiang, C. Lin, L. Wang, *Organic Letters* **2021**, *23*, 7423–7427.

[23] Y. Chen, L. Fu, B. Sun, C. Qian, S. Pangannaya, H. Zhu, J. Ma, J. Jiang, Z. Ni, R. Wang, *Chemistry–A European Journal* **2021**, *27*, 5890–5896.

[24] F. Begato, R. Penasa, G. Licini, C. Zonta, *ACS sensors* **2022**, *7*, 1390–1394.

[25] D. Van Craen, M. G. Kalarikkal, J. J. Holstein, *Journal of the American Chemical Society* **2022**, *144*, 18135–18143.

[26] F. Cui, S. Li, C. Jia, J. S. Mathieson, L. Cronin, X.-J. Yang, B. Wu, *Inorganic Chemistry* **2012**, *51*, 179–187.

[27] S. Grimme, A. Hansen, S. Ehlert, J.-M. Mewes, *The Journal of Chemical Physics* **2021**, *154*.

[28] F. Neese, *WIREs Comput. Mol. Sci.* **2012**, *2*, 73–78.

[29] F. Neese, *WIREs Comput. Mol. Sci.* **2022**, *12*, e1606.

[30] M. J. Frisch, G. W. Trucks, H. B. Schlegel, G. E. Scuseria, M. A. Robb, J. R. Cheeseman, G. Scalmani, V. Barone, G. A. Petersson, H. Nakatsuji, X. Li, M. Caricato, A. V. Marenich, J. Bloino, B. G. Janesko, R. Gomperts, B. Mennucci, H. P. Hratchian, J. V. Ortiz, A. F. Izmaylov, J. L. Sonnenberg, F. Williams, F. Ding, F. Lipparini, F. Egidi, J. Goings, B. Peng, A. Petrone, T. Henderson, D. Ranasinghe, V. G. Zakrzewski, J. Gao, N. Rega, G. Zheng, W. Liang, M. Hada, M. Ehara, K. Toyota, R. Fukuda, J. Hasegawa, M. Ishida, T. Nakajima, Y. Honda, O. Kitao, H. Nakai, T. Vreven, K. Throssell, J. A. J. Montgomery, J. E. Peralta, F. Ogliaro, M. J. Bearpark, J. J. Heyd, E. N. Brothers, K. N. Kudin, V. N. Staroverov, T. A. Keith, R. Kobayashi, J. Normand, K. Raghavachari, A. P. Rendell, J. C. Burant, S. S. Iyengar, J. Tomasi, M. Cossi, J. M. Millam, M. Klene, C. Adamo, R. Cammi, J. W. Ochterski, R. L. Martin, K. Morokuma, O. Farkas, J. B. Foresman, D. J. Fox, Gaussian 16 Revision B.01, Gaussian, Inc., Wallingford CT, **2016**.

[31] A. D. Becke, *Journal of chemical Physics* **1993**, *98*, 1372–1377.

[32] F. Weigend, R. Ahlrichs, *Physical Chemistry Chemical Physics* **2005**, *7*, 3297–3305.

[33] F. Weigend, *Physical chemistry chemical physics* **2006**, *8*, 1057–1065.

[34] V. Barone, M. Cossi, *The Journal of Physical Chemistry A* **1998**, *102*, 1995–2001.

[35] Y.-S. Lin, G.-D. Li, S.-P. Mao, J.-D. Chai, *Journal of Chemical Theory and Computation* **2013**, *9*, 263–272.

[36] http://supramolecular.org/ (visited on 12/30/2022).

[37] P. Thordarson, *Chemical Society Reviews* **2011**, *40*, 1305–1323.

[38] D. B. Hibbert, P. Thordarson, *Chemical Communications* **2016**, *52*, 12792–12805.

[39] K. Hirose in *Analytical Methods in Supramolecular Chemistry*, (Ed.: C. A. Schalley), Wiley-VCH, Weinheim, **2012**, pp. 27–66.

[40] E. G. Sheetz, D. V. Craen, A. H. Flood in *Anion-Binding Catalysis*, (Ed.: O. G. Mancheño), Wiley-VCH, Weinheim, **2022**, pp. 79–109.

[41] P. Belser, S. Bernhard, U. Guerig, *Tetrahedron* **1996**, *52*, 2937–2944.

[42] E. Ziegler, G. Haberhauer, **2009**.

4 STIMULI-RESPONSIVE REVERSIBLE GUEST EXCHANGE CYCLES IN A CHARGE-NEUTRAL METAL HELICATE

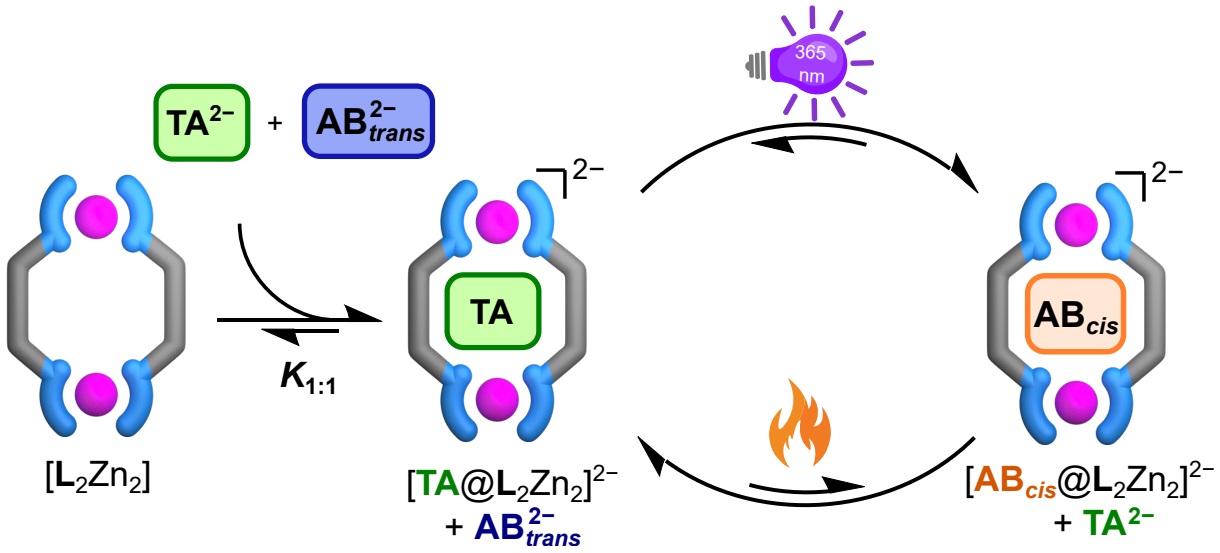

*This chapter is based on a manuscript currently under preparation for publication.

4.1 Introduction

As previously established, the self-assembled, charge-neutral zinc-based metal containers developed by our group exhibit a significant affinity for dianions, with a particular emphasis on dicarboxylates. The previously reported $[\mathbf{L^R}_2Zn_2]$ helicate has demonstrated successful encapsulation of both chiral and non-chiral dicarboxylates, even imparting chirality to the helicate in the former case and thereby extending the receptor's applicability.[1,2] Despite the demonstrated competence of our system in anion recognition, a primary limitation arises from the coordinative interaction between the bound guest and the metal center. This interaction, while beneficial in terms of providing high binding constants and facilitating highly sensitive nano-molar level recognition for carboxylates, creates difficulty in the dissociation of the guest from the system. The helicate's pronounced size-selectivity towards various guests, a potentially advantageous trait for various applications, is hampered by the inability to achieve controlled guest release within the coordination framework.

Achieving controlled guest exchange has gathered significant attention within supramolecular systems.[3–7] Commonly, this is achieved through modifications of the host structure to facilitate guest release and uptake, typically under external stimuli.[8–12] Nevertheless, one of the primary challenges remains in manipulating guest exchange while preserving the host's structure and intrinsic properties. A predominant approach to addressing this issue involves utilizing a stimuli-responsive guest capable of undergoing geometric transformations under specific conditions, thereby allowing the retention of the host while enabling the interchange of the guest and using it as a gateway for the release and uptake of a second guest.[13–16]

Light is the preferred stimulus due to its non-invasive nature, rapid addressability, and compatibility with *in situ* monitoring. Photoswitchable moieties, including spiropyrans[17], dihydropyrene[18], arylpyrazoles[19], stilbene[20,21], and azobenzene[14,22–25], as guests, have demonstrated their efficacy in advancing the prospect of reversible guest release and uptake. Azobenzene, in particular, is a prominent photochromic compound capable of transitioning between its *cis* and *trans* isomeric states in response to light or thermal stimuli. It isomerizes mainly by two ways: (i) rotation about the N=N bond and (ii) in-plane inversion at one nitrogen center.[26] (Figure 4.1) Quantum-chemical calculations place the *trans* isomer lower in energy than the *cis* isomer by $\sim 12\ \mathrm{kcal\,mol^{-1}}$[27,28], so in the dark at room temperature, the equilibrium strongly favors *trans*. Upon UV excitation ($\lambda \approx 320$–365 nm), efficient *trans*→*cis* photoisomerization proceeds via excited-state surface crossings; the reverse *cis*→*trans* process is driven by blue light ($\lambda \approx 400$–450 nm) or by thermal relaxation. The photochemical steps occur on ultrafast (typically picosecond) timescales, whereas thermal back-isomerization of *cis* spans milliseconds to days, depending on substitution, solvent, and temperature.[27]

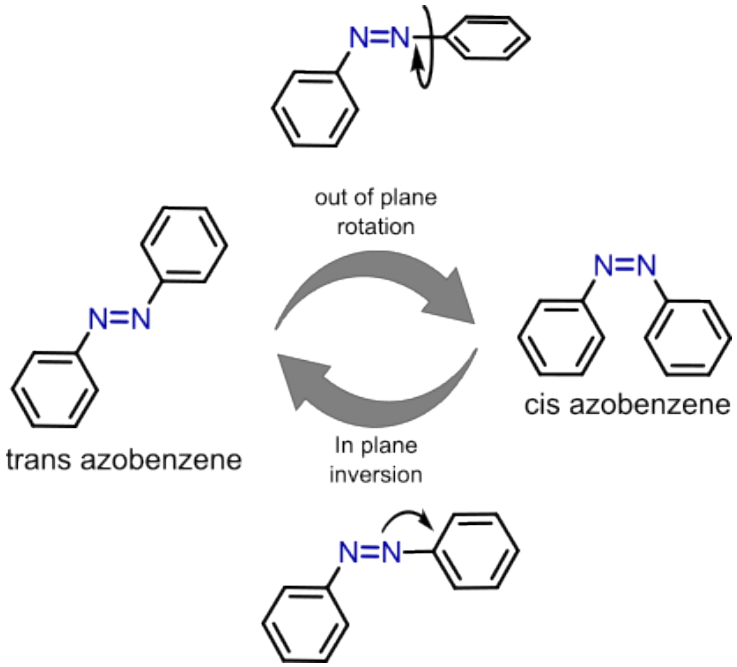

Figure 4.1 Azobenzene *trans-cis* photo-isomerization mechanism.

A variety of receptors incorporate azobenzene within their ligands to facilitate stimulus-responsive guest release.[29] Structural alterations to the azobenzene moiety can modify the extent of isomerization by influencing the photostationary states.[30,31] Instead of altering the ligand structure and risking the host's properties, we introduce a stimuli-responsive competitive guest that can replace the original guest when it switches states. In its alternative configuration, the competition is reversed, thereby enabling an exchange cycle to occur (Figure 4.2).

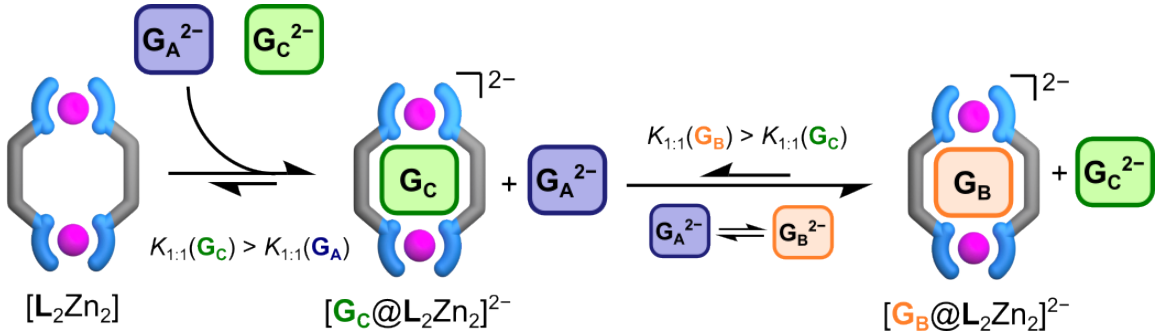

Figure 4.2 The working hypothesis for this project: A stimuli-responsive guest, when introduced to the system, supplants the originally bound guest. Upon reverting under specific stimuli, it is expected that the initially present guest subsequently restores the system into its original state.

Azobenzene-4,4'-dicarboxylate presents an ideal candidate, as our receptor is capable of exploiting its light- and temperature-responsive isomerization. Based on the size selectivity established in the previous study[1], the longer *trans* isomer (C-C distance ≈ 9.9 Å) is expected to be less favored than the shorter *cis* isomer (C-C distance ≈ 5.5 Å),[32] since

the optimal length for $[\mathbf{L^R}_2Zn_2]$ was determined to be around 8 Å in its most rigid form. The optimal fitting guest molecule was identified as naphthalene 2,6-dicarboxylate, and any molecule with a greater length encountered difficulties in accommodating within the binding pocket. Thus, the disparity in size between bent *cis* isomer and its extended *trans* form for azobenzene-4,4'-dicarboxylate, paired with photoisomerization, offers a means to modulate binding affinity by adjusting guest geometry. The selective binding among these isomers enables photo- and thermally induced guest exchange cycles in the presence of a second, non-photoactive guest. The prospect of potential stimuli-responsive controlled guest exchange will be further examined to assess its robustness and practicality with various carboxylate guests in the current chapter.

4.2 Results and discussion

4.2.1 Selective binding of photoswitchable isomers

For this study, we employed the same charge-neutral [$\mathbf{L^R}_2Zn_2$] helicate described in the previous chapter. The receptor was synthesized following the reported procedure in[1], with minor adaptations, as outlined in the previous chapter. Building on its established stability and anion recognition properties, we now explore its interaction with a photoswitchable dicarboxylate guest to achieve light-responsive binding and guest exchange. As a guest capable of interconverting between two distinct states that differ in length, azobenzene-4,4'-dicarboxylate ($\mathbf{AB^{2-}}$) was chosen for this study.

For conducting binding studies, the TBA salt of the thermally stable *trans*-azobenzene-4,4'-dicarboxylate ($\mathbf{AB^{2-}_{\boldsymbol{trans}}}$) was irradiated with 365 nm UV light under dark conditions to switch to the photostable *cis*-azobenzene-4,4'-dicarboxylate ($\mathbf{AB^{2-}_{\boldsymbol{cis}}}$) guest, resulting in a photostationary state characterized by a 10:90 *trans*:*cis* ratio (Figure 4.17). The reverse conversion from the *cis* to *trans* state was achieved either by heating at 100 °C or by irradiating with 455 nm UV light to obtain almost complete conversion with a 100:0 *trans*:*cis* ratio.

Individual ^{1}H NMR titrations were performed for the *cis* and *trans* isomers of azobenzene-4,4'-dicarboxylate with [$\mathbf{L^R}_2Zn_2$] helicate. The *cis* isomer $\mathbf{AB^{2-}_{\boldsymbol{cis}}}$ displayed a slow exchange regime on the NMR timescale, with a distinct set of signals observed for both the free and bound host simultaneously with the gradual addition of the guest (Figure 4.3). Saturation was reached upon the addition of one equiv, consistent with a 1:1 $[(\mathbf{AB_{\boldsymbol{cis}}})@\mathbf{L^R}_2Zn_2]^{2-}$ complexation. Notably, despite the presence of $\sim 10\%$ *trans* isomer in the photostationary mixture, only signals corresponding to the *cis*-bound helicate were observed, demonstrating the strong preference of the receptor for $\mathbf{AB^{2-}_{\boldsymbol{cis}}}$. Refer to the complete titration depicted in Figure 4.18.

In contrast, titration with the *trans* isomer was characterized by intermediate exchange, resulting in the broadening and shifting of signals, along with the appearance of additional signals (Figure 4.4). The data were less straightforward to interpret at one equivalent guest due to the presence of multiple species detected in the NMR spectra. This observation has led to the hypothesis of aggregate formation, as the guest molecule does not fit well within the host structure. Furthermore, at higher equivalents, when the *cis* isomer was present, even at low levels in the guest mixture, the signals corresponding to the *trans*-bound host were replaced by those of the *cis*-bound complex, further confirming the receptor's strong selectivity for $\mathbf{AB^{2-}_{\boldsymbol{cis}}}$. As neither the intermediate nor the slow exchange titrations are suitable for calculating binding constants, isothermal titration calorimetry (ITC) measurements were performed for this purpose. ITC experiments were exclusively

performed with $\mathbf{AB}^{\mathbf{2-}}_{cis}$, as $\mathbf{AB}^{\mathbf{2-}}_{trans}$ did not exhibit clear binding dynamics. The resultant association constant for $\mathbf{AB}^{\mathbf{2-}}_{cis}$ was $K_{1:1} = 306000\,\mathrm{M}^{-1}$ ($\log K_{1:1} = 5.49$) (Figure 4.19), which aligns with the expected range, taking the length of the guest into account.

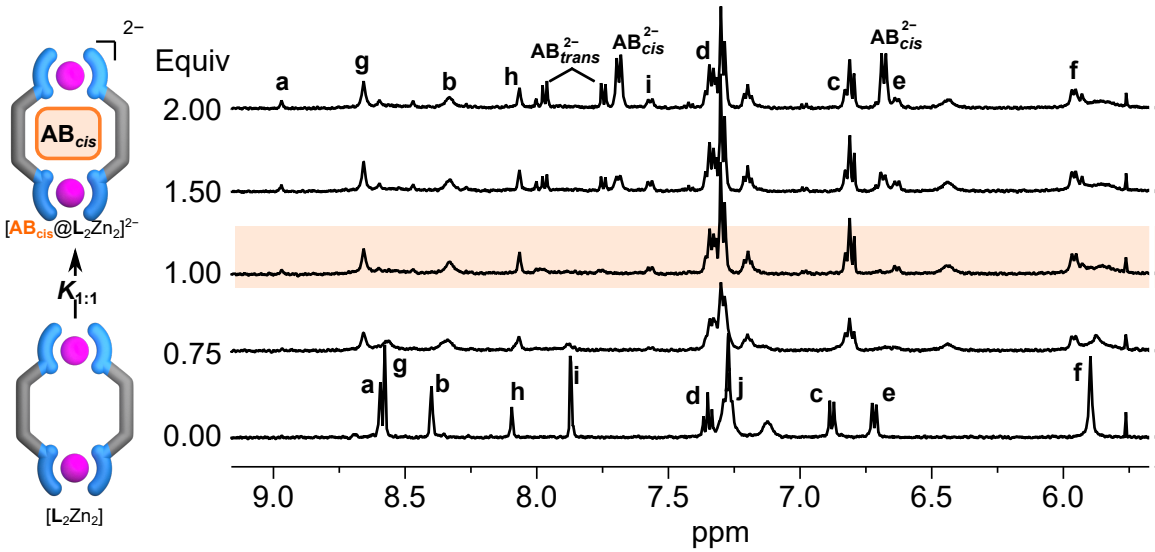

Figure 4.3 ^{1}H NMR (500 µM, 500 MHz, DMSO – d_6, 298 K) of $[\mathbf{L^R}_2\mathrm{Zn}_2]$ with *cis*-azobenzene-4,4'-dicarboxylate $\mathbf{AB}^{\mathbf{2-}}_{cis}$ as TBA salt. The titration data with growing host-guest signals along with loss of free host signals indicates a slow exchange process on the NMR time scale and the formation of 1:1 host-guest complex. Refer to the complete titration depicted in Figure 4.18.

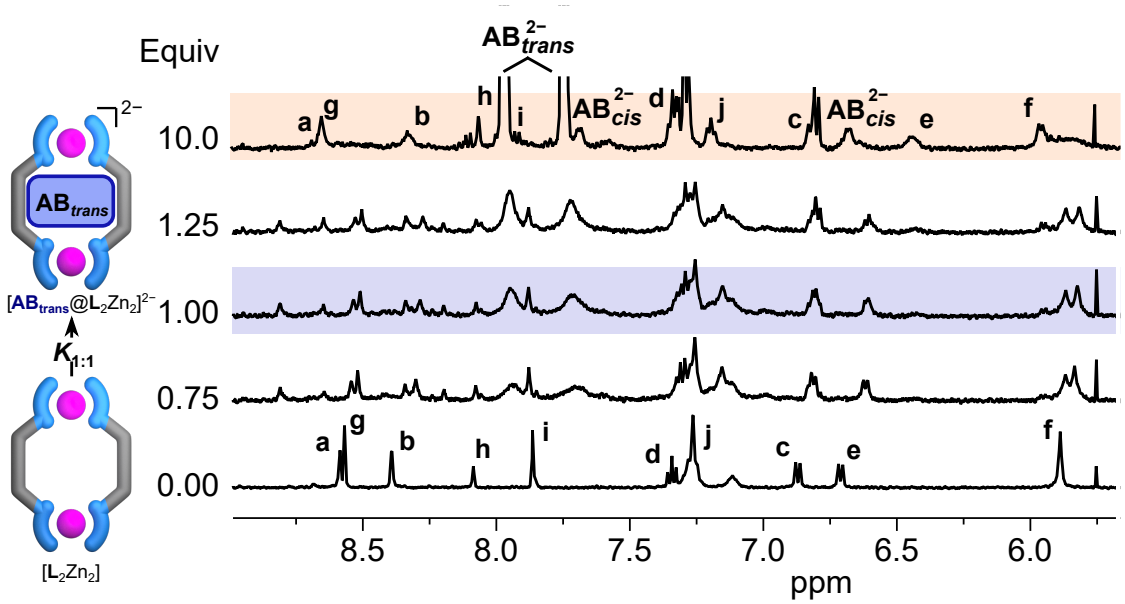

Figure 4.4 ^{1}H NMR (500 µM, 500 MHz, DMSO – d_6, 298 K) of $[\mathbf{L^R}_2\mathrm{Zn}_2]$ with *trans*-azobenzene-4,4'-dicarboxylate $\mathbf{AB}^{\mathbf{2-}}_{trans}$ as TBA salt. The titration data is less straightforward to interpret showing intermediate exchange on the NMR time scale. Refer to the complete titration depicted in Figure 4.20.

It has been determined that D-(−)-tartrate ($\mathbf{D\text{-}TA}^{\mathbf{2-}}$) exhibits a significant affinity for the helicate under investigation, as established by a binding constant of $K_{1:1} = 174000$ M^{-1} ($\log K_{1:1} = 5.24$), as elucidated in the previous chapter. This affinity lies between that

of the *cis* and *trans* isomers of the photoswitchable guest as the *trans* isomer is anticipated to exhibit significantly reduced binding affinity. Consequently, in the presence of $\mathbf{AB}^{\mathbf{2-}}_{trans}$, tartrate is expected to displace the bound *trans* isomer. Upon irradiation, however, the formation of $\mathbf{AB}^{\mathbf{2-}}_{cis}$ in the solution, which binds more strongly than tartrate, should, in turn, displace the bound tartrate, thereby enabling a light-controlled, reversible guest exchange process.

The utilization of tartrate as a non-photoactive competitive agent in the competition experiments further confirmed the binding specificity of the helicate (Figure 4.5). When D-(−)-tartrate was added to a solution containing host and $\mathbf{AB}^{\mathbf{2-}}_{trans}$, the spectra evolved toward $[(\mathbf{D\text{-}TA})@\mathbf{L^R}_2Zn_2]^{2-}$, demonstrating that tartrate outcompetes $\mathbf{AB}^{\mathbf{2-}}_{trans}$. In contrast, the addition of $\mathbf{AB}^{\mathbf{2-}}_{cis}$ to $[(\mathbf{D\text{-}TA})@\mathbf{L^R}_2Zn_2]^{2-}$ resulted in the shifting of the signals toward $[(\mathbf{AB}_{cis})@\mathbf{L^R}_2Zn_2]^{2-}$, indicating the displacement of $\mathbf{D\text{-}TA}^{\mathbf{2-}}$ with lower affinity. Each specific species can be distinguished by their characteristic aromatic region, particularly through the splitting pattern that corresponds to the CH_2 proton (H_f) at $\sim 6.0 - 5.75$ ppm. The binding of $\mathbf{D\text{-}TA}^{\mathbf{2-}}$ is characterized by a distinctive quartet observed at 5.84 ppm. In contrast, the helicate bound with *cis* isomer displays a doublet splitting pattern. This signal provides a means to monitor the bound guest in comparison to others during the competition experiments.

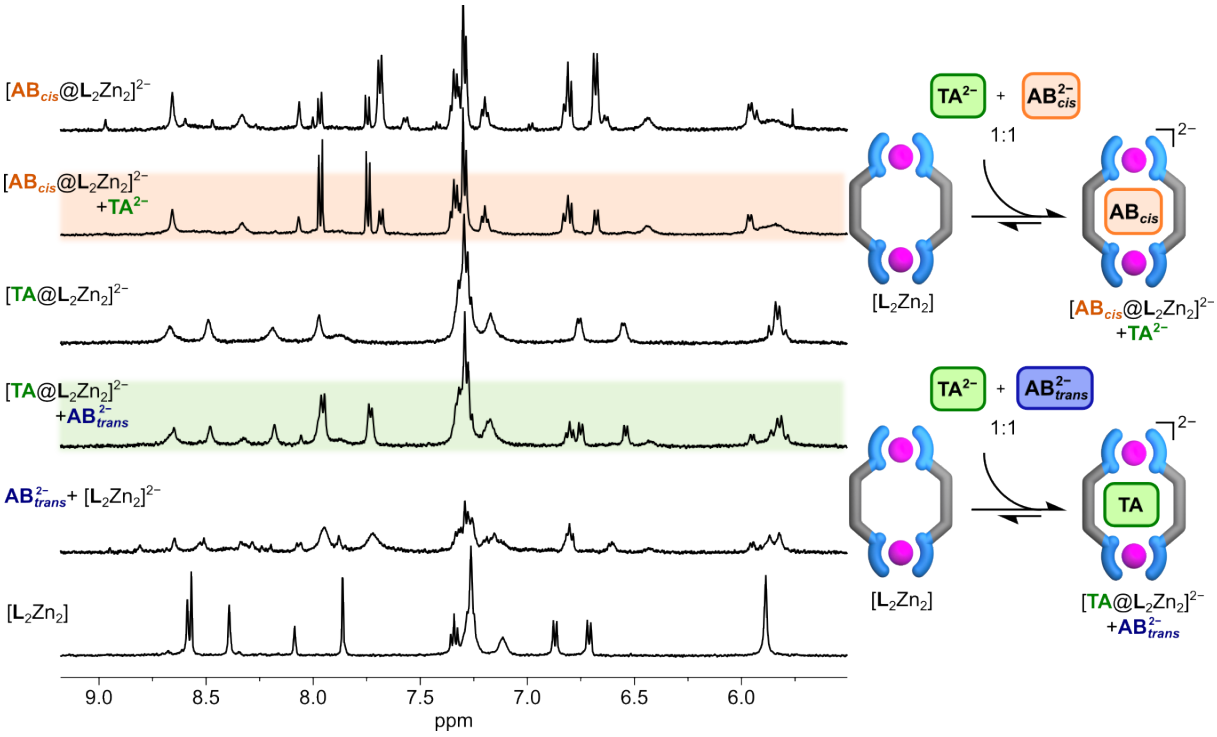

Figure 4.5 ^{1}H NMR competition experiments of $[\mathbf{L^R}_2Zn_2]$ with one equiv. of $\mathbf{AB}^{\mathbf{2-}}_{cis}$, $\mathbf{AB}^{\mathbf{2-}}_{trans}$, and $\mathbf{D\text{-}TA}^{\mathbf{2-}}$ each (500 µM ,500 MHz, DMSO − d_6, 298 K). The addition of $\mathbf{D\text{-}TA}^{\mathbf{2-}}$ to a solution containing the host with $\mathbf{AB}^{\mathbf{2-}}_{trans}$ leads to a spectral transformation into that of the tartrate-bound complex. Whereas the addition of $\mathbf{AB}^{\mathbf{2-}}_{cis}$ to $[(\mathbf{D\text{-}TA})@\mathbf{L^R}_2Zn_2]^{2-}$ results in a spectral shift indicative of the *cis*-bound complex. Each host-guest complex species is distinguished by its unique NMR splitting pattern.

4.2.2 Stabilization of the photostationary state of *cis*-azobenzene-4,4'-dicarboxylate

Mild conditions: Room temperature and ambient visible light

To evaluate whether encapsulation within the helicate influences the thermal or photochemical stability of the *cis* isomer, the photostationary mixture of *cis*-azobenzene-4,4'-dicarboxylate ($\mathbf{AB}^{\mathbf{2-}}_{\boldsymbol{cis}}$) was monitored by ^{1}H NMR spectroscopy over several days at room temperature under ambient visible light (Figure 4.6). In the absence of the host, the free metastable $\mathbf{AB}^{\mathbf{2-}}_{\boldsymbol{cis}}$ gradually reverted to the thermodynamically stable *trans* isomer, with a *cis*:*trans* ratio of 13:87 after three days. In contrast, when $\mathbf{AB}^{\mathbf{2-}}_{\boldsymbol{cis}}$ was bound inside $[\mathbf{L^R}_2\mathrm{Zn}_2]$, the signals corresponding to the host–guest complex $[(\mathbf{AB}_{\boldsymbol{cis}})@\mathbf{L^R}_2\mathrm{Zn}_2]^{2-}$ were preserved, although the excess unbound guest in solution reverted back to the same mixture of 13:87 *cis*:*trans* . This observation demonstrates that complexation within the helicate effectively stabilizes the bound *cis* isomer, preventing its relaxation to the *trans* form and locking the guest in its photoactivated state.

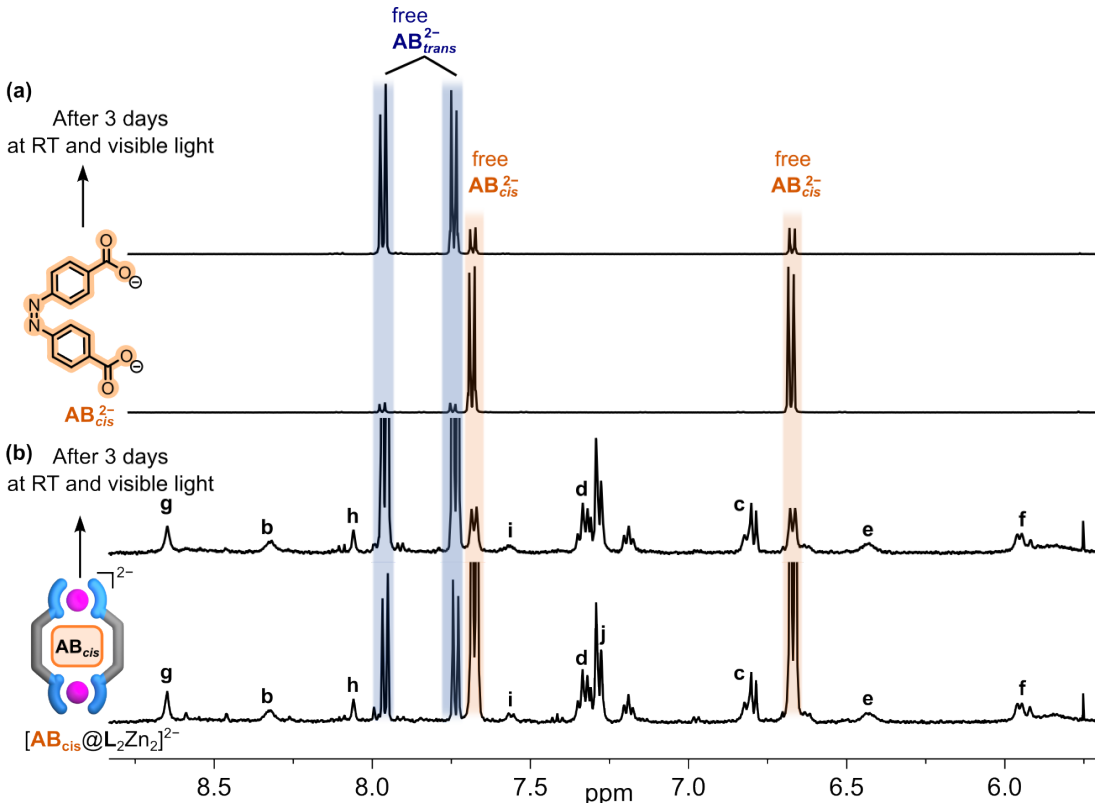

Figure 4.6 ^{1}H NMR spectra of the TBA salt of $\mathbf{AB}^{\mathbf{2-}}_{\boldsymbol{cis}}$ and of the host–guest complex $[(\mathbf{AB}_{\boldsymbol{cis}})@\mathbf{L^R}_2\mathrm{Zn}_2]^{2-}$ containing excess guest after three days at room temperature under ambient visible light (500 µM, 500 MHz, DMSO – d_6, 298 K). In the free guest solution, $\mathbf{AB}^{\mathbf{2-}}_{\boldsymbol{cis}}$ mostly reverted to $\mathbf{AB}^{\mathbf{2-}}_{\boldsymbol{trans}}$, resulting in a 13:87 *cis*:*trans* ratio. By contrast, the host–guest solution maintained the signals of $[(\mathbf{AB}_{\boldsymbol{cis}})@\mathbf{L^R}_2\mathrm{Zn}_2]^{2-}$, despite the excess guest converting back to *trans* in the same ratio.

This stabilization is likely a consequence of the steric and geometric constraints imposed by the helicate binding pocket. The helicate forces the shorter *cis* isomer to bind tightly, while the longer *trans* isomer does not fit well inside the host. Once the *cis* guest is accommodated inside the cavity, the rotational pathway around the central N=N bond required for the thermal *cis* to *trans* back isomerization becomes sterically hindered. In addition, strong coordinative host–guest interactions further lower the probability of relaxation. Together, these effects act to kinetically trap the *cis* isomer inside the host, even under conditions where the free guest readily reverts to *trans*.

To investigate the endurance of this stabilization, D-(−)-tartrate was introduced as a competitor alongside an excess of azobenzene-4,4'-dicarboxylate (four equiv. of $\mathbf{AB^{2-}}$ guest were added to account for the incomplete isomerization ratio). Even under these conditions and over ten days of monitoring by ^{1}H NMR at room temperature under ambient visible light, the characteristic signals of the *cis* complex remained unchanged (Figure 4.7 and the full picture with elaborated steps in Figure 4.27). Thus, the helicate not only 'locks' and stabilizes the metastable *cis* isomer but also resists displacement by tartrate.

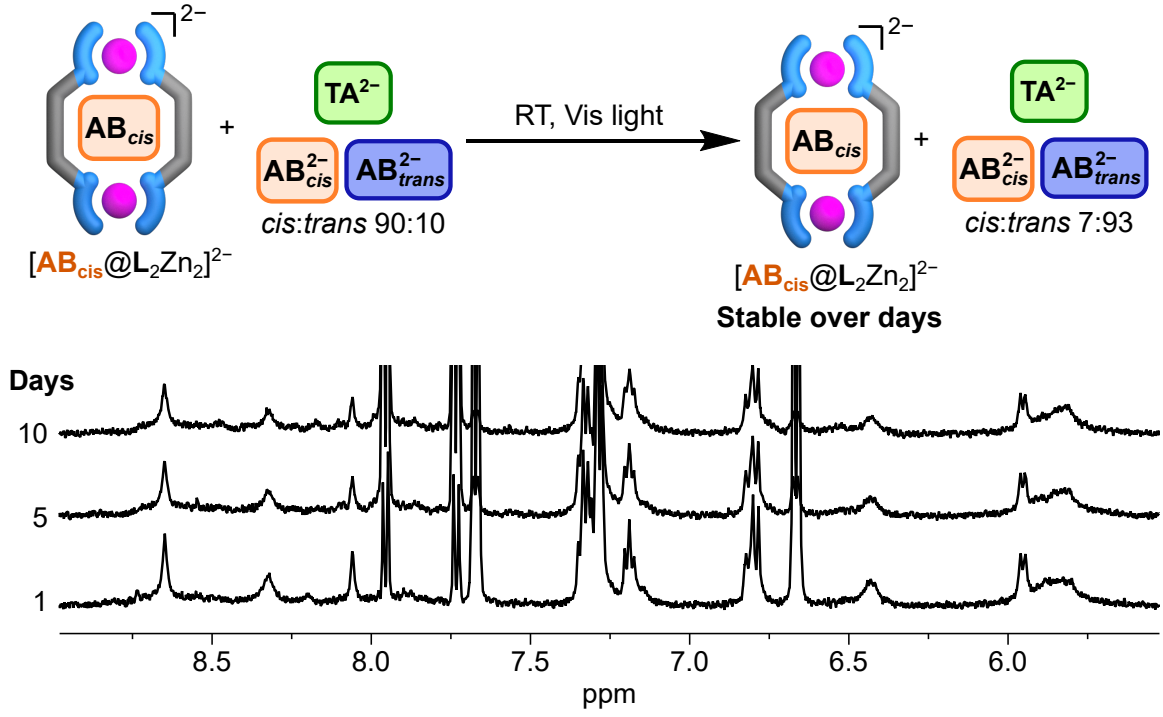

Figure 4.7 ^{1}H NMR spectra of $[(\mathbf{AB}_{cis})@\mathbf{L^R}_2Zn_2]^{2-}$ in the presence of $\mathbf{D\text{-}TA^{2-}}$ (2 equiv.) and excess $\mathbf{AB^{2-}_{cis}}$ (4 equiv.) recorded over 10 days under ambient visible light at room temperature (500 MHz, DMSO – d_6, 298 K). The signals corresponding to the *cis* complex remain unchanged over days, demonstrating that the helicate stabilizes the *cis* isomer even under competitive conditions. Refer to the elaborated steps depicted in complete Figure 4.27.

Irradiation at 455 nm

Under non-confined conditions, free *cis*-guest can revert to the thermodynamically stable *trans* form under mild conditions or upon irradiation with 455 nm light. The effect of

this on the bound-*cis* complex was examined by monitoring the ^{1}H NMR of a sample of $[(\mathbf{AB}_{\boldsymbol{cis}})@\mathbf{L^R}_2Zn_2]^{2-}$ containing 4 equiv. of $\mathbf{AB}^{\mathbf{2-}}_{\boldsymbol{cis}}$ and 2 equiv. of $\mathbf{D\text{-}TA}^{\mathbf{2-}}$ during continuous 455 nm irradiation (Figure 4.28). The excess free *cis* guest moved cleanly towards the *trans* isomer, reaching a 5:95 *cis*:*trans* ratio after 15 min, whereas the signals assigned to $[(\mathbf{AB}_{\boldsymbol{cis}})@\mathbf{L^R}_2Zn_2]^{2-}$ remained unchanged throughout this duration. Thus, the encapsulated *cis* isomer does not undergo detectable photoisomerization at 455 nm, while the unbound guest responds as expected. A comparable event was observed for the sample of $[(\mathbf{AB}_{\boldsymbol{cis}})@\mathbf{L^R}_2Zn_2]^{2-}$ in the absence of any competitive guest as well (Figure 4.29).

Temperature

Thermal relaxation is the most common way to convert *cis* isomer to *trans*. Variable-temperature ^{1}H NMR was used to test the influence of heating on the stabilization enforced for the encapsulated *cis* isomer. In the VT experiment, the sample is continuously heated during acquisition, and the spectra recorded at 50 °C (Figure 4.30) and 60 °C (Figure 4.31) were indistinguishable after cooling to 25 °C, compared to the initial spectrum. At higher temperatures, the chemical shifts for the complex exhibit noticeable alterations; however, they revert to the original pattern upon cooling. Despite these spectral variations, there is no detectable change in the concentration of species over time. Thus, no measurable conversion occurs up to 60 °C. Nonetheless, prolonged heating at 70 °C resulted in the emergence of new peaks, with the process reaching completion within 40 min, as evident in the spectra obtained after cooling down (Figure 4.32). The peaks corresponding to $[(\mathbf{AB}_{\boldsymbol{cis}})@\mathbf{L^R}_2Zn_2]^{2-}$ diminish, whereas those of $[(\mathbf{D\text{-}TA})@\mathbf{L^R}_2Zn_2]^{2-}$ appear.

A second experiment using an external heating block, equilibrating the sample for 10 min at each heating step, produced a relatable result (Figure 4.8). The $[(\mathbf{AB}_{\boldsymbol{cis}})@\mathbf{L^R}_2Zn_2]^{2-}$ signals remained unchanged up to $\sim$ 75 °C and were only completed at 100 °C with a shift to the $[(\mathbf{D\text{-}TA})@\mathbf{L^R}_2Zn_2]^{2-}$ complex (see Figure 4.33 for detailed steps). Simultaneously, in the absence of any competing guest, the $[(\mathbf{AB}_{\boldsymbol{cis}})@\mathbf{L^R}_2Zn_2]^{2-}$ only partially reverted to the *trans* guest form despite being subjected to 30 min of heating at 100 °C (Figure 4.11).

Collectively, these findings indicate that encapsulation significantly inhibits thermal back-isomerization. The free $\mathbf{AB}^{\mathbf{2-}}_{\boldsymbol{cis}}$ relaxes toward *trans* even at room temperature, whereas the bound-*cis* is kinetically trapped and only begins to switch after sustained heating at $\sim 70 - 80$ °C in a competing environment, as the presence of the unbound $\mathbf{D\text{-}TA}^{\mathbf{2-}}$ is crucial for the occupancy of the vacant site during isomerization, which subsequently fuels the displacement. Once the threshold is exceeded, the system relaxes to the expected low-energy state, releases $\mathbf{AB}^{\mathbf{2-}}_{\boldsymbol{trans}}$, and the host recaptures $\mathbf{D\text{-}TA}^{\mathbf{2-}}$, confirming that confinement and host–guest contacts raise the barrier for the *cis* to *trans* pathway inside the helicate.

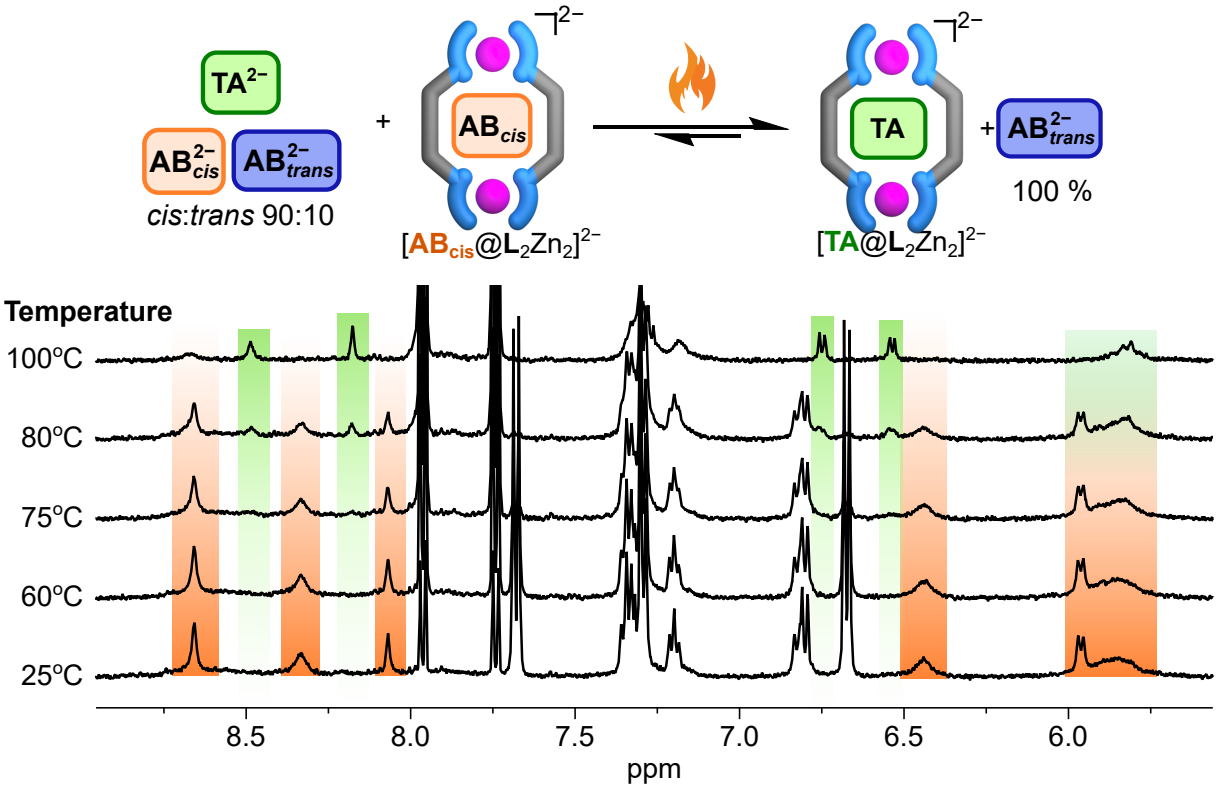

Figure 4.8 ^{1}H NMR spectra (500 µM ,500 MHz, DMSO–d_6, 298 K) of $[(\mathbf{AB}_{cis})@\mathbf{L^R}_2Zn_2]^{2-}$ in the presence of $\mathbf{D\text{-}TA^{2-}}$ (2 equiv.) and excess $\mathbf{AB}^{2-}_{cis}$ (4 equiv.) recorded at increasing temperature (25-100 °C). Sample was heated for 10 min at each step (increments 5-10 °C, full series in Figure 4.33). $[(\mathbf{AB}_{cis})@\mathbf{L^R}_2Zn_2]^{2-}$ is stable up to 80 °C and retains the bound $\mathbf{AB}^{2-}_{cis}$ without switching to $\mathbf{AB}^{2-}_{trans}$.

4.2.3 Light-Controlled Host–Guest Switching with Azobenzene-4,4'-dicarboxylate

To follow the light-driven guest exchange in real time, a pseudo-2D NMR experiment was performed by stacking ^{1}H spectra at fixed intervals, with the sample containing four equiv. of $\mathbf{AB}^{2-}_{trans}$ and two equiv. of $\mathbf{D\text{-}TA^{2-}}$ under continuous irradiation at 365 nm *in situ* in the NMR tube (Figure 4.9). Upon irradiation, $\mathbf{AB}^{2-}_{trans}$ photoisomerizes to $\mathbf{AB}^{2-}_{cis}$ and replaces $\mathbf{D\text{-}TA^{2-}}$ inside the host; accordingly, the intensity of the peaks shaded green, corresponding to $[(\mathbf{D\text{-}TA})@\mathbf{L^R}_2Zn_2]^{2-}$, decreases, while that of the orange peaks, corresponding to $[(\mathbf{AB}_{cis})@\mathbf{L^R}_2Zn_2]^{2-}$, increases.

Spectra were acquired every 15 seconds (see Figure 4.34 for detailed steps). Integrals of a few non-overlapping NMR signals were tracked over time, normalized, divided by proton count, and fitted with simple kinetic models in Bruker Dynamics Center software.[33–35] In agreement with the stacked NMR spectra, the curves corresponding to the tartrate-bound complex (green, a_1-a_3) show a monotonic decay, while those corresponding to the *cis*-bound complex (orange, b_1-b_3) grow to reach a plateau, resembling a first-order-like process. Both NMR and the fit show that the conversion is essentially complete in $\sim$ 5 min at 365

nm. The first-order rate constants calculated for the plotted peaks (Figure 4.37) yielded $k_{\mathrm{TA}} = 0.555 \pm 0.038$ min^{-1} and $k_{\mathrm{AB_{cis}}} = 0.580 \pm 0.016$ min^{-1} (mean $\pm \pm$ SD). A shared global fit of k across all six traces resulted in $k = 0.567 \pm 0.029$min^{-1}, corresponding to time constants $\tau = 1/k \approx 1.8$ min, which represent the time required to reach about 63% of the total change, and the time required for 95% conversion, $t_{95} \approx 3\tau \approx 5.4$min, in line with the plateau ~ 5 min in the stacked spectra.

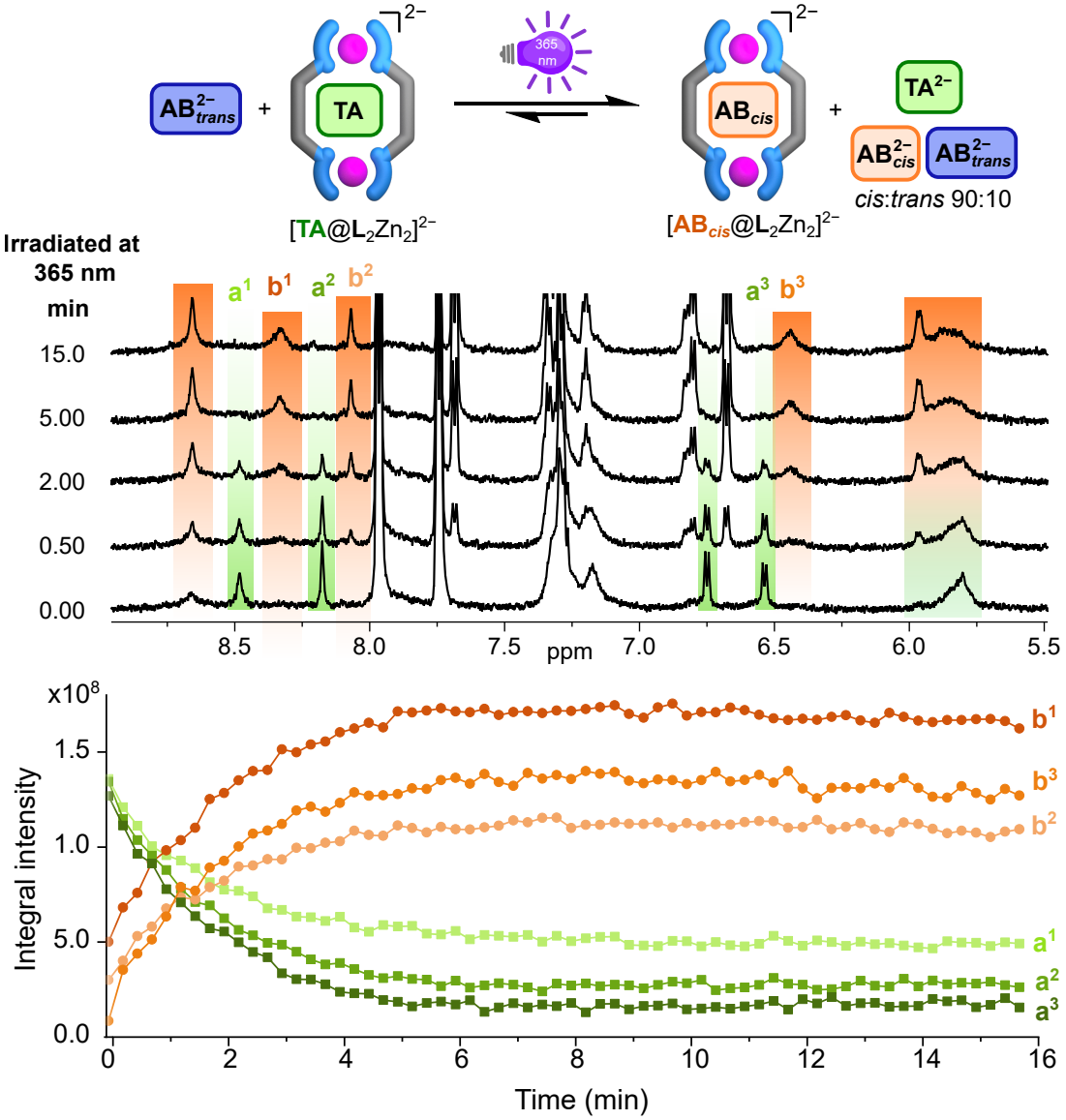

Figure 4.9 (top) ^{1}H NMR spectra recorded for the sample containing host with 4 equiv. $\mathbf{AB^{2-}_{\mathit{cis}}}$ and 2 equiv. $\mathbf{D\text{-}TA^{2-}}$, using pseudo-2D kinetics under continuous irradiation at 365 nm with *in situ* NMR illumination for 15 min (1 mM, 600 MHz, DMSO-d_6, 298 K). Highlighted signals show $[(\mathbf{D\text{-}TA})@\mathbf{L^R}_2\mathrm{Zn_2}]^{2-}$ complex (green) and $[(\mathbf{AB}_{\mathit{cis}})@\mathbf{L^R}_2\mathrm{Zn_2}]^{2-}$ complex (orange). (bottom) Calculated fit from pseudo-2D kinetics experiments plotted for the non-overlapping peaks. Green traces correspond to $[(\mathbf{D\text{-}TA})@\mathbf{L^R}_2\mathrm{Zn_2}]^{2-}$ decays, while orange traces corresponds to $[(\mathbf{AB}_{\mathit{cis}})@\mathbf{L^R}_2\mathrm{Zn_2}]^{2-}$ grow to reach a plateau after 5 min.

The same pseudo-2D series was acquired for $[\mathbf{L^R}_2\mathrm{Zn_2}]$ with azobenzene-4,4'-dicarboxylate alone (Figure 4.10). The time-stack and integral traces show a clean switch from the peaks corresponding to the mixture of $\mathbf{AB^{2-}_{\mathit{trans}}}$ and $[\mathbf{L^R}_2\mathrm{Zn_2}]$ (unknown assembly) to the

cis-bound complex $[(\mathbf{AB}_{cis})@\mathbf{L}^{\mathbf{R}}{}_2Zn_2]^{2-}$. Aligned with earlier observations, *trans*-bound signals decay monotonically, while *cis*-bound signals grow to a common plateau (see Figure 4.38 for detailed steps) consistent with a single, first-order-like process. Calculating the rate constants for the plotted peaks (Figure 4.42) gave $k = 0.425 \pm 0.006$ min^{-1} (mean ± SD), corresponding to $\tau = 1/k \approx 2.35$ min and $t_{95} \approx 3\tau \approx 7.05$ min, in agreement with the ~7 min needed to approach the plateau. The peaks corresponding to $\mathbf{AB}^{\mathbf{2-}}_{trans}$ containing the host-guest mixture undergoing decay were not used for the calculation because of the unknown assembly and non-quantitative complexation. Photoisomerization-driven switching of the azobenzene guest proceeds faster in the presence of tartrate than in its

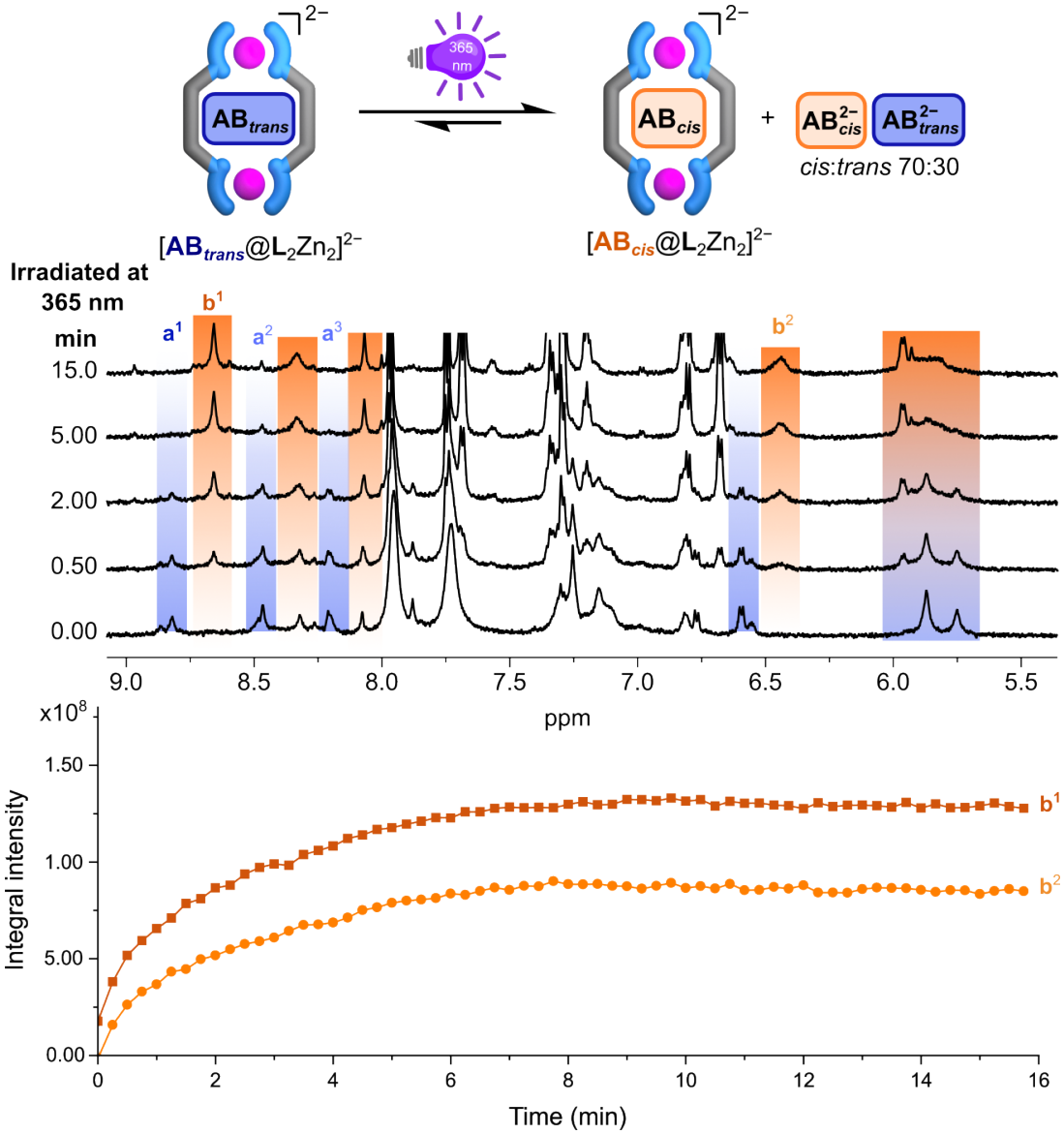

Figure 4.10 (top) ^{1}H NMR spectra recorded for the sample containing host with 2 equiv. $\mathbf{AB}^{\mathbf{2-}}_{cis}$, using pseudo-2D kinetics under continuous irradiation at 365 nm with *in situ* NMR illumination for 15 min (1 mM, 600 MHz, DMSO-d_6, 298 K). Highlighted signals show $[(\mathbf{AB}_{cis})@\mathbf{L}^{\mathbf{R}}{}_2Zn_2]^{2-}$ complex (orange). (bottom) Calculated fit from pseudo-2D kinetics experiment plotted for the non-overlapping peaks. Orange traces corresponds to $[(\mathbf{AB}_{cis})@\mathbf{L}^{\mathbf{R}}{}_2Zn_2]^{2-}$ grow to reach a plateau after 7 min. Peaks corresponding to $\mathbf{AB}^{\mathbf{2-}}_{trans}$ based host-guest assembly is excluded due to the presence of unknown mixture.

absence, with $k_{\mathrm{TA+AB}} = 0.567 \pm 0.029$ min^{-1} ($t_{95} \sim 5.4$ min) versus $k_{\mathrm{AB\ only}} = 0.425 \pm 0.020$ min^{-1} ($t_{95} \sim 7.05$ min). Thus, the AB-only process is comparatively slower, consistent with the reduced competitive driving force for displacement when no external guest is present.

4.2.4 Stimuli-responsive reversible guest-exchange cycle

In a non-competing environment with azobenzene dicarboxylate as the sole guest, a complete reversible cycle could not be produced. Irradiation at 365 nm converts $\mathbf{AB}^{\mathbf{2-}}_{trans}$ to the *cis* isomer and cleanly forms $[(\mathbf{AB}_{cis})@\mathbf{L}^{\mathbf{R}}{}_2\mathrm{Zn}_2]^{2-}$, but this step is noticeably slower than in the presence of a competitor. The reverse process is complicated, as 455 nm irradiation fails to regenerate the *trans*-bound complex, and even heating to 100 °C for 10–30 min yields only partial recovery. While free $\mathbf{AB}^{\mathbf{2-}}$ in solution relaxes toward *trans*, the *cis* isomer remains kinetically trapped inside the helicate, so most of the signal set still corresponds to $[(\mathbf{AB}_{cis})@\mathbf{L}^{\mathbf{R}}{}_2\mathrm{Zn}_2]^{2-}$ even after sustained heating (Figure 4.11).

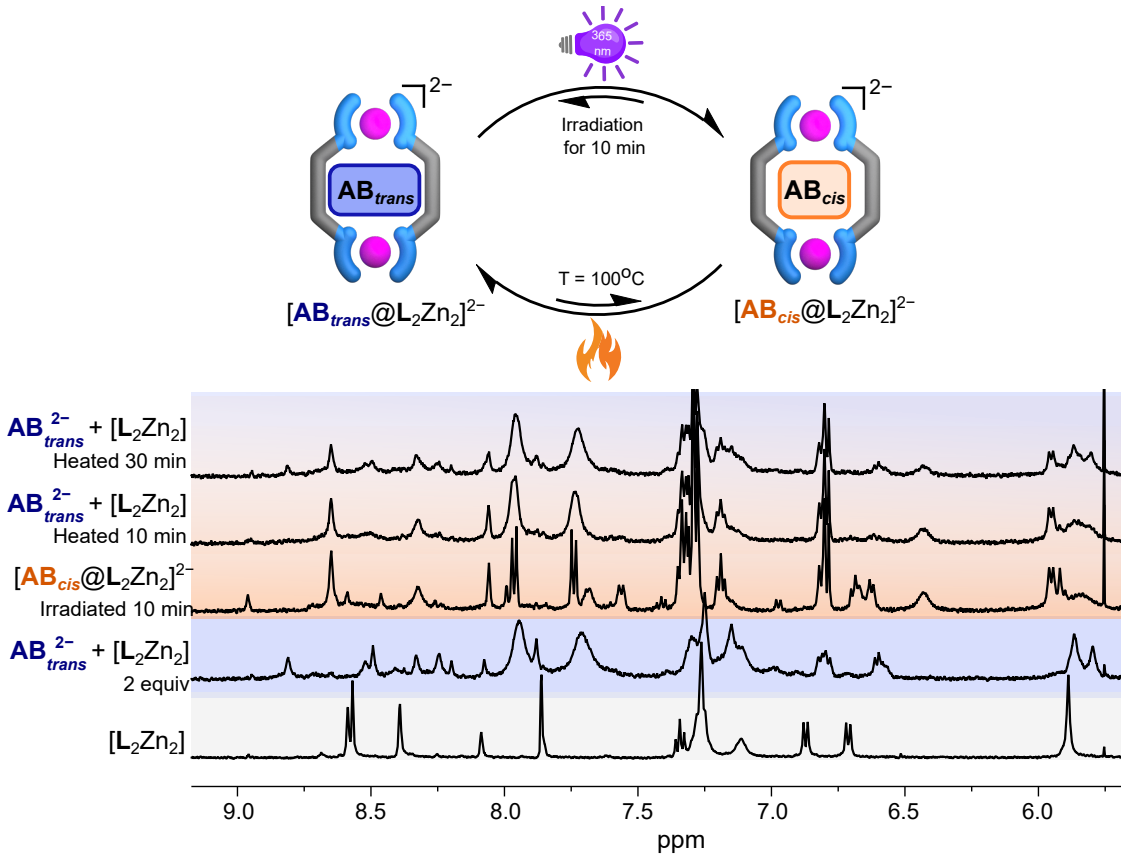

Figure 4.11 Reversible guest switching with azobenzene-4,4'-dicarboxylate in a non-competing environment. ^{1}H NMR spectra (500 µM, 500 MHz, DMSO-d_6, 298 K) with the addition of $\mathbf{AB}^{\mathbf{2-}}_{trans}$ (2 equiv.) to the host leading to an unknown mixture of assemblies including $[(\mathbf{AB}_{trans})@\mathbf{L}^{\mathbf{R}}{}_2\mathrm{Zn}_2]^{2-}$, which is subsequently irradiated to facilitate the transformation of the *trans* guest into *cis*, followed by additional heating at 100 °C for 30 min for the thermal back isomerization.

Consequently, the $\mathbf{AB^{2-}}$-only experiment does not constitute a complete, clean exchange cycle. This motivates the introduction of a competing guest to provide a thermodynamic advantage and facilitate rapid site recapture, enabling light- and heat-gated reversibility.

On introducing D-(−)-tartrate as a competing guest, the exchange becomes fully reversible and stimulus gated. A thermodynamic hierarchy of $K_{\mathrm{ABtrans}} < K_{\mathrm{TA}} < K_{\mathrm{ABcis}}$ has already been established. Thus, 365 nm irradiation of a mixture containing $\mathbf{D\text{-}TA^{2-}}$ (2 equiv.) and $\mathbf{AB^{2-}_{\textit{trans}}}$ (4 equiv.) drives a *cis*-rich photostationary state (∼90:10 *cis*:trans) and results in the clean conversion to $[(\mathbf{AB_{\textit{cis}}})@\mathbf{L^R}_2\mathrm{Zn}_2]^{2-}$, with $\mathbf{D\text{-}TA^{2-}}$ displaced. Brief heating at 100 °C for 10 min returns the excess **AB** guest to *trans* (∼0:100 *cis*:*trans*), and the host recaptures tartrate to regenerate $[(\mathbf{D\text{-}TA})@\mathbf{L^R}_2\mathrm{Zn}_2]^{2-}$. The light/heat sequence can be repeated over multiple cycles with consistent spectral interconversion and without any detectable degradation (Figure 4.12). Continuous irradiation of the host for extended periods of up to an hour has demonstrated potential host degradation. However, implementing alternating heating and irradiation cycles minimally impacts the host. The switching is faster than in the non-competing scenario due to the strong competition at the binding site. Overall, the competing guest provides directionality and accelerates the process, yielding a clean, controlled, stimuli-responsive, reversible guest-exchange cycle .

4.2.5 Reversible ON/OFF CD switching

To translate the NMR-defined exchange into an optical readout, we next targeted an ON/OFF circular dichroism (CD) response driven by the same stimuli. As established earlier, the binding of a chiral guest, such as tartrate, induces chirality in the host by selectively favoring one of its enantiomeric forms over the *meso* form, thereby resulting in the formation of a CD-active complex. In contrast, the interaction with an achiral compound such as $\mathbf{AB^{2-}}$ is anticipated to yield a CD-silent response. Our working hypothesis was that the CD active $[(\mathbf{D\text{-}TA})@\mathbf{L^R}_2\mathrm{Zn}_2]^{2-}$ would persist in the presence of $\mathbf{AB^{2-}_{\textit{trans}}}$, but upon 365 nm irradiation, *trans* converts to *cis* and replaces $\mathbf{D\text{-}TA^{2-}}$ inside the host; however, the resulting $[(\mathbf{AB_{\textit{cis}}})@\mathbf{L^R}_2\mathrm{Zn}_2]^{2-}$ would present a CD "OFF" state.

Experimentally, the first leg behaves as expected, with the CD signal disappearing upon 365 nm irradiation, consistent with guest exchange. Subsequent heating of the solution at 100 °C converts *cis* guest to *trans* and rebinds $\mathbf{D\text{-}TA^{2-}}$ in the cavity. Simultaneous UV-Vis measurements confirm the completion of each exchange step under the applied stimuli, indicating that the cavity is fully repopulated by the intended guest at each stage (Figure 4.56). However, although the CD toggles between ON and OFF, the magnitude of the "ON" state diminishes over successive cycles; i.e., the CD intensity is not sustained beyond approximately three cycles (Figure 4.13). Thus, while the stimuli-responsive guest exchange is clean and reversible, the optical readout exhibits progressive attenuation, and

the origin of this CD decay is currently under investigation.

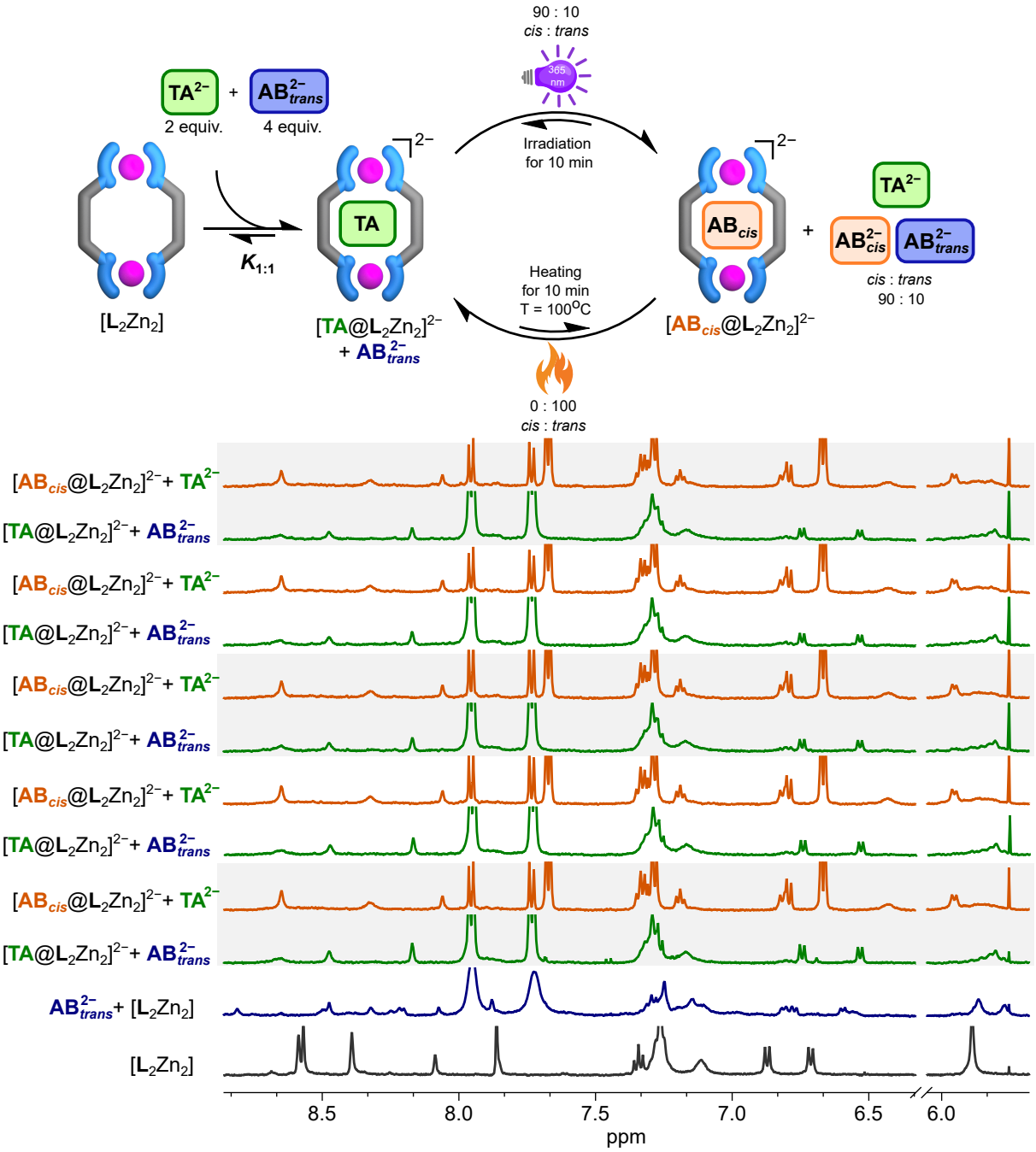

Figure 4.12 Reversible guest exchange cycle with 4,4'-azobenzene dicarboxylate in the presence of tartrate as competing guest. ^{1}H NMR spectra (500 µM, 500 MHz, DMSO-d_6, 298 K) for the sample containing host with $\mathbf{AB}^{2-}$ guest (2 equiv.) and $\mathbf{D\text{-}TA}^{2-}$ (4 equiv.). $[(\mathbf{D\text{-}TA})@\mathbf{L}^{\mathbf{R}}{}_2Zn_2]^{2-}$ mixture irradiated at 365 nm for 10 min produces $[(\mathbf{AB}_{cis})@\mathbf{L}^{\mathbf{R}}{}_2Zn_2]^{2-}$. Upon heating at 100 °C for 10 min $[(\mathbf{D\text{-}TA})@\mathbf{L}^{\mathbf{R}}{}_2Zn_2]^{2-}$ is reformed. This light-heat sequence repeated several times with consistent spectral interconversions.

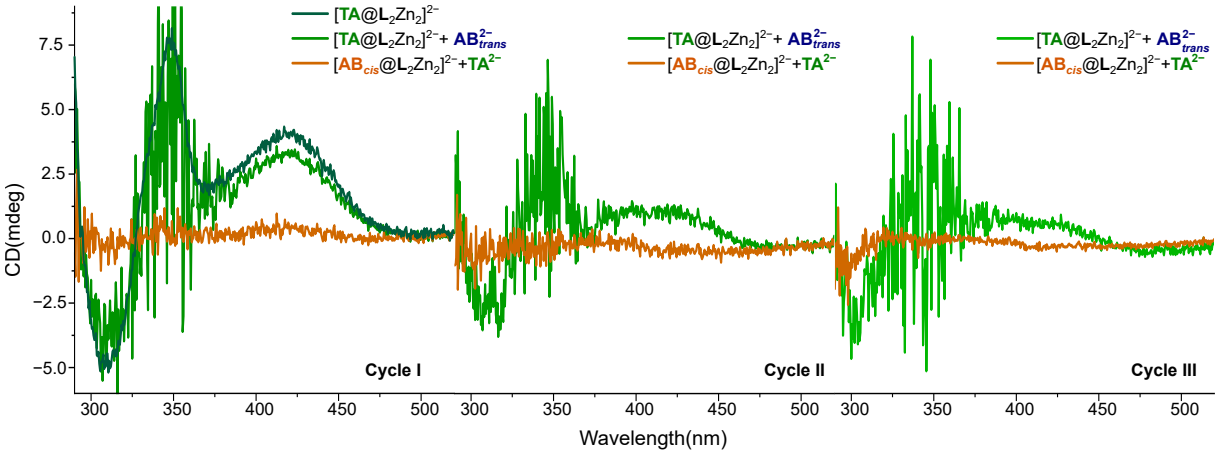

Figure 4.13 Stimuli-responsive CD ON/OFF cycle via reversible guest exchange. CD spectra (500 µM, l =2 mm, DMSO-d_6, 298 K) measured for sample containing host with $\mathbf{AB}^{\mathbf{2-}}_{trans}$ (1.5 equiv.) and $\mathbf{D\text{-}TA}^{\mathbf{2-}}$ (2 equiv.). $[(\mathbf{D\text{-}TA})@\mathbf{L^R}_2Zn_2]^{2-}$ in the presence of $\mathbf{AB}^{\mathbf{2-}}_{trans}$ shows CD "ON" state whereas the $[(\mathbf{AB}_{cis})@\mathbf{L^R}_2Zn_2]^{2-}$ formed upon irradiation at 365 nm shows a CD "OFF" state. Subsequent heating reforms tartrate-bound complex, however the CD amplitude diminishes and not sustained beyond three cycles.

4.2.6 Guest scope for the reversible guest exchange

To expand reversible exchange, we studied carboxylate guests differing in length, rigidity, denticity, and binding affinities with the $[\mathbf{L^R}_2Zn_2]$ host, as shown in Figure 4.14 and Table 4.1. For each system, we examined whether (i) a distinct competitor complex forms with $\mathbf{AB}^{\mathbf{2-}}_{trans}$, (ii) 365 nm irradiation enriches $\mathbf{AB}^{\mathbf{2-}}_{cis}$ and facilitates clean replacement of $[(\mathbf{AB}_{cis})@\mathbf{L^R}_2Zn_2]^{2-}$, and (iii) heating can reverse the isomerization to return to the initial state without any spectral loss.

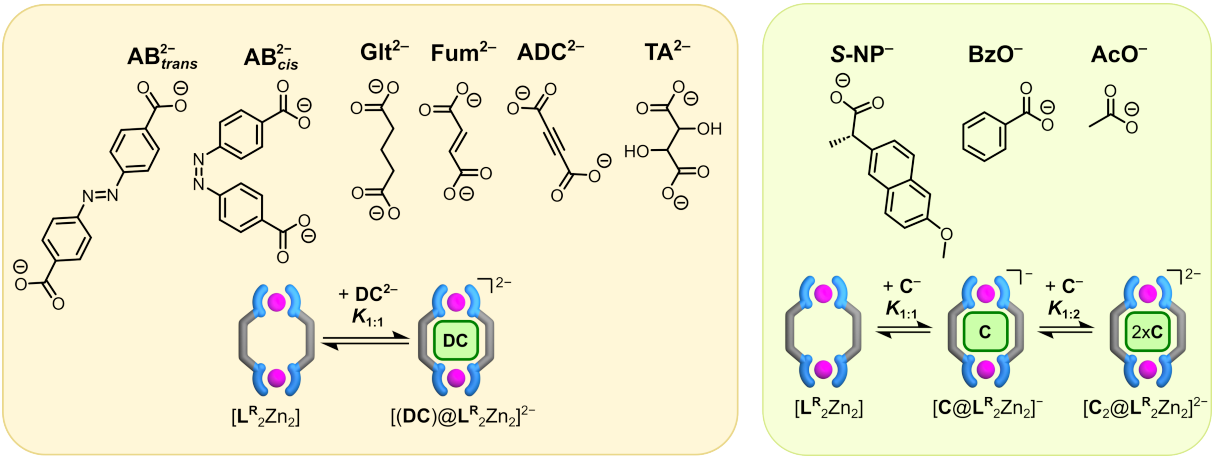

Figure 4.14 Monocarboxylates and dicarboxylates investigated as their TBA salts in this study. Monocarboxylates bind in a 1:2 fashion while dicarboxylates bind in a 1:1 fashion.

Table 4.1 The reported association constants[1,2] for the examined carboxylate guests as TBA salts used to reason their guest exchange behaviour.

Dicarboxylate (**DC**$^{2-}$)	$K_{1:1}$ (M^{-1})	Monocarboxylate (**C**$^{-}$)	$K_{1:1}$ (M^{-1})	$K_{1:2}$ (M^{-1})
Cis-azobenzene-4,4'-dicarboxylate (**AB**$^{2-}_{cis}$)	306 000 ± 31 000	Deprotonated naproxen (**S-NP**$^{-}$)[a]	32 000 ± 6 000	1 800 ± 100
Trans-azobenzene-4,4'-dicarboxylate (**AB**$^{2-}_{trans}$)	n.d	Benzoate (**BzO**$^{-}$)[c]	4860 ± 540	1070 ± 220
Glutarate (**Glt**$^{2-}$)[d]	3 000 000 ± 400 000	Acetate (**AcO**$^{-}$)[c]	2250 ± 400	3810 ± 940
Fumarate (**Fum**$^{2-}$)[d]	1 700 000 ± 400 000			
Acetylene dicarboxylate (**ADC**$^{2-}$) [b]	67 000 ± 13 000			
D-tartrate (**D-TA**$^{2-}$) [a]	174 000 ± 32 000			

*[a] Displaces $\mathbf{AB}^{2-}_{trans}$ from the host and is subsequently displaced by $\mathbf{AB}^{2-}_{cis}$; cycles proceed cleanly and are repeatable. [b] Displaces $\mathbf{AB}^{2-}_{trans}$ but is not fully displaced by $\mathbf{AB}^{2-}_{cis}$; partial recovery after the irradiated state -incomplete cycle. [c] Displaces $\mathbf{AB}^{2-}_{trans}$ and can be displaced by $\mathbf{AB}^{2-}_{cis}$, thermal back isomerization only under forcing conditions (prolonged irradiation and extended heating); cycle continue under forcing conditions. [d] Displaces $\mathbf{AB}^{2-}_{trans}$ and is only partially replaced by $\mathbf{AB}^{2-}_{cis}$; poor reversibility; incomplete cycle.

Deprotonated naproxen ($\boldsymbol{S}$-$\mathbf{NP}^{-}$) was evaluated for its competitive and robust reversible guest exchange behavior. Compared to tartrate, naproxen, a monocarboxylic guest, exhibits a relatively weak competitive nature with a binding constant $\log K_{1:1} = 4.51$ in comparison to that of $\mathbf{D\text{-}TA}^{2-}$, which is 5.24. $\boldsymbol{S}$-$\mathbf{NP}^{-}$ actively replaces the bound-$\mathbf{AB}^{2-}_{trans}$ (1.5 equiv.) from the host cavity when added in excess (5 equiv.). Upon subsequent irradiation at 365 nm, the $\mathbf{AB}^{2-}_{cis}$ guest displaces $\boldsymbol{S}$-$\mathbf{NP}^{-}$. A pseudo-2D NMR experiment conducted for 15 min with continuous irradiation at 365 nm showed a smooth decay of $\boldsymbol{S}$-$\mathbf{NP}^{-}$-based host-guest mixture (teal) (at five equiv. $\boldsymbol{S}$-$\mathbf{NP}^{-}$ is expected to have a population of both $[(\boldsymbol{S}\text{-}\mathbf{NP})@\mathbf{L^R}_2Zn_2]^{-}$ and $[(\boldsymbol{S}\text{-}\mathbf{NP})_2@\mathbf{L^R}_2Zn_2]^{2-}$). While $[(\mathbf{AB}_{cis})@\mathbf{L^R}_2Zn_2]^{2-}$ (orange) grew over time, which is consistent with a first-order–like process (Figure 4.15). An average $k = 0.661 \pm 0.014$ min^{-1} was obtained from the fits calculated for three non-overlapping peaks (Figure 4.48). Thus $\tau = 1/k \approx 1.51$ min and $t_{95} \approx 3\tau \approx 4.5$ min match the rapid approach to the plateau. This rate is faster than the tartrate case ($k = 0.567 \pm 0.029$ min^{-1}) and the $\mathbf{AB}^{2-}$-only case ($k = 0.434 \pm 0.020$ min^{-1}) analyzed previously, although all three datasets show the same clean behavior. The faster rate of $\boldsymbol{S}$-$\mathbf{NP}^{-}$ reflects its weak 1:2 binding in the host, so excess $\boldsymbol{S}$-$\mathbf{NP}^{-}$ was required to increase the population of 1:2 complex $[(\boldsymbol{S}\text{-}\mathbf{NP})_2@\mathbf{L^R}_2Zn_2]^{2-}$ in the solution initially and to actively compete with $\mathbf{AB}^{2-}_{trans}$ on the reversion.

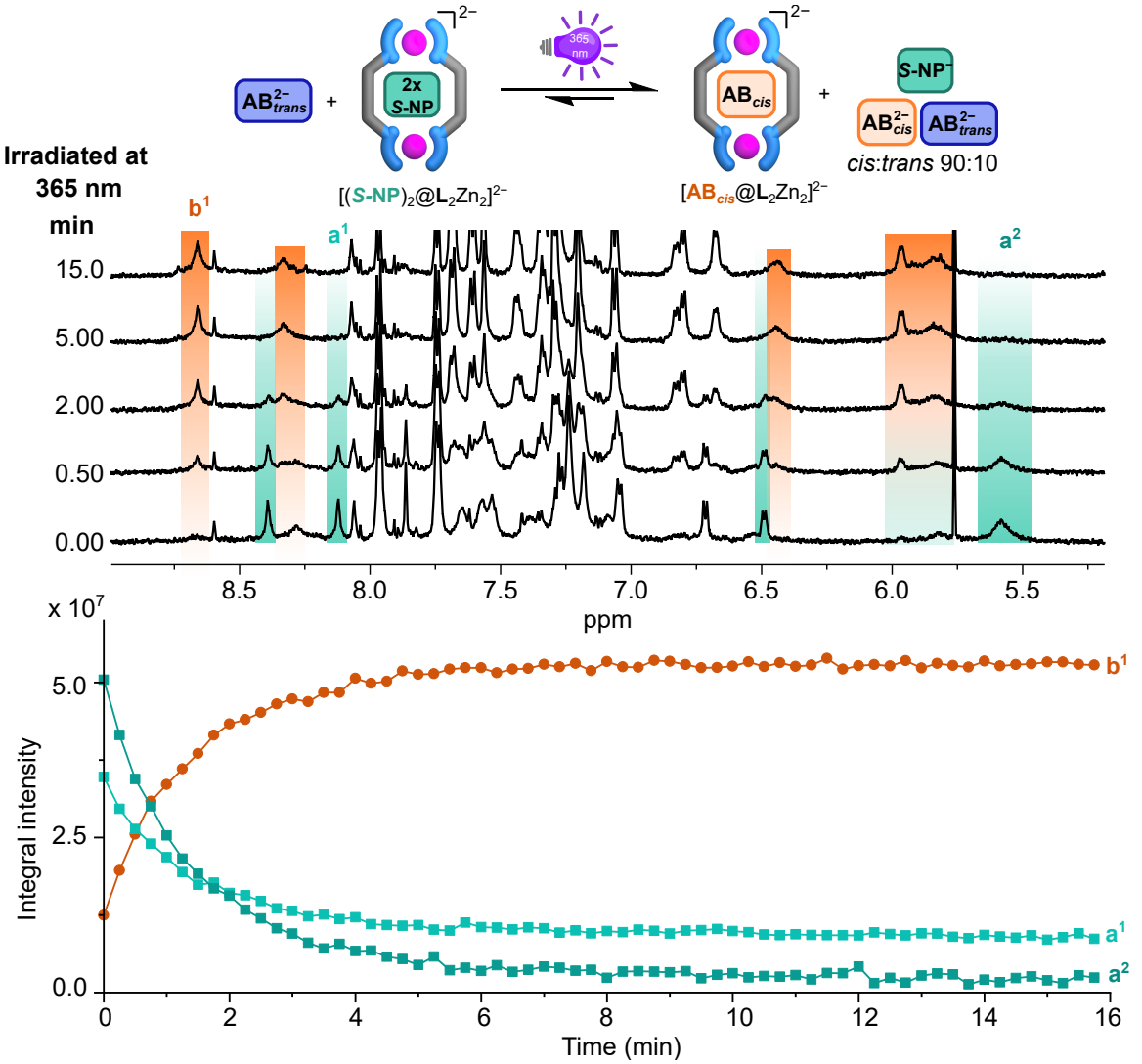

Figure 4.15 (top) ^{1}H NMR spectra recorded for the sample containing host with 1.5 equiv. of $\mathbf{AB}^{\mathbf{2-}}_{\boldsymbol{cis}}$ and 5 equiv. of deprotonated naproxen ($\boldsymbol{S}$-$\mathbf{NP}^-$), using pseudo-2D kinetics under continuous irradiation at 365 nm with *in situ* NMR illumination for 15 min (1 mM, 600 MHz, DMSO-d_6, 298 K). Highlighted signals show $\boldsymbol{S}$-$\mathbf{NP}^-$-based 1:1 and 1:2 host-guest population (teal) and $[(\mathbf{AB}_{\boldsymbol{cis}})@\mathbf{L}^{\mathbf{R}}{}_2\mathrm{Zn}_2]^{2-}$ complex (orange). (bottom) Calculated fit from pseudo-2D kinetics experiments plotted for non-overlapping peaks. Teal traces corresponds to $[(\boldsymbol{S}\text{-}\mathbf{NP})_2@\mathbf{L}^{\mathbf{R}}{}_2\mathrm{Zn}_2]^{2-}$ decays, while orange traces corresponds to $[(\mathbf{AB}_{\boldsymbol{cis}})@\mathbf{L}^{\mathbf{R}}{}_2\mathrm{Zn}_2]^{2-}$ grow to reach a plateau after 4.5 min.

Under 455 nm irradiation, the *cis*-bound complex is largely invariant, with at most partial regeneration of ($\boldsymbol{S}$-$\mathbf{NP}^-$)@[$\mathbf{L}^{\mathbf{R}}{}_2\mathrm{Zn}_2$] (Figure 4.49); whereas heating for 10 min at 100 °C fully reforms ($\boldsymbol{S}$-$\mathbf{NP}^-$)@[$\mathbf{L}^{\mathbf{R}}{}_2\mathrm{Zn}_2$] the light/heat sequence is reversible, as demonstrated for at least two cycles (Figure 4.16). $\boldsymbol{S}$-$\mathbf{NP}^-$ functions but is a less efficient competitor, requiring a larger amount to repopulate the host. Altogether, this establishes a robust, reversible light/heat guest exchange cycle with $\boldsymbol{S}$-$\mathbf{NP}^-$ analogous to tartrate, differing mainly in terms of timescale and amount requirements.

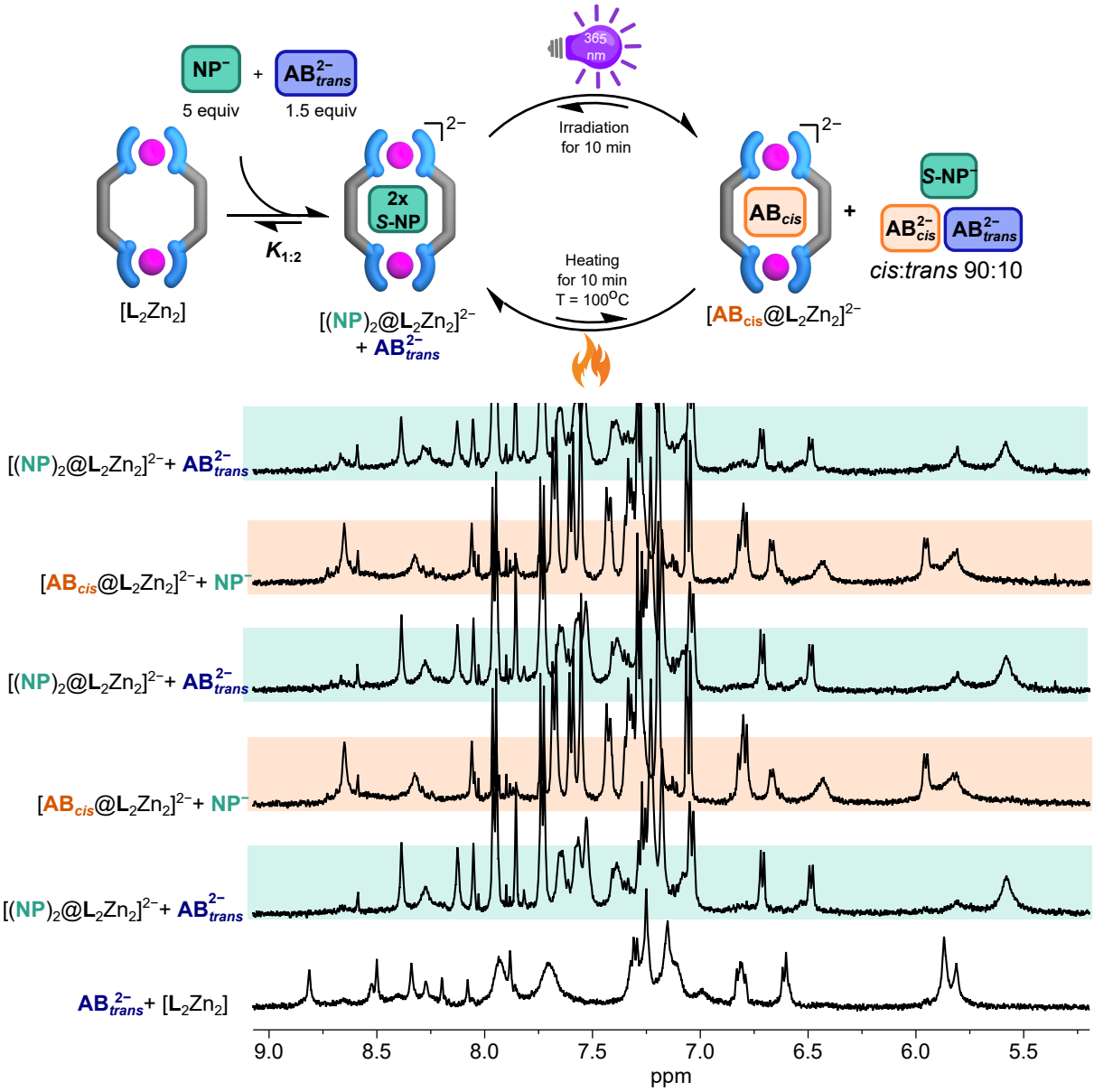

Figure 4.16 Reversible guest exchange cycle with azobenzene-4,4'-dicarboxylate in the presence of deprotonated naproxen as competing guest. ^{1}H NMR spectra (500 µM, 500 MHz, DMSO-d_6, 298 K) for the sample containing host with $\mathbf{AB}^{\mathbf{2-}}_{trans}$ (1.5 equiv.) and $\boldsymbol{S}$-$\mathbf{NP}^-$ (5 equiv.) shows selective formation of 1:1 and 1:2 ($\boldsymbol{S}$-$\mathbf{NP}^-$)@[$\mathbf{L}^{\mathbf{R}}{}_2\mathrm{Zn}_2$] population, which upon irradiation at 365 nm for 10 min produces [($\mathbf{AB}_{cis}$)@$\mathbf{L}^{\mathbf{R}}{}_2\mathrm{Zn}_2$]$^{2-}$. Upon heating at 100 °C for 10 min ($\boldsymbol{S}$-$\mathbf{NP}^-$)@[$\mathbf{L}^{\mathbf{R}}{}_2\mathrm{Zn}_2$] is reformed. This light/heat sequence can be repeated several times with consistent spectral interconversions.

We have also screened a set of other mono- and dicarboxylate guests with the helicate. To conclude, three clear regimes have emerged. First, reversible and clean: D-(−)-tartrate ($\mathbf{D\text{-}TA}^{\mathbf{2-}}$) gives the most robust cycle—365 nm irradiation photoenriches the *cis* guest and drives the quantitative formation of the *cis*-bound complex. On heating, supplants the initial tartrate-bound state. Deprotonated naproxen ($\boldsymbol{S}$-$\mathbf{NP}^-$) behaves similarly, albeit with a excess amount. Second, reversible but harsh: acetate ($\mathbf{AcO}^-$) and benzoate ($\mathbf{BzO}^-$) are fully displaced by *cis*-azobenzene under 365 nm, but the reverse step requires prolonged heating at 100 °C, and repeated cycling shows signs of partial degradation (Figure 4.50,

Figure 4.51). Third, partial or incomplete: among the dicarboxylates, glutarate ($\mathbf{Glt^{2-}}$) and acetylenedicarboxylate ($\mathbf{ADC^{2-}}$) bind readily and replace *trans*-azobenzene; yet, the *cis* isomer only partially displaces them under identical photochemical conditions; thermal relaxation back to the *trans* state is slow, and the overall cycle remains incomplete, owing to their high binding affinity compared to the *cis* guest (Figure 4.52, Figure 4.54). Fumarate ($\mathbf{Fum^{2-}}$) competes even more strongly; adding *cis* guest produces only limited conversion to the *cis*-bound complex (Figure 4.55).

Overall, successful reversible switching requires a sweet spot in guest binding; strong enough to preload a distinct competitor complex, but weak or mismatched enough to be displaced by the photo-generated *cis*-azobenzene guest without harsh conditions. In our hands, tartrate and naproxen meet this criterion; acetate and benzoate demand high temperatures to reset, while glutarate, acetylenedicarboxylate, and fumarate do not deliver clean, fully reversible cycles under comparable conditions.

4.3 Conclusion

This chapter elucidates a multi-stimuli, reversible guest-exchange mechanism in our charge-neutral Zn(II) helicate using azobenzene-4,4'-dicarboxylate as a photoswitchable guest. Owing to the size selectivity of the host, it preferentially accommodates the shorter, bent *cis* isomer over the elongated *trans* form. These states are interconverted under the influence of light and heat. The encapsulated *cis* guest is kinetically stabilized. Confinement and coordinative binding hinder the inversion/rotation isomerization mechanism; thus, the bound *cis* complex persists at room temperature and under ambient visible light, whereas the free *cis* relaxes thermally to *trans*. Sustained 455 nm irradiation converts the unbound fraction, yet leaves the bound *cis* complex unchanged. Switching the encapsulated guest requires sustained heating at elevated temperatures. Efficient exchange further relies on a competing guest of intermediate affinity, such as D-tartrate, which facilitates switching by occupying the cavity as the *cis* isomerizes and departs ($K_{\text{trans}} < K_{\text{TA}} < K_{\text{cis}}$). Additional carboxylate guests were probed to replicate the clean guest exchange cycles produced by tartrate.

Overall, we achieve controlled, stimulus-mediated, reversible guest exchange cycles by modifying the guest while maintaining the inherent properties of the host. This advances the strategies for releasing guests from a strong coordinative environment. Future work will involve the extraction of the desired released guest in appropriate solvent media. One way to achieve this is by improving the solubility of the host (e.g., PEGylation), thereby enhancing compatibility with various solvent systems. Phase-selective extraction will enable clean recovery of the released guest in application relevant solvents, including mixed aqueous systems.

4.4 Experimental section

4.4.1 General methods

4.4.1.1 Materials

NMR spectra were recorded on a Bruker AVANCE III NEO-500 MHz instrument and a Bruker AVANCE III HD-600 MHz instrument with a cryo-broadband probe head. Chemical shifts are reported in δ (ppm) and multiplicities as s (singlet), d (doublet), t (triplet), and m (multiplet).

Irradiation experiments were performed using a 300 W xenon arc lamp (MAX-350) equipped with appropriate band-pass filters or, alternatively, using Thorlabs fiber-coupled LEDs at center wavelengths of 365 nm and 455 nm, operated in a dark enclosure. For *in situ* NMR illumination, a radiation-resistant optical fiber connected to the external LED source was inserted into a 5 mm quartz NMR tube. The illuminated section spanned the detection coil, and spectra were acquired as a pseudo-two-dimensional (pseudo-2D) time series under continuous irradiation. Shimming was performed with the fiber in place, and the VT setpoint (298 K unless otherwise stated) was maintained.

Variable-temperature (VT) NMR spectra were acquired using the probe's VT unit. Where VT was not required, the samples were heated *ex situ* in a thermostated heating block at the specified temperature and then promptly transferred to the spectrometer for acquisition. A cuvette containing a sample for spectroscopy measurements, a hot water bath maintained at 100°°C is utilized.

Isothermal titration calorimetry (ITC) was carried out on a Malvern Microcal PEAQ-ITC (Hastelloy cell) device. UV-Vis spectra were recorded on an Agilent DAD HP-8453 UV-Vis spectrometer, and circular dichroism (CD) measurements were performed at a Photophysics Chirascan qCD Spectrometer using Hellma QS cuvettes ($l = 2$ mm) at room temperature. The CD spectra were accumulated twice with a step size of 0.5 nm and a bandwidth of 1 nm and averaged to reduce the amount of noise, such that smoothing of the data was not necessary. ESI-MS spectra were measured using a Bruker timsTOF spectrometer.

4.4.1.2 Procedures for binding studies

Preparation of TBA salts for guests

The purchased carboxylic acids were converted to their respective tetrabutylammonium (TBA) salts by deprotonation prior to use. Carboxylic acids were dissolved in 5 mL of MeOH, and one and two equivalents of tetrabutylammonium hydroxide (1 M solution in MeOH) were added for mono- and dicarboxylic acids, respectively. The mixture was vortexed for 30 min, and the solvents were removed under reduced pressure. A small amount of water was added to aid subsequent freeze-drying, as pure MeOH freezes poorly, and it was lyophilized for up to three days. The resulting TBA carboxylates were used without further purification.

Analysis of titration data

$\mathbf{AB}^{\mathbf{2-}}_{\boldsymbol{trans}}$ was binding in intermediate exchange, and $\mathbf{AB}^{\mathbf{2-}}_{\boldsymbol{cis}}$ was binding in slow exchange with respect to the NMR timescale; determining the binding constants from NMR was not possible. Therefore, ITC measurements were carried out.

Isothermal Titration Calorimetry (ITC)

ITC measurements were performed on a Malvern MicroCal PEAQ-ITC (Hastelloy cell) and analyzed using the MicroCal PEAQ-ITC Analysis Software. A typical run used a total of 25 injections (1 × 0.4 µL followed by 24 × 1.5 µL) at 25 °C, with a reference power of 10.0 µcal/s, high feedback, and a stir rate of 750 rpm. The initial delay was 60 s; subsequent injections were spaced by 180 s, with an injection duration of 3.0 s.

Pseudo-2D ^{1}H NMR kinetic experiments

Kinetic measurements were carried out using pseudo-two-dimensional (pseudo-2D) ^{1}H NMR experiments on a Bruker spectrometer. A series of 1D spectra were acquired sequentially at fixed time intervals under identical acquisition parameters, and the relevant resonances were monitored over the course of the reaction. Signal intensities of selected, non-overlapping peaks corresponding to starting materials and products were integrated, tracked over time, divided by proton count, and plotted as a function of reaction time. The resulting intensity vs. time profiles were analyzed using Bruker Dynamics Center (Version 2.8.8), which fits the experimental data to appropriate kinetic models (e.g., first-order or multi-exponential functions) to extract rate constants. This approach provides a direct and quantitative method for monitoring reaction progress *in situ* by NMR, in line with established protocols for pseudo-2D kinetic analysis in solution-state NMR spectroscopy.[33–35]

4.4.2 Photoisomerization of azobenzene-4,4'-dicarboxylate

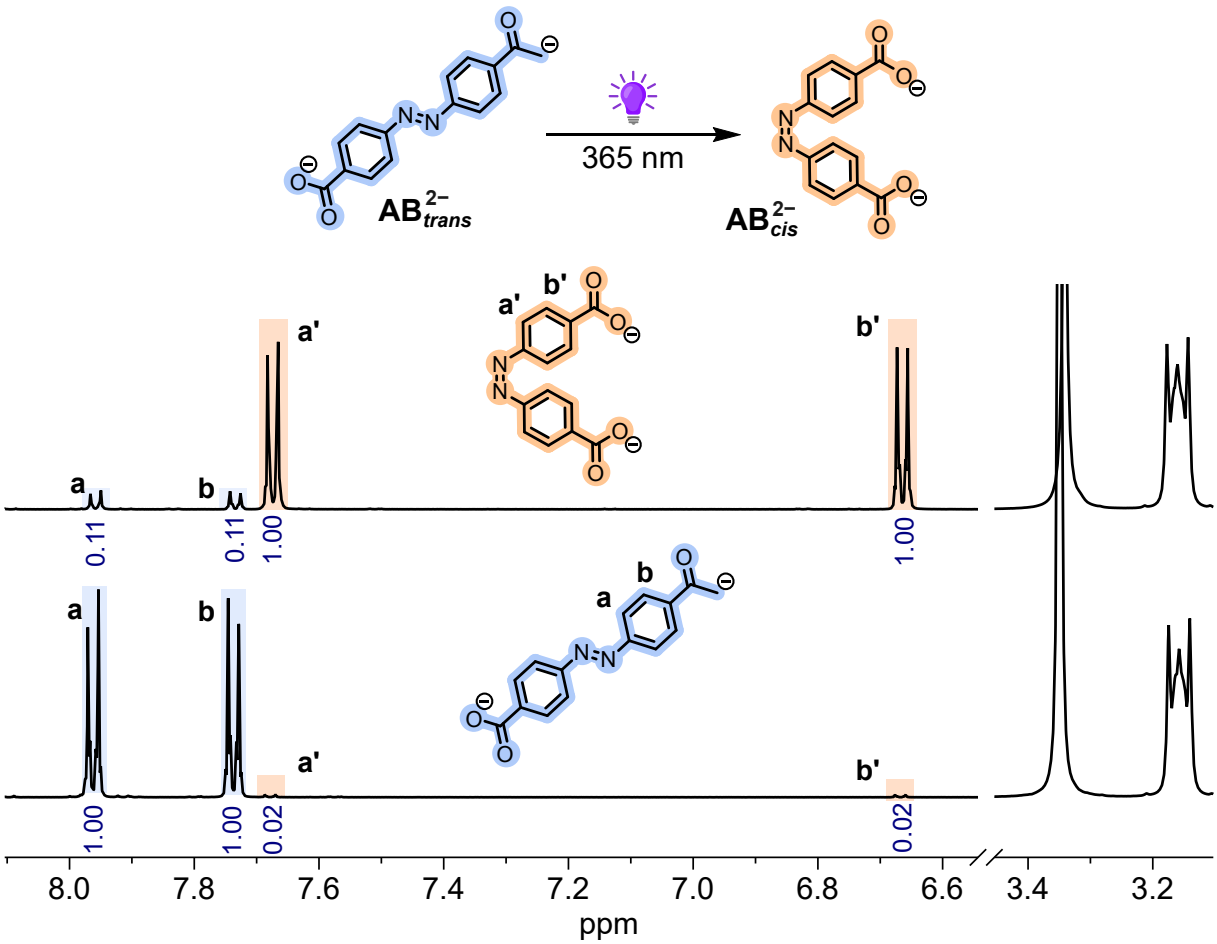

Figure 4.17 The TBA salt of *trans*-azobenzene-4,4'-dicarboxylate ($\mathbf{AB}^{\mathbf{2-}}_{trans}$) was irradiated at 365 nm using a Thorlabs fiber-coupled LED for one hour to convert it to the *cis*azobenzene-4,4'-dicarboxylate ($\mathbf{AB}^{\mathbf{2-}}_{cis}$) isomer. A 10:90 *trans*:*cis* conversion was observed (500 MHz, DMSO – d_6, 298 K).

4.4.3 Binding studies of carboxylate guests

4.4.3.1 *Cis*-azobenzene-4,4'-dicarboxylate

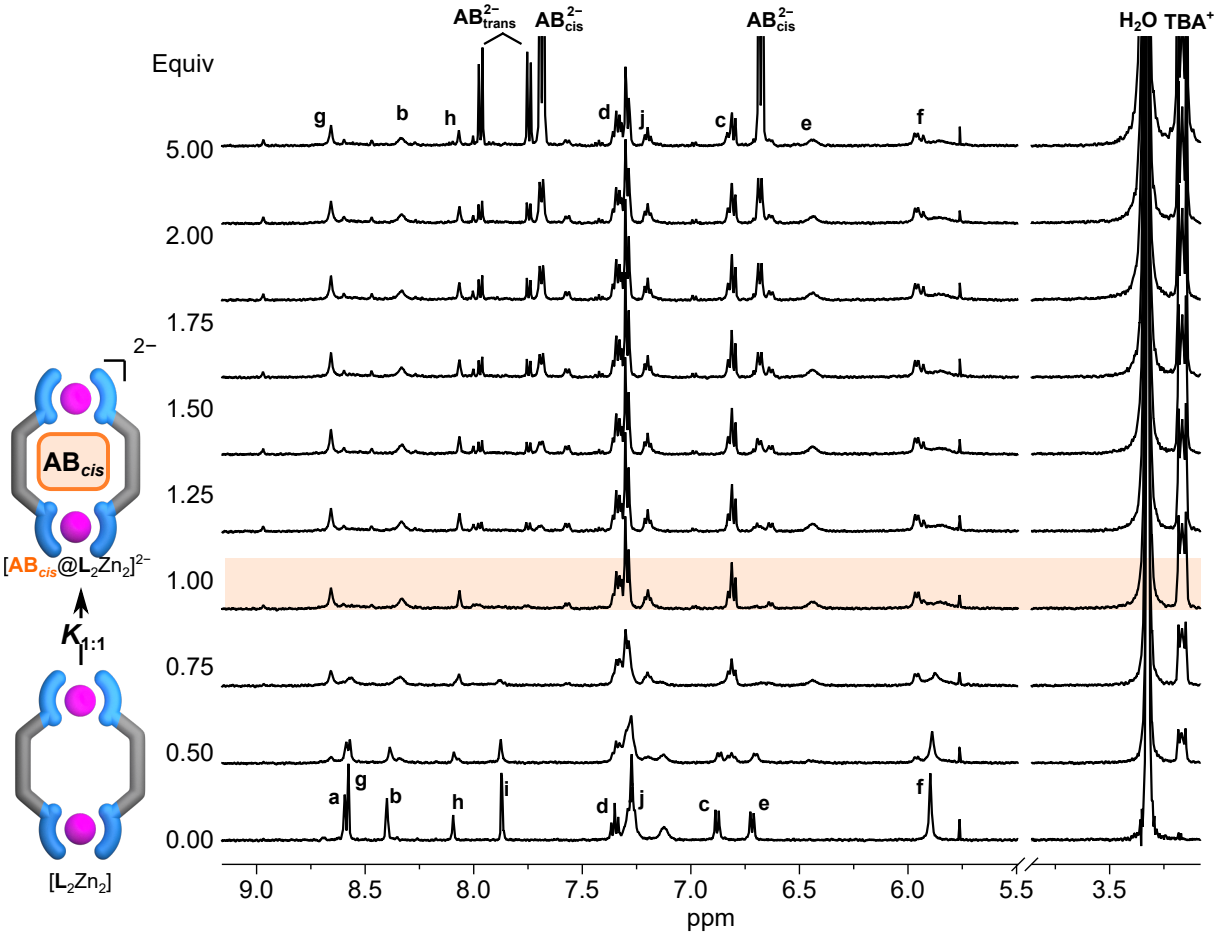

Figure 4.18 ^{1}H NMR (500 µM, 500 MHz, DMSO – d_6, 298 K) of $[\mathbf{L^R}_2Zn_2]$ with *cis*-azobenzene-4,4'-dicarboxylate ($\mathbf{AB^{2-}_{cis}}$) as TBA salt. The titration data with growing host-guest signals along with loss of free host signals indicates a slow exchange process on the NMR time scale and the formation of 1:1 host-guest complex.

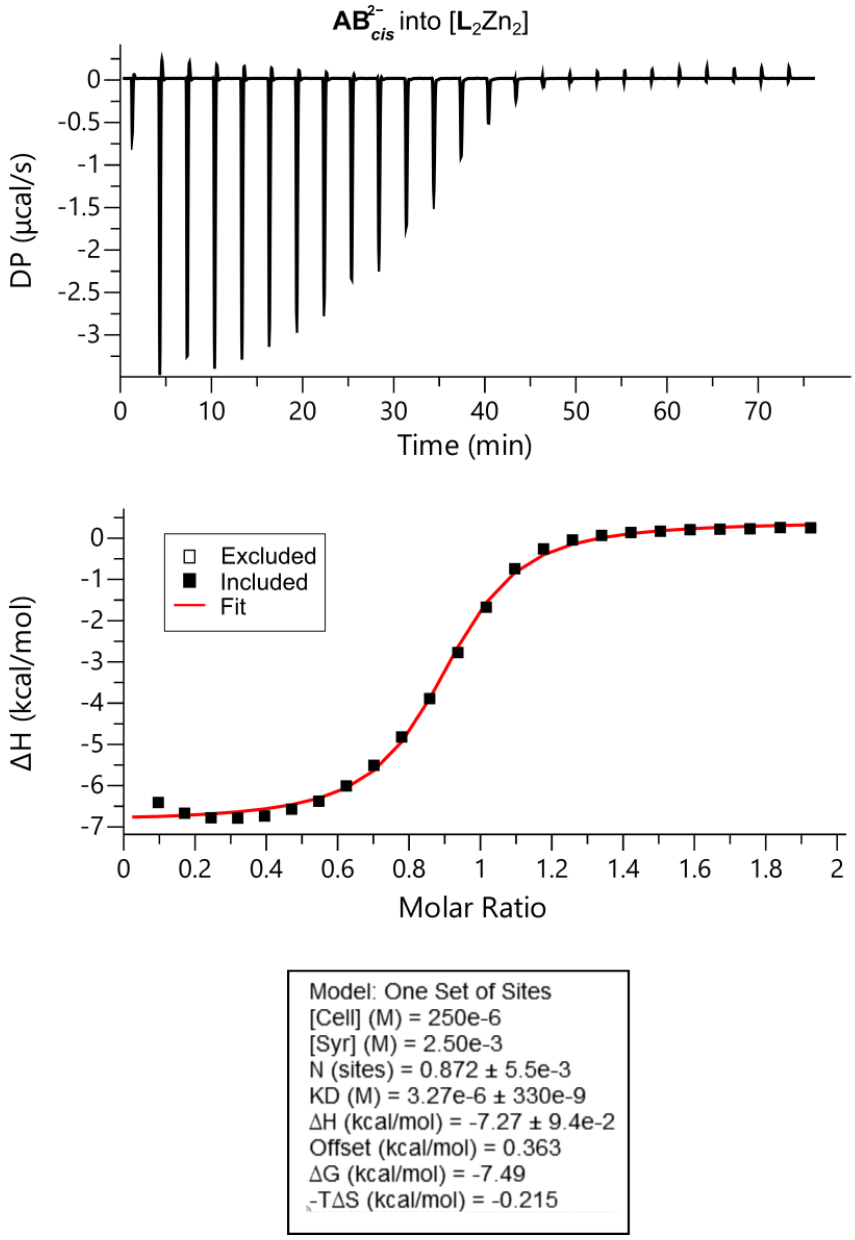

Figure 4.19 Binding constant determined from the ITC titration of $[\mathbf{L^R}_2Zn_2]$ with $\mathbf{AB^{2-}_{cis}}$.

4.4.3.2 *Trans*-azobenzene-4,4'-dicarboxylate

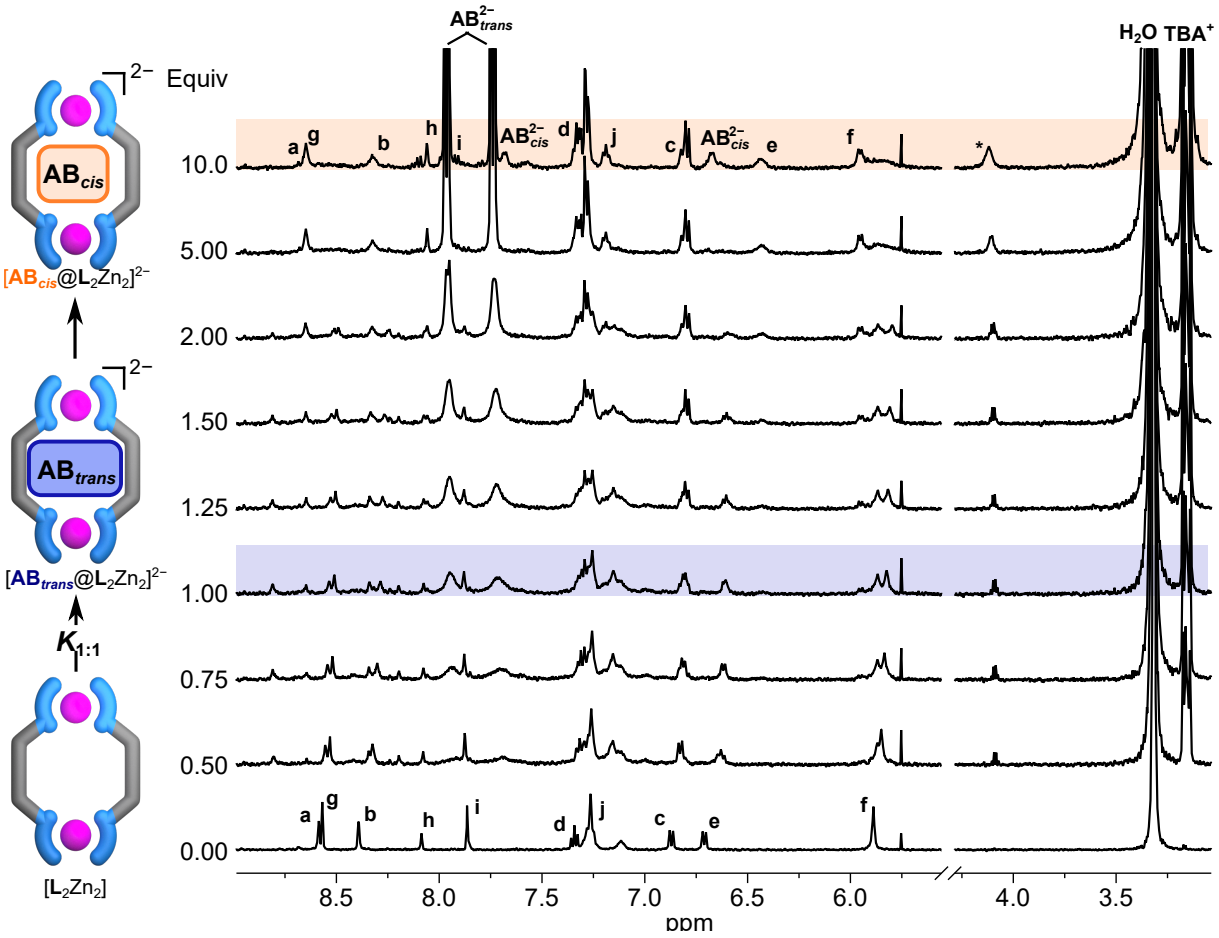

Figure 4.20 ^{1}H NMR (500 µM, 500 MHz, DMSO – d_6, 298 K) of [$\mathbf{L^R}_2Zn_2$] with *trans*-azobenzene-4,4'-dicarboxylate ($\mathbf{AB^{2-}_{\mathit{trans}}}$) as TBA salt. The titration data is less straightforward to interpret showing intermediate exchange on the NMR time scale; although, the signals confirm the formation of 1:1 host-guest complex. At higher equivalents spectrum shifts to that of [($\mathbf{AB}_{\mathit{cis}}$)@$\mathbf{L^R}_2Zn_2$]$^{2-}$ due to the small amount of cis isomer present. *unidentified signal.

4.4.3.3 Fumarate

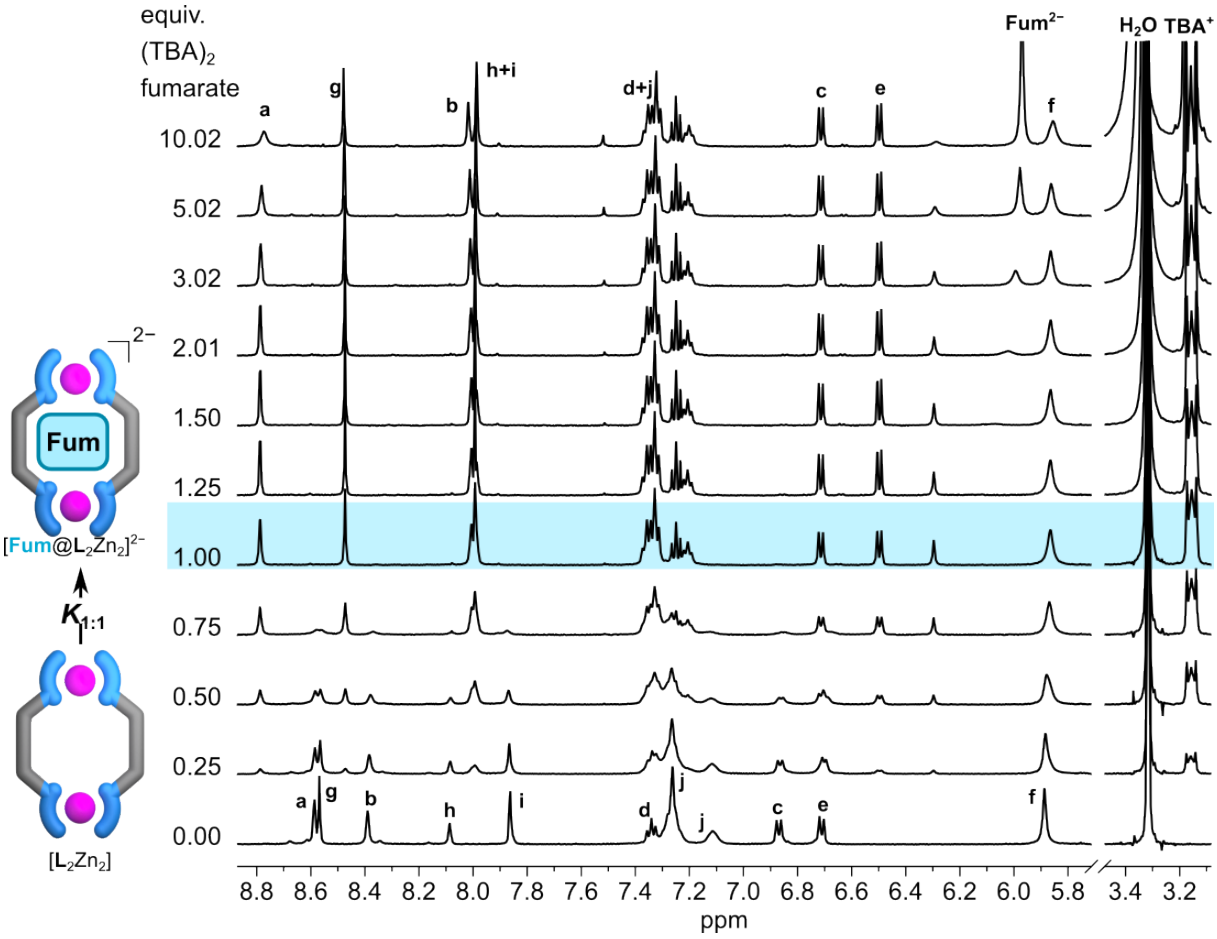

Figure 4.21 ^{1}H NMR (500 µM, 500 MHz, DMSO – d_6, 298 K) of [$\mathbf{L^R}_2Zn_2$] with Fumarate ($\mathbf{Fum^{2-}}$) as TBA salt. The titration data with growing host-guest signals along with loss of free host signals indicates a slow exchange process on the NMR time scale and the formation of 1:1 host-guest complex.

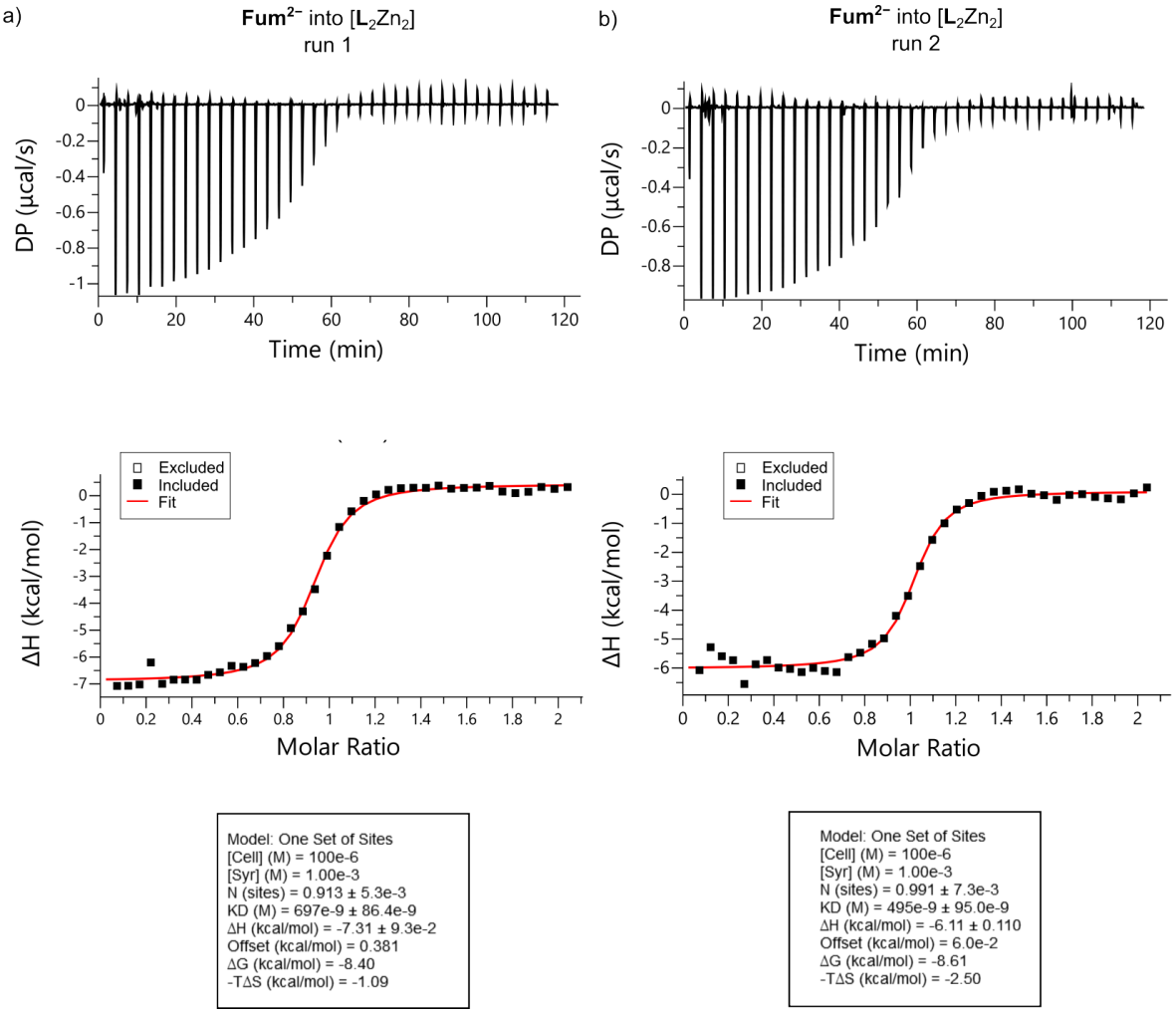

Figure 4.22 Binding constant determined from the ITC titration of [$\mathbf{L^R}_2Zn_2$] with Fumarate ($\mathbf{Fum^{2-}}$).

4.4.3.4 Acetylene dicarboxylate

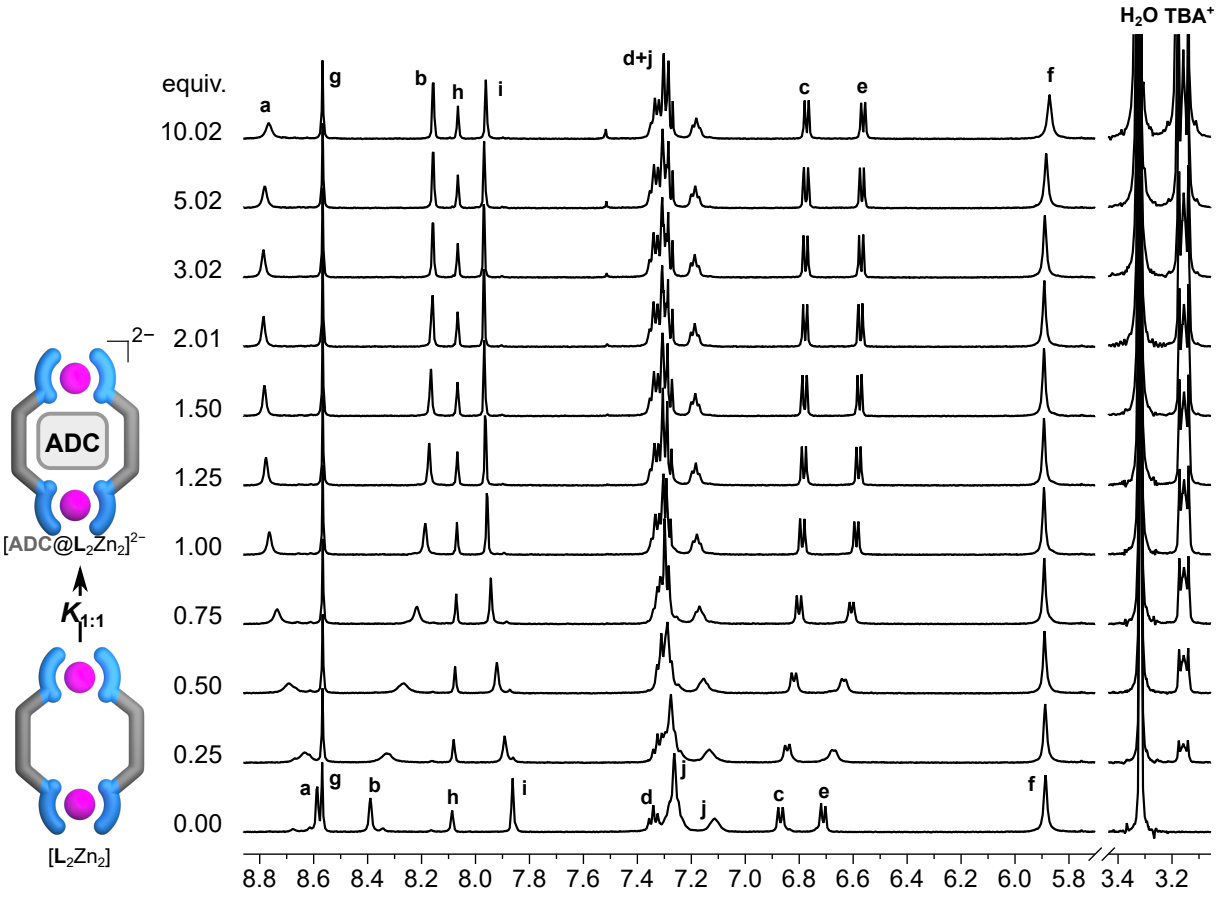

Figure 4.23 ^{1}H NMR titration (500 µM, 500 MHz, DMSO–d_6, 298 K) of [$\mathbf{L^R}_2Zn_2$] with Acetylene dicarboxylate ($\mathbf{ADC^{2-}}$) as TBA salt.

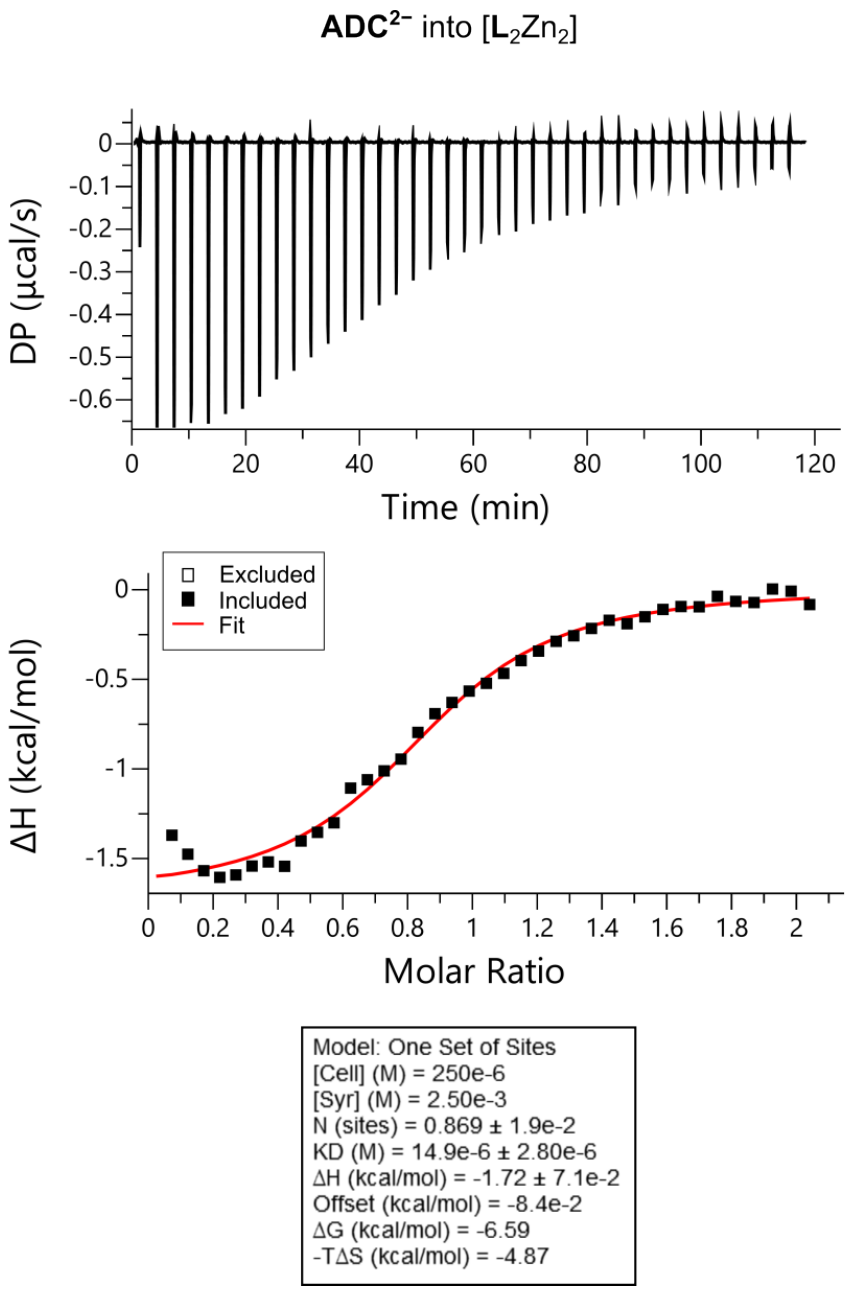

Figure 4.24 Binding constant determined from the ITC titration of [$\mathbf{L^R}_2Zn_2$] with Acetylene dicarboxylate ($\mathbf{ADC^{2-}}$).

4.4.4 Selective binding: ESI-MS Spectra

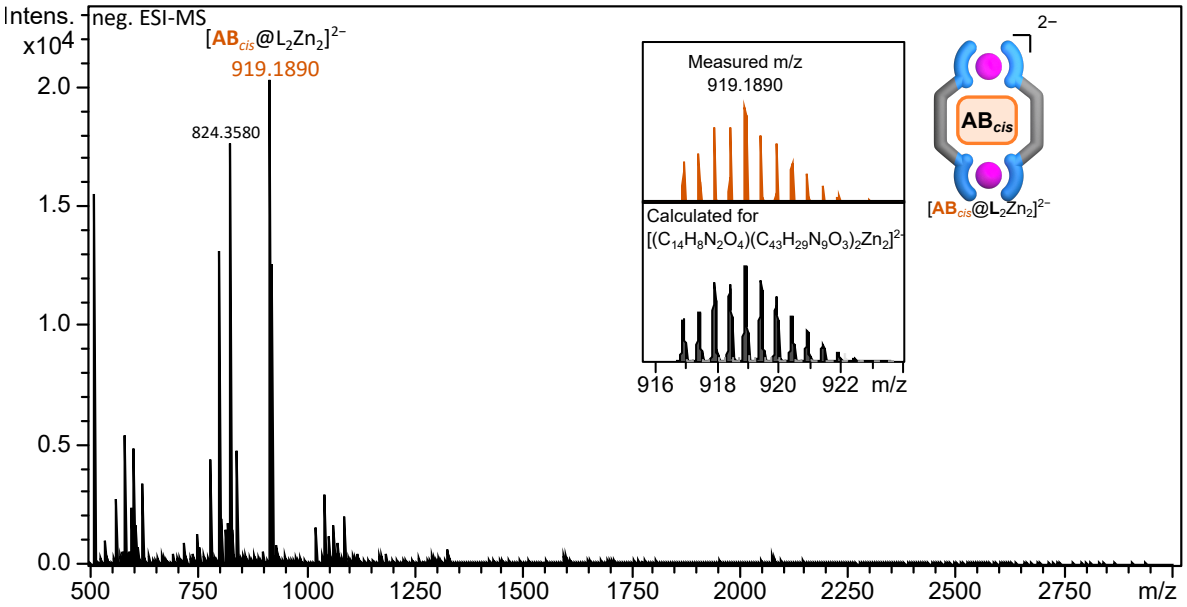

Figure 4.25 Negative ESI-MS spectrum (DMSO:MeOH:MeCN 2:9:9) of $[\mathbf{L^R}_2Zn_2]$ with *cis*-azobenzene-4,4'-dicarboxylate ($\mathbf{AB^{2-}_{\mathit{cis}}}$). The spectrum shows 1:1 host-guest complex as the main species.

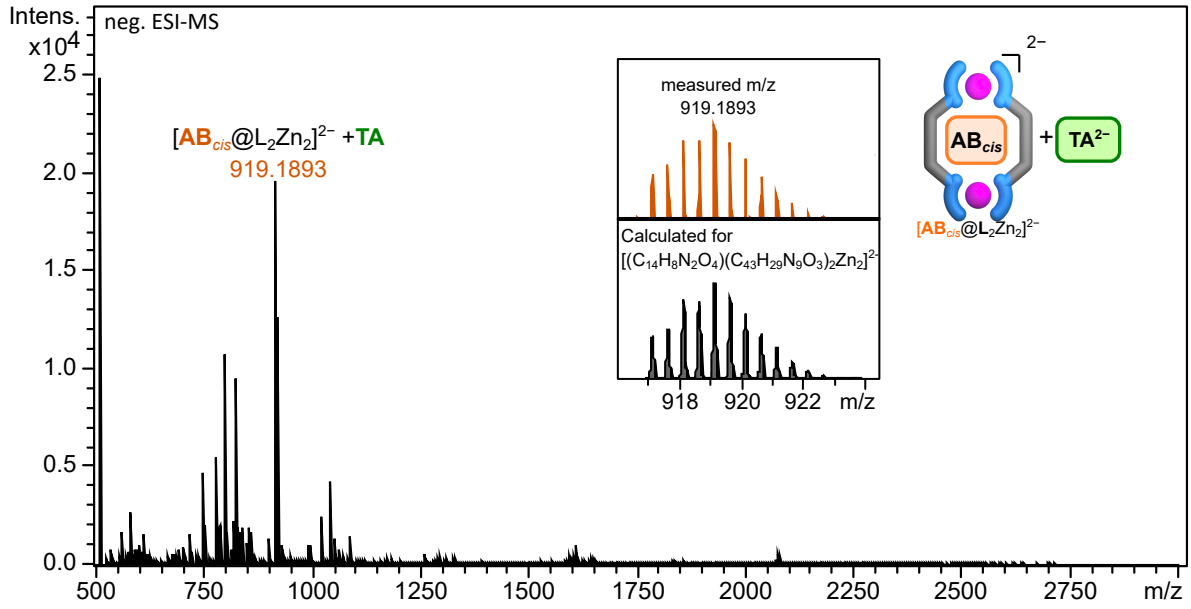

Figure 4.26 Negative ESI-MS spectrum (DMSO:MeOH:MeCN 2:9:9) of $[\mathbf{L^R}_2Zn_2]$ with *cis*-azobenzene-4,4'-dicarboxylate ($\mathbf{AB^{2-}_{\mathit{cis}}}$) and $\mathbf{D\text{-}TA^{2-}}$. The spectrum shows $[(\mathbf{AB}_{\mathit{cis}})@\mathbf{L^R}_2Zn_2]^{2-}$ as the main species. Peak correspond to $[(\mathbf{D\text{-}TA})@\mathbf{L^R}_2Zn_2]^{2-}$ shoud be at 859.1585, which is absent in this case.

4.4.5 Stabilization of Photostationary state of *cis*-azobenzene-4,4'-dicarboxylate

4.4.5.1 Mild conditions

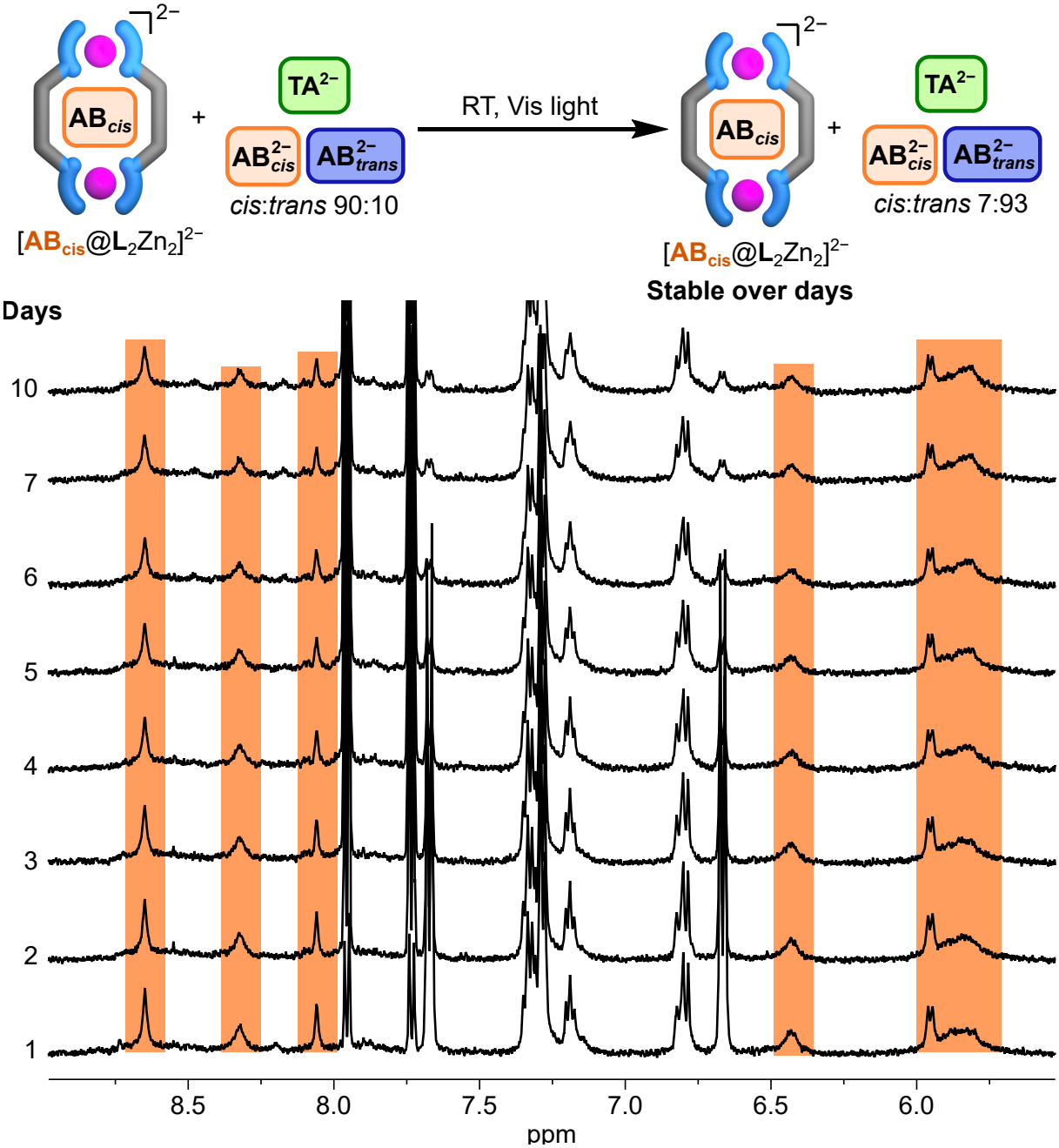

Figure 4.27 ^{1}H NMR stability study of $[(\mathbf{AB}_{cis})@\mathbf{L}^{\mathbf{R}}{}_2Zn_2]^{2-}$ in the presence of tartrate (2 equiv.) and excess *cis*-azobenzene-4,4'-dicarboxylate (4 equiv.), recorded over 10 days under ambient visible light at room temperature (600 MHz, DMSO-d_6, 298 K).

4.4.5.2 Irradiation at 455 nm

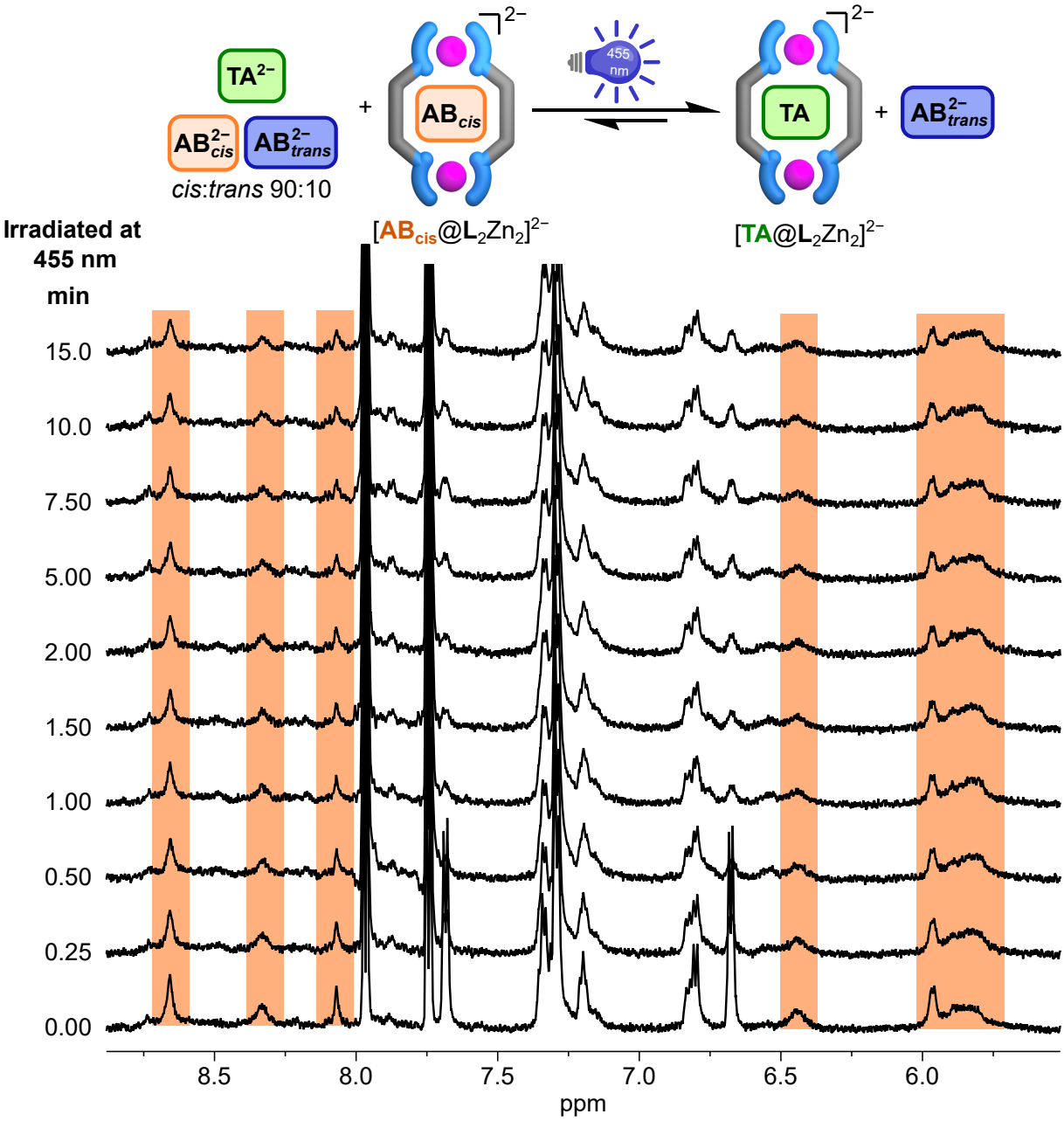

Figure 4.28 ^{1}H NMR spectra recorded for the sample containing host with 4 equiv. of $\mathbf{AB}^{\mathbf{2-}}_{cis}$ and 2 equiv. of $\mathbf{D\text{-}TA}^{\mathbf{2-}}$, using pseudo-2D kinetics under continuous irradiation at 455 nm with *in situ* NMR illumination for 15 min (1 mM, 600 MHz, DMSO-d_6, 298 K). The free guest photoisomerizes to reach a 5:95 *cis*:*trans* ratio, while the complex signals are invariant, indicating no detectable 455 nm-induced isomerization of the bound guest.

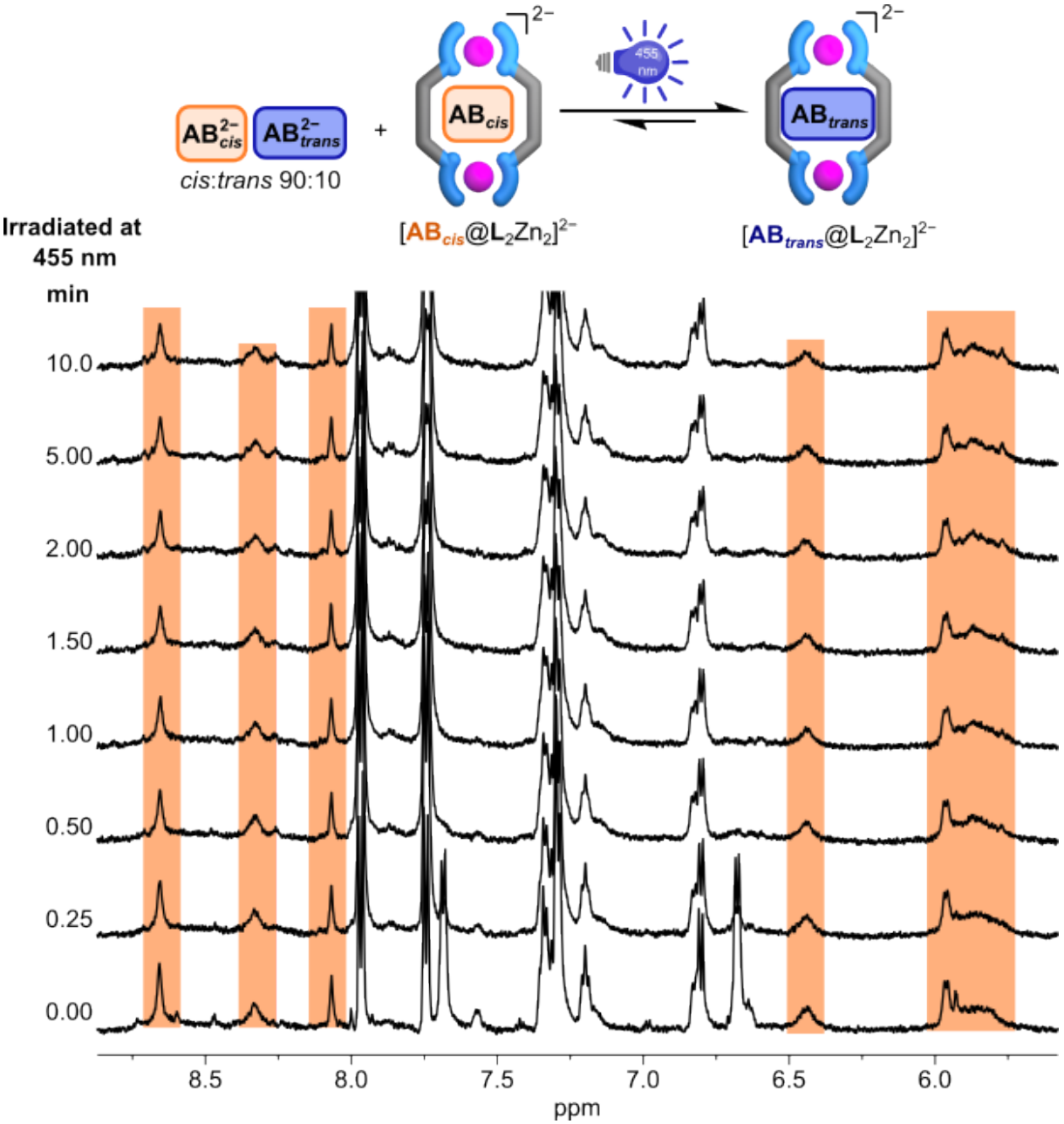

Figure 4.29 ^{1}H NMR spectra recorded for the sample containing host with 2 equiv. $\mathbf{AB}_{cis}^{2-}$, using pseudo-2D kinetics under continuous irradiation at 455 nm with *in situ* NMR illumination for 15 min (1 mM, 600 MHz, DMSO-d_6, 298 K). The free guest undergoes nearly 100% conversion to the *trans*-form, while the complex signals are mostly invariant, apart from a negligible amount of $[(\mathbf{AB}_{trans})@\mathbf{L}^{\mathbf{R}}{}_2\mathrm{Zn}_2]^{2-}$ formed, indicating nearly no reasonable 455 nm-induced isomerization of the bound guest.

4.4.5.3 Thermal relaxation

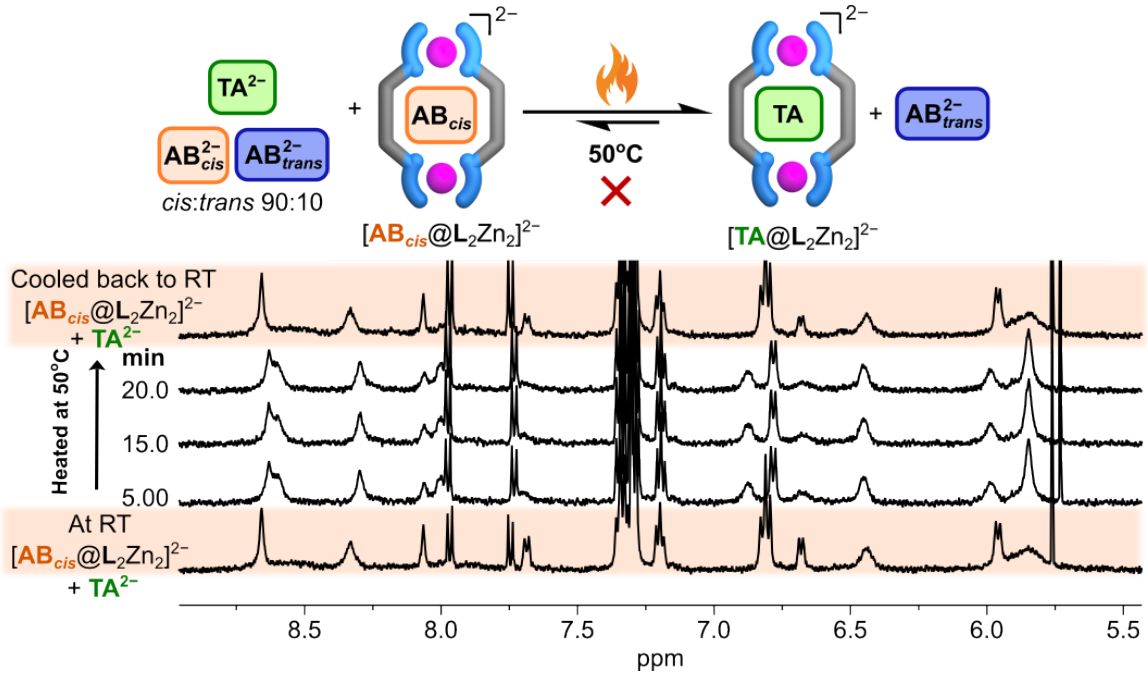

Figure 4.30 Variable temperature (VT) ^{1}H NMR spectra (500 µM, 500 MHz, DMSO-d_6, 298 K) recorded for the sample containing [$\mathbf{L^R}_2$Zn$_2$], $\mathbf{AB^{2-}_{\mathit{cis}}}$ (1 equiv.), $\mathbf{D\text{-}TA^{2-}}$ (1 equiv.) at 50 °C for 20 min. Initial spectrum and final spectrum after cooling down to 25 °C are compared.

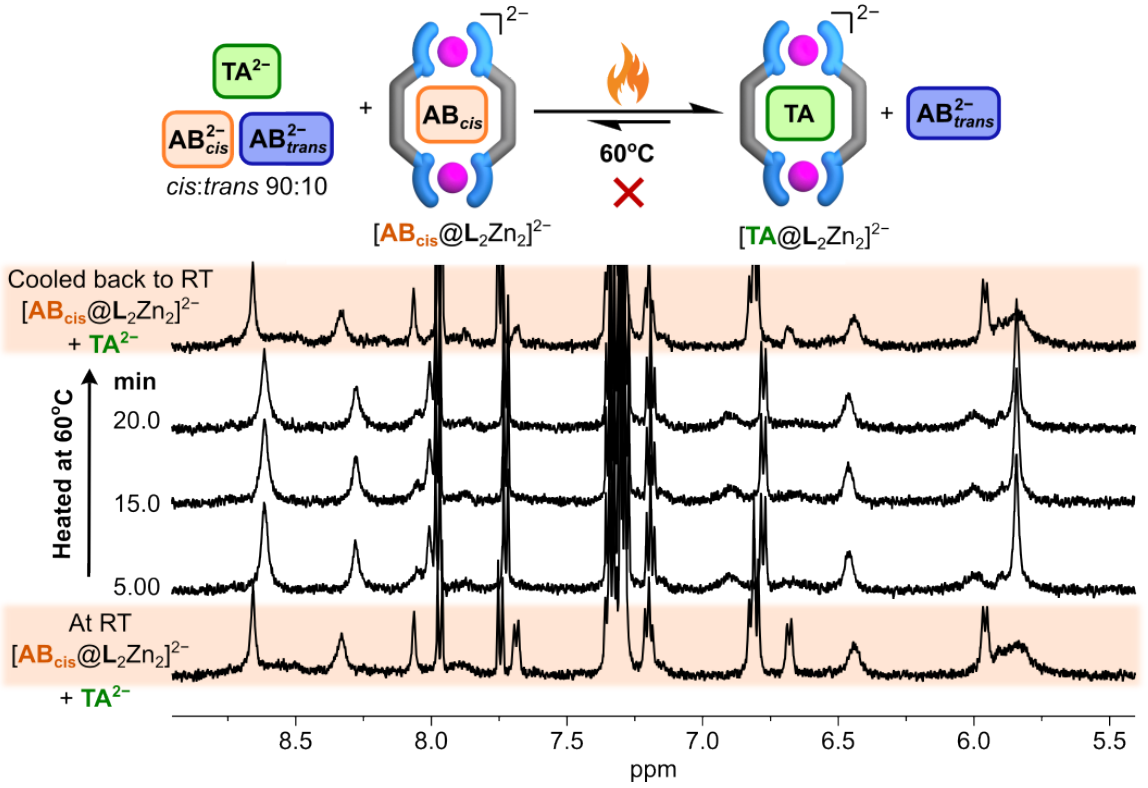

Figure 4.31 Variable temperature (VT) ^{1}H NMR spectra (500 µM, 500 MHz, DMSO-d_6, 298 K) recorded for the sample containing [$\mathbf{L^R}_2$Zn$_2$], $\mathbf{AB^{2-}_{\mathit{cis}}}$ (1 equiv.), $\mathbf{D\text{-}TA^{2-}}$ (1 equiv.) at 60 °C for 20 min. Initial spectrum and final spectrum after cooling down to 25 °C are compared.

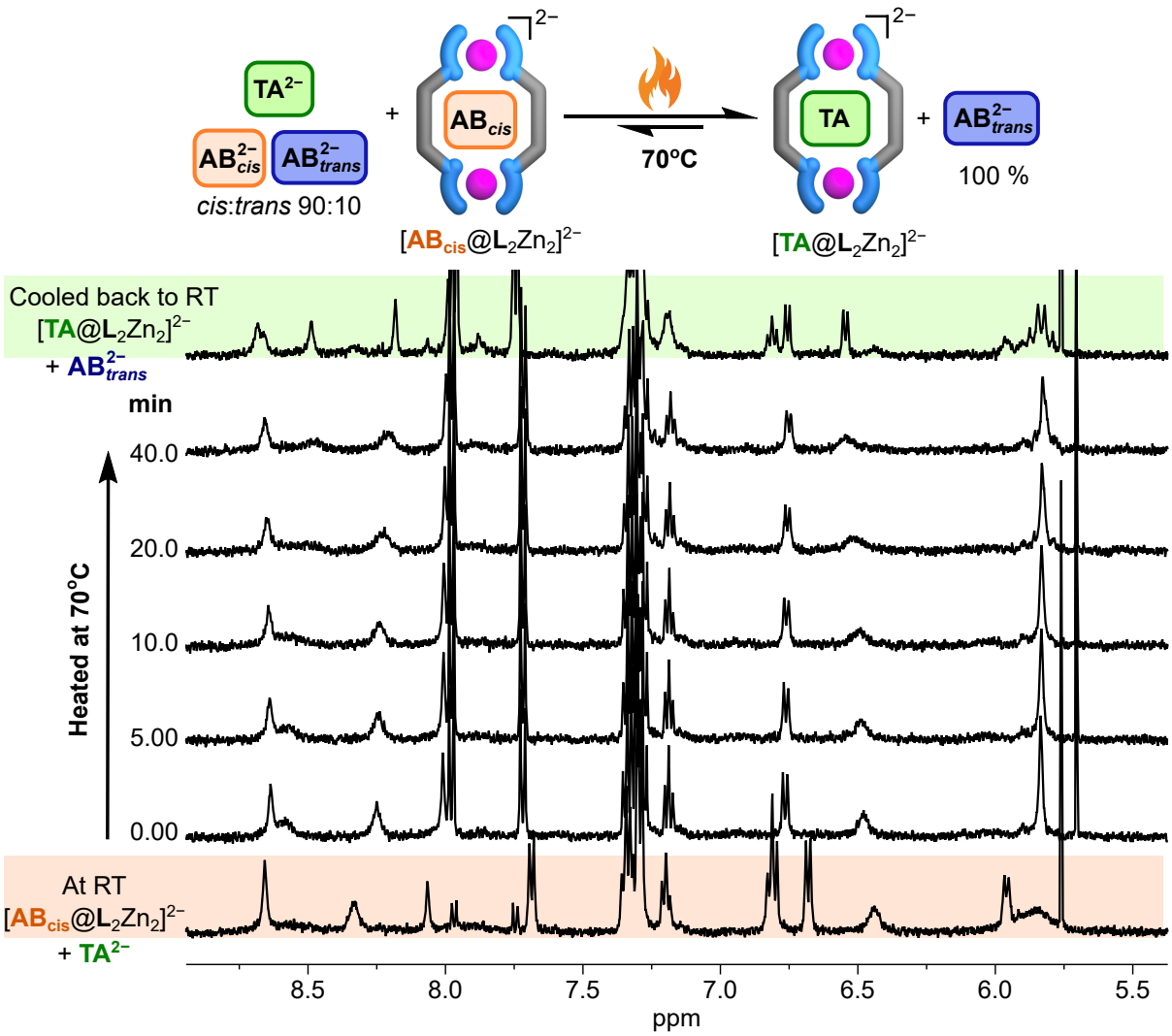

Figure 4.32 Variable temperature (VT) ^{1}H NMR spectra (500 µM, 500 MHz, DMSO-d_6, 298 K) recorded for the sample containing [$\mathbf{L^R}_2Zn_2$], $\mathbf{AB^{2-}_{\mathit{cis}}}$ (1 equiv.), $\mathbf{D\text{-}TA^{2-}}$ (1 equiv.) at 70 °C for 20 min. Initial spectrum and final spectrum after cooling down to 25 °C are compared.

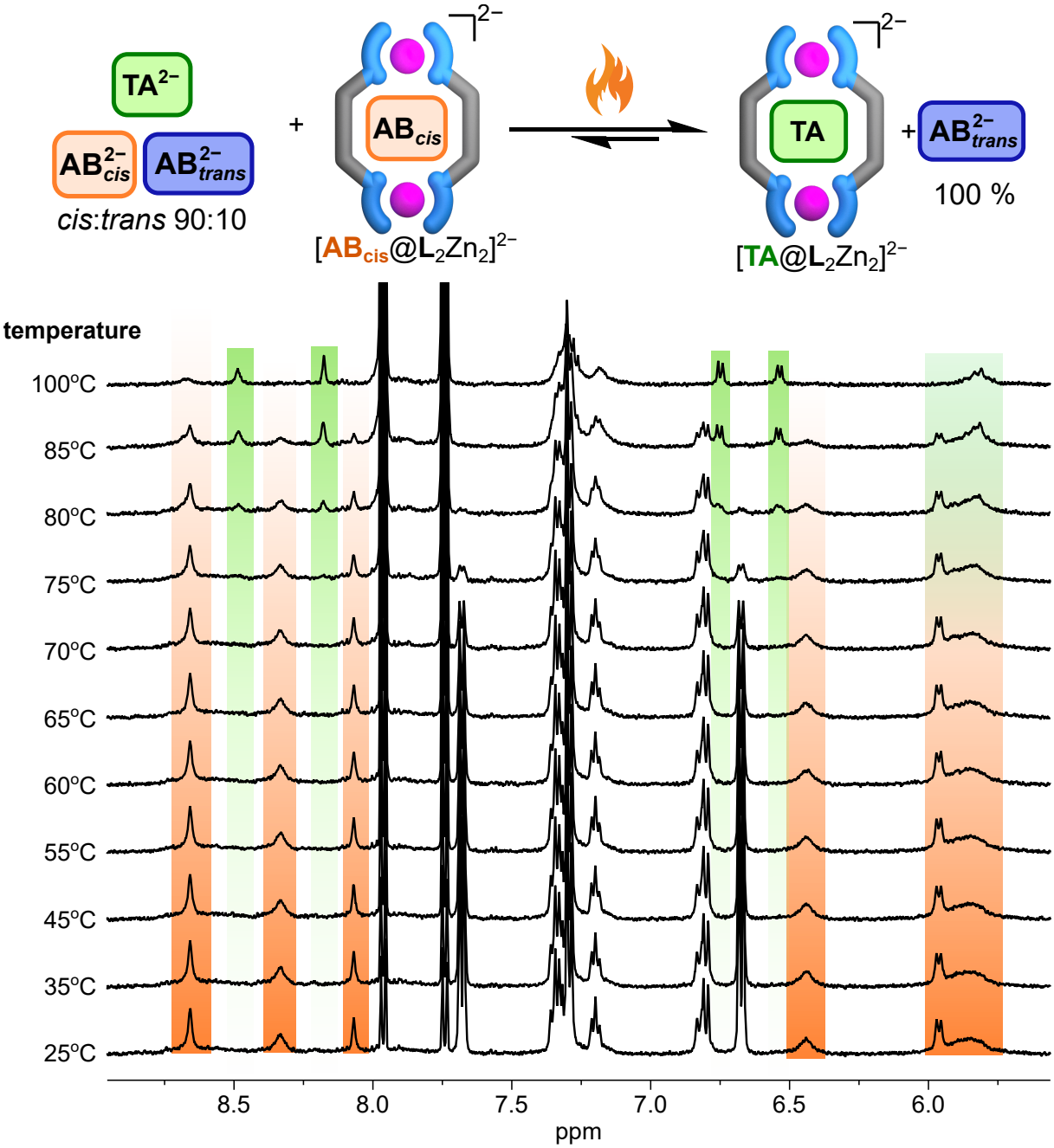

Figure 4.33 ^{1}H NMR spectra of sample containing $[(\mathbf{AB}_{cis})@\mathbf{L}^{\mathbf{R}}{}_2Zn_2]^{2-}$, **D-TA**$^{\mathbf{2-}}$ (2 equiv.) and $\mathbf{AB}^{\mathbf{2-}}_{cis}$ (4 equiv.) recorded at increasing temperature (25-100 °C). Sample was heated externally using a heating block for 10 min at each step, cooled down before measuring the NMR.

4.4.6 Photoisomerization kinetics

4.4.6.1 Photoisomerization under competitive binding

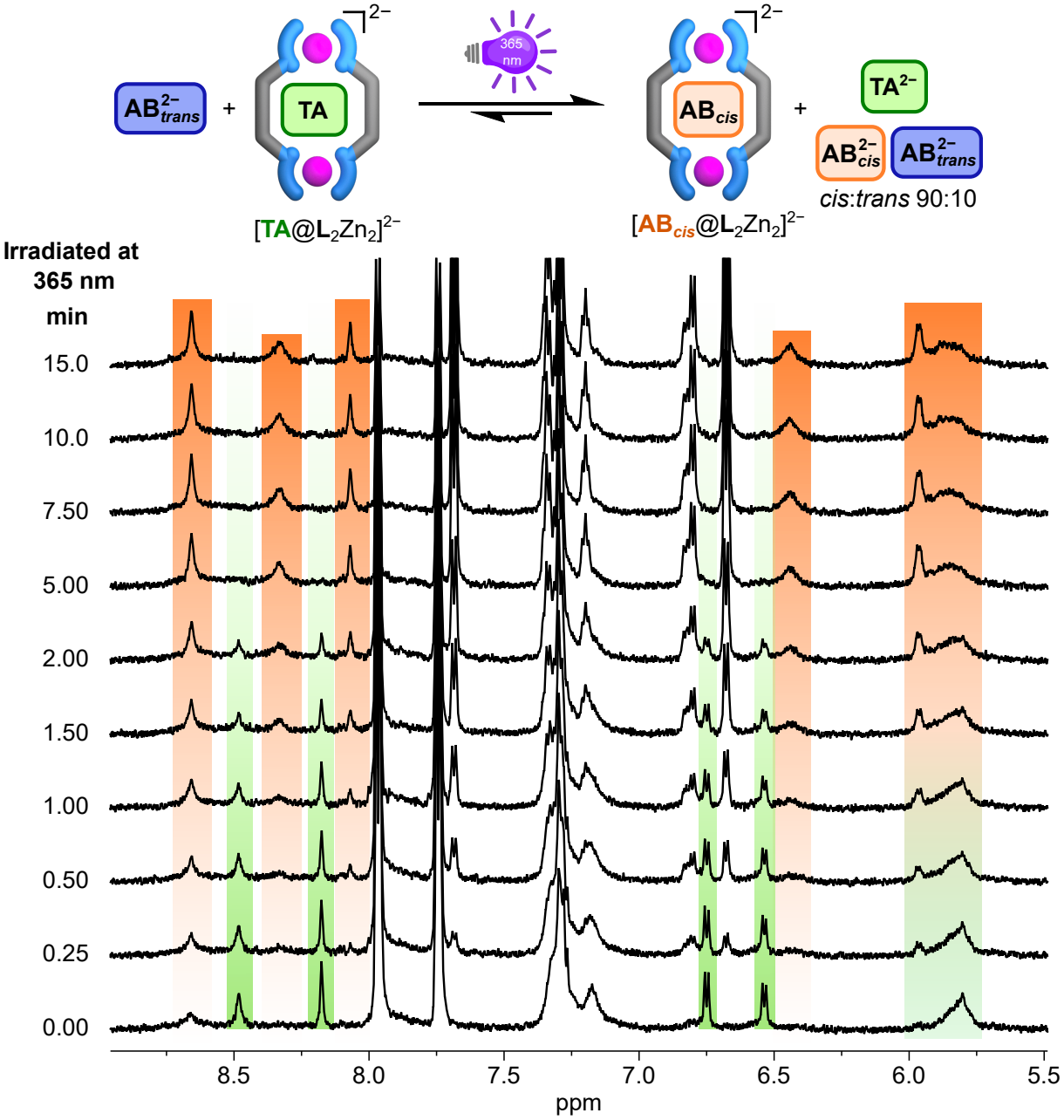

Figure 4.34 ^{1}H NMR spectra recorded for the sample containing host with 4 equiv. $\mathbf{AB}^{\mathbf{2-}}_{trans}$ and 2 equiv. **D-TA**$^{\mathbf{2-}}$, using pseudo-2D kinetics under continuous irradiation at 365 nm with *in situ* NMR illumination for 15 min (1 mM, 600 MHz, DMSO-d_6, 298 K).

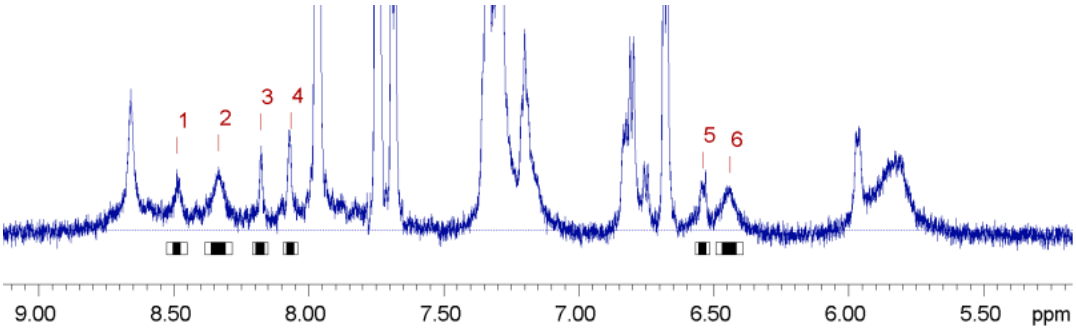

Fitted function alternatives:	f(t) = Io - kt f(t) = Io * exp (-kt) f(t) = Io * exp (-kt) + C f(t) = Io * [1-exp(-kt)] f(t) = Io * [1-exp(-kt)] + C f(t) = Io / [(k2/k1)-1)] * [exp(-k1t) - exp(-k2t)] f(t) = Io / [(k2/k1)-1)] * [exp(-k1t) - exp(-k2t)] + C f(t) = Io * [exp (-k2t) - exp(-k1t)] f(t) = Io * [exp (-k2t) - exp(-k1t)] + C f(t) = Io / (1 + lokt) f(t) = Io / (1 + lokt) + C
Random error estimation of data:	RMS per spectrum (or trace/plane)
Systematic error estimation of data:	worst case per peak scenario
Fit parameter Error estimation method:	from fit using calculated y uncertainties
Confidence level:	95%
Used peaks:	
Used integrals:	area integral
Used time:	all values (including replicates) used

Peak name	F2 [ppm]	k [1/min]	error	fitInfo
1	8.487	0.513	0.008853	Done
2	8.333	0.572	0.007619	Done
3	8.179	0.568	0.006666	Done
4	8.066	0.569	0.008224	Done
5	6.540	0.584	0.006204	Done
6	6.439	0.598	0.008031	Done

Figure 4.35 pseudo-2D analysis result obtained from Bruker Dynamics Center for the experiment depicted in Figure 4.34. (top) Non-overlapping signals and their integration used for calculation. (bottom) Analysis settings and rate constants along with the error estimation extracted from the integrated traces.

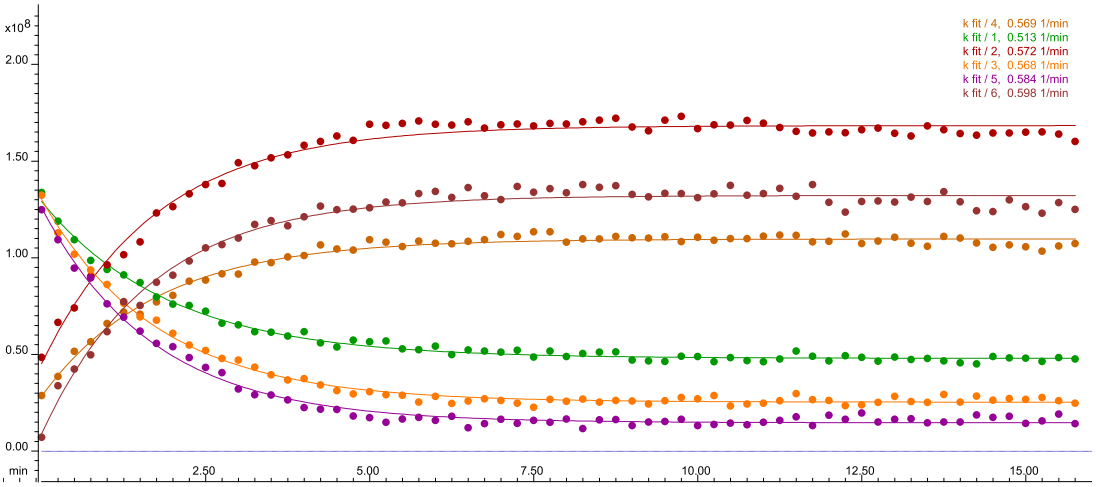

Figure 4.36 Fit and rate constants generated by Bruker Dynamics Center from the pseudo-2D kinetics experiment depicted in Figure 4.34.

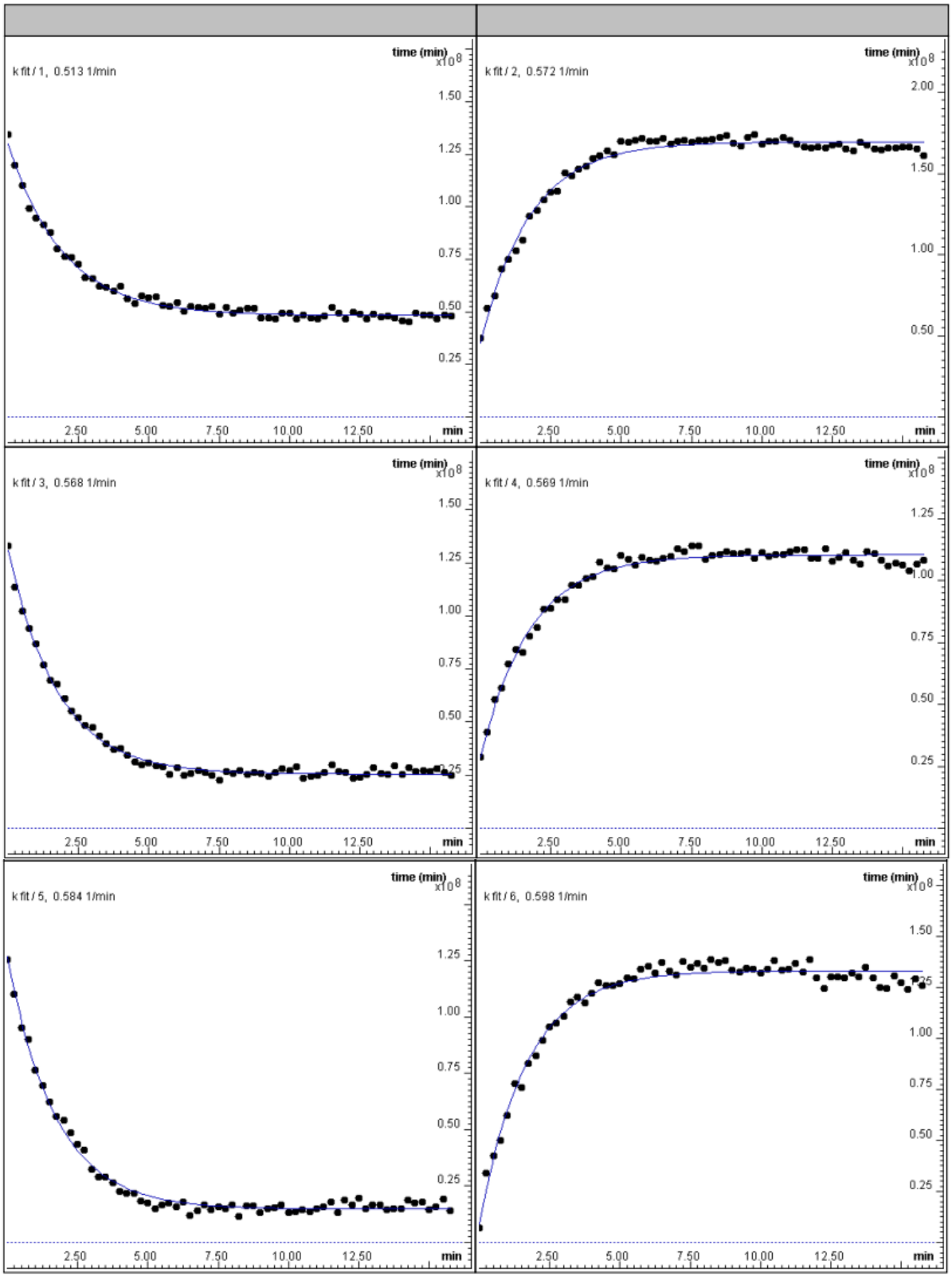

Figure 4.37 Fit and rate constants generated for individual non-overlapping signals by Bruker Dynamics Center from the pseudo-2D kinetics experiment depicted in Figure 4.34.

4.4.6.2 Photoisomerization in the absence of a competing guest

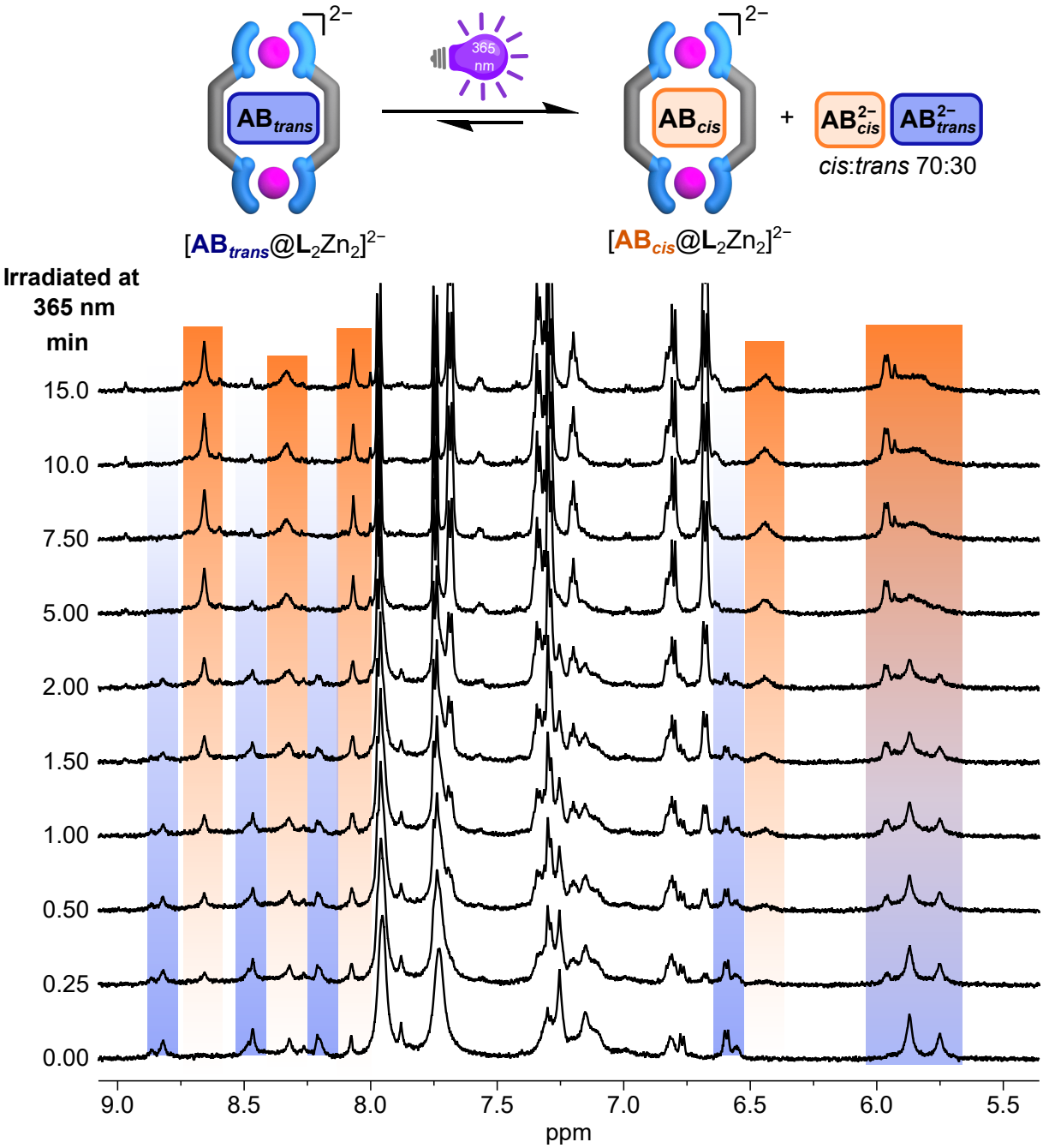

Figure 4.38 ^{1}H NMR spectra recorded for the sample containing host with 2 equiv. $\mathbf{AB}^{2-}_{trans}$, using pseudo-2D kinetics under continuous irradiation at 365 nm with *in situ* NMR illumination for 15 min (1 mM, 600 MHz, DMSO-d_6, 298 K).

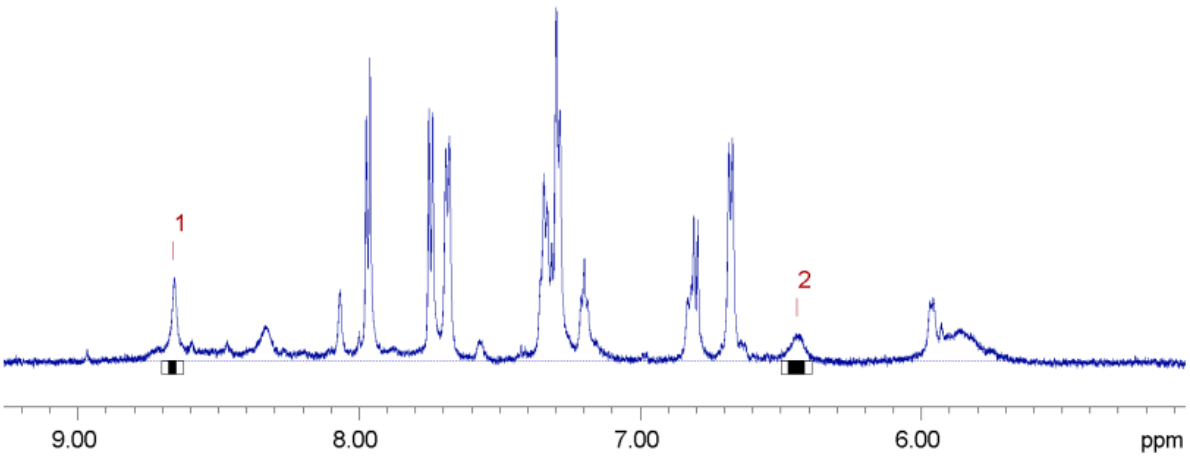

Fitted function alternatives:	f(t) = Io - kt f(t) = Io * exp (-kt) f(t) = Io * exp (-kt) + C f(t) = Io * [1-exp(-kt)] f(t) = Io * [1-exp(-kt)] + C f(t) = Io / [(k2/k1)-1)] * [exp(-k1t) - exp(-k2t)] f(t) = Io / [(k2/k1)-1)] * [exp(-k1t) - exp(-k2t)] + C f(t) = Io * [exp (-k2t) - exp(-k1t)] f(t) = Io * [exp (-k2t) - exp(-k1t)] + C f(t) = Io / (1 + lokt) f(t) = Io / (1 + lokt) + C
Random error estimation of data:	RMS per spectrum (or trace/plane)
Systematic error estimation of data:	worst case per peak scenario
Fit parameter Error estimation method:	from fit using calculated y uncertainties
Confidence level:	95%
Used peaks:	
Used integrals:	area integral
Used time:	all values (including replicates) used

Peak name	F2 [ppm]	k [1/min]	error	fitInfo
1	8.663	0.421	0.002791	Done
2	6.444	0.430	0.004368	Done

Figure 4.39 pseudo-2D analysis result obtained from Bruker Dynamics Center for the experiment depicted in Figure 4.38. (top) Non-overlapping signals and their integration used for calculation. Only the emerging signals are considered. (bottom) Analysis settings and rate constants along with the error estimation extracted from the integrated traces.

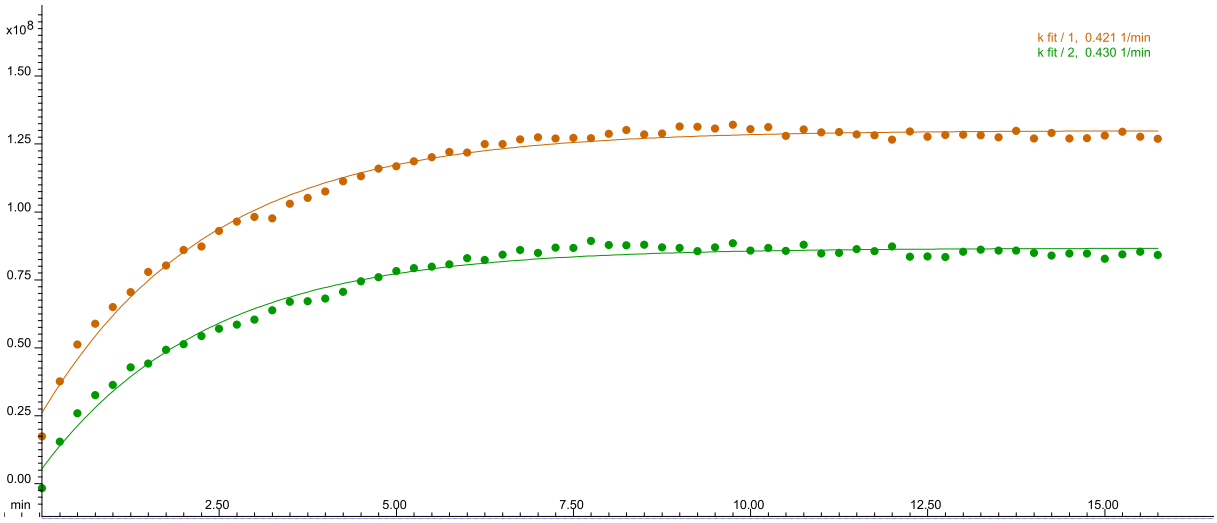

Figure 4.40 Fit and rate constants generated for each non-overlapping growing signal by Bruker Dynamics Center from the pseudo-2D kinetics experiment depicted in Figure 4.38.

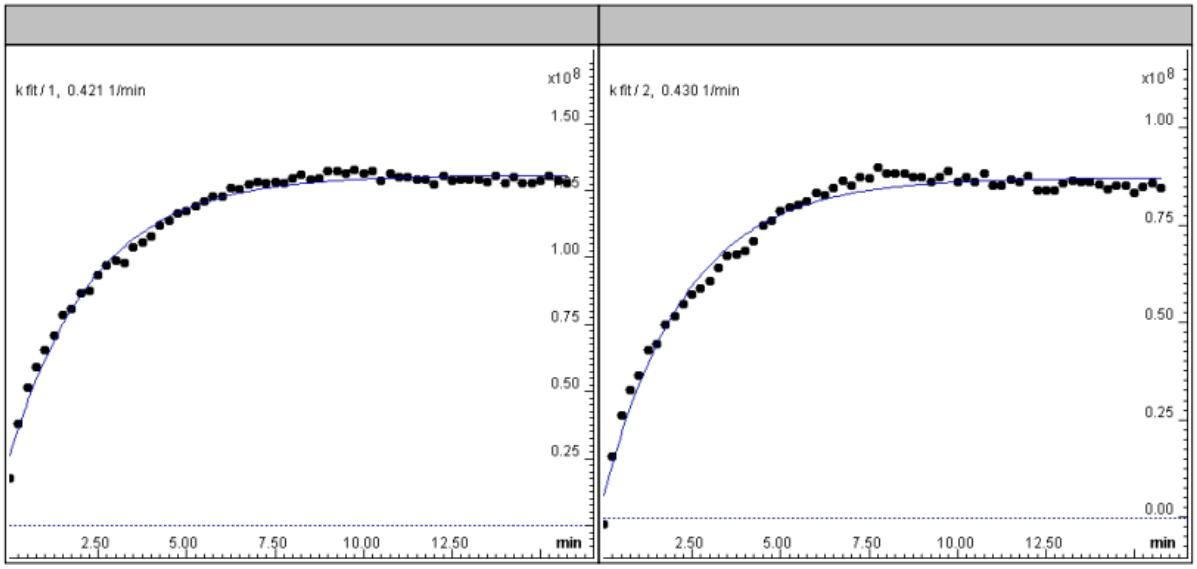

Figure 4.41 Fit and rate constants generated for individual non-overlapping growing signals by Bruker Dynamics Center from the pseudo-2D kinetics experiment depicted in Figure 4.38.

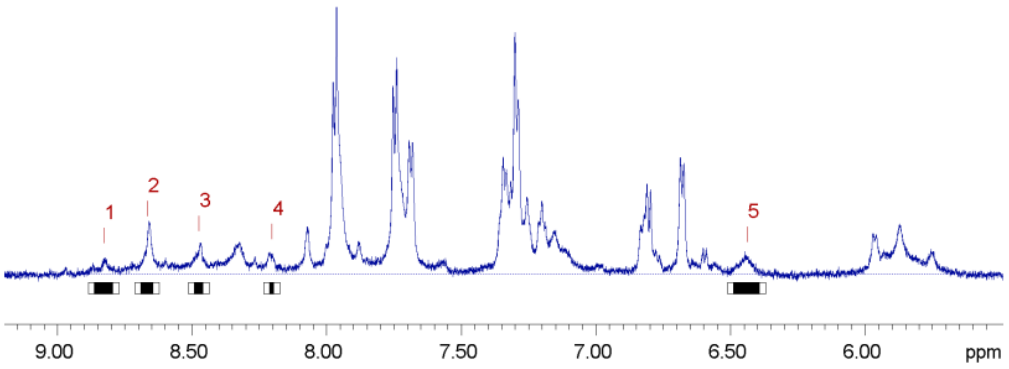

Fitted function alternatives:	f(t) = Io - kt f(t) = Io * exp (-kt) f(t) = Io * exp (-kt) + C f(t) = Io * [1-exp(-kt)] f(t) = Io * [1-exp(-kt)] + C f(t) = Io / [(k2/k1)-1)] * [exp(-k1t) - exp(-k2t)] f(t) = Io / [(k2/k1)-1)] * [exp(-k1t) - exp(-k2t)] + C f(t) = Io * [exp (-k2t) - exp(-k1t)] f(t) = Io * [exp (-k2t) - exp(-k1t)] + C f(t) = Io / (1 + lokt) f(t) = Io / (1 + lokt) + C
Random error estimation of data:	RMS per spectrum (or trace/plane)
Systematic error estimation of data:	worst case per peak scenario
Fit parameter Error estimation method:	from fit using calculated y uncertainties
Confidence level:	95%
Used peaks:	
Used integrals:	area integral
Used time:	all values (including replicates) used

Peak name	F2 [ppm]	k [1/min]	error	fitInfo
1	8.827	0.441	0.006847	Done
2	8.666	0.416	0.002833	Done
3	8.474	0.420	0.005473	Done
4	8.202	0.466	0.006275	Done
5	6.438	0.429	0.004581	Done

Figure 4.42 pseudo-2D analysis result obtained from Bruker Dynamics Center for the experiment depicted in Figure 4.38. (top) Non-overlapping signals and their integration used for calculation. Both growing and decaying signals are considered for the calculation. (bottom) Analysis settings and rate constants along with the error estimation extracted from the integrated traces.

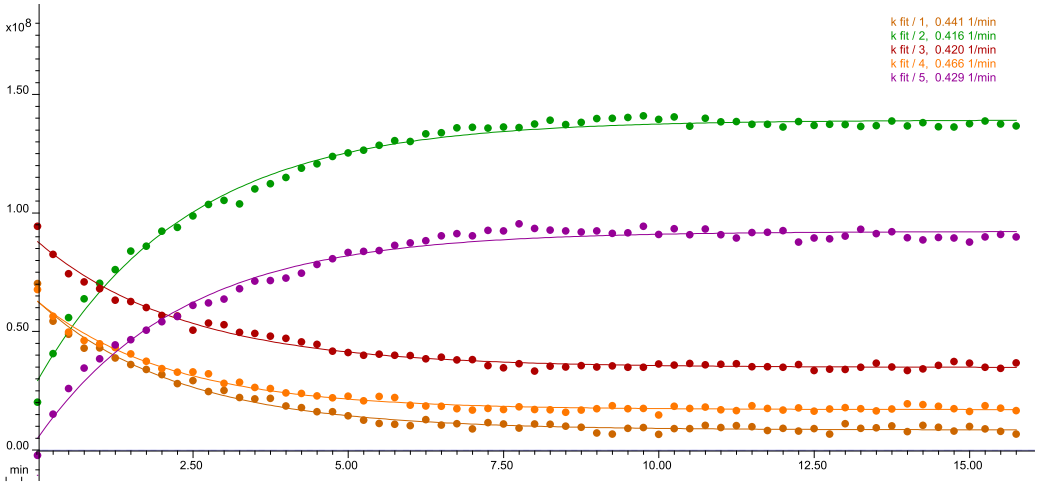

Figure 4.43 Fit and rate constants generated for each non-overlapping signal by Bruker Dynamics Center from the pseudo-2D kinetics experiment depicted in Figure 4.38.

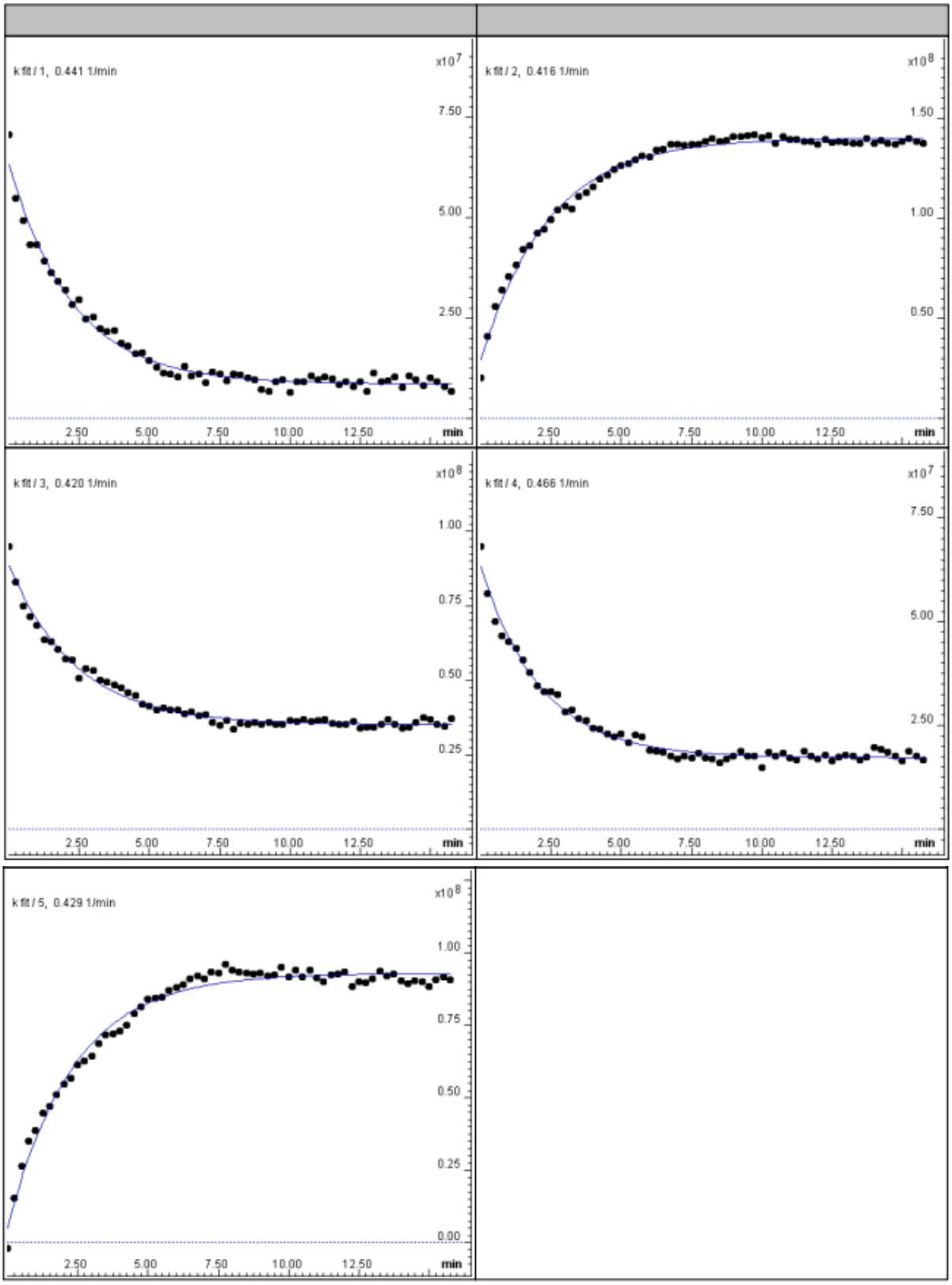

Figure 4.44 Fit and rate constants generated for individual non-overlapping signals by Bruker Dynamics Center from the pseudo-2D kinetics experiment depicted in Figure 4.38.

4.4.7 Guest scope for reversible guest exchange

4.4.7.1 Deprotonated naproxen

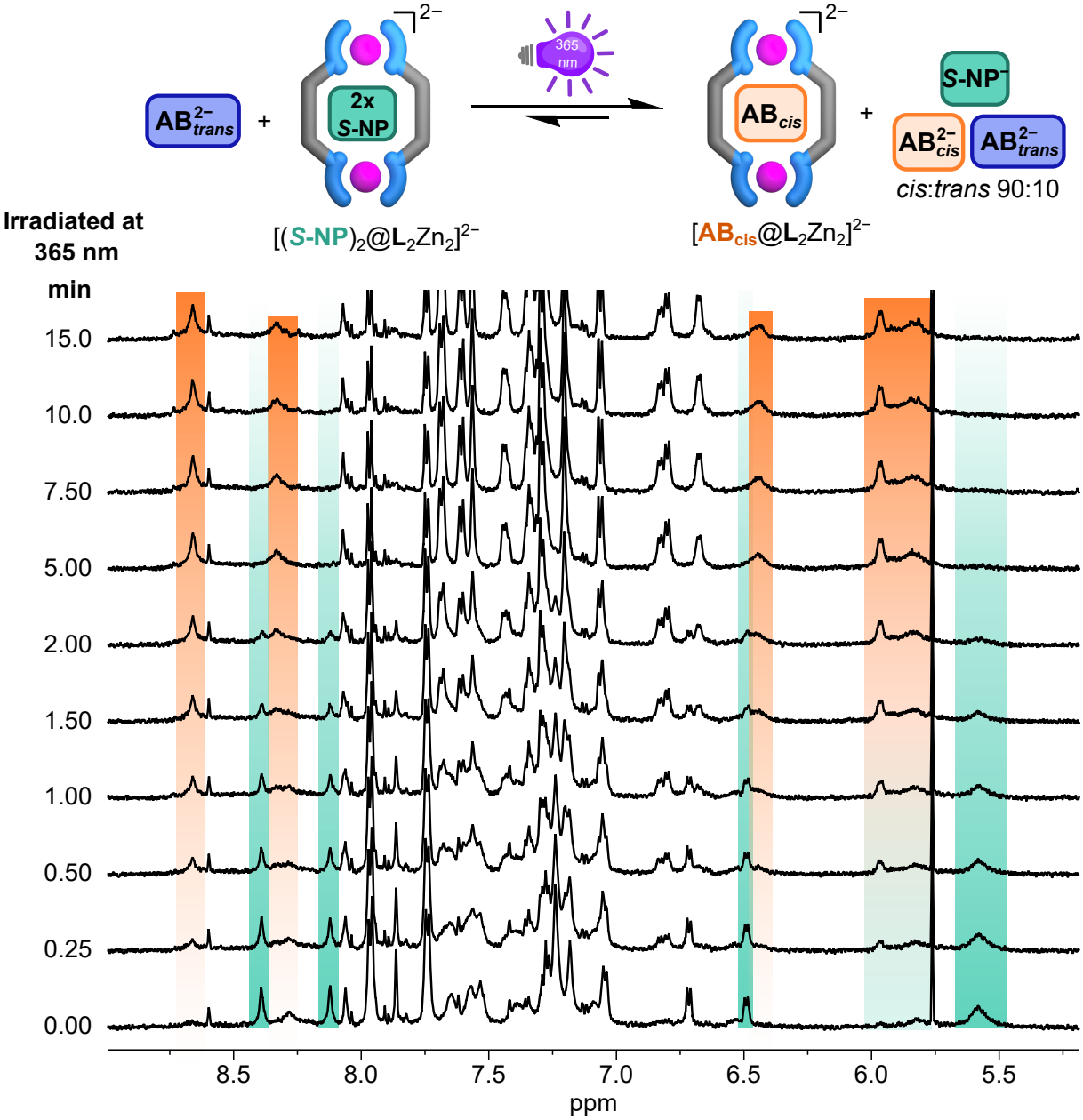

Figure 4.45 ^{1}H NMR spectra recorded the host with 1.5 equiv. $\mathbf{AB}^{2-}_{trans}$ and 5 equiv. $\mathbf{NP}^{-1}$ using pseudo-2D kinetics under continuous irradiation at 365 nm with *in situ* NMR illumination for 15 min (1 mM, 600 MHz, DMSO-d_6, 298 K). Highlighted signals show 1:1 and 1:2 ($\boldsymbol{S}$-$\mathbf{NP}^{-}$)@[$\mathbf{L}^{\mathbf{R}}{}_2\mathrm{Zn}_2$] population (teal) and [($\mathbf{AB}_{cis}$)@$\mathbf{L}^{\mathbf{R}}{}_2\mathrm{Zn}_2$]$^{2-}$ complex (orange).

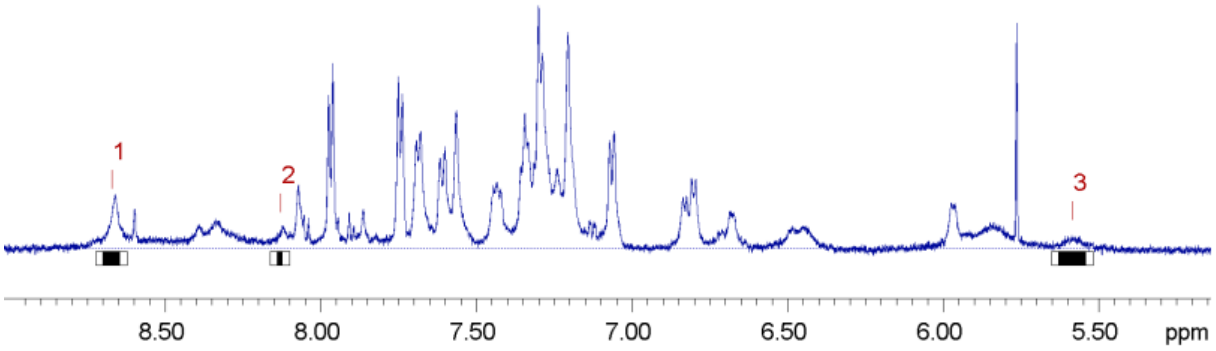

Fitted function alternatives:	f(t) = Io - kt f(t) = Io * exp (-kt) f(t) = Io * exp (-kt) + C f(t) = Io * [1-exp(-kt)] f(t) = Io * [1-exp(-kt)] + C f(t) = Io / [(k2/k1)-1)] * [exp(-k1t) - exp(-k2t)] f(t) = Io / [(k2/k1)-1)] * [exp(-k1t) - exp(-k2t)] + C f(t) = Io * [exp (-k2t) - exp(-k1t)] f(t) = Io * [exp (-k2t) - exp(-k1t)] + C f(t) = Io / (1 + lokt) f(t) = Io / (1 + lokt) + C
Random error estimation of data:	RMS per spectrum (or trace/plane)
Systematic error estimation of data:	worst case per peak scenario
Fit parameter Error estimation method:	from fit using calculated y uncertainties
Confidence level:	95%
Used peaks:	
Used integrals:	area integral
Used time:	all values (including replicates) used

Peak name	F2 [ppm]	k [1/min]	error	fitInfo
1	8.671	0.674	0.005783	Done
2	8.129	0.646	0.007038	Done
3	5.583	0.662	0.005564	Done

Figure 4.46 pseudo-2D analysis result obtained from Bruker Dynamics Center for the experiment depicted in Figure 4.45. (top) Non-overlapping signals and their integration used for calculation. (bottom) Analysis settings and rate constants along with the error estimation extracted from the integrated traces.

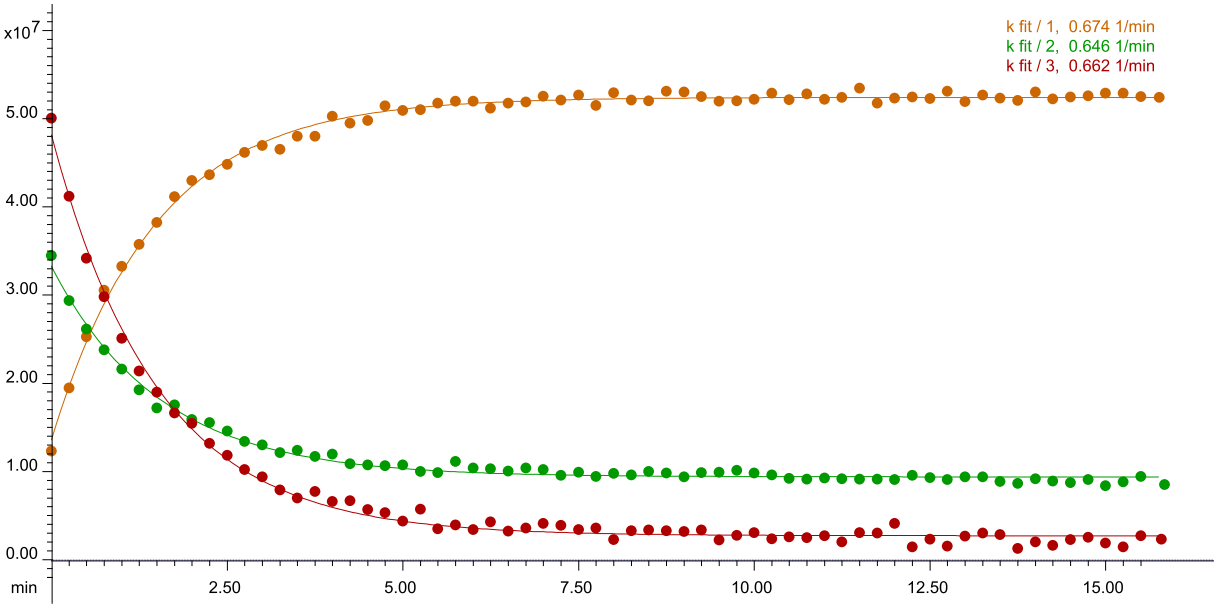

Figure 4.47 Fit and rate constants generated for each non-overlapping signal by Bruker Dynamics Center from the pseudo-2D kinetics experiment depicted in Figure 4.45.

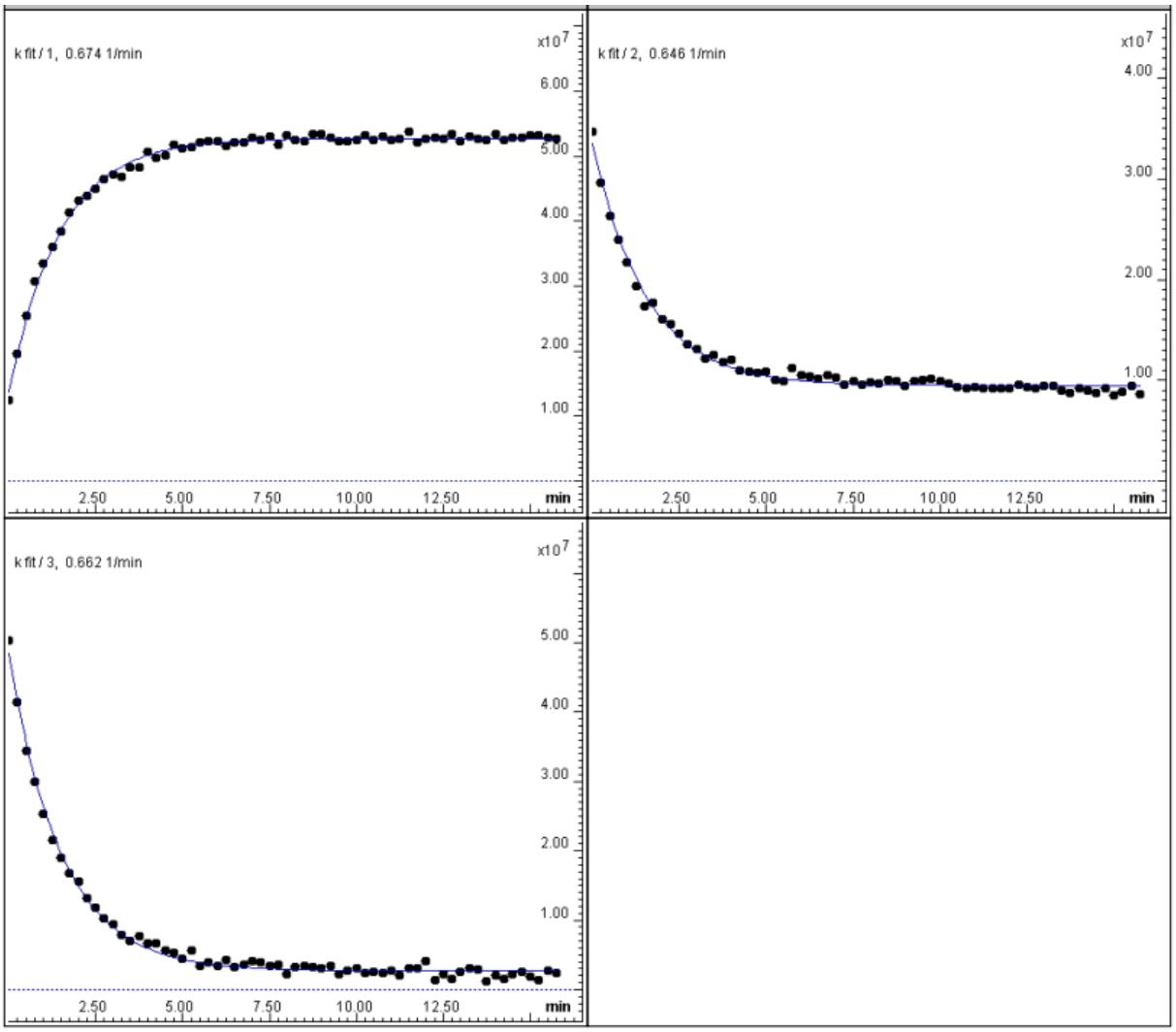

Figure 4.48 Fit and rate constants generated for individual non-overlapping signals by Bruker Dynamics Center from the pseudo-2D kinetics experiment depicted in Figure 4.45.

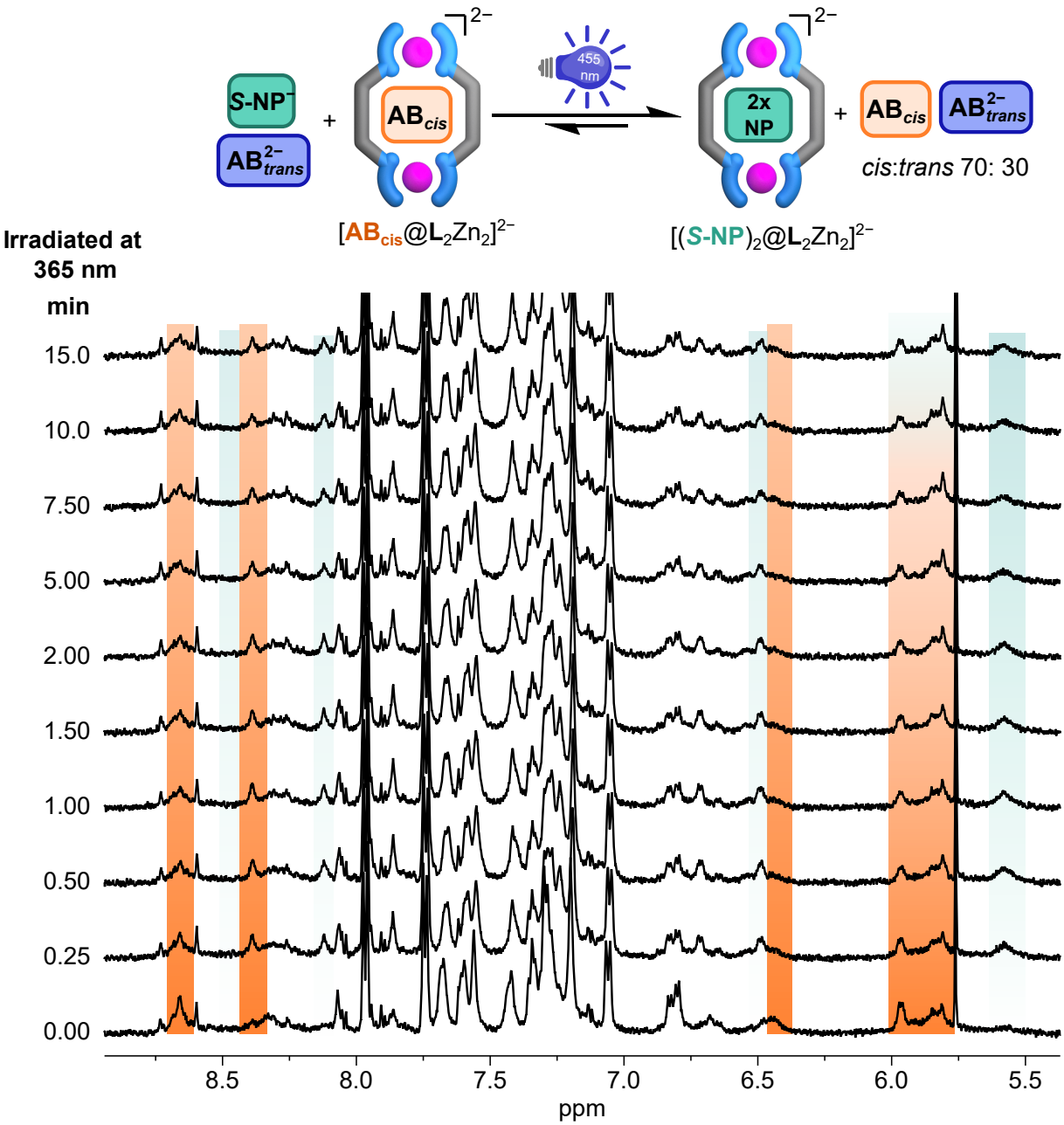

Figure 4.49 ^{1}H NMR spectra recorded for the sample containing host with 1.5 equiv. of $\mathbf{AB}^{\mathbf{2-}}_{\boldsymbol{cis}}$ and 5 equiv. of $\boldsymbol{S}$-$\mathbf{NP}^{-}$, using pseudo-2D kinetics under continuous irradiation at 455 nm with *in situ* NMR illumination for 15 min (1 mM, 600 MHz, DMSO-d_6, 298 K). The $[(\mathbf{AB}_{\boldsymbol{cis}})@\mathbf{L}^{\mathbf{R}}{}_2\mathrm{Zn}_2]^{2-}$ complex signals are mostly invariant, apart from trace amount of $[(\boldsymbol{S}\text{-}\mathbf{NP})_2@\mathbf{L}^{\mathbf{R}}{}_2\mathrm{Zn}_2]^{2-}$ formed, indicating only partial 455 nm-induced isomerization of the bound guest.

4.4.7.2 Acetate

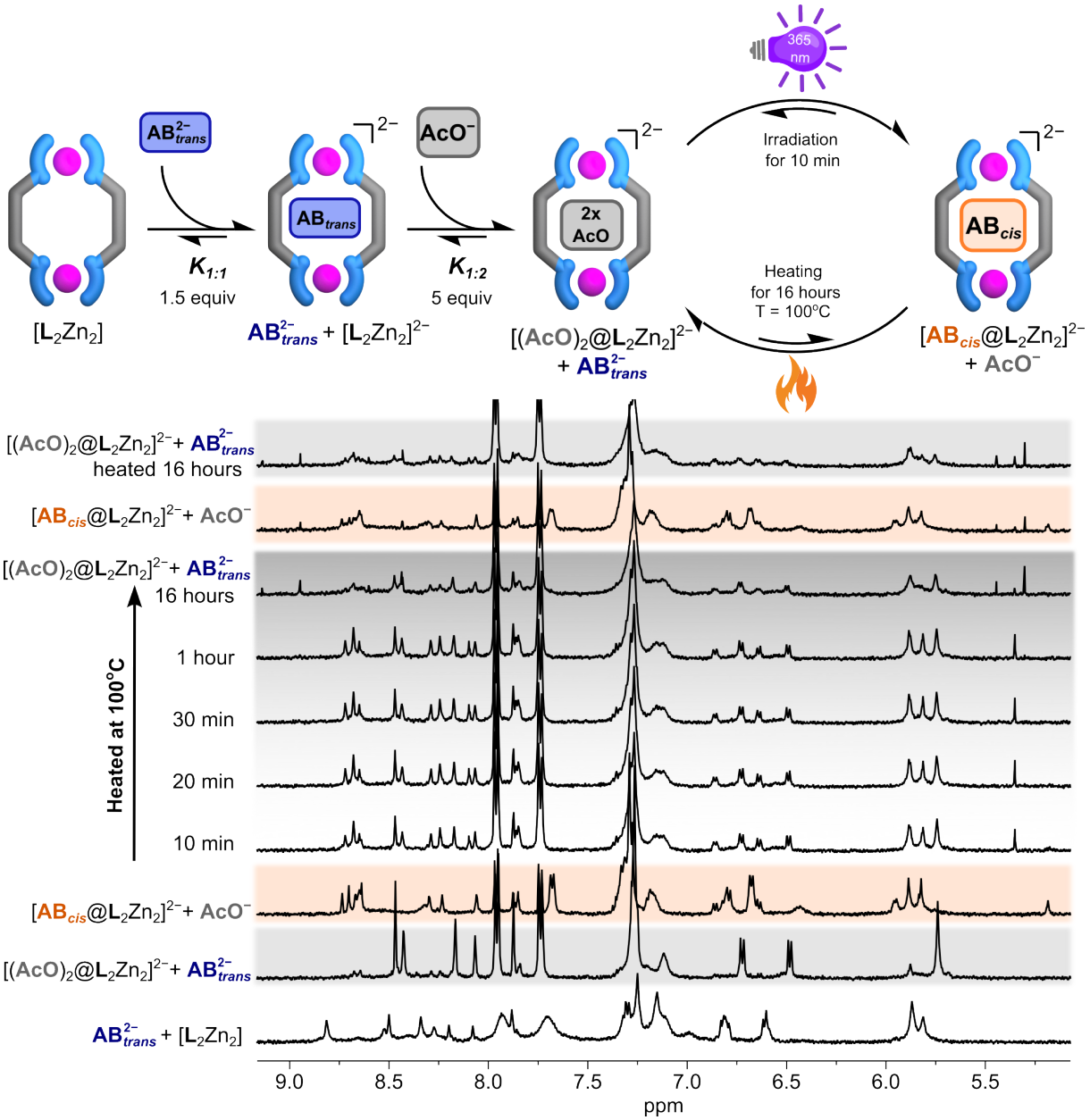

Figure 4.50 ^{1}H NMR spectra recorded for the sample containing host with 1.5 equiv. of $\mathbf{AB^{2-}_{\mathit{cis}}}$ and 5 equiv. of $\mathbf{AcO^-}$ (500 µM, 500 MHz, DMSO-d_6, 298 K). $\mathbf{AcO^-}$ replaces $\mathbf{AB^{2-}_{\mathit{trans}}}$ and get displaced by $\mathbf{AB^{2-}_{\mathit{cis}}}$ when irradiated at 365 nm. The bound *cis* guest get removed only under long hours of heating at 100 °C. Guest exchange cycles can be carried out at harsh conditions although partial degradation is observed after prolonged heating.

4.4.7.3 Benzoate

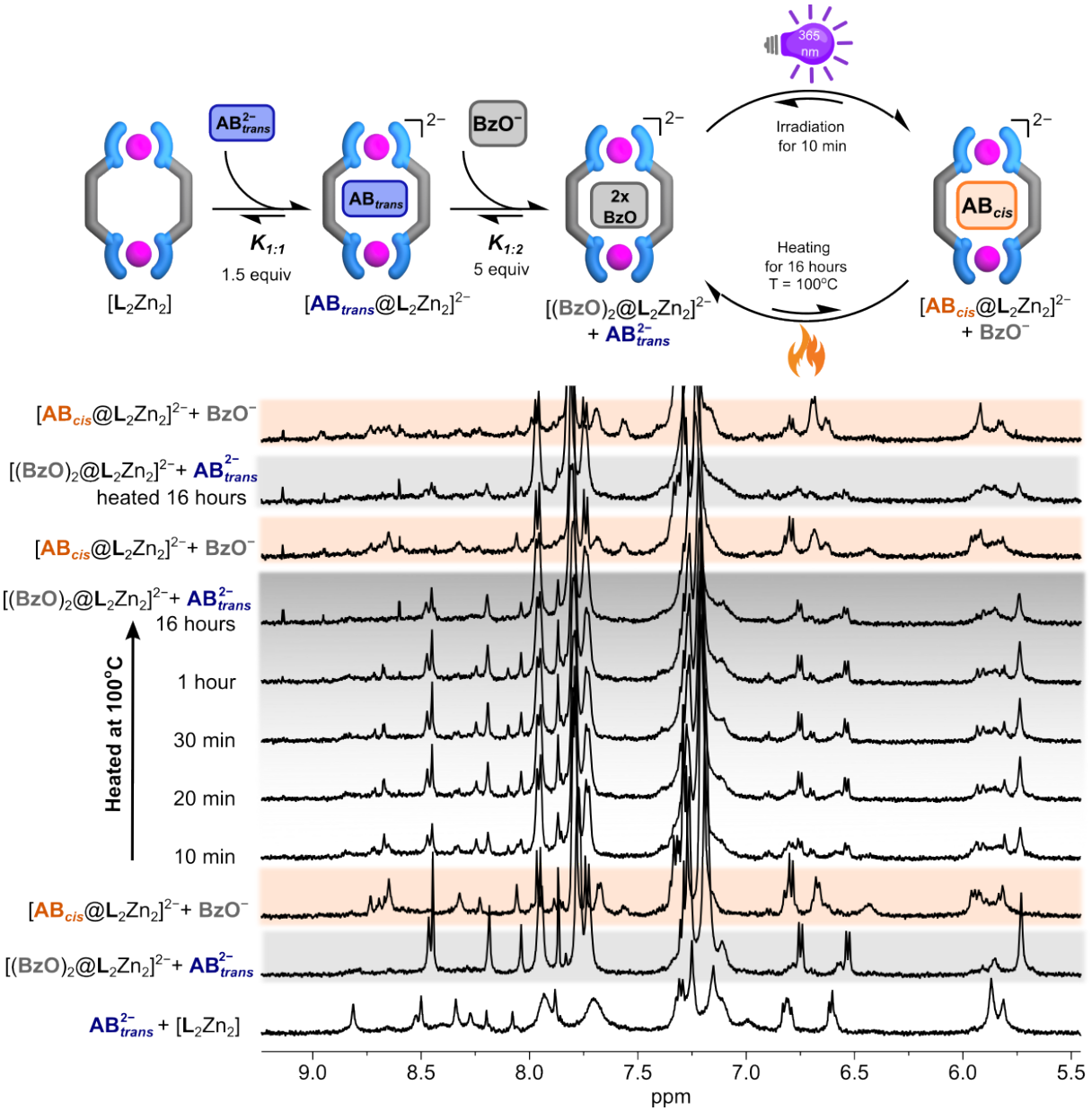

Figure 4.51 ^{1}H NMR spectra recorded for the sample containing host with 1.5 equiv. of $\mathbf{AB}^{\mathbf{2-}}_{cis}$ and 5 equiv. of $\mathbf{BzO}^{-}$ (500 µM, 500 MHz, DMSO-d_6, 298 K). $\mathbf{BzO}^{-}$ replaces $\mathbf{AB}^{\mathbf{2-}}_{trans}$ and get displaced by $\mathbf{AB}^{\mathbf{2-}}_{cis}$ when irradiated at 365 nm. The bound *cis* guest get removed only under long hours of heating at 100 °C. Guest exchange cycles can be carried out at harsh conditions although partial degradation is observed after prolonged heating and irradiation.

4.4.7.4 Glutarate

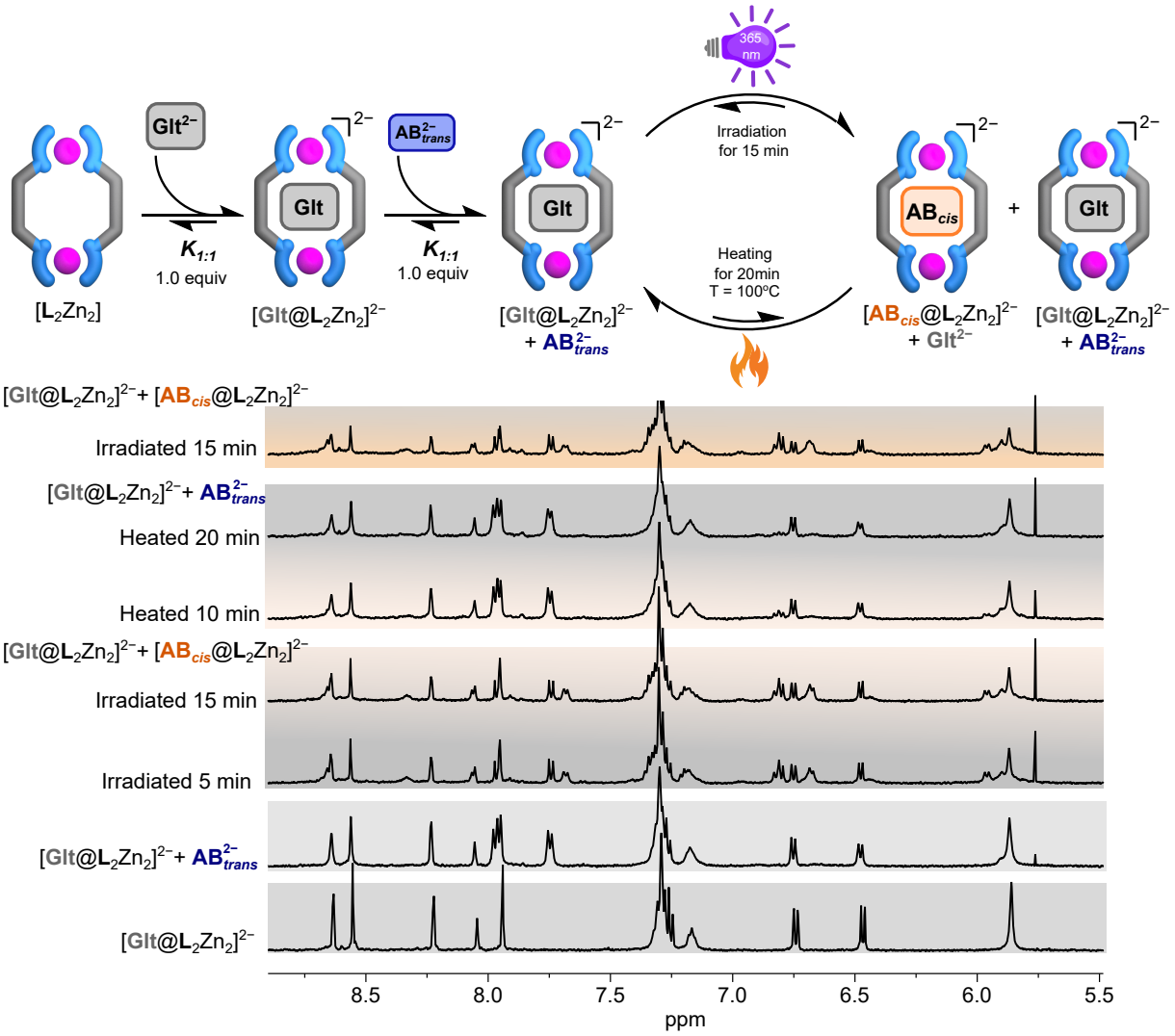

Figure 4.52 ^{1}H NMR spectra recorded for the sample containing host with 1.0 equiv. of $\mathbf{AB}^{\mathbf{2-}}_{cis}$ and 1.0 equiv. of $\mathbf{Glt}^{\mathbf{2-}}$ (500 µM, 500 MHz, DMSO-d_6, 298 K). $\mathbf{Glt}^{\mathbf{2-}}$ replaces $\mathbf{AB}^{\mathbf{2-}}_{trans}$, however only partially displaced by $\mathbf{AB}^{\mathbf{2-}}_{cis}$ after irradiation at 365 nm for 15 min. Thermal relaxation back to $\mathbf{AB}^{\mathbf{2-}}_{trans}$ and reformation of $[(\mathbf{Glt})@\mathbf{L}^{\mathbf{R}}{}_2Zn_2]^{2-}$ takes 20 min of heating at 100 °C. Overall showcases poor reversibility and incomplete cycle

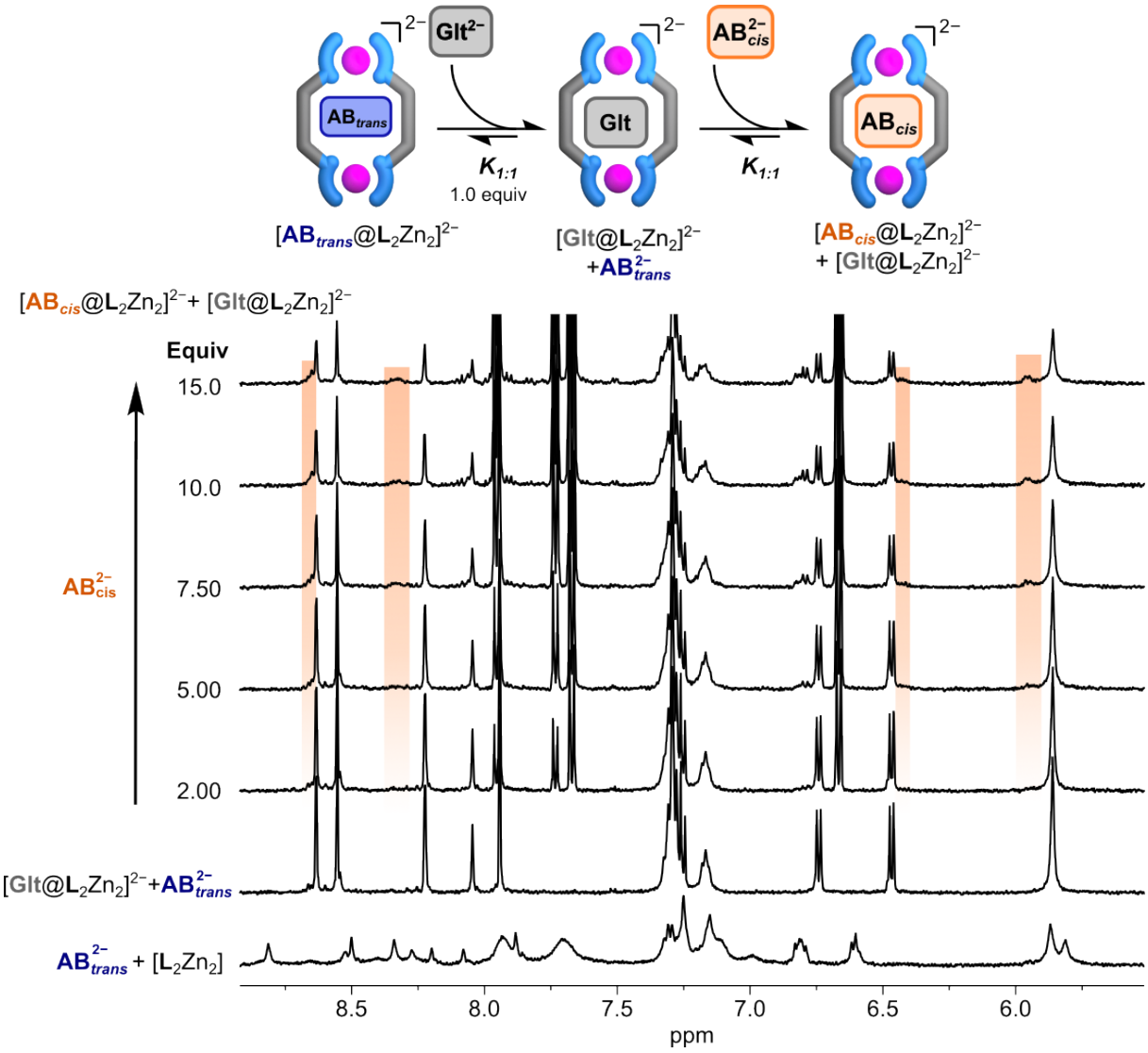

Figure 4.53 ^{1}H NMR titration of $\mathbf{AB}^{\mathbf{2-}}_{cis}$ guest into the sample containing $[(\mathbf{Glt})@\mathbf{L}^{\mathbf{R}}{}_2Zn_2]^{2-}$ formed with 1 equiv. of $\mathbf{Glt}^{\mathbf{2-}}$ and 1 equiv. of $\mathbf{AB}^{\mathbf{2-}}_{trans}$. Only a negligible amount of $[(\mathbf{AB}_{cis})@\mathbf{L}^{\mathbf{R}}{}_2Zn_2]^{2-}$ formed after 15 equiv. addition of cis guest.

4.4.7.5 Acetylene dicarboxylate

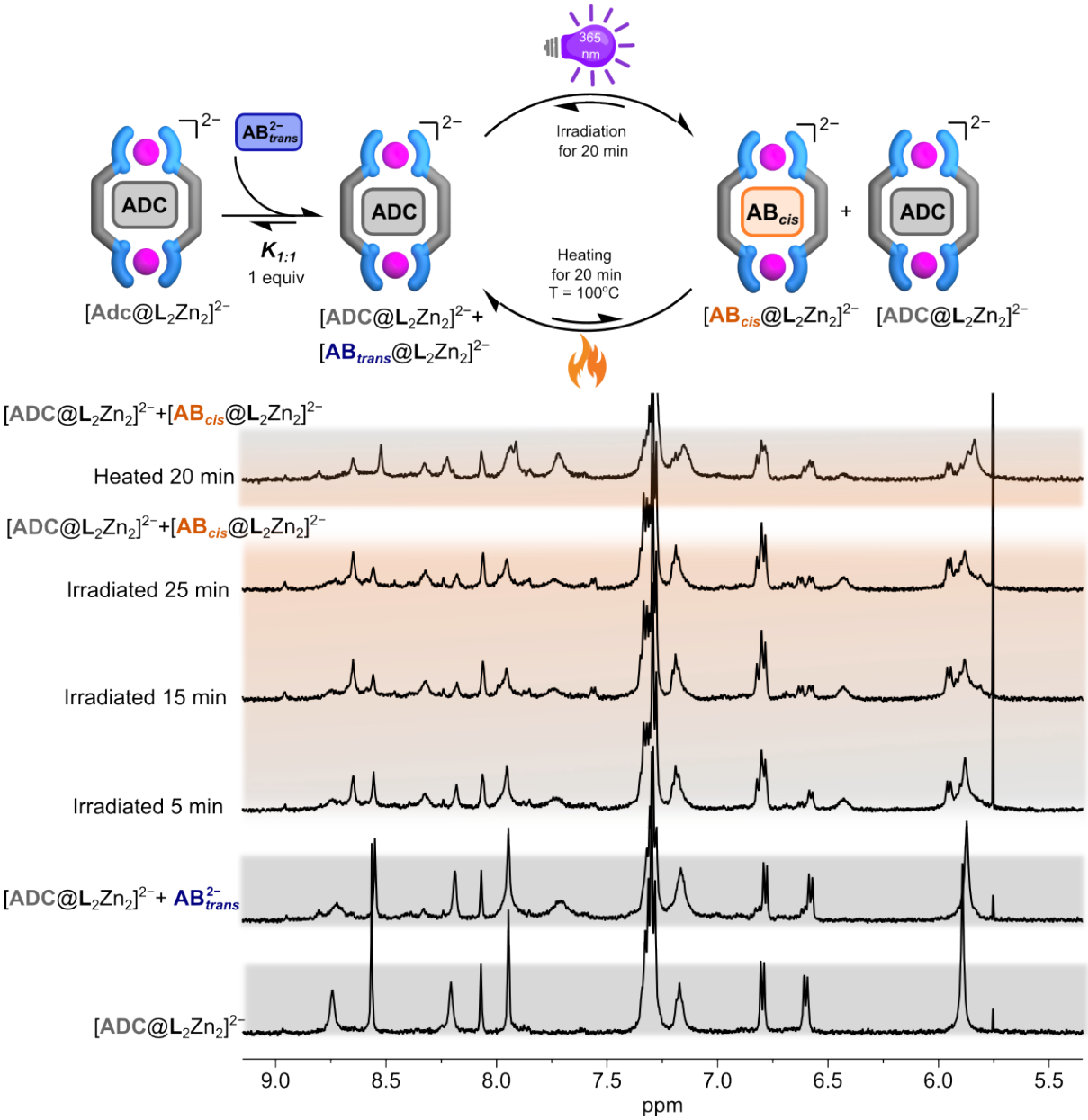

Figure 4.54 ^{1}H NMR spectra recorded for the sample containing host with 1.0 equiv. of $\mathbf{AB}^{\mathbf{2-}}_{cis}$ and 1.0 equiv. of $\mathbf{Adc}^{\mathbf{2-}}$ (500 µM, 500 MHz, DMSO-d_6, 298 K). $\mathbf{Adc}^{\mathbf{2-}}$ replaces $\mathbf{AB}^{\mathbf{2-}}_{trans}$, however only partially displaced by $\mathbf{AB}^{\mathbf{2-}}_{cis}$ after irradiation at 365 nm for 25 min. Thermal relaxation back to $\mathbf{AB}^{\mathbf{2-}}_{trans}$ and reformation of $[(\mathbf{Adc})@\mathbf{L^R}_2Zn_2]^{2-}$ only takes place in a negligible amount. Overall showcases an incomplete cycle.

4.4.7.6 Fumarate

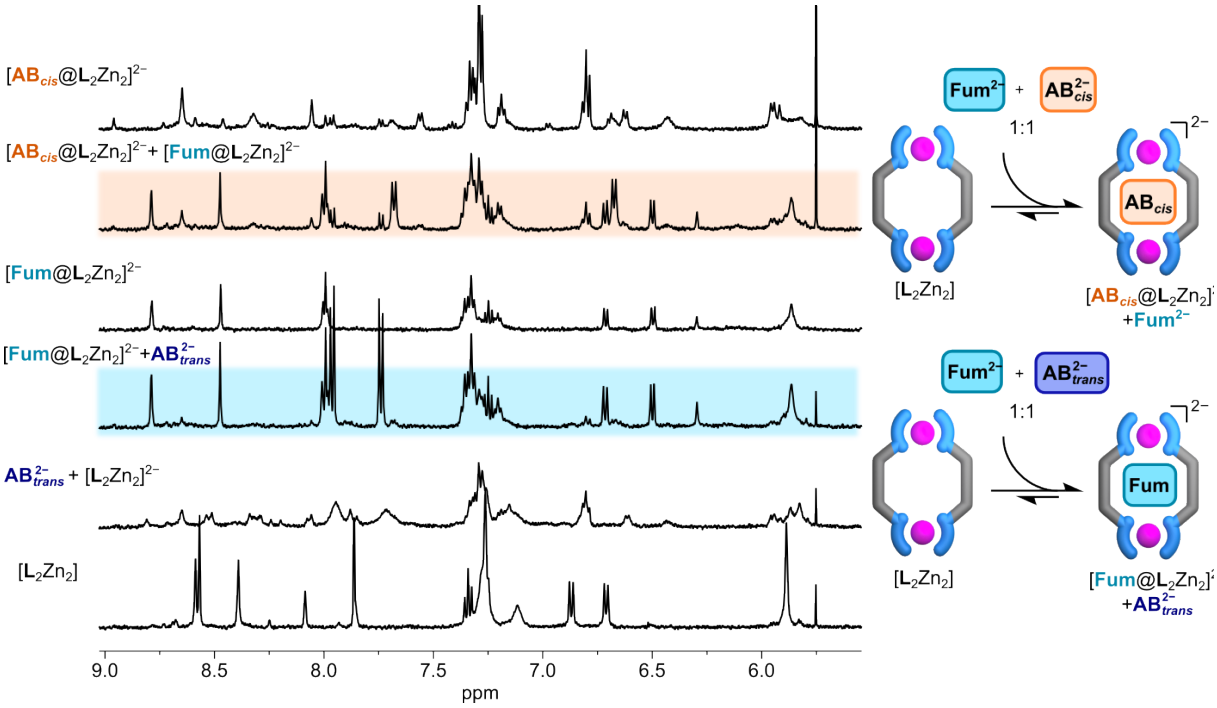

Figure 4.55 ^{1}H NMR competition experiments of [$\mathbf{L^R}_2Zn_2$] with 1 equiv. of $\mathbf{AB^{2-}_{\mathit{cis}}}$, $\mathbf{AB^{2-}_{\mathit{trans}}}$, and $\mathbf{Fum^{2-}}$. Adding $\mathbf{Fum^{2-}}$ to $\mathbf{AB^{2-}_{\mathit{trans}}}$-based host-guest mixture transforms the spectrum to resemble the fumarate-bound complex. Similarly, adding $\mathbf{AB^{2-}_{\mathit{cis}}}$ to [(**Fum**)@$\mathbf{L^R}_2Zn_2$]$^{2-}$ partially forms the *cis*-bound complex. While the binding constant for fumarate is unknown, it likely has higher affinity than $\mathbf{AB^{2-}_{\mathit{cis}}}$.

4.4.8 UV-Vis cycle

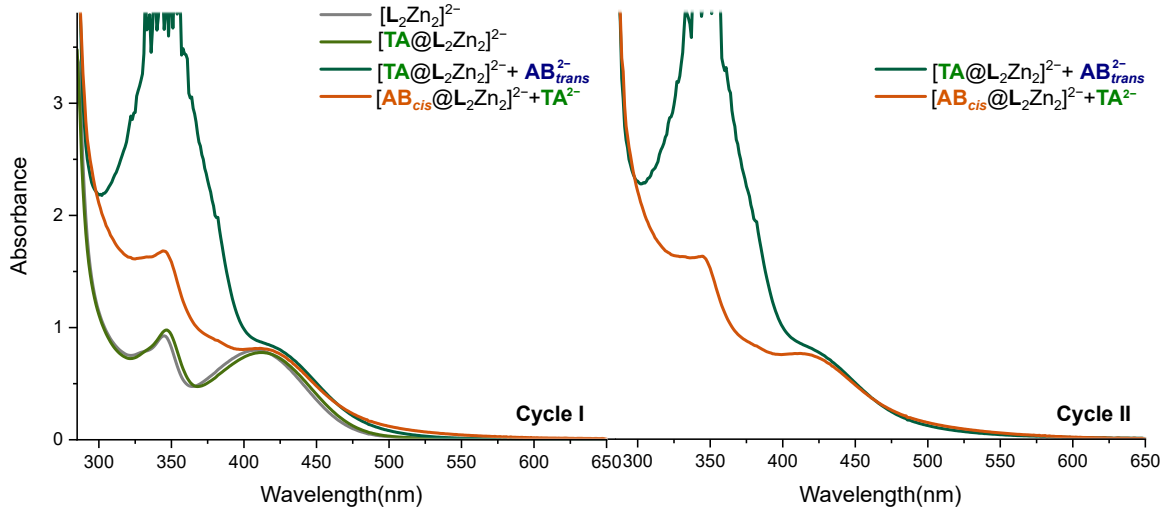

Figure 4.56 The UV-Vis monitored guest exchange cycle for 1.5 equiv. of $\mathbf{AB^{2-}_{\mathit{trans}}}$ and 2 equiv. of $\mathbf{D\text{-}TA^{2-}}$ (500 µM, l =2 mm, DMSO-d_6, 298 K). [(**D-TA**)@$\mathbf{L^R}_2Zn_2$]$^{2-}$ mixture irradiated at 365 nm for 10 min yields [($\mathbf{AB_{\mathit{cis}}}$)@$\mathbf{L^R}_2Zn_2$]$^{2-}$. Heating at 100 °C for 10 min reforms [(**D-TA**)@$\mathbf{L^R}_2Zn_2$]$^{2-}$. This cycle repeats twice with consistent spectral changes.

4.5 References

[1] D. Van Craen, M. G. Kalarikkal, J. J. Holstein, *Journal of the American Chemical Society* **2022**, *144*, 18135–18143.

[2] M. G. Kalarikkal, C. Drechsler, G. Tusha, L. V. Schäfer, D. Van Craen, *Chemistry – A European Journal* **2023**, *29*, e202301613.

[3] M. D. Pluth, K. N. Raymond, *Chemical Society Reviews* **2007**, *36*, 161–171.

[4] A. V. Davis, D. Fiedler, G. Seeber, A. Zahl, R. van Eldik, K. N. Raymond, *Journal of the American Chemical Society* **2006**, *128*, 1324–1333.

[5] J. Santamaría, T. Martín, G. Hilmersson, S. L. Craig, J. Rebek Jr, *Proceedings of the National Academy of Sciences* **1999**, *96*, 8344–8347.

[6] A. Jiménez, R. A. Bilbeisi, T. K. Ronson, S. Zarra, C. Woodhead, J. R. Nitschke, *Angewandte Chemie* **2014**, *126*, 4644–4648.

[7] A. Ghosh, L. Slappendel, B.-N. T. Nguyen, L. K. S. von Krbek, T. K. Ronson, A. M. Castilla, J. R. Nitschke, *Journal of the American Chemical Society* **2023**, *145*, 3828–3832.

[8] R. G. DiNardi, S. Rasheed, S. S. Capomolla, M. H. Chak, I. A. Middleton, L. K. Macreadie, J. P. Violi, W. A. Donald, P. J. Lusby, J. E. Beves, *Journal of the American Chemical Society* **2024**, *146*, 21196–21202.

[9] S. Bivaud, J.-Y. Balandier, M. Chas, M. Allain, S. Goeb, M. Sallé, *Journal of the American Chemical Society* **2012**, *134*, 11968–11970.

[10] Y. Yao, C. Shao, S. Wang, Q. Gong, J. Liu, H. Jiang, Y. Wang, *Communications Chemistry* **2024**, *7*, 43.

[11] M. B. Tipping, L. Pruñonosa Lara, A. B. Solea, L. K. S. von Krbek, M. D. Ward, *Chemical Science* **2024**, *15*, 8488–8499.

[12] W. Xue, T. K. Ronson, Z. Lu, J. R. Nitschke, *Journal of the American Chemical Society* **2022**, *144*, 6136–6142.

[13] C. Colomban, G. Szalóki, M. Allain, L. Gómez, S. Goeb, M. Sallé, M. Costas, X. Ribas, *Chemistry – A European Journal* **2017**, *23*, 3016–3022.

[14] G. H. Clever, S. Tashiro, M. Shionoya, *Journal of the American Chemical Society* **2010**, *132*, 9973–9975.

[15] Y.-R. Zheng, K. Suntharalingam, T. C. Johnstone, S. J. Lippard, *Chemical Science* **2015**, *6*, 1189–1193.

[16] F. Ibukuro, T. Kusukawa, M. Fujita, *Journal of the American Chemical Society* **1998**, *120*, 8561–8562.

[17] J. Wang, L. Avram, Y. Diskin-Posner, M. J. Białek, W. Stawski, M. Feller, R. Klajn, *Journal of the American Chemical Society* **2022**, *144*, 21244–21254.

[18] M. Canton, A. B. Grommet, L. Pesce, J. Gemen, S. Li, Y. Diskin-Posner, A. Credi, G. M. Pavan, J. Andréasson, R. Klajn, *Journal of the American Chemical Society* **2020**, *142*, 14557–14565.

[19] A. I. Hanopolskyi, S. De, M. J. Białek, Y. Diskin-Posner, L. Avram, M. Feller, R. Klajn, *Beilstein Journal of Organic Chemistry* **2019**, *15*, 2398–2407.

[20] T. Kusukawa, M. Fujita, *Journal of the American Chemical Society* **1999**, *121*, 1397–1398.

[21] M. Aggarwal, R. Banerjee, N. Hickey, P. S. Mukherjee, *Angewandte Chemie International Edition* **2024**, *63*, e202411513.

[22] D. Samanta, J. Gemen, Z. Chu, Y. Diskin-Posner, L. J. W. Shimon, R. Klajn, *Proceedings of the National Academy of Sciences* **2018**, *115*, 9379–9384.

[23] K. Hema, A. B. Grommet, M. J. Białek, J. Wang, L. Schneider, C. Drechsler, O. Yanshyna, Y. Diskin-Posner, G. H. Clever, R. Klajn, *Journal of the American Chemical Society* **2023**, *145*, 24755–24764.

[24] H. Dube, D. Ajami, J. Rebek Jr, *Angewandte Chemie* **2010**, *122*, 3260–3263.

[25] J. Gemen, M. J. Białek, M. Kazes, L. J. Shimon, M. Feller, S. N. Semenov, Y. Diskin-Posner, D. Oron, R. Klajn, *Chem* **2022**, *8*, 2362–2379.

[26] J. Maciejewski, A. Sobczuk, A. Claveau, A. Nicolai, R. Petraglia, L. Cervini, E. Baudat, P. Miéville, D. Fazzi, C. Corminboeuf, *Chemical science* **2017**, *8*, 361–365.

[27] E. Merino, M. Ribagorda, *Beilstein journal of organic chemistry* **2012**, *8*, 1071–1090.

[28] A. Goulet-Hanssens, M. Utecht, D. Mutruc, E. Titov, J. Schwarz, L. Grubert, D. Bléger, P. Saalfrank, S. Hecht, *Journal of the American Chemical Society* **2017**, *139*, 335–341.

[29] T. Muraoka, K. Kinbara, T. Aida, *Nature* **2006**, *440*, 512–515.

[30] H. D. Bandara, S. C. Burdette, *Chemical Society Reviews* **2012**, *41*, 1809–1825.

[31] C. Knie, M. Utecht, F. Zhao, H. Kulla, S. Kovalenko, A. M. Brouwer, P. Saalfrank, S. Hecht, D. Bléger, *Chemistry – A European Journal* **2014**, *20*, 16492–16501.

[32] M. K. Purkait, M. K. Sinha, P. Mondal, R. Singh in *Interface Science and Technology*, *Vol. 25*, (Eds.: M. K. Purkait, M. K. Sinha, P. Mondal, R. Singh), Elsevier, **2018**, pp. 115–144.

[33] A. Flook, G. C. Lloyd-Jones, *The Journal of Organic Chemistry* **2024**, *89*, 16586–16593.

[34] Bruker BioSpin GmbH, Dynamics Center User Manual, Version 2.8.8, Kinetics and lineshape analysis from sequential 1D (pseudo-2D) data, Bruker BioSpin GmbH, Rheinstetten, Germany, **2025**.

[35] Bruker BioSpin GmbH, *Dynamics Center*, version 2.8.8, Bruker BioSpin GmbH, **2025**.

5 CHARGE-NEUTRAL TRIPHENYLAMINE-BASED Zn(II) HELICATES FOR ENHANCED PHOTOPHYSICAL PROPERTIES

5.1 Introduction

The charge-neutral zinc(II) helicates developed by our group and their characteristics have been elucidated in the preceding chapters.[1,2] The system's primary advantages include a size-selective cavity that leads to a high binding affinity for dicarboxylates in competitive media. Its highly sensitive nature, as applied in emission spectroscopy, has proven to be particularly effective for the binding and detection of anions in solution. Small but noticeable color intensity changes were observed, aligning with the enhancement of emission upon guest binding. The subsequent objective is to modify the host design to refine this property, thereby improving its sensing capabilities.

Enhancing the photophysical response of such hosts can, in principle, be achieved by embedding chromophores into the ligand backbone so that guest binding alters intense, visible transitions. The BODIPY moiety is typical for strong, narrow visible absorption and environment-sensitive emission; both free sensors and encapsulated BODIPYs show pronounced spectral modulation upon binding or confinement, including recognizable color changes in solution.[3,4] Furthermore, the structural motifs of rhodamine and coumarin similarly exhibit these properties.[5–7] This motivates our attempts to provide the helicate with naked-eye or turn-on fluorescence responses through chromophore integration.

Within the design modification scope, Triphenylamine (TPA) offers a synthetically feasible, π-donor-rich panel that can be readily integrated into the ligand through "click" chemistry. Additionally, TPA has the potential to grant optical enhancements to the host system. Despite not being an inherent chromophore, this ability is attributable to its electron-rich and redox-active characteristics.[8–13] To investigate the potential applications of guest molecules, perfluorinated dicarboxylates were selected as model compounds, as they represent a substantial advancement toward addressing the challenges posed by these toxic environmental pollutants, particularly in light of their bioaccumulative properties and the strict regulatory measures governing such chemicals.[14–18] This chapter presents the synthesis of the TPA-containing ligand and its Zn(II) double-stranded helicate self-assembly, the absorption and emission characteristics of the host, and binding studies with selected perfluorinated guests, accompanied by a comparative analysis with the respective

non-fluorinated guests.

5.2 Results and discussion

5.2.1 Synthesis and self-assembly of the modified TPA-based charge-neutral helicate

The ligand $\mathbf{L^{TPA}}$-H_2 was synthesized employing the two synthon approach, which is generally followed within our experimental protocol, by combining the hydroxyquinoline-based azide with a triphenylamine-based diyne through a CuAAC reaction, followed by self-assembly to yield the corresponding [$\mathbf{L^{TPA}}_2Zn_2$] helicate (Scheme 5.1). The quinolinol azide (**1**) was obtained in five steps from *o*-anisidine and methacrolein according to the established procedure used for our charge-neutral receptors, providing a handle for subsequent CuAAC coupling. The triphenylamine backbone was introduced via nucleophilic aromatic substitution of 1,3-dibromo-5-fluorobenzene with diphenylamine, followed by Sonogashira alkynylation to deliver 3,5-diethynyl-*N*,*N*-diphenylaniline (**5**). The "click" reaction between these fragments yielded $\mathbf{L^{TPA}}$-H_2 as a greenish solid after purification.

Self-assembly was performed under standard conditions with minor alterations. The ligand was treated with excess zinc acetate (1.5 equiv.) while stirring at 50 °C and removing excess acetate salts by lyophilization and washing, which afforded the charge-neutral double stranded helicate [$\mathbf{L^{TPA}}_2Zn_2$] in quantitative yield as a yellow solid. The neutrality of the complex arises from the deprotonation of the two 8-hydroxyquinoline units on each ligand upon chelation to Zn(II), as previously established for the parent [L_2Zn_2] system[1].

The ^{1}H NMR spectrum of the complex in DMSO-d_6 shows clean signals that are diagnostic of a single, symmetric assembly. Compared to the free ligand, the phenolic OH signal at 9.9 ppm is absent, consistent with chelation to Zn(II). The hydroxyquinoline and triazole signals shift in a manner consistent with metal coordination and rigidification. ^{13}C NMR could not be obtained at analytical concentrations due to limited solubility; however, 2D NOESY correlations support a geometry analogous to that of the parent hydroxyquinoline helicates templated by Zn(II). The NOESY contacts between the triazole group (H_g) and protons (H_i) and (H_h) show the common dynamic behavior of the helicate backbone that preserves the stoichiometry, topology, and charge-neutrality upon the introduction of the TPA unit.

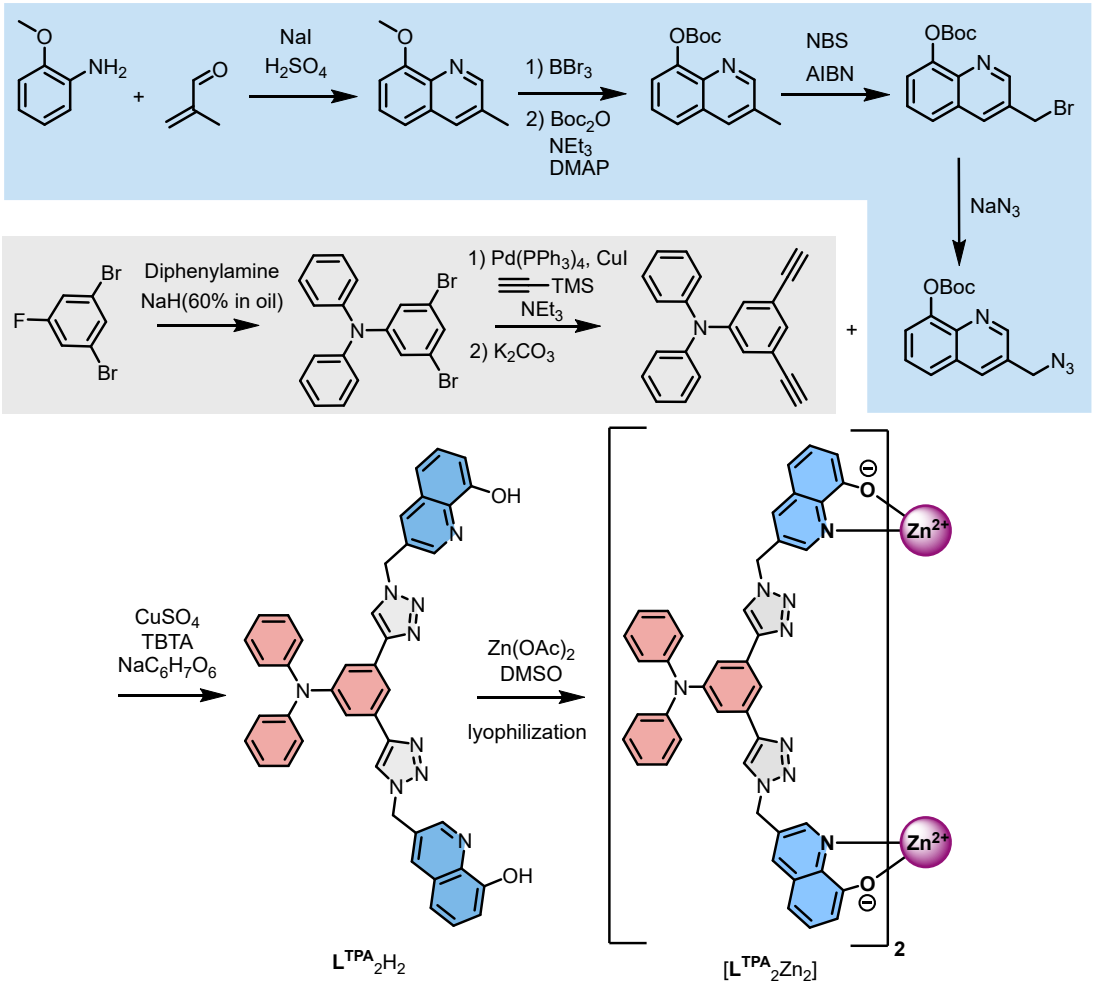

Scheme 5.1 Overall synthesis of ligand $\mathbf{L^{TPA}}$-H_2 and complexation of $[\mathbf{L^{TPA}}_2Zn_2]$.

5.2.2 Absorption and emission properties of the $[\mathbf{L^{TPA}}_2\mathbf{Zn_2}]$ receptor

At matched concentrations in DMSO, the TPA-modified helicate $[\mathbf{L^{TPA}}_2Zn_2]$ displays two ligand-centered absorption bands at 350 nm and 410 nm that are characteristic of the 8-hydroxyquinolinate-zinc complex units. Their intensities are comparable to those of the parent $[\mathbf{L^{R}}_2Zn_2]$ complex bearing diphenylamide solubilizing groups, indicating that the quinolinolate chromophores retain essentially the same characteristics upon the replacement of the amide with the amine core. In addition, a new higher intensity band at 305 nm is observed for $[\mathbf{L^{TPA}}_2Zn_2]$, which we attribute to a triphenylamine-centered transition (Figure 5.1).

Fluorescence was evaluated under three excitation conditions that selectively address the different absorption maxima: λ_{exc} = 410 nm, 350 nm, and 305 nm (Figure 5.1). Under identical instrumental settings and concentration ranges, excitation at 410 nm and 350 nm yields lower emission intensity for $[\mathbf{L^{TPA}}_2Zn_2]$ compared to $[\mathbf{L^{R}}_2Zn_2]$, indicating quenching

when the hydroxyquinoline-zinc units are directly excited. In contrast, excitation at 305 nm produces an emission intensity for [$\mathbf{L^{TPA}}_2Zn_2$] that is similar in magnitude to that of the parent complex excited at 410 nm, consistent with intense absorption via the TPA-centered band, but without a clear overall enhancement in brightness. Collectively, these data show that TPA incorporation does not translate into a dramatic improvement in steady-state emission in the current architecture.

These observations are consistent with limited electronic communication between the TPA core and the hydroxyquinoline-zinc scaffold and/or the introduction of additional non-radiative decay channels (for example, intermolecular charge-transfer (ICT), faster internal conversion, or short-range quenching inside the cavity).[8,19] To distinguish poor coupling from fast deactivation and to establish whether any delayed pathways are operative, further measurements are needed, such as quantum yield calculations and time-resolved spectroscopy, to probe charge-separated or triplet states.[20]

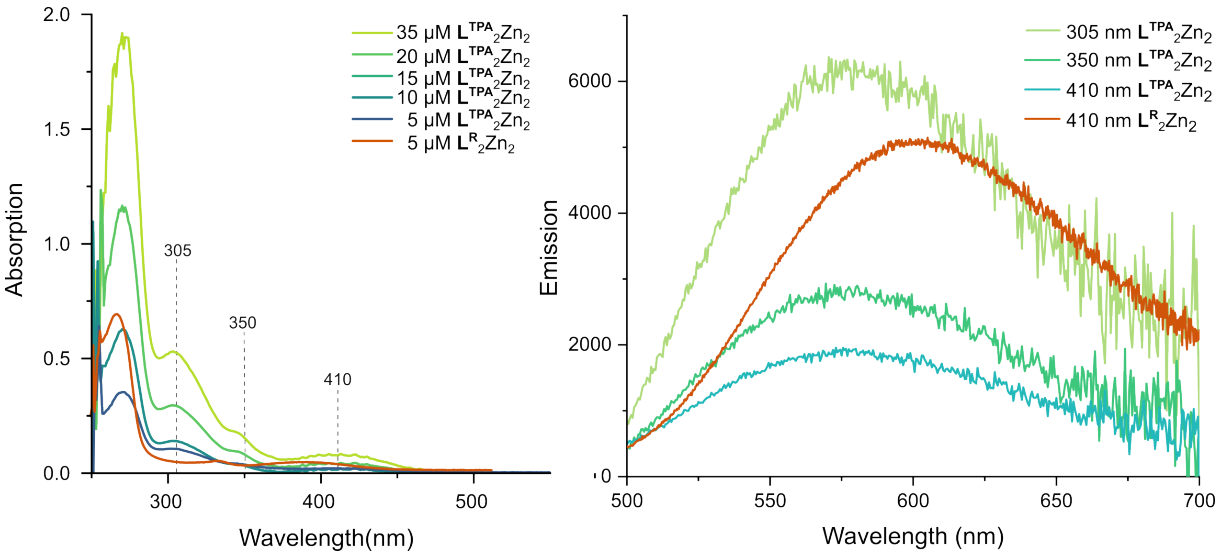

Figure 5.1 (left) UV-Vis spectra of the complex [$\mathbf{L^{TPA}}_2Zn_2$] at concentrations between 35 µM and 5 µM and UV-Vis spectra of the complex [$\mathbf{L^{R}}_2Zn_2$] (DMSO-d_6, l = 1 cm) at 5 µM (right) Emission spectra of the complex [$\mathbf{L^{TPA}}_2Zn_2$] at 5 µM (λ_{exc} = 305 nm, 350 nm, 410 nm) (no accumulation) and the complex [$\mathbf{L^{TPA}}_2Zn_2$] at 5 µM (λ_{exc} = 410 nm) (average of two accumulations).

5.2.3 Binding studies with perfluorinated carboxylates

Four selected perfluorinated guests were evaluated as their TBA salts in the new receptor: 2,3,5,6-tetrafluoroterephthalate (**F4TP^{2-}**), 2,3,4,5,6-pentafluorobenzoate (**F5BzO^{-}**), 2,2,3,3-tetrafluorosuccinate (**F4Suc^{2-}**) and 2,2,3,3,4,4,5,5,6,6,7,7,8,8,9,9-hexadecafluorodecanedioate (**F16Seb^{2-}**). All titrations were performed by ^{1}H NMR in DMSO-d_6, and exchange regimes were assigned from the evolution of the diagnostic aromatic signals of [$\mathbf{L^{TPA}}_2Zn_2$].

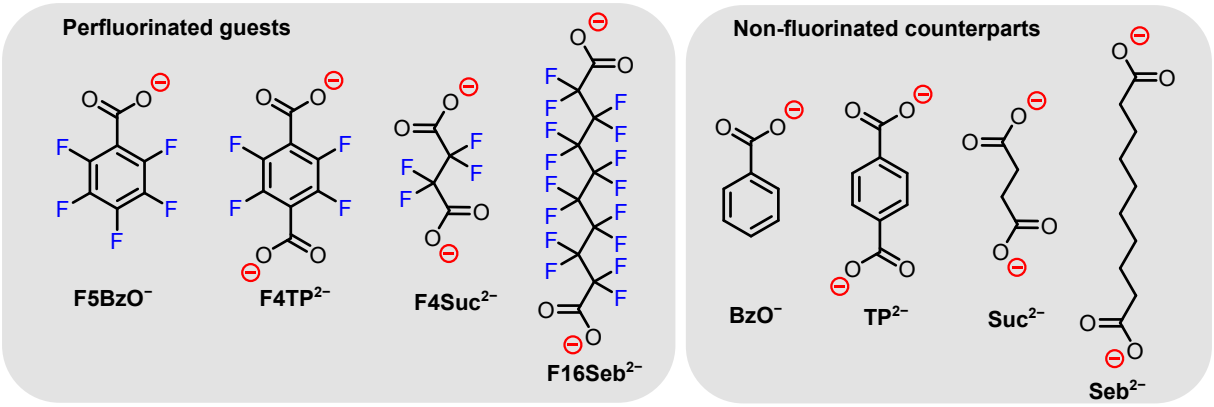

Figure 5.2 Perfluorinated mono- and dicarboxylates investigated as their TBA salts in this study and their non-fluorinated counterparts used for comparative analysis. Monocarboxylates bind in a 1:2 fashion while dicarboxylates bind in a 1:1 fashion. The binding studies involving non-fluorinated guest molecules were referenced from the previous investigation using the parent receptor.[1]

The addition of $\mathbf{F4TP^{2-}}$ produced clean, averaged shifts characteristic of fast exchange on the NMR timescale, consistent with a single 1:1 binding process (Figure 5.12). Fitting the chemical shifts with BindFit afforded $K_{1:1} = 1222\ \mathrm{M}^{-1}$ ($\log K_{1:1} = 3.09$). In contrast, the non-fluorinated terephthalate ($\mathbf{TP^{2-}}$) binds to the parent $[\mathbf{L^R}_2\mathrm{Zn}_2]$ helicate under slow exchange, with a much larger association constant ($\log K_{1:1} = 7.59$) determined previously by fluorescence fits[1], which is consistent with strong 1:1 encapsulation. For $\mathbf{F5BzO^-}$, line broadening and loss of resolution were observed immediately after 0.5 equiv of the guest (Figure 5.13), indicating the presence of unknown additional equilibria. A reliable equilibrium constant could not be extracted from this data. Notably, the non-fluorinated benzoate behaves in fast exchange with the parent helicate, ($K_{1:1} = 5240\ \mathrm{M}^{-1}$), which underscores the qualitative weakening upon perfluorination.

$\mathbf{F4Suc^{2-}}$ showed a fast exchange with smooth, monotonic chemical shifts consistent with 1:1 binding (Figure 5.14). While the present dataset did not yet allow for a robust fit (insufficient steps in the most sensitive concentration window), the non-fluorinated succinate binds markedly stronger to $[\mathbf{L^R}_2\mathrm{Zn}_2]$, forming a 1:1 complex with an intermediate to slow exchange binding regime, albeit with some minor sub-stoichiometric processes noted in the study. In this regard, fluorinated succinate helps in a clean complexation.The addition of $\mathbf{F16Seb^{2-}}$ did not result in any noticeable changes in the spectrum. (Figure 5.16), indicating no observable binding under these conditions. This outcome contrasts sharply with sebacate ($\mathbf{Seb^{2-}}$), which binds well to $[\mathbf{L^R}_2\mathrm{Zn}_2]$ in an intermediate to slow exchange manner.

Across the series, perfluorination consistently reduces binding affinity relative to the non-fluorinated counterparts. We attribute this to (i) the strongly electron-withdrawing character of fluorine substituents, which lowers carboxylate basicity and weakens coordination with zinc, and (ii) a possible mismatch in the orientation or solvation

for highly fluorinated, apolar guests owing to the polar DMSO solvent environment. Furthermore, no alteration in color or emergence of fluorescence is detected upon the introduction of the guest to the host.

5.3 Conclusion

This chapter reports the synthesis of a triphenylamine-based ligand and its self-assembly into a charge-neutral [$\mathbf{L^{TPA}}_2Zn_2$] double helicate. The modified host preserves the hydroxyquinoline-centered absorption bands at 350 and 410 nm with comparable intensity to the parent [$\mathbf{L^{R}}_2Zn_2$], while introducing a much more intense band at 305 nm attributable to the TPA unit. Under steady-state conditions, the anticipated emissive enhancement is not realized. Excitation at 350 and 410 nm leads to a quenched intensity relative to the parent complex, while excitation at 305 nm yields an intensity comparable to that of the parent excited at 410 nm. Thus, in this topology, the TPA unit does not deliver a practical enhancement of photophysical properties. Binding studies with perfluorinated carboxylates show systematically reduced affinities compared to the non-fluorinated analogs studied previously with the parent receptor. The overall trend is consistent with the electron-withdrawing nature of fluorine, which lowers carboxylate basicity and weakens Zn–O coordination.

Looking ahead, to obtain robust colorimetric or turn-on responses, a true visible chromophore, such as BODIPY, should be integrated into the ligand backbone so that binding perturbs an intense visible transition rather than relying on TPA. Moreover, the mechanistic photophysics of the current TPA host should be resolved through further analysis, including time-resolved spectroscopy to probe charge-transfer or triplet pathways. Because TPA is a π-donor moiety, screening electron-poor carboxylates as guests is also motivated to test donor–acceptor interactions without sacrificing coordination.

5.4 Experimental section

5.4.1 General methods

5.4.1.1 Materials

Unless otherwise stated, reagents were purchased from Sigma-Aldrich, chemPUR, TCI, BLDpharm, Alfa Aesar, and VWR and were used as received. Tetrabutylammonium hydroxide (1.0 M in MeOH) was procured from Sigma-Aldrich. DMSO-d_6 (99.8% D) for binding and spectroscopic studies was sourced from Deutero and Eurisotop. Experiments were performed under an inert argon atmosphere using standard Schlenk techniques where required. Reactions were monitored using thin-layer chromatography (TLC) with pre-coated silica plates (Merck, silica 60, F254). For column chromatography, silica (Merck, silica 60, 0.02–0.063 mesh) was used as the stationary phase. Lyophilization was performed on a CHRIST Alpha 2-4 LSC basic freeze dryer (coil -80 °C, $\sim 1\times10^{-3}$ mbar). NMR spectra were recorded on Bruker AVANCE III NEO 500 and 600 instruments. Chemical shifts are reported in δ (ppm) with multiplicities indicated as s (singlet), d (doublet), t (triplet), and m (multiplet). UV-Vis spectra were recorded on an Agilent DAD HP-8453 UV-Vis spectrometer using Hellma QS cuvettes ($l = 2$ mm) at room temperature. Fluorescence spectra were recorded on a Jasco FP-8300 fluorescence spectrometer. ESI-MS spectra were measured using a Bruker timsTOF spectrometer.

5.4.1.2 Procedures for binding studies

Purchased carboxylic acids were converted to their respective tetrabutylammonium (TBA) salts by deprotonation prior to use.Carboxylic acids were dissolved in 5 mL of MeOH, and one and two equivalents of tetrabutylammonium hydroxide (1 M solution in MeOH) were added for mono- and dicarboxylic acids, respectively. The mixture was vortexed for 30 min, and the solvents were removed under reduced pressure. A small amount of water was added to aid subsequent freeze-drying, as pure MeOH freezes poorly, and it was lyophilized for up to three days. The resulting TBA carboxylates were used without further purification.

NMR titrations were carried out to analyze the binding behavior of the guest. Binding constants corresponding to fast exchange processes were obtained by fitting with BindFit.[21–23]

5.4.2 Synthesis of ligands

5.4.2.1 Synthesis of 3-(azidomethyl)quinolin-8-yl tert-butyl carbonate (1)

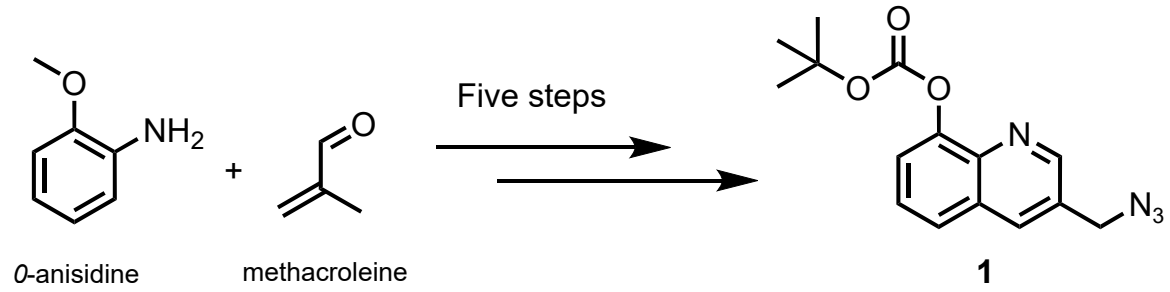

Azide compound **(1)** was synthesized via a five-step sequence starting with *o*-anisidine and methacrolein, following the procedure detailed in Chapter 3 as reported by Van Craen and colleagues[1].

5.4.2.2 Synthesis of 3,5-dibromo-*N,N*-diphenylaniline (4)

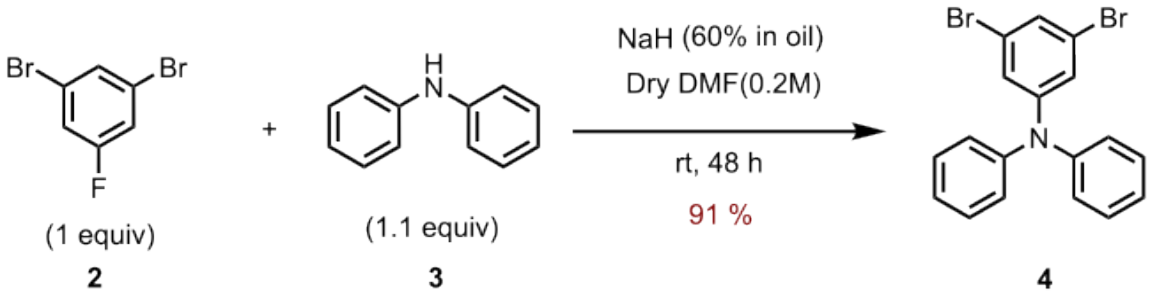

Diphenylamine **(3)** (1.47 g, 8.66 mmol, 1.1 equiv) and sodium hydride (60% in oil) (1.32 g, 55.14 mmol, 7.0 equiv) were added to a Schlenk flask under argon. Dry DMF (40 mL, 0.20 M) was added, and the mixture was purged with argon. The suspension was stirred at room temperature for 2 hours for deprotection. 1,3-dibromo-5-fluorobenzene **(2)** (2.00 g, 7.88 mmol, 1.0 equiv) was added under argon. the reaction was stirred at room temperature for 48 hours, during which the mixture gradually became dark red. The reaction was cooled to room temperature and quenched with water. The layers were separated, and the aqueous phase was extracted with ethyl acetate. The combined organic layer was washed with brine, dried over anhydrous magnesium sulfate, filtered, and concentrated. The residue was purified by flash column chromatography (pentane 100%) to afford 3,5-dibromo-N,N-diphenylaniline **(4)** (2.88 g, 7.14 mmol, 91%)

^{1}H NMR (500 MHz, $CDCl_3$, 298 K): δ = 7.31 (dd, J = 8.4, 7.3 Hz, 4H), 7.20 (t, J = 1.7 Hz, 1H), 7.14 – 7.08 (m, 6H), 7.06 (d, J = 1.7 Hz, 2H) ppm.

5.4.2.3 Synthesis of 3,5-diethynyl-*N,N*-diphenylaniline (5)

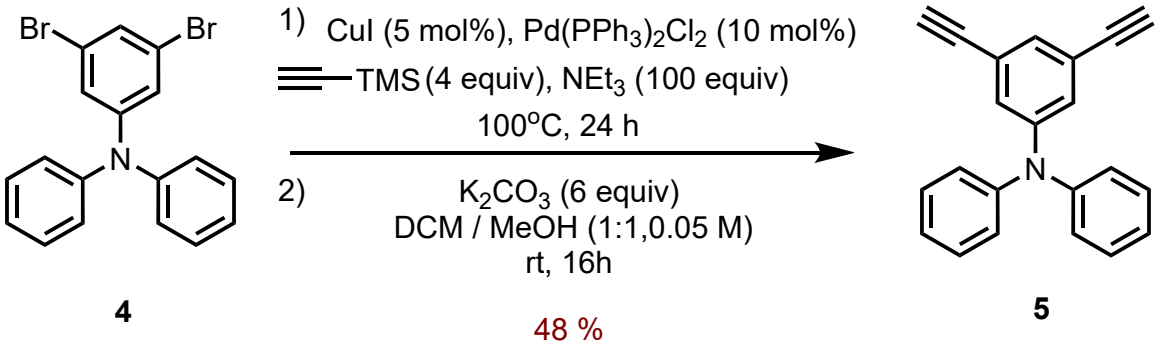

4 48 % **5**

A Schlenk tube was charged with 3,5-dibromo-N,N-diphenylaniline **(4)** (1.0 g, 2.48 mmol, 1 equiv), $Pd(PPh_3)_2Cl_2$ (174.12 mg, 0.248 mmol, 10 mol%), and triethylamine (34.58 mL, 248.0 mmol, 100 equiv), which was then degassed by three freeze–pump–thaw cycles, after which CuI (23.6 mg, 0.124 mmol, 5 mol%) and trimethylsilylacetylene (1.41 mL, 9.92 mmol, 4 equiv) were added under argon. The sealed tube was heated at 100 °C for 24 h. After cooling to room temperature, the reaction mixture was diluted with dichloromethane and washed with saturated aqueous NH_4Cl. The aqueous layer was extracted with dichloromethane, and the combined organic phases were dried over anhydrous magnesium sulfate, filtered, and concentrated under reduced pressure. Purification by column chromatography on silica gel (pentane 100%) afforded the TMS-protected diyne (693.1 mg, 1.58 mmol, 63%).

^{1}H NMR (500 MHz, $CDCl_3$, 298 K): δ = 7.29 – 7.24 (m, 6H), 7.22 (t, J = 1.4 Hz, 1H), 7.11 (d, J = 1.4 Hz, 2H), 7.07 – 7.03 (m, 6H), 0.20 (s, 18H).

The TMS-protected product was then deprotected in a 1:1 mixture of dichloromethane and methanol (10 mL, 0.05 M) with K_2CO_3 (1.31 g, 9.50 mmol, 6.0 equiv) and stirred at room temperature overnight. The mixture was diluted with dichloromethane and washed with water. The combined organic layers were dried over anhydrous magnesium sulfate, filtered, and concentrated under reduced pressure. Filtration through a silica plug (pentane/diethyl ether 5:1) yielded 3,5-diethynyl-*N,N*-diphenylaniline **(5)** with slight impurities, used as is in the next reaction (350 mg, 1.19 mmol, 75%).

^{1}H NMR (500 MHz, $CDCl_3$, 298 K): δ = 7.31 – 7.26 (m, 4H), 7.20 (s, 1H), 7.15 (d, J = 1.4 Hz, 2H), 7.09 – 7.05 (m, 6H), 3.01 (s, 2H) ppm.

5.4.2.4 Synthesis of 3,3'-(((5-(diphenylamino)-1,3-phenylene)bis(1H-1,2,3-triazole-4,1-diyl))bis(methylene))bis(quinolin-8-ol) ($L^{TPA}H_2$)

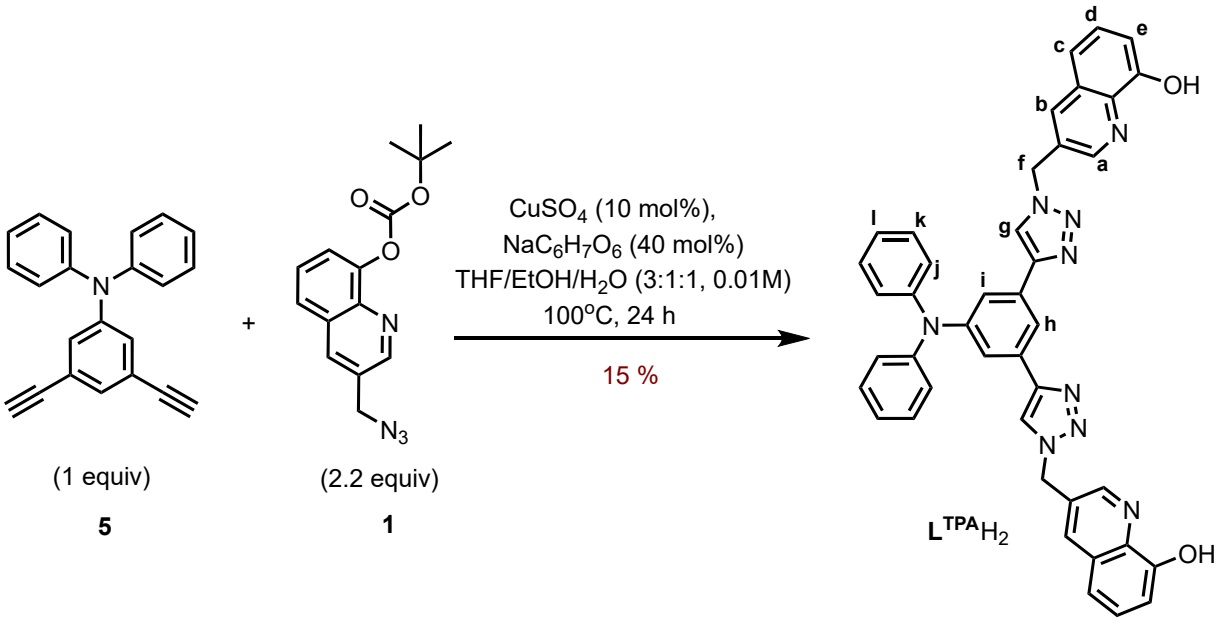

A Schlenk tube was equipped with azide **(1)** (80.0 mg, 0.266 mmol, 2.2 equiv) and a 3:1:1 mixture of THF/EtOH/H_2O (15 mL, 0.008 M). The solution was degassed for 30 min by vigorous argon bubbling. Under argon, $CuSO_4$ (1.93 mg, 0.012 mmol, 10 mol%) and sodium ascorbate (9.59 mg, 0.048 mmol, 40 mol%), were added successively. TBTA was omitted, in contrast to the common procedure described in the literature for the ease of purification. Dialkyne **(5)** (35.52 mg, 0.121 mmol, 1.0 equiv) was then introduced, the tube was sealed, and the mixture was heated at 100 °C for 24 h. After cooling to room temperature, the reaction mixture was diluted with dichloromethane and washed with 0.025 M basic aqueous EDTA. The aqueous layer was extracted with dichloromethane, the combined organic phases were dried over anhydrous magnesium sulfate, filtered, and concentrated under reduced pressure. Purification by column chromatography on silica gel (dichloromethane/methanol 1% → 5%) yielded the crude ligand. Contrary to the reported procedure for a similar click reaction, the ligand had already been deprotected of the Boc groups after the reaction. The reaction yielded the ligand $\mathbf{L^{TPA}\text{-}H_2}$ as a colorless solid (12.5 mg, 0.018 mmol, 15%).

^{1}H NMR (500 MHz, DMSO-d_6, 298 K): δ = 9.91 (s, 2H, OH), 8.87 (d, J = 2.1 Hz, 2H, H_a), 8.69 (s, 2H, H_g), 8.24 (d, J = 2.2 Hz, 2H, H_b), 7.94 (t, J = 1.6 Hz, 1H, H_h), 7.47 (d, J = 1.5 Hz, 2H, H_i), 7.45 (t, J = 7.9 Hz, 2H, H_d), 7.38 (d, J = 8.1 Hz, 2H, H_c), 7.31 (t, J = 7.8 Hz, 4H, H_k), 7.08 (d, J = 7.3 Hz, 2H, H_e), 7.07 – 7.04 (m, 6H, H_{j+l}), 5.86 (s, 4H, H_f) ppm.

^{13}C NMR (151 MHz, DMSO-d_6, 298 K): δ = 153.88, 149.00, 148.64, 147.52, 146.62, 138.50, 135.80, 132.93, 130.13, 129.70, 128.68, 125.06, 124.49, 123.74, 122.57, 119.94, 118.27, 117.23, 112.40, 51.23 ppm.

HRMS (positive ESI-MS, DMSO/MeCN 1:9, acidified) : m/z = 694.2467 (M + H^+, $C_{42}H_{31}N_9O_2{}^+$, calcd. 694.2673).

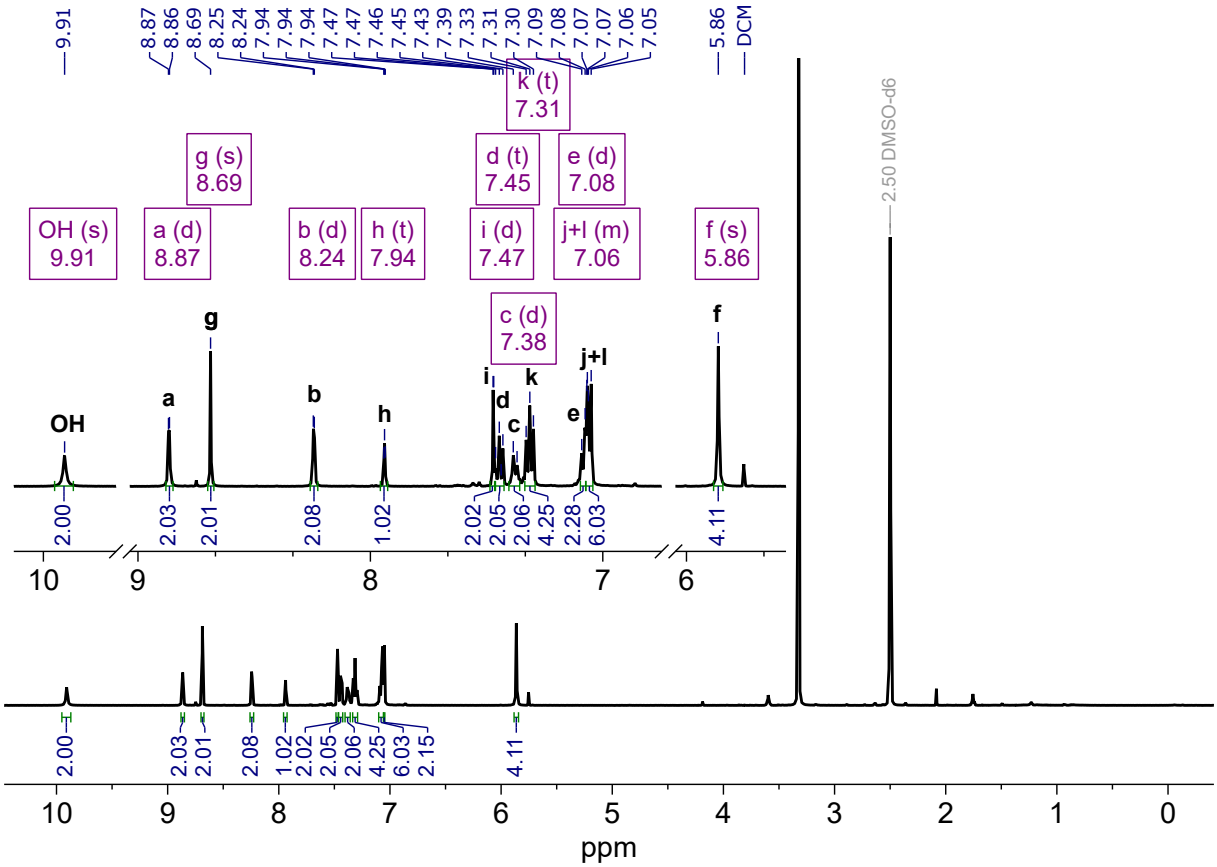

Figure 5.3 ^{1}H NMR spectrum of ligand $\mathbf{L^{TPA}}$-H_2 in DMSO – d_6.

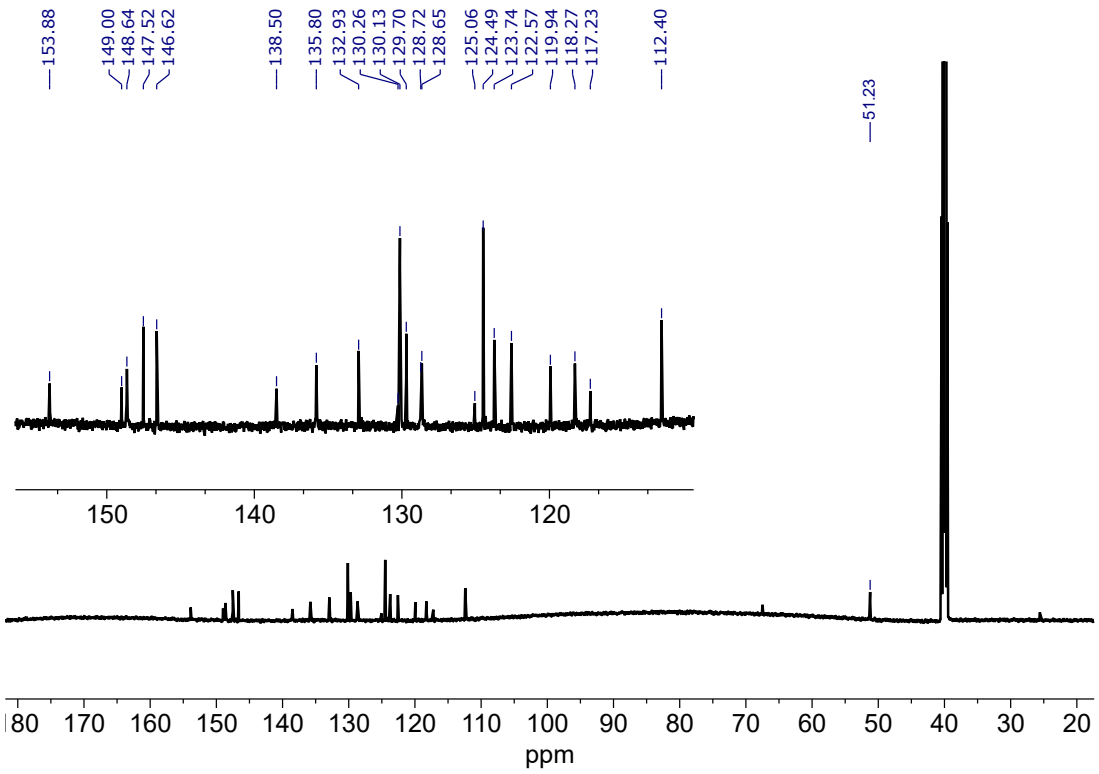

Figure 5.4 ^{13}C NMR spectrum of ligand $\mathbf{L}^{\mathbf{TPA}}$-$H_2$ in DMSO – d_6.

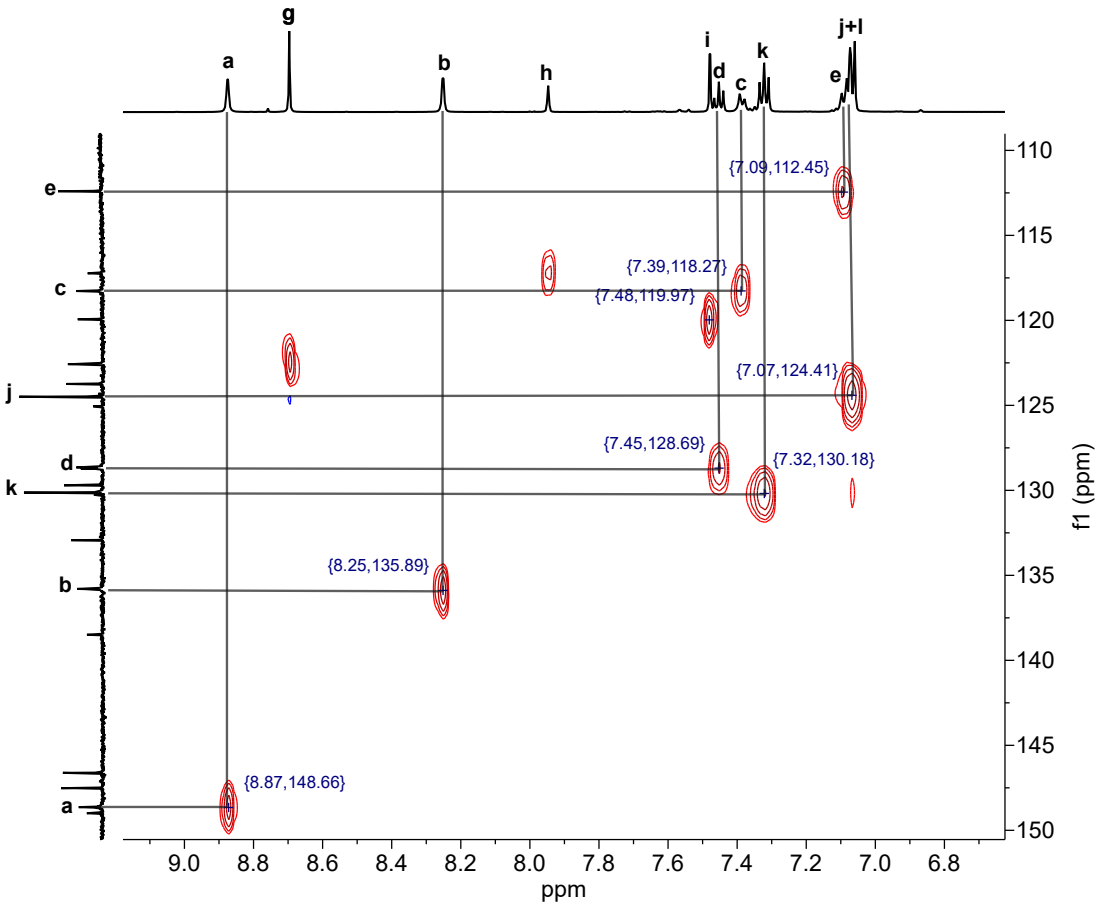

Figure 5.5 HSQC NMR spectrum of ligand $\mathbf{L}^{\mathbf{TPA}}$-$H_2$ in DMSO – d_6.

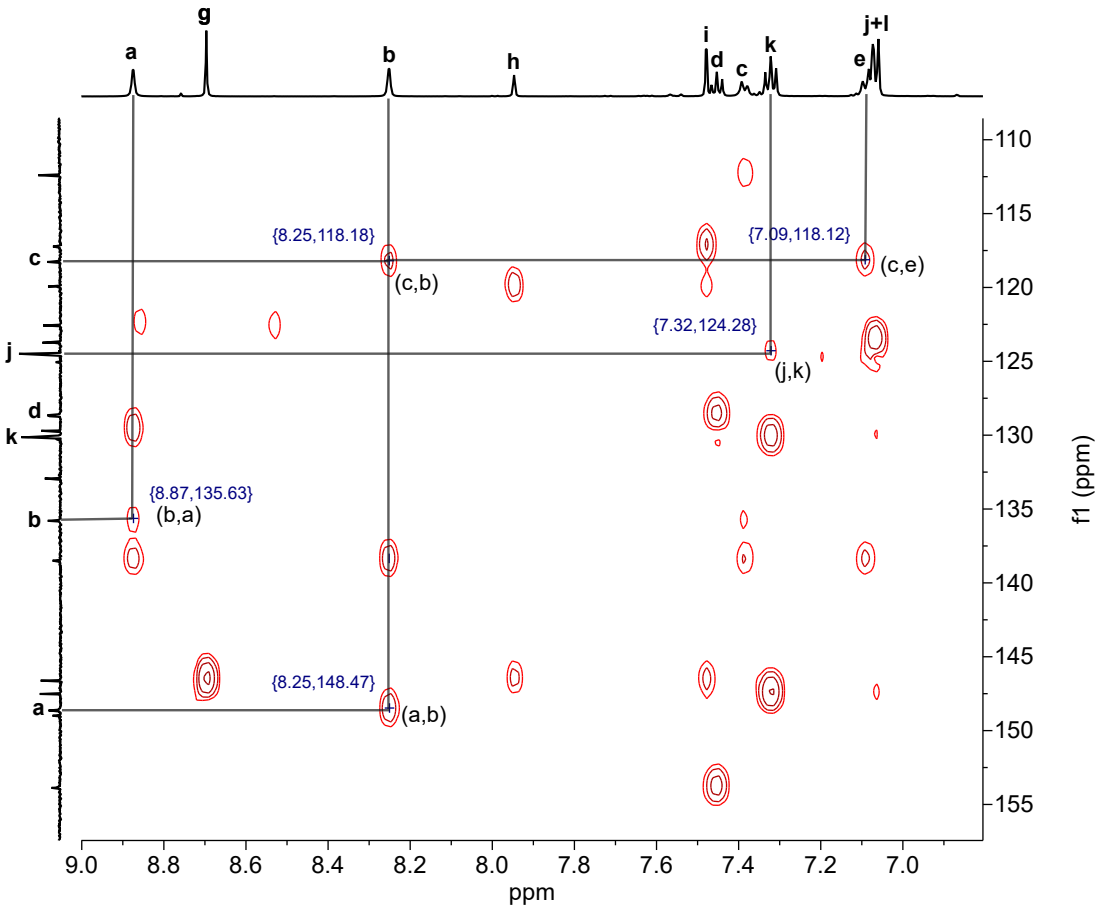

Figure 5.6 HMBC NMR spectrum of ligand $\mathbf{L}^{\mathbf{TPA}}$-$H_2$ in DMSO – d_6.

5.4.3 Complexation of charge-neutral $[\mathbf{L}^{\mathbf{TPA}}{}_2\mathbf{Zn_2}]$ receptor

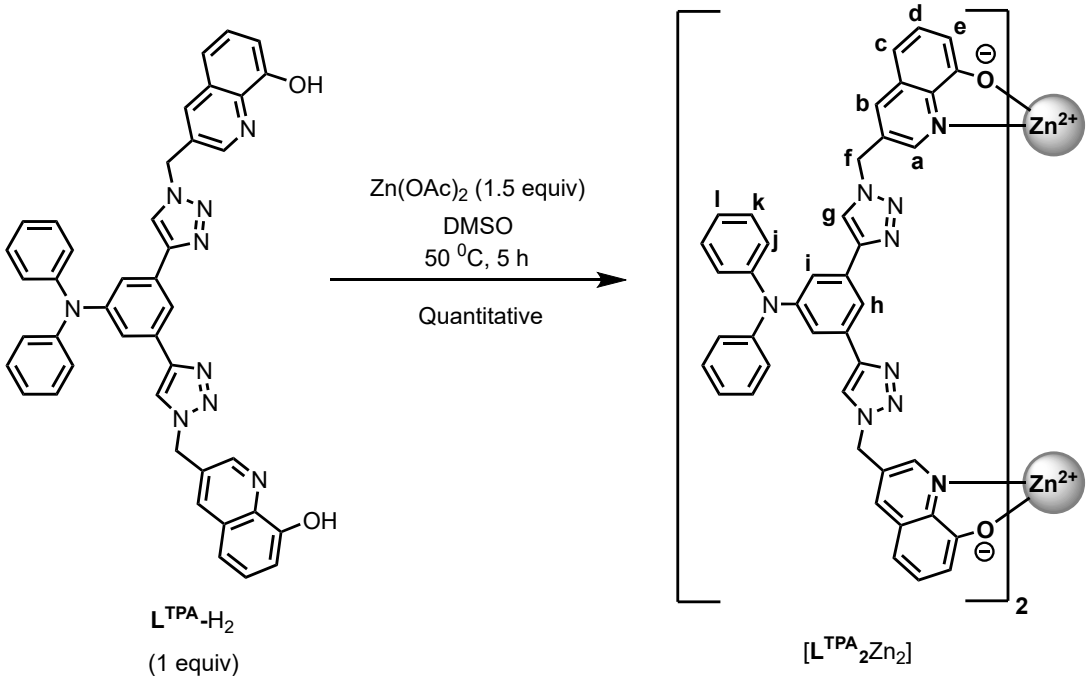

$\mathbf{L}^{\mathbf{TPA}}$-$H_2$
(1 equiv)

$[\mathbf{L}^{\mathbf{TPA}}{}_2\mathbf{Zn_2}]$

The $\mathbf{L}^{\mathbf{TPA}}$-$H_2$ ligand (1.0 equiv) was dissolved in DMSO (0.005 M), and excess solid zinc acetate (1.5 equiv) was added to the stirred solution. An immediate color change to yellow was observed. The reaction mixture was stirred at 50 °C for 5 hours to ensure complete dissolution and conversion. The solution was subsequently lyophilized and later washed with water and methanol to remove the remaining excess zinc acetate. This afforded the charge-neutral complexes $[\mathbf{L}^{\mathbf{TPA}}{}_2Zn_2]$ as yellow solids in quantitative yield.

^{1}H NMR (500 MHz, DMSO-d_6, 298 K): δ = 8.57 (s, 2H, H_g), 8.55 (s, 2H, H_a), 8.35 (s, 2H, H_b), 7.76 (s, 1H, H_h), 7.47 (s, 2H, H_i), 7.36 – 7.26 (m, 6H, H_{d+k}), 7.10 – 7.02 (m, 6H, H_{j+l}), 6.85 (d, J = 8.1 Hz, 2H, H_c), 6.69 (d, J = 7.8 Hz, 2H, H_e), 5.86 (s, 4H, H_f) ppm. The complex solubility was not enough for obtaining a ^{13}C NMR.

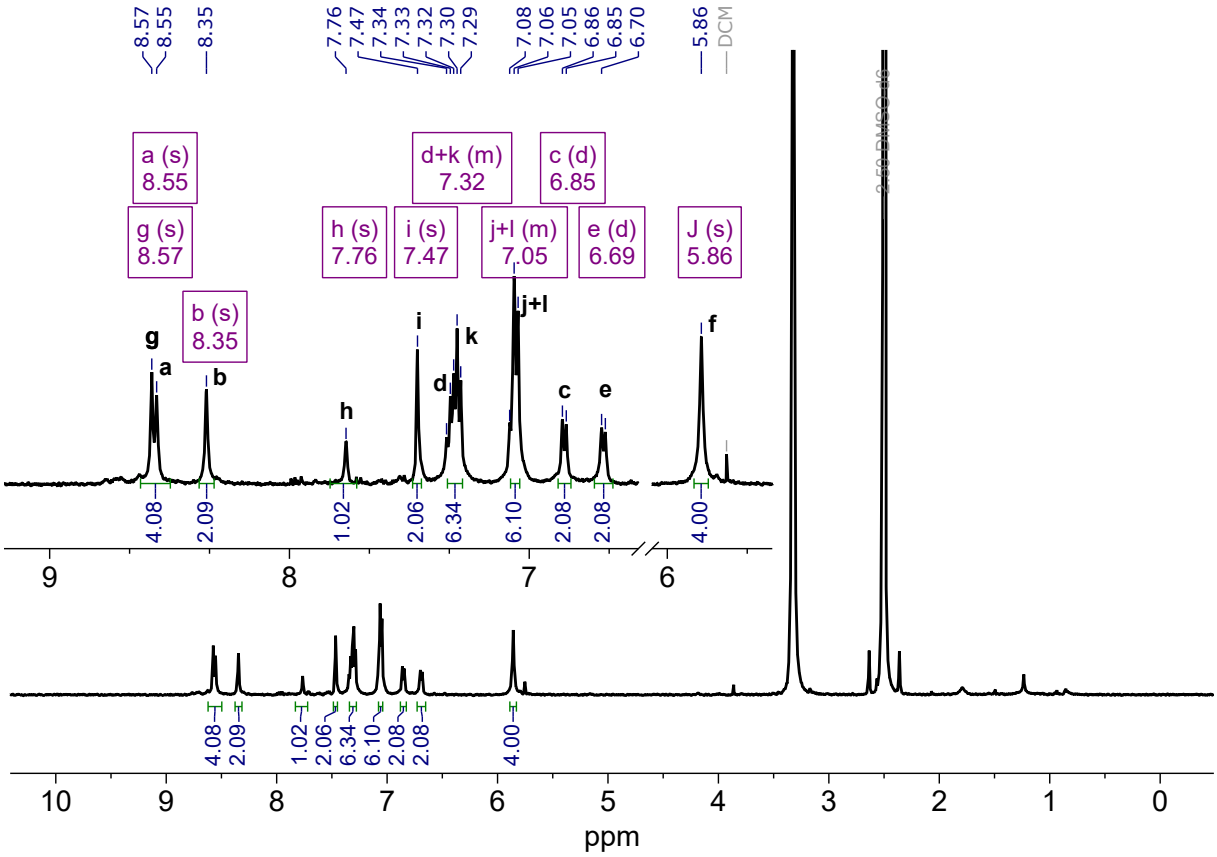

Figure 5.7 ^{1}H NMR spectrum of the complex $[\mathbf{L}^{\mathbf{TPA}}{}_2Zn_2]$ in DMSO – d_6

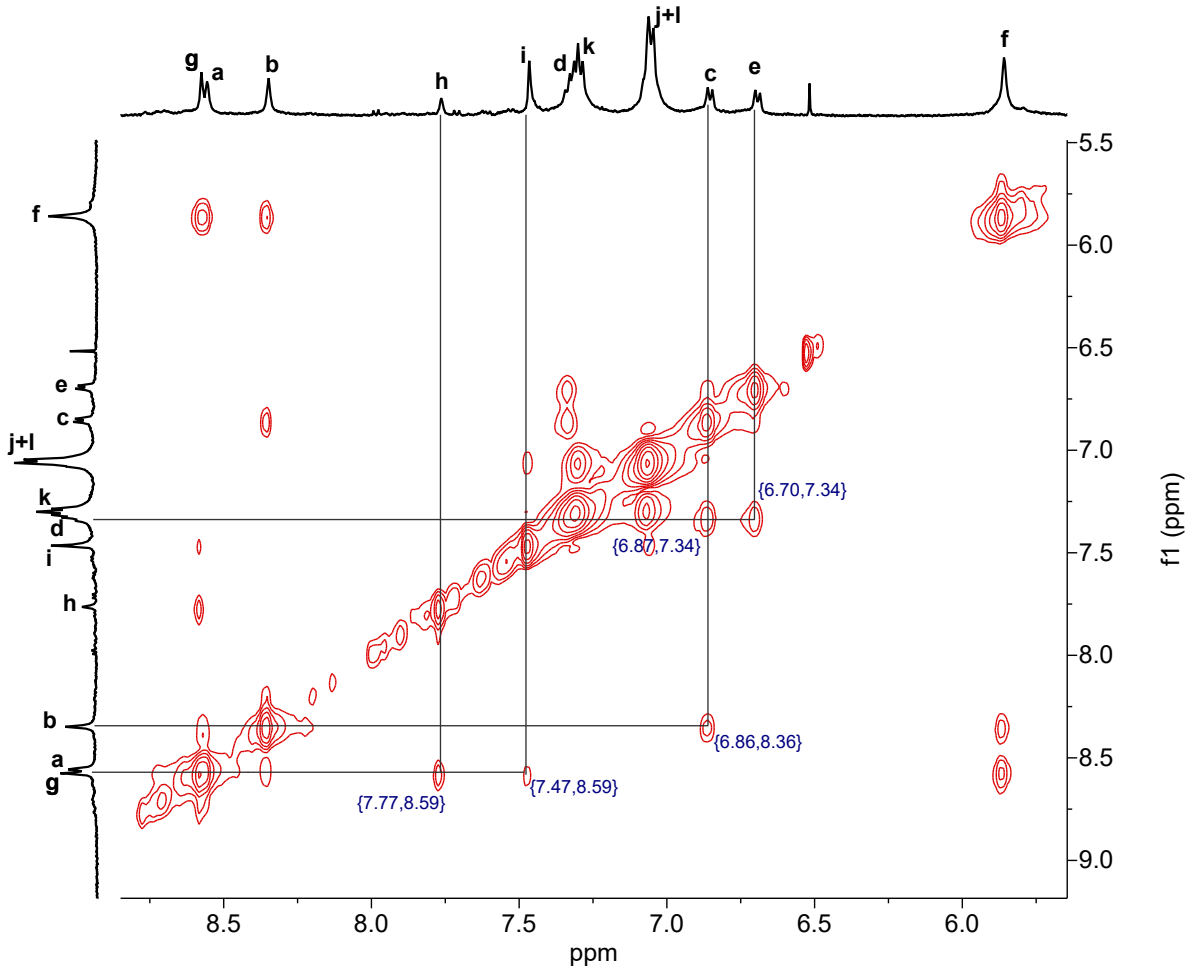

Figure 5.8 NOESY NMR spectrum of the complex $[\mathbf{L}^{\mathbf{TPA}}{}_2Zn_2]$ in DMSO$-d_6$

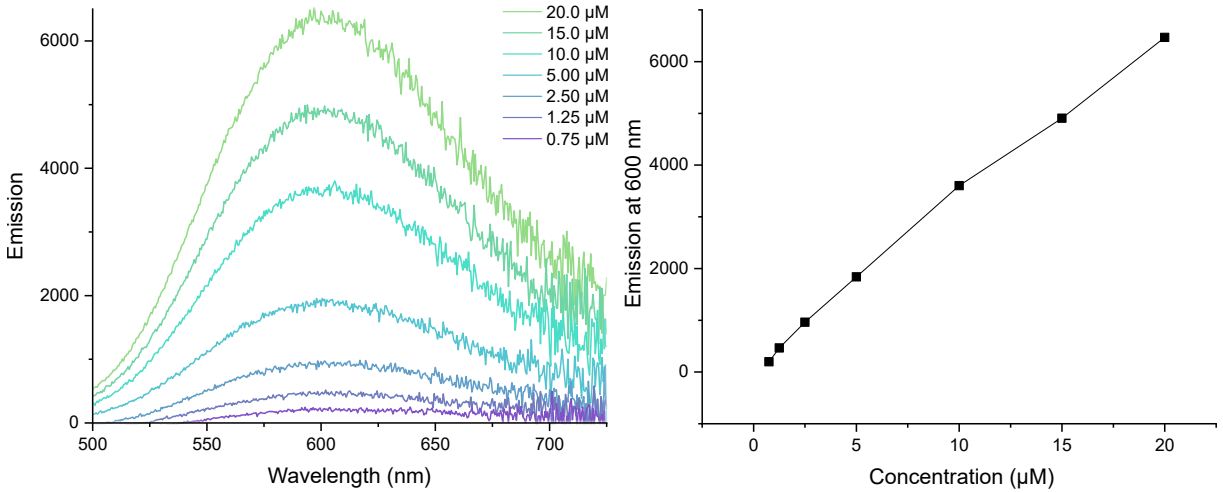

Figure 5.9 Emission spectra (λ_{exc} = 410 nm, DMSO$-d_6$) of the receptor $[\mathbf{L}^{\mathbf{TPA}}{}_2Zn_2]$ at concentrations between 20 µM and 0.75 µM.

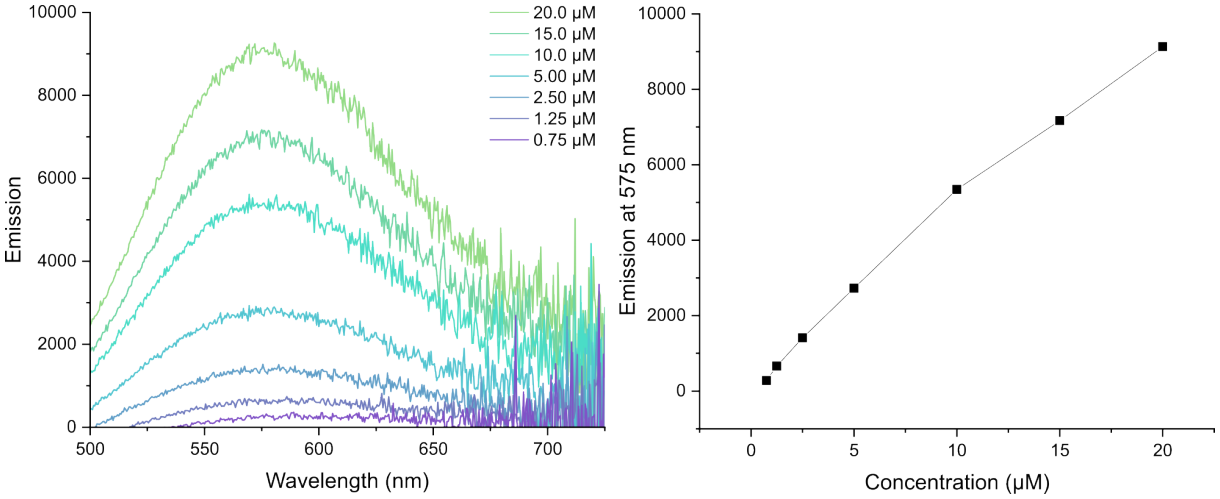

Figure 5.10 Emission spectra (λ_{exc} = 350 nm, DMSO – d_6) of the receptor [$\mathbf{L}^{\mathbf{TPA}}{}_2Zn_2$] at concentrations between 20 µM and 0.75 µM.

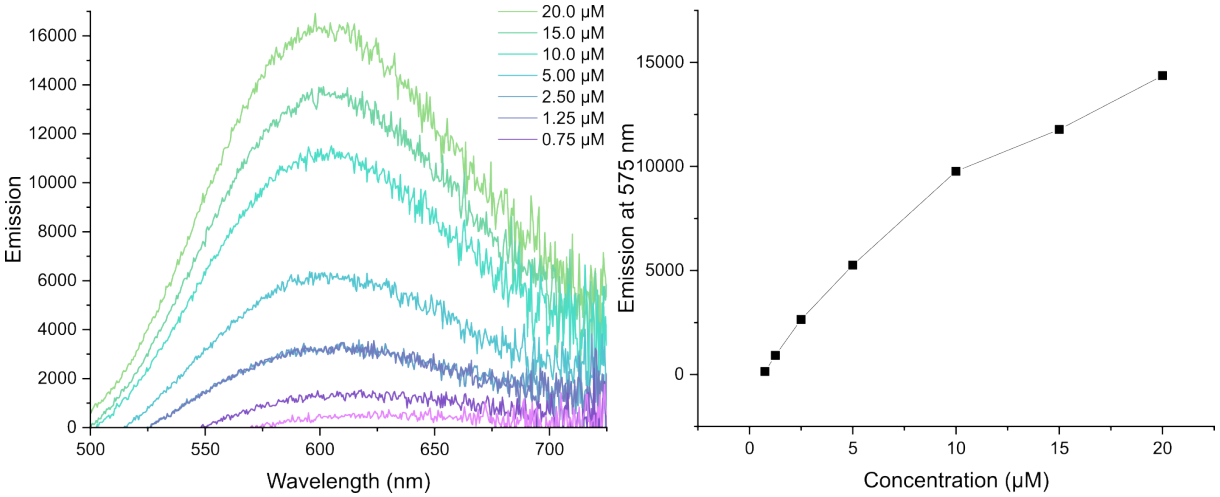

Figure 5.11 Emission spectra (λ_{exc} = 305 nm, DMSO – d_6) of the receptor [$\mathbf{L}^{\mathbf{TPA}}{}_2Zn_2$] at concentrations between 20 µM and 0.75 µM.

5.4.4 Binding studies of perfluorinated carboxylates

5.4.4.1 Tetrafluoroterephthalate

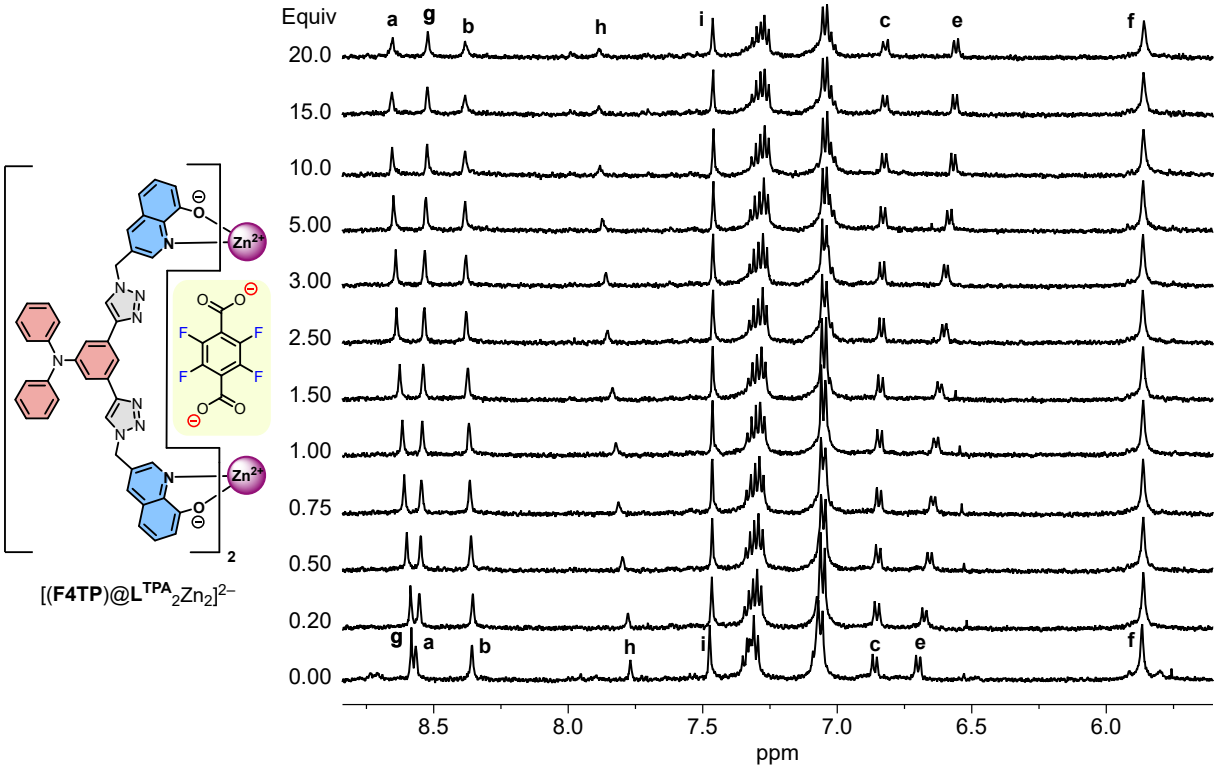

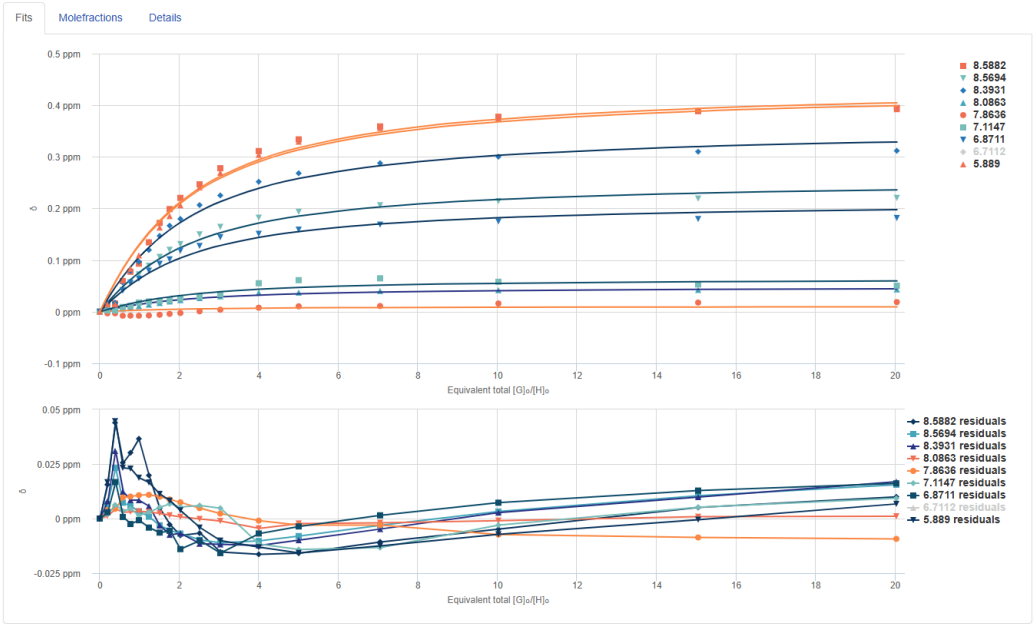

Parameters

Parameter (bounds)	Optimised	Error	Initial
K (0 → ∞)	1222.62 M⁻¹	± 6.4801 %	100.00 M⁻¹

Figure 5.12 ^{1}H NMR titration of [$\mathbf{L^{TPA}}_2Zn_2$] with 2,3,5,6-tetrafluoroterephthalate ($\mathbf{F4TP^{2-}}$) as TBA salts (500 MHz, 500 µM, DMSO-d_6, 298 K). Bottom: Binding isotherm obtained by fitting the chemical shift changes with BindFit using a 1:1 model.

5.4.4.2 Pentafluorobenzoate

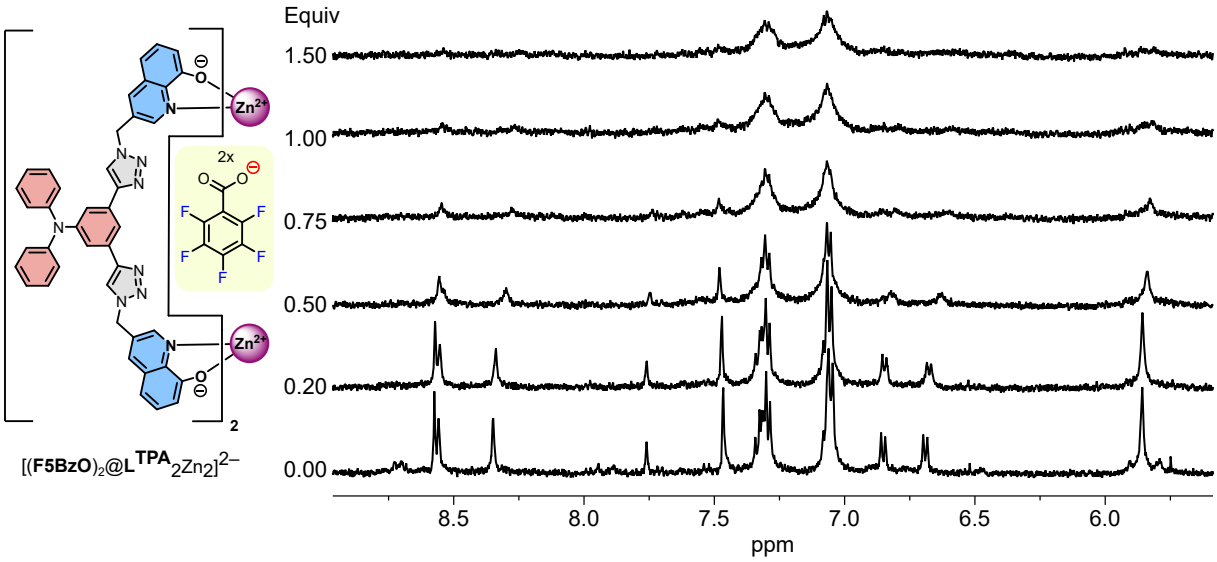

Figure 5.13 ^{1}H NMR titration of [$\mathbf{L}^{\mathbf{TPA}}{}_2Zn_2$] with 2,3,4,5,6-pentafluorobenzoate (**F5BzO**$^-$) as TBA salts (500 MHz, 500 µM, DMSO-d$_6$, 298 K).

5.4.4.3 Tetrafluorosuccinate

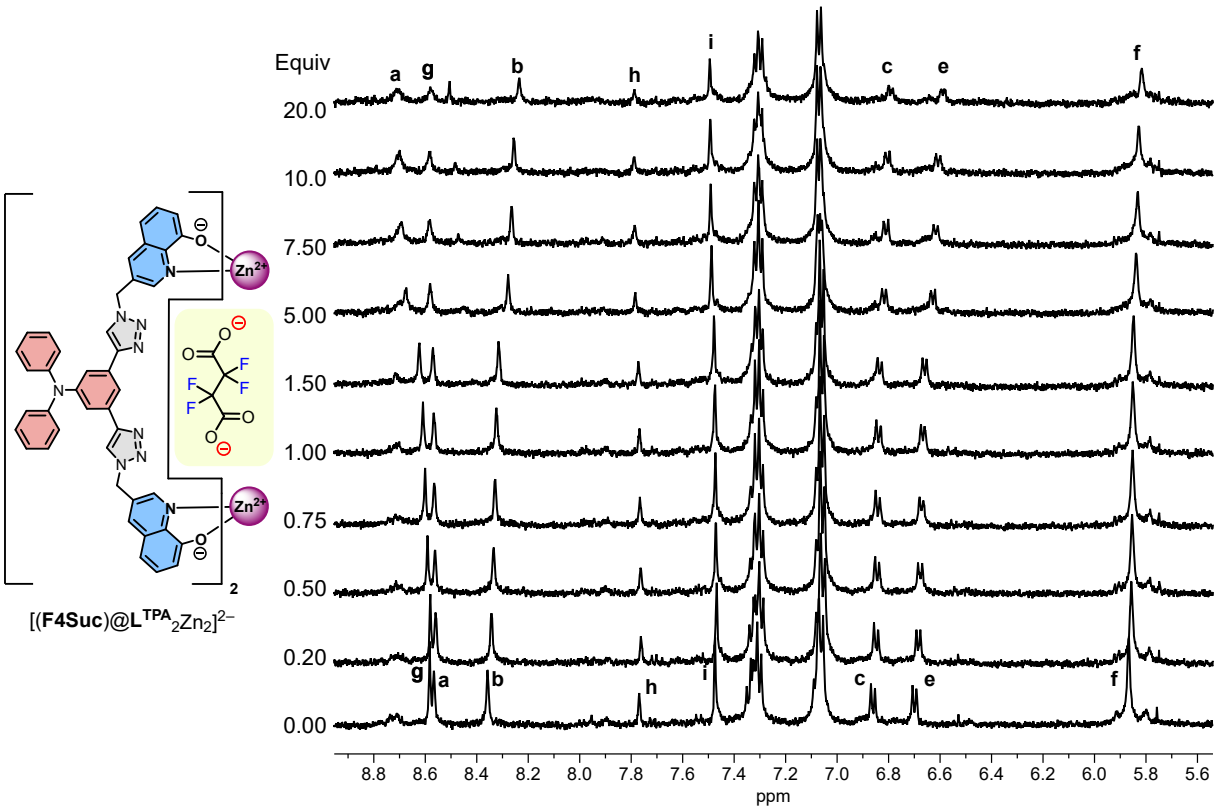

Figure 5.14 ^{1}H NMR titration of [$\mathbf{L}^{\mathbf{TPA}}{}_2Zn_2$] with 2,2,3,3-tetrafluorosuccinate (**F4Suc**$^{\mathbf{2-}}$) as TBA salts (500 MHz, 500 µM, DMSO-d$_6$, 298 K).

5.4.4.4 Hexadecafluorosebacate

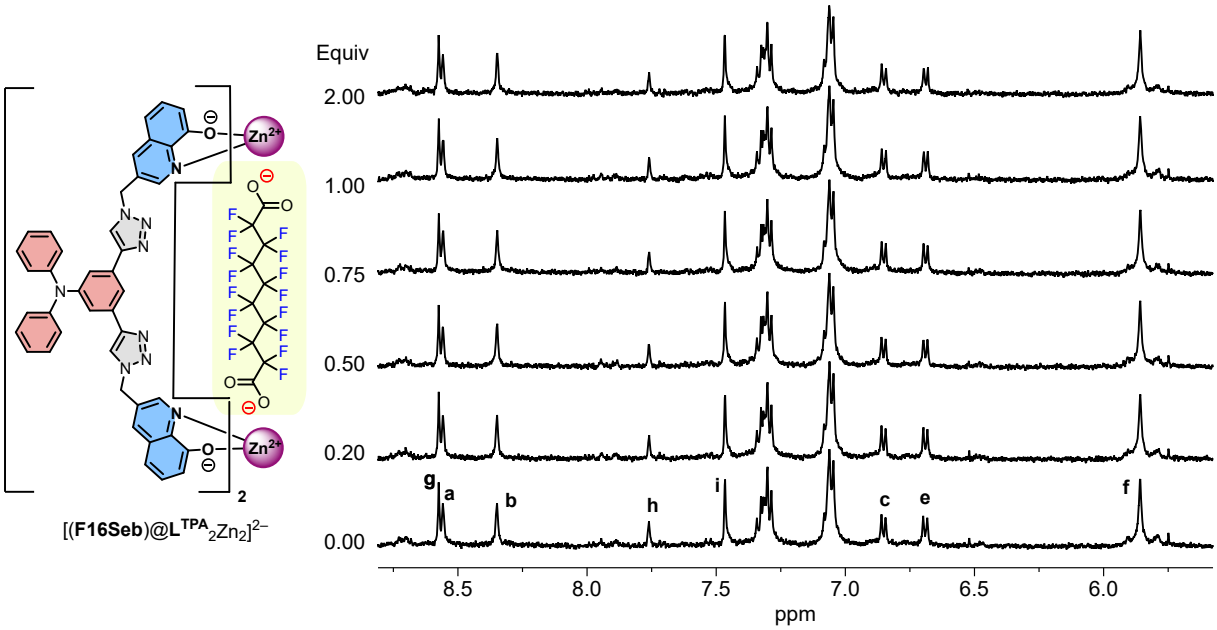

Figure 5.15 ^{1}H NMR titration of [$\mathbf{L^{TPA}}_2Zn_2$] with 2,2,3,3,4,4,5,5,6,6,7,7,8,8,9,9-hexadecafluorodecanedioate (**F16Seb^{2-}**) as TBA salts (500 MHz, 500 µM, DMSO-d_6, 298 K).

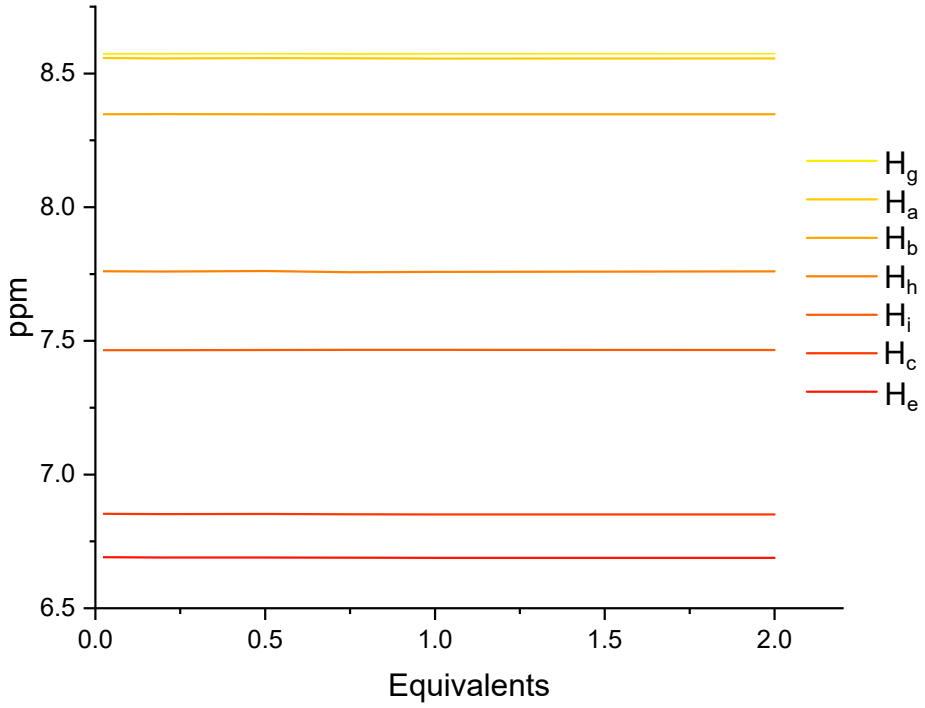

Figure 5.16 ^{1}H NMR peaks corresponding to protons H_g, H_a, H_b, H_h, H_i H_c, H_e are plotted against equivalents of (**F16Seb^{2-}**) shows no change upon guest addition until two equivalents.

5.5 References

[1] D. Van Craen, M. G. Kalarikkal, J. J. Holstein, *Journal of the American Chemical Society* **2022**, *144*, 18135–18143.

[2] M. G. Kalarikkal, C. Drechsler, G. Tusha, L. V. Schäfer, D. Van Craen, *Chemistry – A European Journal* **2023**, *29*, e202301613.

[3] J. Gemen, J. Ahrens, L. J. W. Shimon, R. Klajn, *Journal of the American Chemical Society* **2020**, *142*, 17721–17729.

[4] M. Vedamalai, S.-P. Wu, *Organic & Biomolecular Chemistry* **2012**, *10*, 5410–5416.

[5] Y. Wang, X. Wang, W. Ma, R. Lu, W. Zhou, H. Gao, *Chemosensors* **2022**, *10*, DOI 10.3390/chemosensors10100399.

[6] D. K. Iyer, A. Shaji, S. P. Singh, A. Tripathi, A. Hazra, S. Mandal, P. Ghosh, *Coordination Chemistry Reviews* **2023**, *495*, 215371.

[7] D. Cao, Z. Liu, P. Verwilst, S. Koo, P. Jangjili, J. S. Kim, W. Lin, *Chemical Reviews* **2019**, *119*, 10403–10519.

[8] A. Karak, S. K. Manna, A. K. Mahapatra, *Analytical Methods* **2022**, *14*, 972–1005.

[9] X.-M. Song, Z.-C. Feng, Y. Wu, J.-L. Song, L.-F. Wei, S.-Y. Zeng, *Journal of Molecular Liquids* **2022**, *365*, 120086.

[10] Y. Li, S. S. Rajasree, G. Y. Lee, J. Yu, J.-H. Tang, R. Ni, G. Li, Kendall. N. Houk, P. Deria, P. J. Stang, *Journal of the American Chemical Society* **2021**, *143*, 2908–2919.

[11] R. Ham, C. J. Nielsen, S. Pullen, J. N. H. Reek, *Chemical Reviews* **2023**, *123*, 5225–5261.

[12] N. Niamnont, N. Kimpitak, K. Wongravee, P. Rashatasakhon, K. K. Baldridge, J. S. Siegel, M. Sukwattanasinitt, *Chemical Communications* **2013**, *49*, 780–782.

[13] J. S. Wagner, M. A. Siegler, A. L. Tomlinson, J. R. Reynolds, *Advanced Optical Materials* **2024**, *12*, 2400855.

[14] B. W. Purse, J. Rebek Jr, *Chemical Communications* **2005**, 722–724.

[15] Z. Zheng, H. Yu, W.-C. Geng, X.-Y. Hu, Y.-Y. Wang, Z. Li, Y. Wang, D.-S. Guo, *Nature Communications* **2019**, *10*, 5762.

[16] T.-N. Gao, S. Huang, R. Nooijen, Y. Zhu, G. Kociok-Köhn, T. Stuerzer, G. Li, J. H. Bitter, G. I. J. Salentijn, B. Chen, F. M. Miloserdov, H. Zuilhof, *Angewandte Chemie International Edition* **2024**, *63*, e202403474.

[17] C. Zhong, Z. Wu, Y. Mao, B. Zhao, Y. Sun, M. Zheng, M. Zhou, G. Chang, Y. Xu, *New Journal of Chemistry* **2025**, *49*, 4376–4386.

[18] S. Breimaier, R. F. Winter, *European Journal of Organic Chemistry* **2021**, *2021*, 4690–4700.

[19] J. S. Train, A. B. Wragg, A. J. Auty, A. J. Metherell, D. Chekulaev, C. G. P. Taylor, S. P. Argent, J. A. Weinstein, M. D. Ward, *Inorganic Chemistry* **2019**, *58*, 2386–2396.

[20] F. H. Quina, G. T. M. Silva, *Journal of Photochemistry and Photobiology* **2021**, *7*, 100042.

[21] http://supramolecular.org/ (visited on 12/30/2022).

[22] P. Thordarson, *Chemical Society Reviews* **2011**, *40*, 1305–1323.

[23] D. B. Hibbert, P. Thordarson, *Chemical Communications* **2016**, *52*, 12792–12805.

6 CONCLUSION AND OUTLOOK

This thesis establishes a charge-neutral, double-stranded zinc(II) helicate, $[\mathbf{L^R}_2Zn_2]$, which serves as a versatile platform for anion recognition in polar media. The incorporation of stereodynamic triazole linkers imparts a controllable mechanism for the *meso*-to-racemate equilibrium, thereby facilitating the selective enrichment of one helicate enantiomer upon interaction with a chiral guest. Furthermore, a regulated guest exchange cycle was achieved via the introduction of a stimuli-responsive competing guest into this receptor system. Additionally, efforts to provide the receptor with colorimetric guest sensing capabilities were undertaken by integrating a triphenylamine moiety into the ligand architecture.

Chiral recognition of carboxylates, such as tartrate, facilitates the induction of preferential helicity, resulting in opposite mirror image CD profiles. This characteristic enables the helical receptor to act as a chiroptical probe for estimating enantiomeric excess (*ee*) within specified concentration parameters. The next step forward in this context would involve the modification of ligand design to incorporate a chiral moiety, thereby rendering the host inherently chiral rather than depending on induced helical chirality. This will give new means for enhanced chirality analysis and reliable enantiomeric excess (*ee*) determination.

To address the inability of guest release associated with strong coordinative binding, the incorporation of a stimuli-responsive guest molecule, azobenzene dicarboxylate, into the helicate receptor was explored. The process of photoisomerization under illumination at 365 nm results in the formation of a *cis*-enriched mixture. Wherein the *cis* isomer exhibits an optimal length and a stronger binding affinity compared to the *trans* isomer. When in the presence of a second guest possessing an intermediate level of affinity, this asymmetry facilitates a reversible light- and heat-gated guest exchange mechanism, including the photochemical capture of the switchable guest, thermal transfer to the competitor, and the capability for repeated cycling. In future research, the focus will be on extracting the desired guest released within suitable solvent environments. This can be accomplished by enhancing the solubility of the host, which will improve its compatibility with a range of solvent systems. Solubility, in general, has posed a disadvantage for our charge-neutral assemblies, thereby constraining their functional capabilities. This can be mitigated by incorporating appropriate solubilizing groups within the ligand architecture.

Furthermore, the photophysical properties of the ligand were modified by incorporating a triphenylamine (TPA) unit. Although the absorption characteristics were altered as anticipated, the expected enhancement in brightness and strong colorimetric contrast was not achieved, suggesting that the energy or charge transfer channels into the quinolinolate core are subtle and easily quenched. Simultaneously, perfluorinated carboxylates exhibited

consistently lower binding affinity compared to their non-fluorinated counterparts, underscoring the requirement for additional hydrogen bonding or stronger donor interactions. These results distinctly outline the advantages of the present scaffold as well as the aspects that require redesign. For accurate colorimetric results, it is preferable to use intense visible chromophores, such as BODIPY, rhodamine, and coumarin, strategically incorporated into the ligand. Quantum yields and time-resolved spectroscopy are the way forward to truly understand the photophysical properties of the modified hosts.

In conclusion, the L_2Zn_2 helicates exhibit sensitivity to the geometry of guest molecules, allowing for a modifiable helical preference that is reflected in measurable optical signals. Effective guest exchange is achieved by allocating control to the shape shifting guest instead of excessively modifying the host system. With these advancements, the working charge-neutral helicates exhibit promising potential as chiroptical probes and reversible exchange facilitators.

List of abbreviations

AB^{2-}	azobenzene-4,4'-dicarboxylate
Abe^{-}	abietate (deprotonated abietic acid)
AcO^{-}	acetate
ADC^{2-}	acetylenedicarboxylate
AIBN	azobisisobutyronitrile
ATP	Adenosine triphosphate
$BArF^{-}$	tetrakis[3,5-bis(trifluoromethyl)phenyl]borate
BF_4^{-}	tetrafluoroborate
BHandHLYP	Becke half-and-half LYP DFT functional
$BGlu^{-}$	*N*-Boc-*L*-glutamate
BODIPY	boron-dipyrromethene
$BPro^{--}$	*N*-Boc-*L*-prolinate
$BPip^{-}$	I-Boc-*L*-pipecolinate
BzO^{-}	benzoate
C4P	calix[4]pyrrole
CD	circular dichroism
CD_2Cl_2	deuterated dichloromethane
CD_3NO_2	deuterated nitromethane
CFTR	cystic fibrosis transmembrane conductance regulator
CPL	circularly polarized luminescence
CuAAC	copper-catalyzed azide–alkyne cycloaddition ("click")
D-TA^{2-}	*D*-tartrate
def2-SVP	split-valence polarized basis set
DFT	density functional theory
DMAP	4-dimethylaminopyridine
DMSO-d_6	deuterated DMSO
ECD	electronic circular dichroism
ee	enantiomeric excess
ESI-MS	electrospray ionization mass spectrometry
$F16Seb^{2-}$	perfluorosebacate (hexadecafluorodecanedioate)
$F4Suc^{2-}$	2,2,3,3-tetrafluorosuccinate
$F4TP^{2-}$	2,3,5,6-tetrafluoroterephthalate
$FBzO^{-}$	pentafluorobenzoate
Gaussian16	quantum-chemistry software package
GC	gas chromatography

Glt^{2-}	glutarate
HMBC	heteronuclear multiple-bond correlation (2D NMR)
HPLC	high-performance liquid chromatography
HRMS	high-resolution mass spectrometry
HSQC	heteronuclear single-quantum correlation (2D NMR)
HT^-	hydratropate (S-HT^-)
ICT	intramolecular charge transfer
ITC	isothermal titration calorimetry
LED	light-emitting diode (irradiation source)
LOQ	limit of quantification
MeCN	acetonitrile
MeOH	methanol
NBS	N-bromosuccinimide
NOESY	nuclear Overhauser effect spectroscopy (2D NMR)
NP^-	2-(6-methoxy-2-naphthyl)propionate
NMR	nuclear magnetic resonance
OTf^-	trifluoromethanesulfonate (triflate)
PEAQ-ITC	MicroCal PEAQ-ITC instrument/software
PF_6^-	hexafluorophosphate
PFAS	Per- and Polyfluoroalkyl Substances
PFOA	Perfluorooctanoic Acid
PFOS	Perfluorooctanesulfonic Acid
PFNA	Perfluorononanoic Acid
PFHxS	Perfluorohexanesulfonic Acid
qCD	Chirascan qCD spectropolarimeter model
r2SCAN-3c	composite meta-GGA DFT method
SFC	supercritical fluid chromatography
TBA	tetrabutylammonium (counter-cation)
TBTA	tris(benzyltriazolylmethyl)amine (CuAAC ligand)
TD-DFT	time-dependent density functional theory
TLC	thin-layer chromatography
TMS	trimethylsilyl (protecting group/reagent)
TPA	triphenylamine
UV-Vis	ultraviolet–visible spectroscopy
VIE	vibration-induced emission
VT-NMR	variable-temperature NMR

Acknowledgements

As I reach the final chapter of my PhD, I'm filled with gratitude. Applying for a PhD abroad was one of the best decisions of my life as it changed my course for the better.

First, my deepest thanks to my supervisor, Dr. David Van Craen. It's been an honor to be the first member of your lab and the first student to graduate under your guidance. Thank you for making my first days in Germany feel easy, for involving me in your research and publications, and for consistently giving me clear, thoughtful ideas and support.

I'm also sincerely grateful to Prof. Guido Clever for welcoming us into your group, providing everything I needed for my work, and serving as my co-examiner. Your leadership and research continue to inspire me. Being part of the Clever lab, a large, diverse, motivated, friendly, and supportive team, made this journey so much smoother.

I thank the graduate school GRK 2376 for the interdisciplinary training, networking, and collaborations. Your support let me attend international conferences, meet inspiring scientists, and see more of the world.

Even as a small team, the Van Craen lab achieved a lot. David Ocklenburg, you were my only lab-mate for years. Thank you for making my early scientific days in Germany enjoyable. Abhinu, you joined later but lit up the lab. I never expected to have a Malayali lab-mate. Always keep that brilliant smile, you'll do great leading the lab ahead.

To everyone in Cleverlab, past and present, thank you for every quick favor, corridor question, and friendly chat. Sudhakar, thank you for helping me find people and accommodation when I arrived here. Irene, Jacopo, Qianqian, and Shing (even though you left early), I'm grateful. Hasi, you goofy ball, I think of you often, especially since I'm living in your former home. Thanks for passing it on. André and Christina, I've always felt a sisterly warmth from you both. Christoph, collaborating with you, really took my project to the next level. Alex and Elie, we shared the most conferences and GRK sessions. Elie, your sharp mind helped my science a lot. Alex, thanks for the camping lessons, the pasta recipe, and your company through travels, parties, and everything in between. Laura, we still have plans to finish. Can't wait for our next photo walk. Ertugrul, you were my go-to person for the fume hood, chemicals, anything, your helpful spirit was a gift, and I felt your absence when you left. Björn, you've been a great support and are the soul of Cleverlab's social life. Aleks and Joseph, your knowledge and willingness to help, even while juggling a million things, made a real difference. Aiswarya, as both a colleague and roommate, I'm lucky to have you to share the highs and the hard days. Armin, Lars, Jenny, Shaian, Julian, Laura S, Franzi, and Kathrin, you matter just as much, and I thank you.

A big thank you to the team who keeps everything running behind the scenes: Gabi, Birgit, Astrid, Christina, and Maike. Navigating in a foreign administration was not easy; your help at every step has made it possible.

Outside the lab, I found people who taught me to enjoy a very different kind of life and I grew to love it. Amrutha, Vivek, and Arjun: those lunch breaks, venting and laughing, kept me sane. Devu, you have been an amazing roommate and companion. Akhil and Neelima, you were wonderful additions. And to friends spread around the world, Annu (bestie), Thoma, PK, Kavya, Shradha, Anagha, Anandhu, Honey (and more!) thank you for staying close across the distance.

Finally, my constant backbone: my family. Achan and Amma, I could not ask for better parents. You always believed in me; I was always the number one in your eyes. Now I can finally place my thesis on the shelf beside Achan's PhD thesis, which has always been the dream. To my lovely sister, I do not think I can ever repay the love and support you give me. Sugin, the newest member of our family, you make it feel complete. To my cousins and extended family, thank you for sharing every bit of joy along the way. And to my partner, thank you for the long, reassuring talks, the steady support, and care. You are just as much a part of this achievement as I am.

If there's one lesson I'm taking with me, it's this: there will always be people who try to minimize what you have done. Believe in yourself, find a few kind people who have your back, and keep going. With the right mindset, so much is possible.